

Optical Feedback Effects within 1.55 µm InP-Based DFB Laser integrated Mach-Zehnder Modulators for up to 100 GBd Data Transmission

vorgelegt von

M.Sc.

Sophie Gloria Lange

geb. in Berlin

von der Fakultät IV – Elektrotechnik und Informatik
der Technischen Universität Berlin
zur Erlangung des akademischen Grades

Doktor der Ingenieurwissenschaften
- Dr.-Ing. -

genehmigte Dissertation

Promotionsausschuss:

Vorsitzender:	Prof. Dr. Bernd Szyszka
Gutachter:	Prof. Dr. Klaus Petermann
Gutachter:	Prof. Dr. Martin Schell
Gutachter:	Prof. Dr.-Ing. Markus-Christian Amann

Tag der wissenschaftlichen Aussprache: 15. Oktober 2018

Berlin 2019

I. Zusammenfassung

Es werden optische Transmitter in Indiumphosphid-Technologie mit einer Wellenlänge von 1550 nm, für Intra- und Inter-Data-Center-Transceiver-Module der nächsten Generation, mit einer Reichweite von einigen bis zu einigen zehn Kilometern entwickelt. Transceiver-Module für zukünftige Datenzentren benötigen gleichzeitig eine hohe Geschwindigkeit, einen geringen Leistungsverbrauch und niedrige Kosten. Diese Herausforderungen werden gelöst, indem ein Wanderwellenelektroden Mach-Zehnder oder In-Phase und Quadrature (IQ)-Modulator, mit hoher Bandbreite und niedriger Schaltspannung, zusammen mit einem Laser mit verteilter Rückkopplung (DFB Laser), auf demselben Chip integriert wird. Die monolithische Laserintegration führt zu einer kleineren Transmittergröße, nahezu vernachlässigbaren Koppelverlusten am Laser-Modulator Übergang, einer geringeren Montagezeit und einem geringeren Montageaufwand, was die Transmitter Leistungs- und die Kosteneffizienz erhöht. Die hergestellten DFB Laser Mach-Zehnder/ IQ-Modulator Transmitter haben vergleichbare Dimensionen wie Referenz-Mach-Zehnder/ IQ-Modulatoren, ohne Laser und liefern niedrige 2 V-Schaltspannungen und 3-dB-Bandbreiten bis zu 54 GHz.

Ein Nachteil der monolithischen Integration ist die fehlende Laser-Modulator Isolation. Obwohl die Auswirkungen der passiven und dynamischen optischen Rückkopplung auf das Laserverhalten intensiv untersucht wurden, sind die Auswirkungen auf Datensignale verschiedener Modulationsformate nicht bekannt. Diese Arbeit konzentriert sich daher auf die theoretische und experimentelle Untersuchung der Leistung der entwickelten DFB-Laser-Mach-Zehnder/ IQ-Modulator Transmitter unter optischer Rückkopplung. Basierend auf den Lang-Kobayashi-Gleichungen wird ein Simulationsmodell erzeugt. Die Ergebnisse zeigen, dass die Transmitter unter der schwachen optischen Rückkopplung des Regimes I eine Selbstphasenmodulation erzeugen, insbesondere bei Modulationsfrequenzen unterhalb der Laserrelaxationsfrequenz. Die Selbstphasenmodulation beeinflusst die Qualität gemessener intensitätsmodulierter Signale kaum. Phasenmodulierte Binär- und Quadraturphasenumtastungs (BPSK und QPSK)-Signale hingegen, zeigen erhöhte Phasenschwankungen und Fehlervektorgrößen bei Modulationsfrequenzen kleiner 25 GHz. Bei höheren Modulationsfrequenzen verringert sich der Einfluss der modulierten optischen Rückkopplung und die Fehlervektorgrößen der BPSK und QPSK Signale sind hauptsächlich linienbreitenabhängig. Transmitter Simulationen und Messungen zeigen, dass auch die Laserlinienbreite von der optischen Rückkopplung beeinflusst wird, abhängig vom Transmitterarbeitspunkt.

Trotz der optischen Rückkopplung wird eine gute Transmitter Leistung bei optimaler Transmitterarbeitspunktauswahl und bei Modulationsfrequenzen größer als 25 GHz erreicht. 32 GBd QPSK-Betrieb mit einer Fehlervektorgröße kleiner 10% und niedriger 3 V_{pp} Modulationsspannung wird mit einem DFB-Laser IQ-Modulator Transmitteraufbau mit differenziellem Treiber demonstriert. Der Transmitteraufbau hat einen geringen 1,1 W Leistungsverbrauch, was dem angestrebten Leistungsbudget entspricht. Zum ersten Mal wird auch eine Signalübertragung von 100 Gb/s Non-Return-To-Zero (NRZ)-Wechselschrift über bis zu 1,8 km und 200 Gb/s 4-Level Pulsamplitudenmodulation (PAM4)- über 1,2 km mit einem monolithischen DFB-Laser Mach-Zehnder Modulator Transmittermodul demonstriert. Digitale Signalverarbeitung wird dabei verwendet, um Transmitter-Imperfektionen sowie Rauschen zu kompensieren. Das Transmittermodul ist besonders attraktiv für Zwei-Kanal-400 Gbit/s Anwendungen mit kurzen Reichweiten.

II. Abstract

Indium phosphide-based 1550 nm wavelength optical transmitters are developed, suitable for next generation transceiver modules for intra- and inter-data center connections from a few kilometers to tens of kilometers range. The challenges of designing high-speed, low power and low-cost transceivers for future data centers are met by integrating a high bandwidth and low switching voltage travelling wave electrode Mach-Zehnder or in-phase and quadrature (IQ) modulator, on the same chip with a distributed feedback (DFB) laser. The monolithic laser integration leads to a smaller transmitter size, almost zero coupling loss at the laser modulator interface and less assembly time and effort, making the transmitters power and cost efficient. The fabricated DFB laser Mach-Zehnder/ IQ modulator transmitters have a comparable footprint as the reference Mach-Zehnder/ IQ modulators and provide low 2 V switching voltages and up to 54 GHz 3-dB bandwidths.

A drawback of the monolithic integration is the missing isolation between the laser and the modulator. Although, the effects of passive and dynamic optical feedback on the laser behavior has been intensively studied, the effects on modulated signals are not well known. Thus, this work focusses on the theoretical and experimental investigation of the developed DFB laser Mach-Zehnder/ IQ modulator transmitter performance with optical feedback. A simulation model of a laser with passive and modulated optical feedback is generated, based on the Lang-Kobayashi equations. The results show that the weak optical feedback of regime I leads to a transmitter self-phase modulation, especially at modulation frequencies lower than the laser relaxation oscillation frequency.

In the transmitter measurements, the self-phase modulation barely affects the performance of intensity modulated signals. Phase modulated binary and quaternary phase shift keying signals, however, suffer from increased phase variations and error vector magnitudes at modulation frequencies up to 25 GHz. At higher modulation frequencies, the influence of the modulated optical feedback diminishes, and the transmitter binary and quaternary phase shift keying (BPSK and QPSK) error vector magnitudes are mostly linewidth dependent. Simulations and measurements show that the laser linewidth is affected by the optical feedback, depending on the transmitter bias point. Thus, a careful bias point selection is important to achieve the best performance of DFB laser Mach-Zehnder/ IQ modulator transmitters with optical feedback.

Despite the weak optical feedback, a good transmitter performance is achieved at the optimum bias point and at modulation frequencies larger than 25 GHz. 32 GBd QPSK operation with an error vector magnitude less than 10% and a low modulation voltage of 3 V_{pp} is demonstrated with a DFB laser IQ modulator transmitter with differential driver subassembly. The transmitter subassembly has a low power consumption of 1.1 W, which complies with the targeted transceiver module power budget. For the first time, 100 GBd operation is demonstrated with a packaged monolithic DFB laser Mach-Zehnder modulator transmitter module. Digital signal processing is utilized to overcome transmitter imperfections as well as noise limitations. 100 Gb/s non-return-to-zero (NRZ) on-off keying transmission over up to 1.8 km and 1.2 km 200 Gb/s 4-level pulse amplitude modulation (PAM4) transmission at a 1550 nm wavelength is achieved, making the device attractive for dual-lane 400 Gb/s short reach applications.

III. Table of Contents

I.	Zusammenfassung.....	3
II.	Abstract	5
III.	Table of Contents	6
1.	Introduction	9
1.1	Motivation	9
1.2	Goals of this work	13
1.3	Structure and Methodology of this Work	13
2.	Optical Transmitters	15
2.1	Single Mode Lasers	15
2.1.1	Structure.....	15
2.1.2	Distributed Feedback (DFB) and Distributed Bragg Reflector (DBR) Lasers	17
2.1.3	Direct Modulation	19
2.2	Optical Modulators	19
2.2.1	Electro-Optic Effects.....	20
2.2.2	Electroabsorption Modulator.....	21
2.2.3	Mach-Zehnder Modulator	21
2.2.4	Signal Electrode	26
2.2.5	In-Phase and Quadrature Mach-Zehnder Modulator (IQM)	28
2.3	Modulation Formats	29
2.4	Transmitter Integration	31
2.4.1	Hybrid Integration.....	31
2.4.2	Heterogeneous Integration	31
2.4.3	Monolithic Integration.....	31
2.4.4	Integration Platforms.....	32
3.	State of the Art: Monolithic Transmitters in Indium Phosphide	33
3.1	Electroabsorption Modulated Laser (EML).....	33
3.2	Laser Mach-Zehnder Modulator.....	33
3.3	Laser In-Phase and Quadrature (IQ) Mach-Zehnder Modulator.....	33
4.	1550 nm DFB Laser Integrated Mach-Zehnder/ IQ Modulator Transmitter PICs	35

4.1	Transmitter Photonic Integrated Circuit (PIC) Architectures	35
4.2	Distributed Feedback (DFB) Laser Section.....	37
4.3	Mach-Zehnder Modulator Section.....	40
4.4	Fabrication Process.....	42
4.5	Performance.....	48
4.5.1	Reference DFB Lasers	49
4.5.2	DFB-Laser Mach-Zehnder/ IQ Modulator Transmitter Photonic Integrated Circuits.....	61
4.5.3	Direct current (dc) Characterization.....	61
4.5.4	Mach-Zehnder Modulator Model.....	66
4.5.5	Electro-Optic Modulation Response	68
5.	1550 nm DFB Laser Integrated Mach-Zehnder/ IQ Modulator Transmitter Module/ Subassemblies	72
5.1	DFB Laser Mach-Zehnder Modulator Transmitter Optical Subassembly (TOSA) Module.....	72
5.1.1	Architecture.....	72
5.1.2	Optical Spectrum, Relative Intensity Noise and Linewidth	73
5.1.3	Electro-Optic Modulation Response	78
5.1.4	Transient Chirp.....	79
5.1.5	Large Signal Operation	81
5.2	DFB laser IQ modulator Transmitter Subassembly with Dual Differential Driver	90
5.2.1	Architecture.....	90
5.2.2	Optical Spectrum, Relative Intensity Noise and Linewidth	92
5.2.3	Large Signal Operation	94
6.	Theoretical Study of Lasers with Optical Feedback.....	102
6.1	Laser with Optical Feedback: Passive Behavior.....	102
6.2	Laser with Optical Feedback: Dynamic Behavior	104
6.2.1	Lang Kobayashi Model	104
6.2.2	Steady state model of Laser with Optical Feedback.....	106
6.2.3	Laser Linewidth with Optical Feedback.....	107
6.2.4	Laser without Optical Feedback.....	108
6.2.5	Laser with Passive Optical Feedback	110
6.2.6	Laser with Dynamic Optical Feedback (Sine-Wave).....	115
7.	Optical Feedback within DFB Laser Mach-Zehnder/ IQ Modulator Transmitter PICs	121

7.1	Sources of Optical Feedback within the DFB laser Mach-Zehnder/ IQ Modulator Transmitters	122
7.1.1	Laser Linewidth of DFB Laser Mach-Zehnder Modulator Transmitter with Optical Feedback ...	125
7.2	Effects of Opt. Feedback inside DFB Laser Mach-Zehnder Modulator Transmitters on Modulated Signals	130
8.	High-speed Operation of DFB laser Mach-Zehnder/ IQ Modulator Transmitter Module/ Subassembly ...	135
8.1	DFB Laser Mach-Zehnder Modulator Transmitter Module 100 GBd Operation.....	135
8.2	32 GBd QPSK operation of DFB Laser IQ Modulator Subassembly with Differential Driver.....	139
9.	Conclusions and Outlook	143
IV.	Appendix.....	146
IV.I	Runge-Kutta Solver	146
IV.II	Error Vector Magnitude Calculation	147
V.	List of Abbreviations.....	149
VI.	List of Symbols	153
VII.	Acknowledgments.....	158
VIII.	Published Work.....	159
IX.	References.....	161

1. Introduction

1.1 Motivation

Communication networks are spanned around the world to transfer data for various applications, like the internet. While long haul and submarine networks cover long distances between countries and continents, metropolitan networks connect local networks inside the cities. During the last years, the global internet traffic has increased dramatically and keeps growing continuously. Especially, in metropolitan networks the traffic is expected to grow more than twice as fast as in long-haul systems in the next years [1]. In data centers, the traffic is strongly expanding, due to cloud services and digital media [2]. Data rates of up to 400 Gb/s and 1.6 Tb/s are currently under discussion for future metro and short reach systems [3], [4]. Fiber-optic communication is mandatory to provide the required capacity for the networks. A typical optical link from the data source to the sink consists of transmitter (TX) electronics and optics, a communication channel and receiver (RX) optics and electronics (Fig. 1).

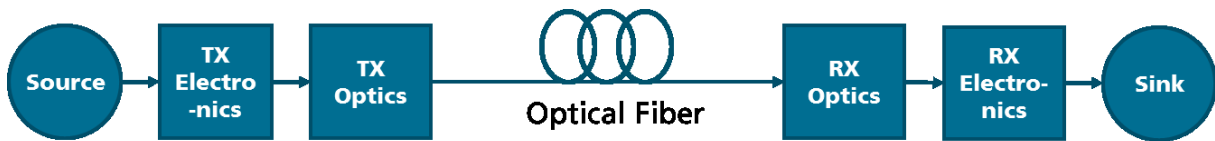


Fig. 1. Typical optical link structure.

The transmitter and receiver optics and part of the electronics are embedded into optical transceiver modules, which are placed into the network nodes, such as rack servers, switches and routers, and connected to the optical fiber channel. Due to the massive traffic growth during the last years, optical transceiver solutions for 100 Gb/s, 200 Gb/s and 400 Gb/s are required, which should be scalable to 1.6 Tb/s. Transceiver modules are evolving in terms of form factor, power consumption and speed [2], [5].

The main challenges in the transceiver development are to meet the requirements for a higher bit rate, while supporting higher-order modulation formats and satisfying the key factors of high bandwidth, low power consumption, small footprint and low cost.

The simplest modulation format is non-return-to-zero (NRZ) on-off keying, where the electrical signal is modulated onto the light's intensity, so that a digital “1” corresponds to a higher intensity level than a “0”. An optical NRZ signal eye diagram, where the optical bits are overlaid for easier signal quality evaluation, is displayed in Fig. 2.

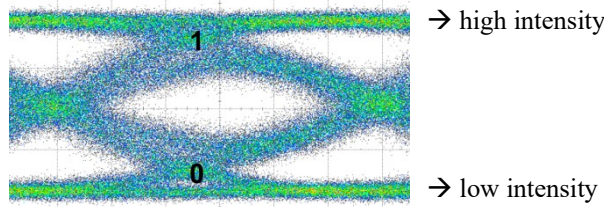


Fig. 2. Optical NRZ signal eye diagram.

Due to bandwidth limitations of the electrical and optical components, bit rates of 100 Gb/s and higher are difficult to achieve with NRZ. A promising solution is to increase the spectral efficiency by using higher order modulation formats, including more than one bit per symbol. 4-pulse amplitude modulation (PAM4), for example, consists of four intensity levels with each level corresponding to a combination of two bits (Fig. 3).

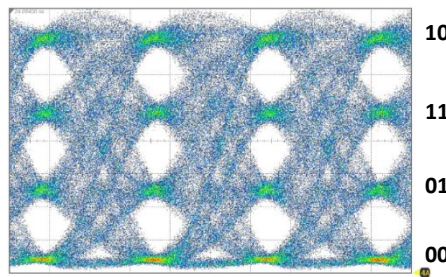


Fig. 3. Optical PAM4 signal eye diagram.

The advantage of PAM4 is, that with the same bandwidth requirements as NRZ, twice the bit rate is achieved. Other modulation formats with a higher spectral efficiency, such as PAM8 with eight intensity levels or discrete multitone, are more complex to generate and receive. Thus, for 100 Gb/s links, PAM4 is probably the most attractive choice. Intensity modulated signals are received with simple and cost-efficient direct detection, making intensity modulation and direct detection (IMDD) schemes especially promising for short reach links from 0.5 to 5 km, where simple and cost effective solutions are necessary [6]. To reach higher data rates and longer transmission distances, coherent detection is a key technology. Although, the coherent receiver is more complicated and has a larger power consumption, cost and size, as the direct detection one, it enables advanced digital signal processing, giving increased flexibility and robustness against transmission impairments. With a coherent receiver, not only the light's intensity but also its phase is detected. This opens a two-dimensional symbol space, where a high spectral efficiency is reached. Using quaternary phase shift keying (QPSK) and 16-quadrature amplitude modulation (QAM16), two or four bits are encoded per symbol, respectively. Coherent technologies are currently a standard for long reach optical systems [7] and are gaining more and more interest for future high speed metro systems with tens of km range [6].

To achieve bit rates of 400 Gb/s and higher in a single link, several channels are multiplexed in frequency, polarization or time. Different combinations of channel rate and channel count are possible to reach 400 Gb/s, e.g. 8×50 Gb/s, 4×100 Gb/s or 2×200 Gb/s. While with a high channel rate and a low channel count, the optical link is less bulky, the bandwidth requirements for the electrical and optical components increase. A good compromise for a 400 Gb/s link is the 4×100 Gb/s configuration. Employing higher-order modulation formats, is an attractive way to increase the transceiver bit rate. How to meet the other transceiver requirements of low power consumption, high bandwidth, small footprint and low cost is the topic of this work. The final goal is to 10

develop optical transmitters for intra- and inter-data center connections from a few km to tens of km range, suitable for the CFP4 module [5].

Photonic integrated circuits (PICs), combining several optical components on a single chip, are a promising solution to fulfil the transceiver requirements. Integrating the transmitter, which typically consists of a light source and a modulator, on a single chip is a fundamental step to reduce the transceiver power consumption, due to almost lossless coupling.

Currently, the most popular transceiver optics material platforms are silicon and indium phosphide (InP). The silicon technology is well established, due to the history of manufacturing low cost electrical integrated circuits for the mass-market industry in the last decades [8]. Another advantage of silicon is the small form factor of the devices, while the main draw-back is the challenging integration of the light source. Contrary to silicon, the InP platform allows for full integration of active and passive components, on a common material system, which is referred to as monolithic integration. InP photonic integrated circuits, combining more than 170 functionalities on a single chip have been presented [9]. Since a small transceiver size is wanted, the InP platform is chosen for this work.

The simplest and cheapest InP transmitter is the directly modulated laser (DML). Transmissions of up to 56 Gb/s NRZ over 10 km [10] and 112 Gb/s PAM4 over 2 km [11] at 1.3 μm wavelength have been achieved with directly modulated lasers. For higher modulation rates and transmission distances, external intensity modulators are integrated with the laser. Two common types are the electroabsorption modulators (EAM) and the Mach-Zehnder modulator (MZM). The Mach-Zehnder modulator has larger dimensions as the directly modulated laser and the electroabsorption modulator, but benefits from a larger bandwidth [12] and almost zero chirp, which increases the transmission range. Moreover, two Mach-Zehnder modulators can be easily combined to form an in-phase and quadrature (IQ) modulator for coherent applications.

For this work, transmitters for up to tens of km range and a high bandwidth are desired, where the laser integrated Mach-Zehnder modulator is the best candidate. In particular, the travelling wave electrode Mach-Zehnder modulator is favored. Although, a lumped electrode is simpler, it must be short to achieve a high bandwidth, giving it a low efficiency. The travelling wave electrode solves the problem by segmenting the electrode, so that it provides at the same time a high bandwidth and a good efficiency. Previously, several InP-based travelling wave electrode Mach-Zehnder modulators [13]–[15] and IQ modulators [12], [15]–[18] have been demonstrated for operation at 100 Gb/s and beyond.

In this work, travelling wave electrode Mach-Zehnder and IQ modulators are integrated with a laser. The monolithic laser integration, optimally, eliminates the coupling loss, reducing the transmitter power consumption. An external laser is either located inside the module, coupled with coupling optics, such as lenses and isolators, or outside, requiring an additional optical fiber. The monolithic integration saves material costs for the fiber and coupling optics and 50 % of the coupling time and effort, improving the transceiver cost, arising mainly due to packaging. The challenge of the monolithic laser integration is that the previous laser and modulator structures are

different in general, in terms of width, thickness and crystal direction. Integrating the laser and the modulator with negligible coupling loss, without increasing the chip size and decreasing the performance, is one goal of this work.

A drawback of the monolithic transmitter integration is that an isolator between the laser and the other components is difficult to realize. Due to internal reflections, e.g. at the chip facets, the laser is exposed to optical feedback, influencing its performance (Fig. 4).

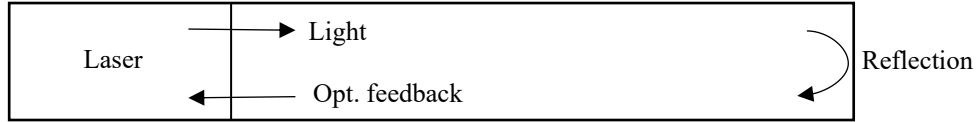


Fig. 4. Optical feedback within a monolithic transmitter chip.

The optical feedback effects on lasers with reflections from passive external cavities outside and inside the chip have been intensively studied [19]–[22]. Since reflections from outside the chip can be mainly suppressed, this work focusses on the remaining reflections inside the photonic integrated circuit. The difference of an integrated modulator to a passive external cavity is, that the reflected light is dynamically modulated in its intensity and phase. Only a few papers on the impact of modulated optical feedback on the laser have been published so far [23]–[25]. The impact of the modulated feedback on the performance of data transmissions is unknown, yet. Especially, higher-order modulation formats, are sensitive to intensity or phase fluctuations of the laser, which are caused by optical feedback. Thus, the second important goal of this work is to investigate experimentally and theoretically the impact of optical feedback on the laser integrated transmitter performance.

The photonic integrated circuit development process is structured as follows:

- 1) Design and simulation
- 2) Process development
- 3) Computer assisted design (CAD) layout
- 4) Fabrication
- 5) Characterization
- 6) Assembly and packaging
- 7) Transmission experiments

All seven steps are covered in this work. The design and simulation of the transmitters is based on previously developed distributed feedback (DFB) laser and travelling wave electrode Mach-Zehnder modulator devices at 1550 nm wavelength, which are optimized and merged for the integration on a single chip. The laser and modulator fabrication processes are efficiently combined into a single one and the transmitters manufactured at Fraunhofer HHI. The focus of this work lies on the characterization and performance evaluation of Mach-Zehnder and IQ modulator transmitter photonic integrated circuits with integrated DFB laser, compared to stand-alone laser and modulator devices.

1.2 Goals of this work

The goals of this work are:

- to develop, fabricate, characterize and operate optical 1550 nm transmitter modules and subassemblies, which
 - consist of an optical InP transmitter photonic integrated circuit, with a DFB laser and a travelling wave electrode Mach-Zehnder or IQ modulator, and
 - are suitable for next generation C form-factor pluggable 4 (CFP4) transceiver modules for intra- and inter-data center connections from a few km to tens of km range,
- to investigate the impact of optical feedback on the developed and fabricated transmitter photonic integrated circuit performance experimentally and theoretically.

To the best of my knowledge, the impact of optical feedback within DFB laser integrated travelling wave electrode Mach-Zehnder modulator transmitters have not been considered, yet. Especially the impact on data transmissions of higher-order modulation formats is unknown so far.

1.3 Structure and Methodology of this Work

In chapter 2, an introduction to optical transmitters and the modulation formats in optical transmission links is given. In particular, the structure and working principles of the DFB laser and the travelling wave electrode Mach-Zehnder modulator are explained. The ways to integrate the laser and the modulator are discussed and the different material platforms are compared.

The InP platform is chosen for the transmitter fabrication. A state of the art of InP-based monolithic transmitter photonic integrated circuits is given in chapter 3.

The design, fabrication and characterization of the developed DFB laser Mach-Zehnder modulator/ IQ modulator transmitter photonic integrated circuits is described in chapter 4.

For transmission experiments, long-term experiments and easier handling, the transmitters are embedded into modules or subassemblies. The transmitter module and subassembly structures and their characterization are described in chapter 5.

To study the effects of passive and modulated optical feedback on the device performance, a theoretical overview of optical feedback effects on lasers is given in chapter 6. A rate equation-based laser-modulator model is developed and numerical examples for the influence of passive and dynamic optical feedback on integrated lasers are given.

In chapter 7, the influence of optical feedback, in particular on the developed DFB laser Mach-Zehnder and IQ modulator photonic integrated circuits is considered. Simple models to estimate the optical feedback effects on the integrated laser linewidth are implemented. Moreover, the rate equation-based laser-modulator model from chapter 6 is extended, to show the effects of modulated optical feedback on the modulated signal performance. The simulation results from chapter 6 and 7 are compared with the DFB laser Mach-Zehnder and IQ modulator

measurement results from chapter 4 and 5, to find the optimum operating conditions for the transmitters with optical feedback.

Finally, in chapter 8, the DFB laser Mach-Zehnder/ IQ modulator transmitter modules are operated under optimum conditions, to achieve high-speed data transmissions for short reach application and in chapter 9, the conclusions and outlook are given.

2. Optical Transmitters

The main task of an optical transmitter in communication systems is to convert electrical input data into corresponding optical output signals (Fig. 5).

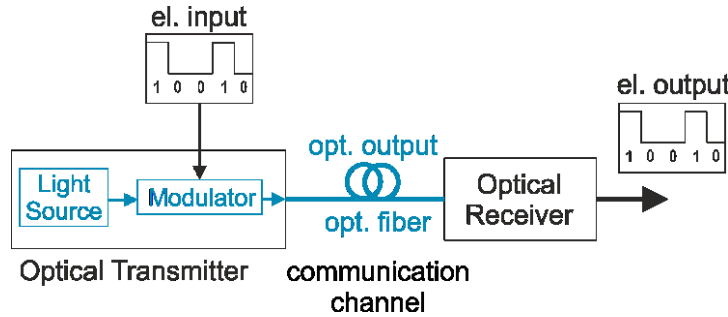


Fig. 5. Basic structure of an optical transmitter in an optical link.

The signal is launched into the optical fiber of the connected communication network, converted into the electrical domain by suitable photodetectors and demodulated by receiver electronics. The basic layout of an opt. transmitter consists of a light source (e.g. laser) and a modulator. The monolithic laser modulator integration is attractive for the next generation transceiver modules, due to its potential advantages in terms of footprint, packaging effort, number of optical interfaces, power consumption, robustness and cost. The laser and modulator building blocks and their integration capabilities are described in the next sub-chapters.

2.1 Single Mode Lasers

In fiber-optic communication systems, semiconductor components like light emitting diodes (LEDs) or lasers are used as light sources, due to their advantages in size, cost and having the right wavelength range. The performance of lasers, generating coherent light with stimulated emission, is superior in terms of angular spread, output power and spectral width compared to LEDs, which generate light using spontaneous emission. Single mode lasers, like InP-based distributed feedback (DFB) lasers or tunable distributed Bragg reflector (DBR) lasers, are required for the targeted transceiver modules and are thus the preferred light sources [26].

In this work, optical transmitters for intra- and inter-data center connections are developed. For intra-data center connections of tens of kilometer range, a wavelength around the loss minimum at 1550 nm of standard single mode optical fibers (SSMF) is favorable. This wavelength range is referred to as the C-band (1530- 1565 nm). In intra-data center connections of up to a few kilometers, the chromatic dispersion is a bigger issue than the loss. Thus, lasers with a wavelength in the O-band (1260- 1360 nm), around the 1310 nm zero dispersion wavelength, are preferred.

2.1.1 Structure

In semiconductor components, the light is guided through waveguides, where the core is made of a higher refractive index material than the cladding layers. In the active parts, typically a pin diode structure is implemented, with p- and n-doped cladding layers and an intrinsic active layer. The laser pin diode is operated by applying a bias current in forward direction. Through stimulated emission, photons with energy larger than the active material

bandgap energy $E_{\text{gap}} = E_c - E_v$ are generated, where E_c corresponds to the conduction and E_v to the valence band energy (Fig. 6).

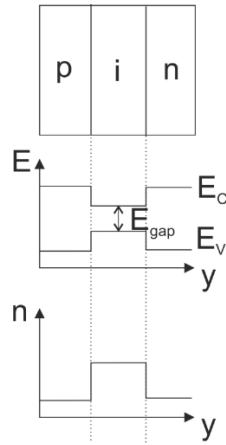


Fig. 6. Double-heterostructure pin diode; structure, energy band diagram and refractive index n in vertical direction.

The cladding material bandgap energy is larger than the active material one, to avoid light absorption in the claddings and to confine the electrical carriers in the active region [27]. This structure is referred to as double-heterostructure pin diode, providing at the same time optical and electrical confinement.

Instead of a bulk active layer, typically thin multi quantum well (MQW) layers are used, increasing the carrier confinement and the probability of recombination. The advantages of multi quantum well lasers are an increased efficiency, a higher spectral purity and a decreased active volume, lowering the threshold current, compared to bulk active layers [27]. By applying compressive strain to the quantum well layers, the threshold current and differential gain in the transverse electric polarization direction is even further improved [27]. Since one or a few quantum wells are too thin to confine the optical wave, the active region is enlarged with separate confinement heterostructure (SCH) layers, enclosing the multi quantum wells.

For lateral confinement, commonly implemented waveguide architectures are of ridge waveguide (RW) or buried heterostructure (BH) type. In shallow ridge waveguides (Fig. 7a), the cladding is etched to just above the active region, providing current confinement and weak optical confinement.

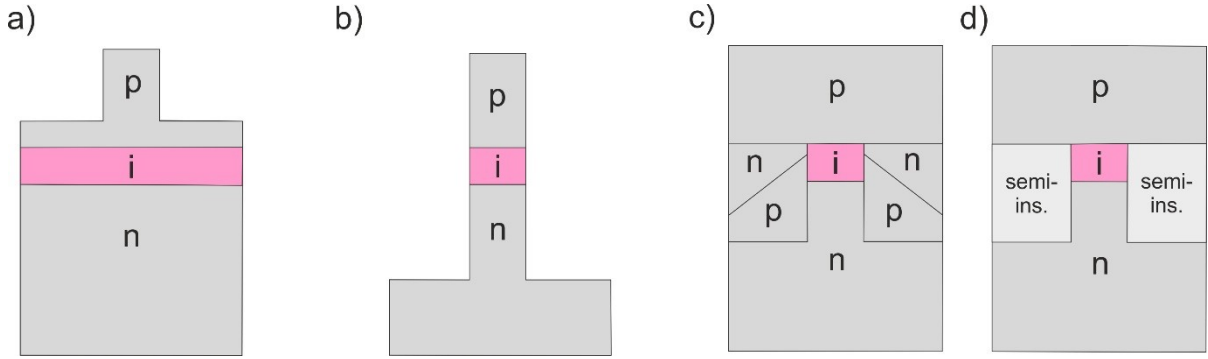


Fig. 7. Waveguide cross-sections a) shallow ridge waveguide, b) deep-ridge waveguide, c) buried heterostructure waveguide with pn blocking layers, d) buried heterostructure waveguide with semi-insulating blocking layers.

The shallow ridge also leads to single lateral mode selection and is easy to fabricate. To improve the current, electrical and optical confinement, the ridge is etched to below the active layer, giving a deep-ridge waveguide (Fig. 7b). If the active region should be covered, e.g. to protect it from oxidation, a lower refractive index cladding material is grown next to the ridge (Fig. 7c+d). This structure is referred to as buried heterostructure. To prevent current flowing through the lateral claddings, the material is made of pn blocking layers (Fig. 7c), where a reversed biased pn junction provides the current blocking, or semi-insulating material (Fig. 7d) [27].

The advantages of buried heterostructure lasers compared to ridge waveguide lasers are a lower threshold current and power consumption, while ridge waveguide lasers are easier to fabricate. For the optical transceivers, a low power consumption is crucial, so that the buried heterostructure laser type is preferred.

In the longitudinal direction, the laser is built as a resonator. At the threshold current, the generated light in the resonator overcomes the losses and lasing occurs. Single mode operation is achieved by integrating Bragg gratings into the laser structure, filtering out a single longitudinal mode. Bragg gratings are realized by periodic refractive index steps inside the laser cavity, which provide at the same time a distributed reflectivity and a longitudinal mode filtering.

2.1.2 Distributed Feedback (DFB) and Distributed Bragg Reflector (DBR) Lasers

In the distributed feedback (DFB) laser, the grating is etched into the top separate confinement heterostructure layer, above the multi quantum well (Fig. 8).

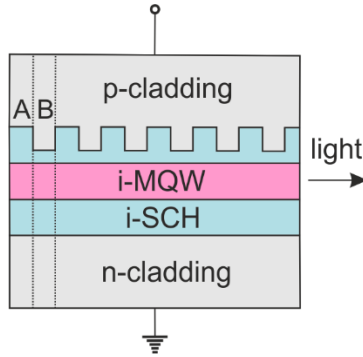


Fig. 8. DFB laser schematic structure with Bragg grating, longitudinal view (i: intrinsic).

Coupling of the waves in forward and backward direction happens at the Bragg wavelength λ_{Br} , satisfying the Bragg condition (2.1) [28], where Λ is the grating period and m an integer.

$$\Lambda = m(\lambda_{Br}/2\bar{n}_{eff,Br}) \quad (2.1)$$

$\bar{n}_{eff,Br} = n_{eff,A} + n_{eff,B}/2$ is the average effective grating refractive index. $n_{eff,A}$ and $n_{eff,B}$ are the effective refractive indices in the grating regions A and B, respectively and are calculated by optical mode simulations, e.g. in Fimmwave. The Bragg grating acts as a narrow filter, so that only modes close to the Bragg wavelength experience lasing. The coupling coefficient κ defines the grating strength and is calculated, using equation (2.2) [28], where $\Delta n_{eff,Br} = n_{eff,A} - n_{eff,B}$ is the effective refractive index difference between the regions A and B.

$$\kappa = \frac{2\Delta n_{eff,Br}}{\lambda_{Br}} \quad (2.2)$$

The coupling coefficient is adjusted by varying the etching depth in region B.

In DFB lasers, the opposing reflections in forward and backward direction at the Bragg wavelength are destructive, so that they are anti-resonant at the Bragg wavelength and two symmetric modes around the Bragg frequency lase. To obtain single mode lasing at the Bragg frequency, a quarter wavelength shift is introduced in the grating center. This configuration is referred to as the quarter-wave-shifted DFB.

Another distributed feedback laser type is the distributed Bragg reflector (DBR) laser. The difference to the DFB laser is the location of the Bragg grating. In DFB lasers, the grating is located inside the active region, while in DBR lasers, passive waveguides (WGs) with Bragg gratings enclose the active region (Fig. 9).

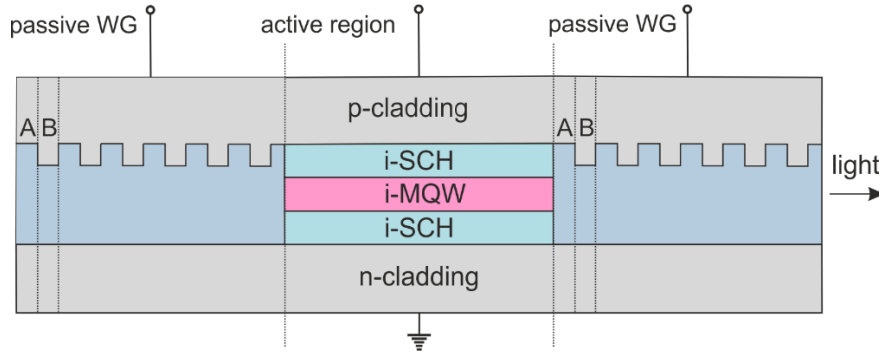


Fig. 9. DBR laser schematic structure, longitudinal view (i: intrinsic).

Widely tunable DBR laser types typically include two grating sections and a phase section between the gain and grating sections for fine-tuning. While DBR lasers can achieve a wide tuning range, DFB lasers typically are simpler, easier to fabricate and have lower losses, enabling lower threshold currents [27].

The DBR grating reflection can be approximated with the effective mirror model, assuming a discrete mirror reflection from a distance L_{eff} . The magnitude reflection $|r_{g,0}|$ of a lossless grating is given by eq. (2.3) [27], where L_g is the grating length. When including the internal laser losses α_{int} , the grating magnitude reflection becomes $|r_g|$ (eq. (2.4), [27]) and the grating reflectivity is $R_g = |r_g|^2$.

$$|r_{g,0}| = \tanh(\kappa L_g) \quad (2.3)$$

$$|r_g| = |r_{g,0}| e^{-\alpha_{\text{int}} L_{\text{eff}}} \quad (2.4)$$

The effective length L_{eff} is given by eq. (2.5) [27].

$$L_{\text{eff}} = \frac{1}{2\kappa} \tanh(\kappa L_g) \quad (2.5)$$

Since laser tunability is not mandatory for this work and since a low threshold current is beneficial to decrease the electrical power consumption, a DFB laser is chosen as the light source for the optical transmitter.

2.1.3 Direct Modulation

Direct modulation of the laser intensity is possible by driving the laser current with the electrical input data signal. The laser current is set to a point above threshold, so that the current modulation translates linearly to a power modulation. The directly modulated laser is the simplest transmitter configuration, cost efficient and easy to assemble. Its bandwidth is however limited by the speed of the injection and stimulated recombination of electrical carriers and is thus typically around 30 GHz [29].

2.2 Optical Modulators

The directly modulated laser speed limitations are overcome, when employing an external modulator, while operating the laser in continuous wave (CW). For this work, optical transmissions at 100 Gb/s and beyond are desired. Thus, the focus is on transmitters with external modulators.

2.2.1 Electro-Optic Effects

In external modulators, electro-optic (E-O) effects are used to get a material refractive index change Δn . By applying an electrical field E to the waveguide, electrorefractive or electroabsorptive effects are induced. Electrorefractive effects, including the linear Pockels ($\Delta n \sim E$) and the quadratic Kerr effect ($\Delta n \sim E^2$), change the refractive index and are applied to build phase modulators. Electroabsorptive effects, such as the Franz-Keldysh effect, change the material absorption. The energy bands tilt when applying an electric field and the electron and hole wave function tails overlap into the bandgap. This increases the probability, that photons with energy lower than the bandgap are absorbed. Following the Kramers-Kronig relation [30], [31], the absorption change leads to a refractive index change. In quantum wells (QWs), excitons occur in addition to the electroabsorptive effect. Excitons are electron-hole pairs, bound by the Coulomb force. Excitons are excited by photons with energies lower than the bandgap. In the absorption spectrum, excitons are visible as resonances, close to the absorption edge. A reverse biased pin junction with a single intrinsic InGaAsP quantum well within InGaAsP quantum barriers and p- and n-doped InP claddings is simulated in the software Harold. The simulated absorption and refractive index spectra different reverse bias voltages are displayed in Fig. 10a and Fig. 10b, respectively.

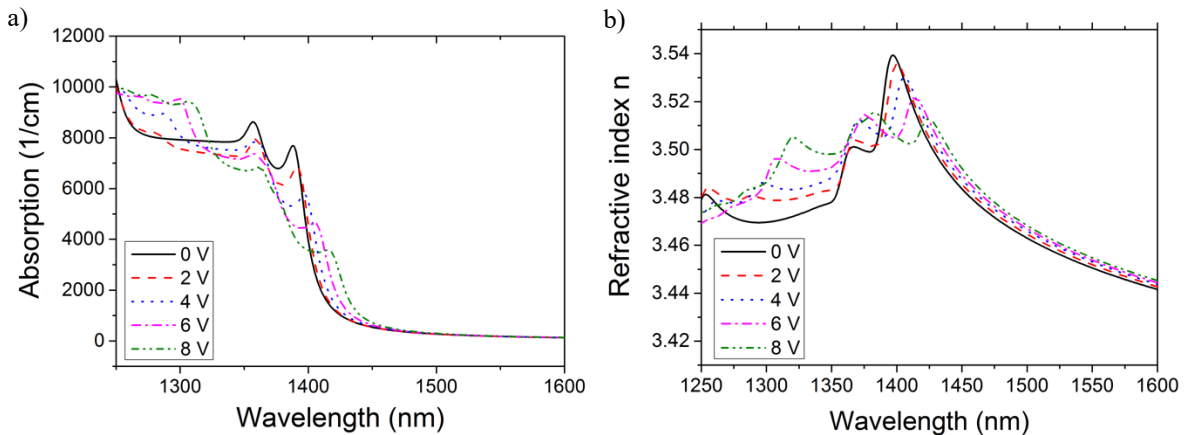


Fig. 10 Simulated absorption and refractive index spectra of an InGaAsP quantum well at different bias voltages

Two exciton resonances at the absorption edge are visible due to the light and heavy holes. When increasing the reverse bias voltage, the band tilting intensifies, shifting the absorption edge and the exciton resonances to lower energies and longer wavelengths. This effect is called the Stark effect. In quantum wells, the Stark effect is much stronger than in bulk material and thus referred to as quantum confined Stark effect (QCSE). Close to the absorption edge, the refractive index shift is the highest. However, due to the high absorption, phase modulators are operated at signal wavelengths, more than 150 nm beyond the absorption edge. At wavelengths much longer than the absorption edge, the refractive index shift, due to the Franz-Keldysh effect, Δn_{FK} is quadratic (eq. (2.6)), where the constant decreases at increasing wavelength [32].

$$\Delta n_{FK}(\lambda) = \text{const}(\lambda) \cdot E^2 \quad (2.6)$$

For the simulated InGaAsP quantum well, the refractive index Δn and the absorption shift, depending on the reverse bias voltage at 1550 nm wavelength are obtained from Fig. 10 and depicted in Fig. 11.

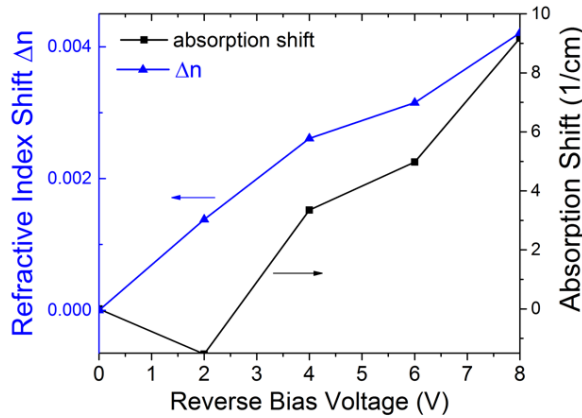


Fig. 11. Refractive index and absorption shift depending on reverse bias voltage for an InGaAsP multi quantum well at 1550 nm wavelength.

With increasing bias voltage, an increase in absorption and refractive index shift are observed. In the InGaAsP quantum well, a mixture of electro-optic effects is expected with a dominant contribution of the quadratic quantum confined Stark effect and some contribution of the linear Pockels effect.

A refractive index change in the waveguide is also obtained by injecting or depleting free carriers to or from a pin junction. The absorption and the refractive index are proportional to the free carrier density [32]. The speed of the carrier effects depend on the carrier lifetime, which makes the carrier injection effect slower than the field effects and bandwidth limited at modulation rates larger than 40 GHz [33]. The carrier depletion effect uses a reverse bias voltage to sweep out the carriers and to improve its speed, it is however typically less efficient than the carrier injection effect [34].

For this work, the optical transmitters need to operate at modulation rates up to 100 GHz, in order to fulfil the requirements for future optical transceivers. Thus, the transmitter design concentrates on electroabsorptive and electrorefractive effects, to avoid bandwidth limitations due to carrier injection and to achieve the best modulation efficiency.

2.2.2 Electroabsorption Modulator

The simplest modulator type is the electroabsorption modulator, employing the quantum confined Stark or Franz-Keldysh effect close to the absorption edge for intensity modulation. Electroabsorption modulators have the advantages of a small footprint and a simple structure. However, due to the Kramers-Kronig relation, the intensity modulation leads to unwanted phase modulation, referred to as chirp. Chirp degrades the modulation performance and limits the transmission distance in dispersive optical fibers.

2.2.3 Mach-Zehnder Modulator

A good alternative to the electroabsorption modulator is the Mach-Zehnder modulator, which has a larger size than the directly modulated laser or the electroabsorption modulator but can be designed for nearly chirp-free operation and bandwidths larger than 67 GHz [12]. Another advantage is that two Mach-Zehnder modulators are easily combined to form an IQ modulator, generating higher order modulation formats for coherent applications. For this work, the transmitters need to be suitable for operation at 100 Gb/s and beyond and transmission distances of up

to tens of kilometers. Also, the transmitters should support higher order modulation formats. Thus, the Mach-Zehnder modulator is the best suitable modulator and this work will further focus on Mach-Zehnder modulator-based transmitters.

Structure

The waveguide structure is based on a Mach-Zehnder interferometer, where the input optical carrier is split into two arms and combined at the signal output (Fig. 12a).

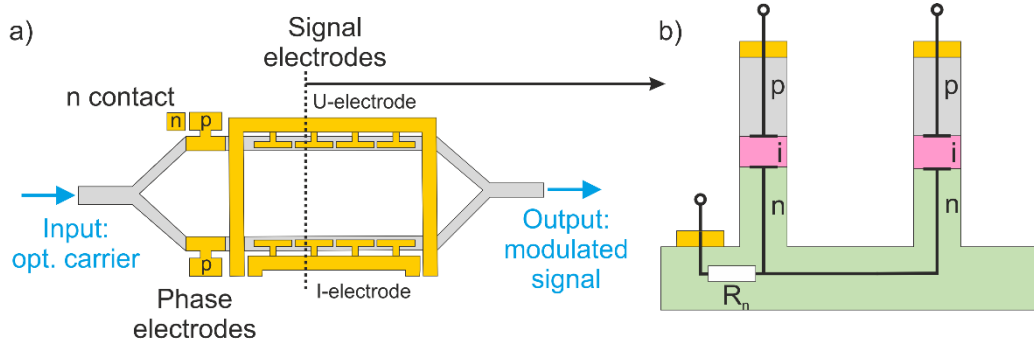


Fig. 12. Mach-Zehnder modulator a) top view waveguide structure and b) cross-section.

To apply voltages to the Mach-Zehnder modulator, signal and phase electrodes are placed on top of the waveguides and an n contact electrode is connected to the n-doped layer. A schematic of the Mach-Zehnder modulator top view with a travelling-wave type signal electrode is given in Fig. 12a and a cross-section of the device is sketched in Fig. 12b. To achieve a large optical confinement in the active layer and thus a good electro-optic efficiency, a deep-ridge waveguide structure is favorable. Typically, the waveguides are designed as heterostructure pin-diodes [15], but also other approaches, using npin [35] or nipn [12] structures, have been presented. The active layer is either an intrinsic bulk or multi quantum well layer and has a higher refractive index than the p- and n-doped claddings for optical confinement. The wavelength at the active material absorption edge is around 150 nm shorter than the signal wavelength to reduce the modulator insertion loss. Since the Mach-Zehnder modulator is operated using reverse bias voltages, the pin-diodes are approximated in the electrical scheme as capacitances with intrinsic region thicknesses (IRT) of a few hundred nanometers. For the n-doped layer, a resistance R_n is included.

Operation

Due to linear and quadratic electro-optic effects, such as the Pockels, Franz-Keldysh or the quantum confined Stark effect, applying a reverse bias voltage to the signal or phase electrodes, changes the refractive index and thus the phase of the optical signals inside the waveguides. When varying the phase shift between the signals in the two arms, the output signal power changes in a sinusoidal way. A measured dc transfer function of a 1550 nm InP Mach-Zehnder modulator with a multi quantum well active layer is given in Fig. 13.

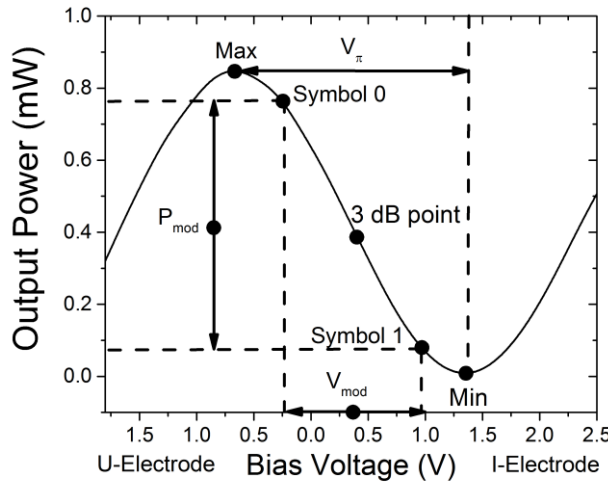


Fig. 13. Sinusoidal Mach-Zehnder modulator dc transfer function with modulation indicated around the 3 dB working point. Other working points are the maximum (Max) and the minimum (Min).

The dc transfer function in Fig. 13 is obtained by applying a voltage to either the U- or the I-electrode of the modulator in Fig. 12a and measuring the modulator output power. When the signals in the modulator arms are in-phase, the maximum output power is obtained, while the power is minimized when they have a 180 degrees phase shift. The required switching voltage V_{π} , to achieve a 180° between the two signals is an important modulator figure of merit. In Fig. 13, the switching voltage is measured between the maximum and minimum, giving V_{π} : 2 V.

The electrical data signal V_{mod} is applied with a voltage source to the signal electrodes, which are terminated by a load resistance (Fig. 15a). The voltage swings around a working point in the transfer function, which translates into a modulator output power swing P_{mod} . The modulator working point is selected, by initially applying a phase bias voltage V_{phase} , to one of the phase electrodes setting the phase shift between the signals in the two Mach-Zehnder modulator arms. Typical working points are the maximum, the minimum or the 3 dB point, centered between the maximum and the minimum. In Fig. 13, the modulator is operated at the 3 dB point as it is the case for non-return-to-zero (NRZ) on-off keying modulation. The output signal consists of two symbols with different intensities, When the Mach-Zehnder modulator working point is set to the minimum, typically, a modulation voltage swing of about two times the switching voltage is applied (Fig. 14a).

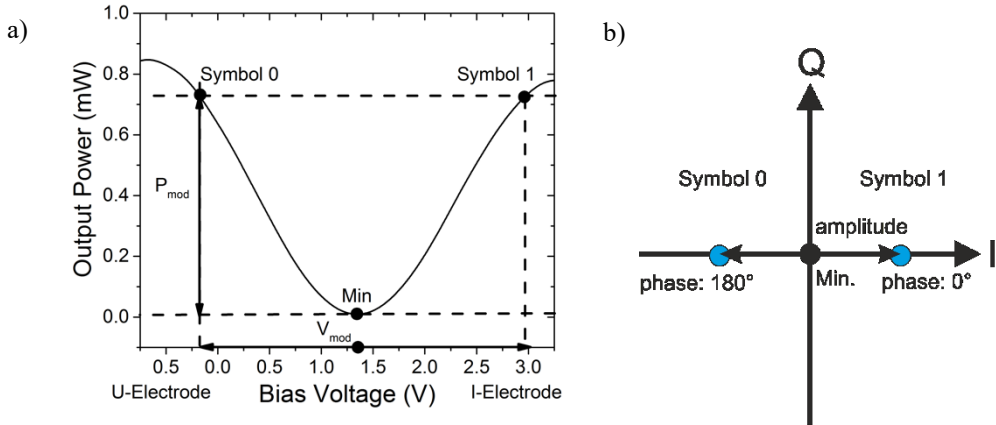


Fig. 14. a) Modulator dc transfer function with modulation indicated around the minimum working point, b) Signal depicted in constellation diagram.

The output signal has two symbols with the same intensities and 180° phase shift. This configuration is used, e.g. for binary phase shift keying (BPSK) modulation. The output signal is typically displayed in a complex constellation diagram, as in Fig. 14b, where the axes display the in-phase (I) and quadrature (Q) signal amplitudes. At the modulator minimum bias point, which is located at the axes crossing point, the amplitude is ideally zero, if both Mach-Zehnder modulator arms are symmetric. The Mach-Zehnder modulator output signal has no quadrature component, so that the output signal swings around zero on the in-phase axis. The two symbols are points on the in-phase axis with the same amplitudes and either zero or 180 degrees phase.

Push-Pull Operation

For frequency chirp-free output signals, the Mach-Zehnder modulator is operated in the push-pull configuration. The phase of the signals in the Mach-Zehnder modulator arms is changed equally in opposite directions, so that when they add up, the output signal phase and thus the frequency, remain constant at all times. Two driving schemes are commonly implemented for push-pull operation [36]. In the single-ended driving scheme, a single voltage source is connected to the signal electrodes, which are terminated with a $50\ \Omega$ resistor, to avoid reflections (Fig. 15a+b).

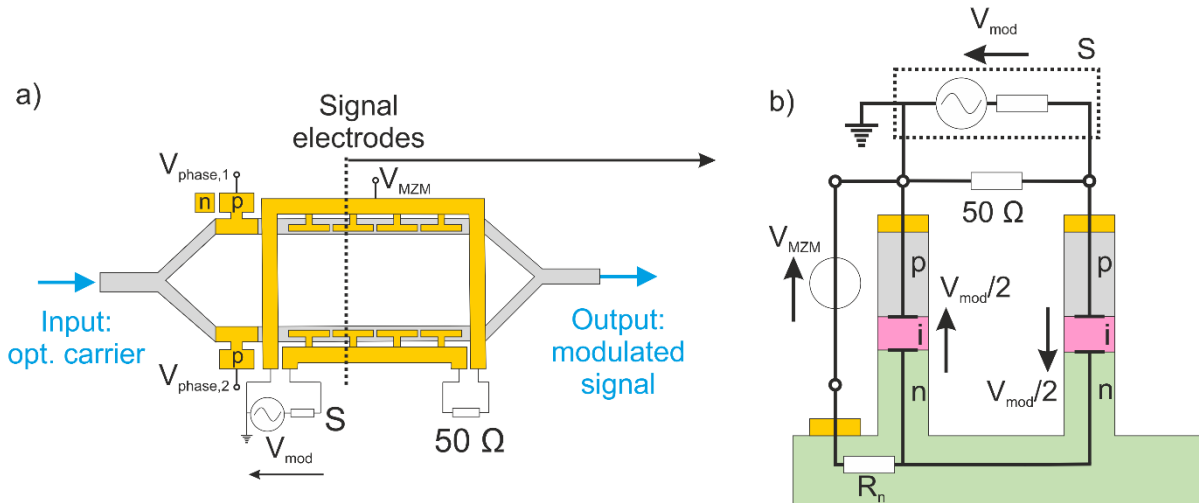


Fig. 15. Schematic Mach-Zehnder modulator structure in single-ended push-pull configuration a) top view and b) cross-section.

One electrode is connected to the signal S and the other one to ground. In this configuration, half of the modulation voltage V_{mod} drops at the active region of the upper modulator arm while the other half drops at the active region of the lower arm in opposite directions (Fig. 15b). In addition, a modulator bias voltage V_{MZM} is applied, generating an initial electric field in the active layers. Due to the contribution of quadratic electro-optic effects, the modulation is more efficient at stronger electric fields.

In the differential driving scheme, the signal s_+ : $V_{mod}/2$ and the inverted signal s_- : $-V_{mod}/2$ are applied separately to the two Mach-Zehnder modulator arms with a differential voltage source (Fig. 16a+b).

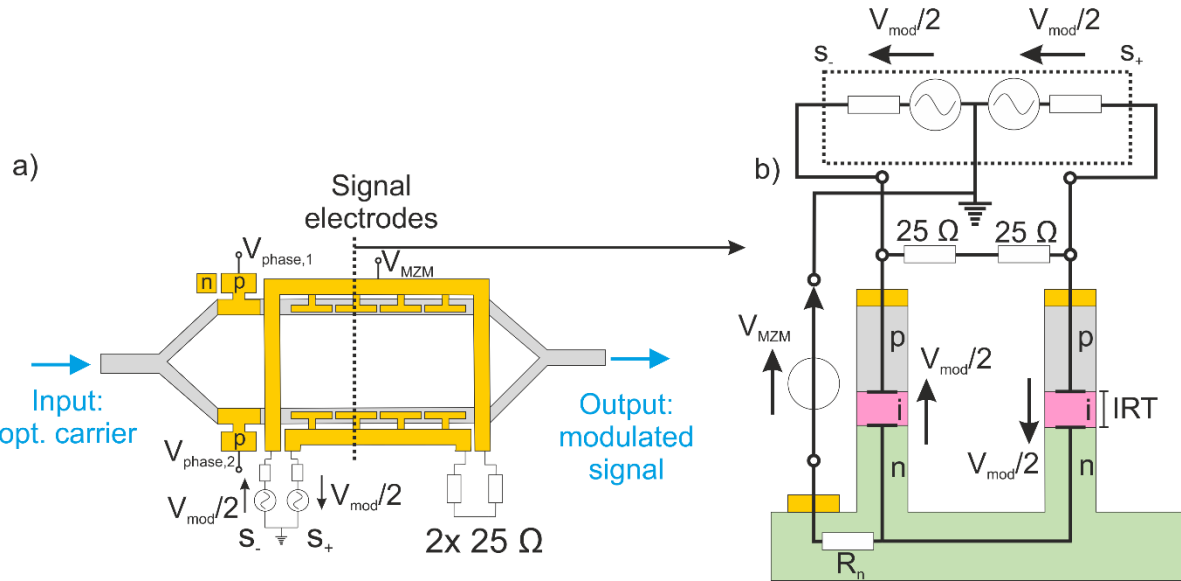


Fig. 16. Schematic Mach-Zehnder modulator structure in differential push-pull configuration a) top view and b) cross-section.

Both signals s_+ and s_- are referenced to ground and the signal electrodes are terminated with $2 \times 25 \Omega$ resistors. The modulator bias voltage V_{MZM} is applied between the n contact and ground. The differential driving scheme is

symmetric, making it more stable, against cross-talk or other parasitic effects than the single-ended driving scheme [36].

2.2.4 Signal Electrode

Depending on the transmitter application, different signal electrode designs exist. Lumped electrodes, typically used for directly modulated laser and electroabsorption modulators, have a small size and are simple to fabricate. However, they are bandwidth limited by the total amount of parasitic line elements, so that the lumped electrode must remain short, to achieve a high bandwidth. For the electroabsorption and Mach-Zehnder modulator, a shorter electrode leads to a lower electro-optic efficiency. To overcome the bandwidth limitations, while achieving at the same time a good efficiency, travelling wave electrode designs are implemented for the transmitters in this work.

2.2.4.1 Travelling-Wave Electrode (TWE)

In travelling wave electrode designs, the influence of parasitic elements is distributed along capacitive segments along the transmission line. This improves the bandwidth limitations compared to lumped electrodes and allows for long electrodes with a high efficiency [37]. A schematic of a capacitively loaded travelling wave electrode Mach-Zehnder modulator is given in Fig. 17 [33].

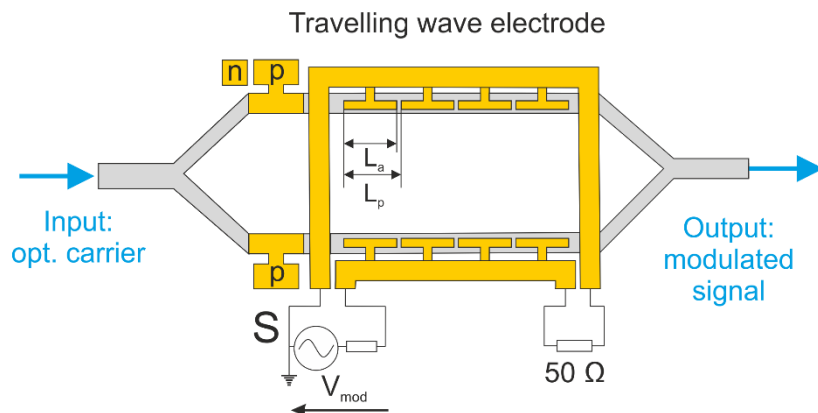


Fig. 17. Schematic top view of a Mach-Zehnder modulator with a capacitively loaded travelling wave electrode.

The capacitive segments with a length L_a are periodically placed at a distance L_p on top of the waveguides and connected to the signal electrodes via air bridges. The total active modulator length $L_{act,MZM}$ is the sum of the capacitive segment lengths. The travelling wave electrode is typically designed for a characteristic impedance Z_m : 50Ω and terminated with a 50Ω load resistance.

To achieve the best efficiency, the travelling wave electrode is designed so that the electrical and the optical wave travel along the waveguide at the same speed. In case of a velocity mismatch, the Mach-Zehnder modulator bandwidth and efficiency decline. The electrical phase velocity v_{el} is matched to the optical group velocity $v_{gr,opt}$, by slowing down the electrical wave with capacitive loads inside the travelling electrode. Equation (2.7) shows that in this condition, the microwave index of the loaded electrical line $n_{el,load}$ and the optical group refractive index and $n_{gr,opt}$, must be equal (c is the speed of light in vacuum).

$$v_{el} = \frac{c}{n_{el,load}} ! = \frac{c}{n_{gr,opt}} = v_{gr,opt} \quad (2.7)$$

The travelling wave electrode is approximated as a loaded transmission line, where the electrode segments are the capacitive loads. The unloaded travelling wave electrode, assuming low loss, is characterized by its inductance L_0 , capacitance C_0 and impedance Z_0 (eq. (2.8)) per unit length and its microwave index n_{el} (eq. (2.9)) [38].

$$Z_0 = \sqrt{\frac{L_0}{C_0}} \quad (2.8)$$

$$n_{el} = c \sqrt{L_0 \cdot C_0} \quad (2.9)$$

For the loaded travelling wave electrode, the characteristic impedance Z_m is given by eq. (2.10), where C_L is the capacitive load per unit length, and the microwave index is given by eq. (2.11).

$$Z_m = \sqrt{\frac{L_0}{C_0 + C_L}} \quad (2.10)$$

$$n_{el,load} = c \sqrt{L_0 \cdot (C_0 + C_L)} ! = n_{gr,opt} \quad (2.11)$$

For velocity matching, $n_{el,load}$ should be equal to $n_{gr,opt}$, so that L_0 and $C_0 + C_L$ can be written as in the equations (2.12) and (2.13), respectively.

$$L_0 = \frac{n_{el,load} Z_m}{c} = \frac{n_{gr,opt} Z_m}{c} \quad (2.12)$$

$$C_0 + C_L = \frac{n_{el,load}}{c Z_m} = \frac{n_{gr,opt}}{c Z_m} \quad (2.13)$$

By combining the equations (2.8) to (2.13), expressions for C_0 (eq. (2.14)) and C_L (eq. (2.15)) are obtained.

$$C_0 = \frac{n_{el}^2}{c Z_m n_{gr,opt}} \quad (2.14)$$

$$C_L = \frac{n_{gr,opt}^2 - n_{el}^2}{c Z_m n_{gr,opt}} \quad (2.15)$$

The travelling wave electrode line elements C_0 , C_L and L_0 can thus be completely determined, knowing $n_{gr,opt}$, n_{el} and Z_m .

The speed of the electrical wave is adjusted with the fill factor $FF = L_a / L_p$ [33]. The optimum fill factor for velocity match of a fabricated travelling wave electrode Mach-Zehnder modulator can be determined by measuring its intrinsic waveguide region capacitance C_{IRT} and intrinsic region thickness with capacitance over voltage (CV)

measurements. The optimum fill factor for velocity match FF_{match} is then calculated with eq. (2.16), where w_{MZM} is the Mach-Zehnder modulator waveguide width.

$$FF_{\text{match}} = \frac{2C_L}{C_{\text{IRT}} w_{\text{MZM}}} \quad (2.16)$$

The switching voltage V_π of the Mach-Zehnder modulator can be adjusted to a desired value $V_{\pi,\text{des}}$, by replacing FF with FF_{match} and by changing the total active length L_{act} to $L_{\text{act,new}}$ according to eq. (2.17).

$$L_{\text{act,new}} = \frac{FF \cdot V_\pi}{FF_{\text{match}} \cdot V_{\pi,\text{des}}} L_{\text{act}} \quad (2.17)$$

2.2.4.2 Segmented Electrodes

An alternative electrode design which should be mentioned, is the segmented signal electrode. It consists of multiple lumped electrodes, where each electrode is modulated individually. This gives the flexibility to do the electrical and optical wave velocity matching externally in the electrical domain. The segments can also be exploited to provide digital-to-analog converter (DAC) functionalities, so that an external DAC is not needed and the overall transmitter power consumption is reduced [39].

2.2.5 In-Phase and Quadrature Mach-Zehnder Modulator (IQM)

An in-phase and quadrature (IQ) modulator is constructed by nesting two Mach-Zehnder modulators, child 1 and child 2, within a common Mach-Zehnder interferometer (parent) (Fig. 18a) [40].

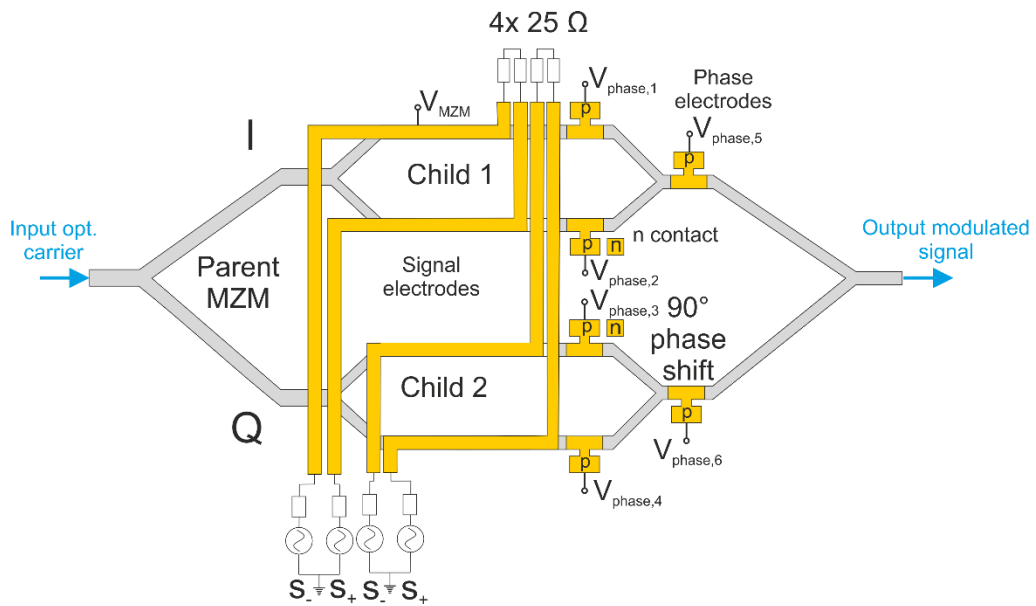


Fig. 18. Schematic IQ modulator structure in differential push-pull configuration, top view.

The two Mach-Zehnder modulators are best operated in the differential push-pull configuration. Using single-ended driving, the modulated optical signal is overlaid by amplitude distortions, resulting from quadrature errors and low frequency chirp, which is avoided with the differential driving scheme [36].

The second Mach-Zehnder modulator optical output is phase shifted by 90 degrees, generating the quadrature signal component, while the first Mach-Zehnder modulator contributes to the in-phase component. The 90 degrees phase shift is generated either by applying a voltage to one of the phase electrodes or by implementing optical output couplers with a 90 degrees phase shift, such as 2x2 multi-mode interference couplers (MMIs). At the modulator output, the in-phase and quadrature components are added. The complex output signal is typically displayed in a two-dimensional constellation diagram, where one axis corresponds to the in-phase I and the other axis to the quadrature component Q, respectively (Fig. 19).

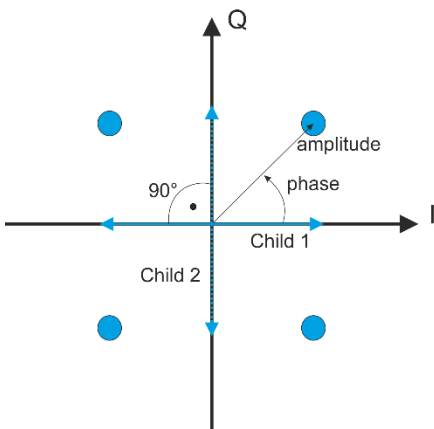


Fig. 19. IQ modulator output signal, displayed in constellation diagram.

Both Mach-Zehnder modulator working points are set to the minimum, corresponding to zero in the constellation diagram. When applying electrical data signals to the two Mach-Zehnder modulators, the output amplitude of the first one varies along the I axis, while the output amplitude of the second one varies along the Q axis. The added IQ modulator output signal is depicted in the two-dimensional plane, where each symbol has a certain amplitude and phase. The advantage of an IQ modulator is, that not only the amplitude but also the signal phase is modulated. IQ modulators are used to generate higher-order, spectrally efficient modulation formats, which are further described in chapter 2.3.

2.3 Modulation Formats

The simplest modulation format is on-off keying (OOK), where the electrical data is modulated onto the optical carrier intensity so that a digital “1” corresponds to a higher intensity than a digital “0”. The main on-off-keying configurations are non-return-to-zero (NRZ) and return-to-zero (RZ). The difference is, that during one bit, return-to-zero signals always return to zero, while non-return-to-zero signals remain constant. In optical systems, mainly non-return-to-zero is used, since depending on the pulse width, non-return-to-zero requires typically a lower bandwidth than return-to-zero [22]. On-off-keying signals are received with simple and cost-efficient direct detection. The transmitted data rate, however, is only 1 bit per symbol.

A better spectral efficiency is achieved with higher order modulation formats. If the signal comprises of 2^m symbols, one symbol has m bits and the symbol rate R_s is m times lower for a given bit rate R.

$$R_s[Bd] = \frac{R[\text{bit}]}{\text{s}} \quad (2.18)$$

The advantage of higher order modulation formats is, that with the same bandwidth requirements of non-return-to-zero on-off-keying signals, m times the bit rate is achieved.

For short reach and metro systems, intensity modulation and direct detection (IMDD) schemes, have gained a lot of attention, especially, in combination with higher order modulation formats, like pulse-amplitude modulation (PAM). Typical transmitters for intensity modulation and direct detection schemes include directly modulated lasers, electroabsorption modulators or Mach-Zehnder modulators.

For longer transmission distances, e.g. tens of kilometers, coherent technologies are very attractive. By modulating the in-phase and quadrature signal components, a two-dimensional symbol space is created. The signal is detected with homodyne or heterodyne techniques, requiring a more complex coherent optical receiver with a local oscillator, than in direct detection. Benefits are the possibly high spectral efficiency, the improved receiver sensitivity [26] and the use of digital processing to increase the flexibility and the robustness against transmission impairments.

Coherent technologies are used to generate phase shift keying (PSK) signals with different phase states and a constant amplitude. On the transmitter side, typically a laser with an external modulator is used. For phase shift keying signals, a narrow laser linewidth and a stable phase are crucial. Binary phase shift keying (BPSK) comprises of two symbols with a 180° phase shift. Alternatively, the data is encoded in the phase difference between two adjacent symbols. This configuration is referred to as differential phase shift keying (DPSK). Differential phase shift keying does not require the absolute signal phase and is thus more tolerant to phase fluctuations, than binary phase shift keying [26]. BPSK and DPSK are the simplest and most robust phase shift keying formats. Quaternary phase shift keying (QPSK) signals have four symbols, separated by 90 degrees phase shift, where each symbol is encoded by 2 bits (Fig. 20a).

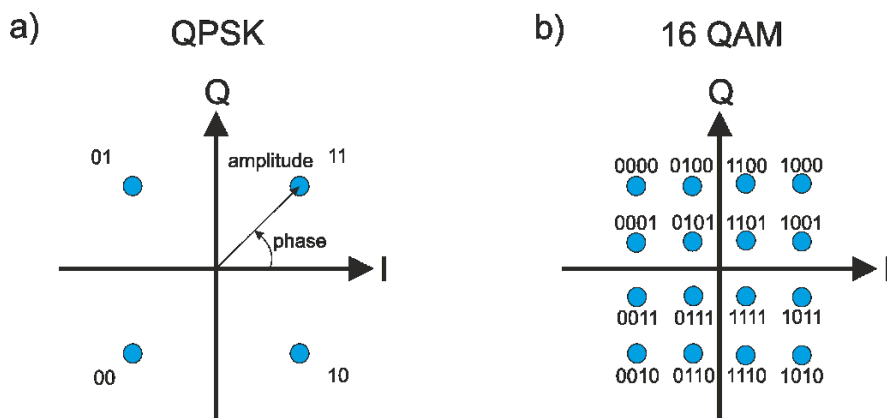


Fig. 20. Constellation diagrams of a) QPSK and b) QAM16 modulation formats.

The highest spectral efficiency is achieved with quadrature amplitude modulation (QAM) formats, where at the same time the signal amplitude and phase are modulated. A 16-symbol quadrature amplitude modulation signal consists of 16 symbols with different amplitudes and phases, arranged in a square, where each symbol represents

four bits (Fig. 20b). For coherent applications, in-phase and quadrature (IQ) modulators are best suited. Up to QAM256 transmissions with eight bits per symbol have been demonstrated with an InP-based segmented IQ modulator [41].

To further double the spectral efficiency, polarization division multiplexing (PDM) is implemented, where signals are multiplexed onto the transverse electric (TE) and transverse magnetic (TM) polarization light components. TE and TM polarized signals can be and transmitted on a single frequency without influencing each other, since they are orthogonal. Typically, dual polarization (DP) transmitters consist of two modulators optimized for TE operation. The output signal of one of the modulators is converted to transverse magnetic polarization, inside [42] or outside [35] the photonic integrated circuit and then combined with the TE signal of the other modulator.

2.4 Transmitter Integration

When an external modulator is employed, different approaches exist, to integrate the modulator with the laser. The integration avoids bulky transmitter setups and enables embedding the components into small transceiver modules. The transmitter designs, range from hybrid over heterogeneous to monolithic integration. While hybrid integration allows independent design and fabrication of the transmitter parts, heterogeneous and monolithic designs, where the devices are on the same chip, require less assembly time and effort and have almost zero coupling loss. The monolithic integration is best done with direct semiconductors, such as indium phosphide, where both lasers and modulators can be fabricated.

2.4.1 Hybrid Integration

When using hybrid integration, the devices are fabricated independently, in the same or different material systems. This has the advantage, that each device is optimized individually. The light coupling is done, for example, by using optical lenses. Another advantage is that the laser can be isolated from the modulator optically, with optical isolators and thermally, by using individual temperature controllers. Using hybrid integration, a compact transmitter module with a highly reliable tunable distributed laser array and a lens coupled Mach-Zehnder modulator was demonstrated [43]. The drawback of hybrid integration is, that each device has to be coupled independently, consuming assembly effort and cost.

2.4.2 Heterogeneous Integration

To combine the advantages of different material platforms and at the same time reduce the coupling effort and time, devices of different semiconductor platforms, such as InP and Si, are grown together on the same substrate [44]. This approach is referred to as heterogeneous integration. However, heterogeneous integration is challenging, since it is difficult to merge materials with different lattice constants on a common substrate, without inducing unwanted strain.

2.4.3 Monolithic Integration

With monolithic integration, devices from the same material system are integrated on a single chip, enabling almost lossless coupling. Unwanted strain is avoided by choosing materials, lattice matched to the substrate. Integrating the laser and the modulator monolithically, reduces the transmitter size and power consumption. In transceiver modules, due to the reduced number of optical interfaces, monolithic devices significantly reduce the coupling

effort, time and cost and improve the robustness. Moreover, no coupling optics are needed, saving space inside the transceiver module.

For this work, a small size and a low power consumption are essential, to make the optical transmitters suitable for future transceiver modules. Thus, the monolithic transmitter integration approach is chosen for the transmitter design.

2.4.4 Integration Platforms

Different semiconductor material platforms exist for the transmitter fabrication. The silicon (Si)-platform is well established and best known for the electrical component production. Integrating optical components in silicon, is nowadays strongly desired. However, silicon is an indirect bandgap semiconductor and does not generate light.

In the gallium arsenide (GaAs) and indium phosphide platforms, on the other hand, lasers are well established. Lattice matched gallium arsenide lasers operate in the wavelength range between 0.8 μm and 0.9 μm. In indium phosphide, the laser active material is typically made of lattice matched quaternary alloys, such as indium gallium arsenide phosphide (InGaAsP), emitting at wavelengths between 1.1 μm and 1.6 μm, depending on the composition [22]. For optical communication systems, laser operation in the 1.3- 1.6 μm range is favorable, making InGaAsP lasers best suitable.

For silicon based transmitters, the light source is typically made of direct bandgap semiconductor material and integrated with hybrid approaches [45]. Attempts to make Si light emitting are demonstrated [46], but did not show sufficient efficiency, yet. Another approach is to grow direct semiconductor materials directly on Si, which is challenging due to the lattice mismatch [47]. Although, silicon photonics have the advantage of smaller footprints and a more experienced technology, using direct bandgap material platforms, such as indium phosphide, is the simplest and most promising approach for the transmitter integration.

2.4.4.1 The Indium Phosphide (InP) Platform

The indium phosphide platform is chosen for this work, because it allows at the same time monolithic laser integration and light emission at wavelengths in the optical communication range.

The main advantage of the indium phosphide platform is that it includes both passive and active devices, such as light sources. Optical components with various functionalities are easily integrable on a single chip. Passive devices range from simple waveguides to multi-mode interference couplers, spot-size converters and arrayed waveguide gratings [48]. Active components include phase, Mach-Zehnder and electroabsorption modulators. Moreover, semiconductor optical amplifiers (SOAs) and light sources, including various laser types, such as distributed feedback and tunable distributed Bragg reflector lasers [11], [49], are available with wavelengths in the optical communication bands. Light absorbing materials, such as indium gallium arsenide (InGaAs), latticed matched to indium phosphide are employed to build photodiodes and balanced photodetectors [50]. Different devices are either designed with the same active waveguide layer or selectively regrown and connected through butt-joints. Indium phosphide devices are combined in various ways to form photonic integrated circuits for different applications like optical transceivers, switches and sensors.

3. State of the Art: Monolithic Transmitters in Indium Phosphide

Monolithic optical transmitters in indium phosphide are particularly interesting because they operate at wavelengths in the optical communication range around 1300 nm and 1550 nm. In short reach and metro systems, where the availability of high-speed, cost-efficient, compact pluggable transceivers is mandatory, monolithic transmitters are very attractive, due to their small form factor and low power consumption. Various monolithic indium phosphide transmitters with high bandwidths and low switching voltages, have already been demonstrated, making them attractive for next generation 400 Gb/s or faster optical networks. In this chapter, an overview of monolithic indium phosphide transmitter photonic integrated circuits (PICs) and their latest achievements is given.

3.1 Electroabsorption Modulated Laser (EML)

A transmitter with a laser and an integrated electroabsorption modulator is referred to as electroabsorption modulated laser (EML). Its small form factor and at the same time high bandwidth make the electroabsorption modulated laser very attractive for short reach systems. An EML module with a distributed feedback (DFB) laser and a lumped electrode electroabsorption modulator inside has been reported, having a bandwidth of 59 GHz at 1305 nm wavelength [51]. The high module bandwidth was achieved by directly soldering the EML directly next to the radio frequency circuit board by using flip-chip technology, in order to avoid the parasitic bond wire inductances. With the EML module, up to 10 km standard single mode fiber (SSMF) transmission of 100 GBd 4-level pulse amplitude modulation (PAM4) at 1.2 V_{pp} modulation voltage, with a bit error rate (BER) below the 7 % overhead forward error correction (FEC) threshold [51] was demonstrated. Moreover, 250 Gb/s discrete multitone modulation below the 20 % FEC threshold was achieved [52].

3.2 Laser Mach-Zehnder Modulator

Laser integrated Mach-Zehnder modulator transmitter photonic integrated circuits are an attractive alternative to electroabsorption modulated lasers, since they can be designed for an even higher bandwidth and zero chirp. A 1550 nm wavelength tunable transmitter photonic integrated circuit, with a distributed Bragg reflector (DBR) laser and a travelling wave electrode Mach-Zehnder modulator, operating at up to 40 Gbit/s non-return-to-zero (NRZ) on-off-keying has been demonstrated [53].

3.3 Laser In-Phase and Quadrature (IQ) Mach-Zehnder Modulator

Transmitter photonic integrated circuits for the highest spectrally efficiency, include an in-phase and quadrature (IQ) modulator. An IQ modulator is typically generated, by combining two Mach-Zehnder modulators.

A C-band (1530- 1565 nm) tunable sampled grating DBR laser, integrated with two IQ modulators for dual polarization (DP) operation was presented, demonstrating up to 32 GBd 16-level quadrature amplitude modulation (QAM16) with a switching voltage below 2 V [54]. By integrating multiple IQ modulators with other transceiver components, transceiver photonic integrated circuits with the most functionalities and the highest transmission rates, have been developed. Recently, a compact pluggable module, embedding a large scale photonic integrated

circuit with 14 channels and over 200 optical devices was presented [9]. Each channel includes a C-band tunable laser, a dual-polarization IQ Mach-Zehnder modulator and semiconductor optical amplifiers. With the large scale photonic integrated circuit, up to 44 GBd QAM16 operation has been demonstrated, so that when combining all the channels, the PIC could potentially achieve operation at 4.9 Tbit/s. The QAM16 transmission with the highest Baud rate at 88 GBd and transmission over up to 80 km standard single mode fiber, has been achieved with a 2-channel dual-polarization IQ modulator, integrated with two C-band widely tunable lasers [55].

4. 1550 nm DFB Laser Integrated Mach-Zehnder/ IQ Modulator Transmitter PICs

Optical transmitter photonic integrated circuits (PICs) for future optical transceiver modules for transmissions over a few up to tens of kilometers are developed in this work. Based on the optical transmitter overview in the previous chapters, it has been figured out, that monolithically integrated transmitters in the indium phosphide platform are the best suitable. In particular, the chosen transmitter designs consist of the following components:

- Distributed feedback (DFB) laser with buried heterostructure waveguide
- Deep-ridge waveguide travelling wave electrode (TWE) Mach-Zehnder or IQ modulator

Two monolithic indium phosphide transmitter architectures are developed. The first one integrates a DFB laser and a TWE Mach-Zehnder modulator (DFB-MZM), while the second one consists of a DFB laser and a TWE IQ modulator (DFB-IQM). Both transmitter types are designed for operation in the C-band, around 1550 nm. While the DFB laser, Mach-Zehnder and IQ modulator designs are based on previously developed devices, this work concentrates on the following points:

- Optimization of DFB laser Mach-Zehnder and IQ modulator device structures for monolithic integration
- Development of a combined fabrication process
- Characterization and operation of the monolithic transmitter photonic integrated circuits

In this chapter, the developed transmitter photonic integrated circuit architectures and the integrated DFB laser and Mach-Zehnder modulator structures will be described. Then, the photonic integrated circuit fabrication process is explained and discussed. Finally, the transmitters are characterized and tested for large signal operation and their characteristics and performance are compared to the ones of transmitters with isolated laser and modulator components.

4.1 Transmitter Photonic Integrated Circuit (PIC) Architectures

The DFB laser integrated Mach-Zehnder modulator (DFB-MZM) transmitter schematic layout and a photograph of the fabricated photonic integrated circuit are depicted in Fig. 21a and Fig. 21b, respectively.

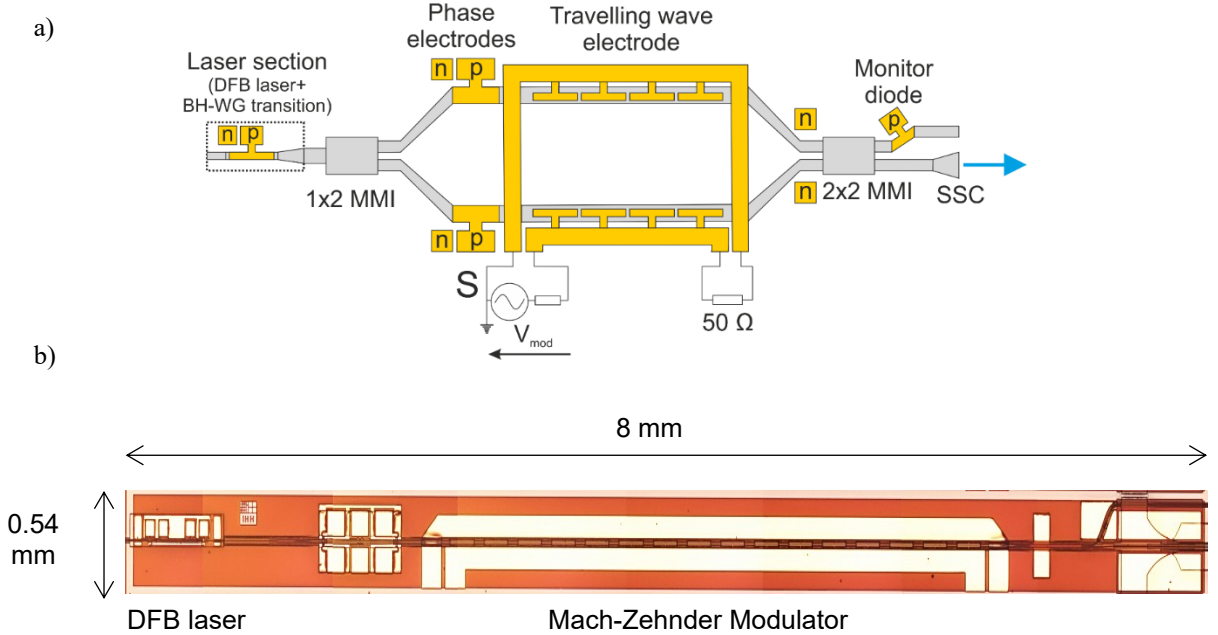


Fig. 21. Schematic structure a) and photograph b) of the DFB laser Mach-Zehnder modulator (DFB-MZM) transmitter PIC.

From the chip facet to the DFB laser output, the waveguide has a buried heterostructure architecture. At the DFB laser output, the buried heterostructure to deep-ridge (BH-RW) waveguide transition element is integrated, to couple the light to the deep-ridge waveguide modulator section.

For splitting and coupling the light in the Mach-Zehnder interferometer, 1x2 and 2x2 optical multi-mode interference (MMI) couplers are implemented, due to their advantages in fabrication tolerance, polarization insensitivity and large bandwidth operation [56]. The Mach-Zehnder modulator has a capacitively loaded travelling wave electrode with a $50\ \Omega$ characteristic impedance [14]. Phase electrodes and an additional output with a monitor photo diode are included for bias control. At the modulator output a spot-size converter (SSC) is integrated for alignment tolerant and low loss fiber-chip coupling. For large signal operation, the electrical signal is connected to the radio frequency travelling wave electrode input, while the output is terminated with a $50\ \Omega$ resistance.

The DFB laser IQ modulator (DFB-IQM) photonic integrated circuit schematic structure and photograph are displayed in Fig. 22a and Fig. 22b, respectively

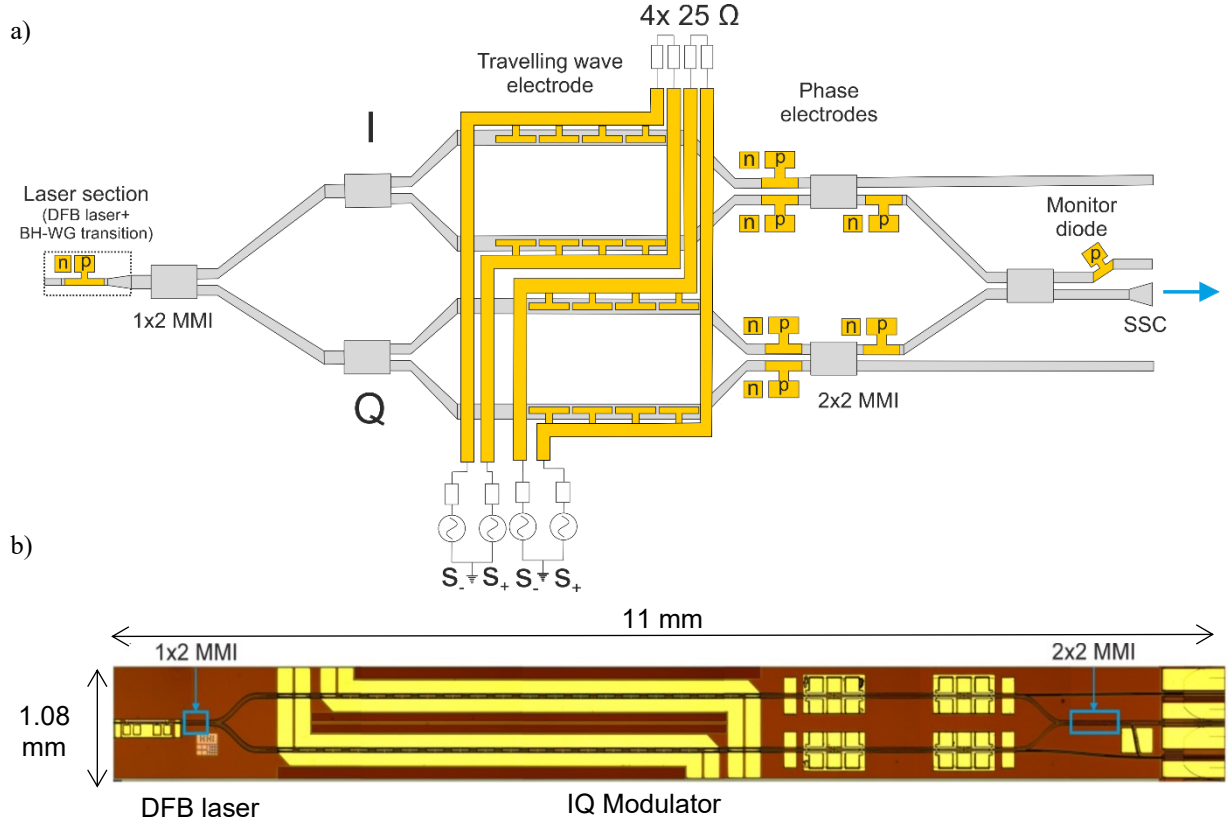


Fig. 22. Schematic structure a) and photograph b) of the DFB laser IQ modulator (DFB-IQM) transmitter PIC.

The IQ modulator includes two travelling wave electrode Mach-Zehnder modulators, one for in-phase (I) and one for the quadrature (Q) signal component, which have a similar structure to the Mach-Zehnder modulator in the DFB-MZM PIC. The IQ modulator is typically operated in the differential driving scheme, where two differential signals are connected to the travelling wave electrode inputs, while the outputs are terminated with two $25\ \Omega$ resistors, respectively. Phase electrodes are placed on each of the four Mach-Zehnder modulator arms. For combining the signals, 2x2 multi-mode interference couplers are used. The 2x2 MMI at the output introduces the 90 degrees phase shift between the I and Q signal components, which can be fine-tuned by the phase electrodes on the outer Mach-Zehnder interferometer. The additional output waveguides are for separately monitoring the output power of the two Mach-Zehnder modulators and for tapping the output signal power with a monitor photo diode. At the IQ modulator output, a spot-size converter is integrated.

The transmitters have the same dimensions as identical Mach-Zehnder modulator ($0.54 \times 8\text{ mm}^2$) and IQ modulator PICs ($1.08 \times 11\text{ mm}^2$), without integrated laser.

4.2 Distributed Feedback (DFB) Laser Section

The laser waveguide cross-section, consisting of a double-heterostructure pin diode is displayed in Fig. 23.

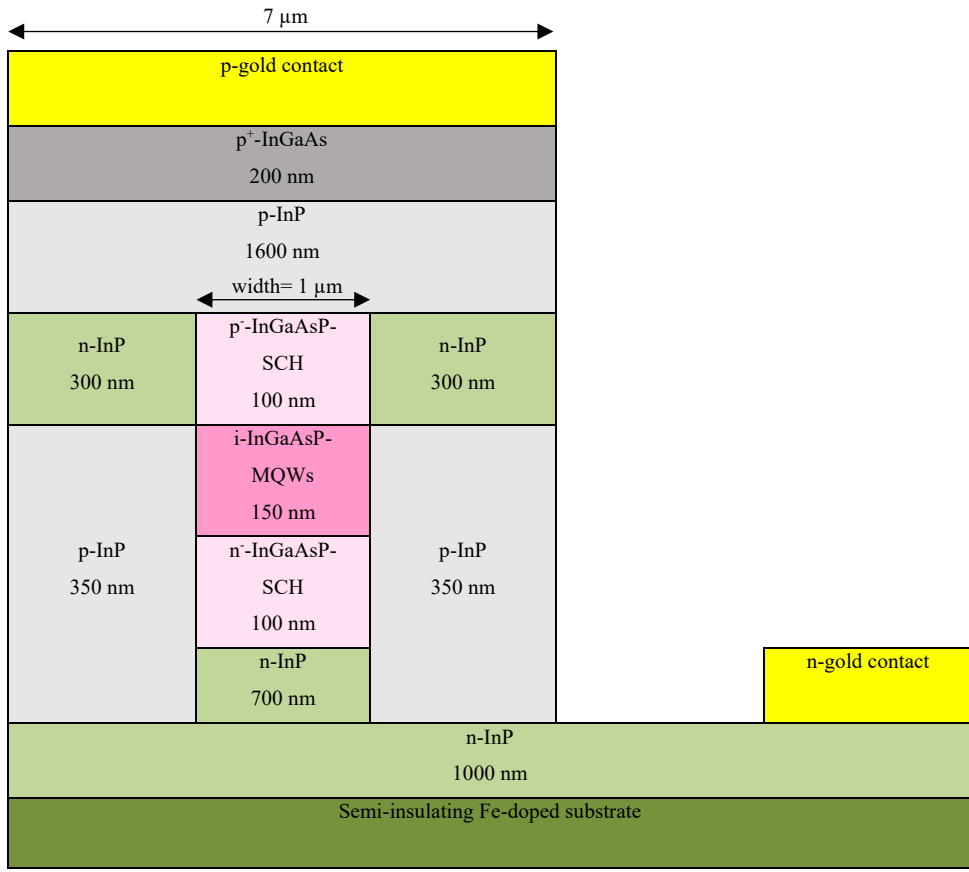


Fig. 23. DFB laser buried heterostructure waveguide cross-section.

The active layer includes compressively strained indium gallium arsenide phosphide (InGaAsP) multi quantum wells (MQWs) with a 1550 nm photoluminescence wavelength (Due to NDA restrictions more details about the multi quantum well core cannot be given). Since the multi quantum well layer is only 150 nm thick, 100 nm InGaAsP separate confinement heterostructure (SCH) layers are placed on either side for better electrical and optical confinement. In addition, the combined laser SCH and MQW layer thickness matches better the Mach-Zehnder modulator waveguide thickness. The SCH layers are only weakly p- or n-doped and have a bandgap wavelength of 1150 nm, much lower than the lasing wavelength, to minimize the absorption.

The waveguide layer is surrounded by p- and n-doped indium phosphide cladding layers. Towards the active region, the p- and n-doping concentration is decreased to reduce the absorption, especially in the p-doped regions [57]. For a low contact resistance, the indium phosphide doping concentration is gradually increased towards the metal contacts. An indium gallium arsenide (InGaAs) layer, which can be highly p-doped, is inserted between the indium phosphide and the p-contact metal. The n-contact metal is deposited on the laser top side. The laser bottom side is not conducting, since the transmitters are grown on semi-insulating iron (Fe)-doped substrate.

The laser waveguide lateral structure is a buried heterostructure type with p- and n-doped indium phosphide blocking layers. A buried heterostructure waveguide is preferred to the ridge waveguide structure since a lower threshold current is expectable.

The laser section top-view, including the DFB laser and the buried heterostructure to deep-ridge waveguide (BH-RW) transition element, is sketched in Fig. 24.

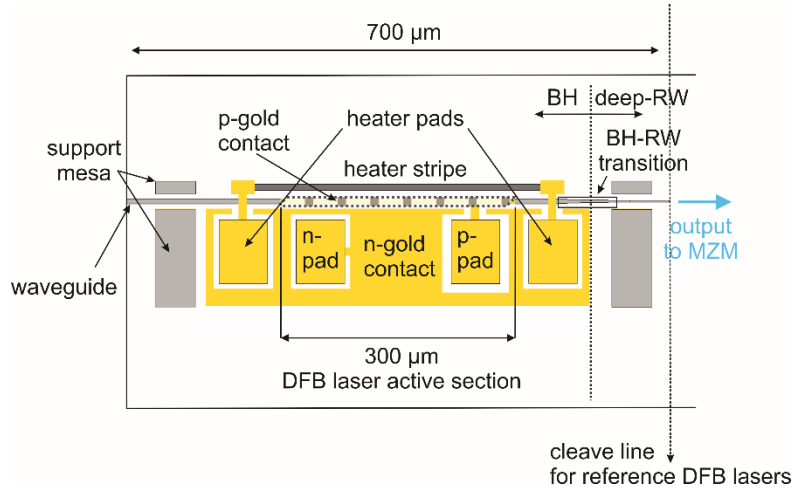


Fig. 24 DFB laser section top-view.

The 100 μm long transition is based on the one published in [58]. The 1 μm buried heterostructure waveguide width is adiabatically increased to 2.2 μm . The adiabatic transition minimizes the reflections and the coupling loss and prevents the excitation of higher order modes. The transition element insertion loss is determined by fabricating and measuring test devices with 12 consecutive transition elements. The 12 consecutive transition elements have 1 dB insertion loss in total, so that the loss of a single transition element is only about 0.1 dB.

In the integrated transmitter photonic integrated circuit, the laser section replaces the Mach-Zehnder modulator input spot-size converter. The total laser section length (700 μm) is comparable to the spot-size converter length, so that it can be integrated, without increasing the Mach-Zehnder modulator chip-size. Reference DFB lasers are fabricated on the wafers together with the transmitters, which have the same structure as the integrated DFB laser section and are cleaved at the output to the modulator.

The laser has different multi quantum wells and waveguide layers than the modulator. The 300 μm long laser island is surrounded by epitaxially regrown modulator layers. The waveguide facets between the laser and the modulator regions are connected through 7 degrees angled butt-joints, avoiding reflections. A 50 nm deep distributed feedback (DFB) grating is etched along the total laser length L, into the top separate confinement heterostructure layer. To increase the power ratio between the lasing mode and the next probable side mode and to ensure a stable single mode operation, a lambda quarter shift is included in the center of the grating. The grating is designed to give a κL product of 3 ($\kappa = 100 \text{ cm}^{-1}$), which is an empirical value from previous DFB laser components with sufficient performance in terms of output power, relative intensity noise and linewidth. DFB lasers for three wavelengths in the C-band are designed (1550 nm, 1554 nm, 1558 nm), by employing different grating periods (238.462 nm, 239.077 nm, 239.692 nm), calculated with equation (2.1).

Gold contacts are deposited on the p-doped laser waveguide top and the n-doped layer and a platinum heater stripe is integrated next to the DFB laser for wavelength fine-tuning. The p- and n- contacts and the heater are connected

via air bridges to gold contact pads, placed on mesas. Support mesas are placed at the edges of the laser section to protect the waveguides during chip cleaving.

4.3 Mach-Zehnder Modulator Section

The Mach-Zehnder modulator waveguide consists of a pin-double heterostructure with an indium gallium arsenide phosphide (InGaAsP) multi quantum well core (Fig. 25) (Due to NDA restrictions more details about the multi quantum well core and the intrinsic region cannot be given).

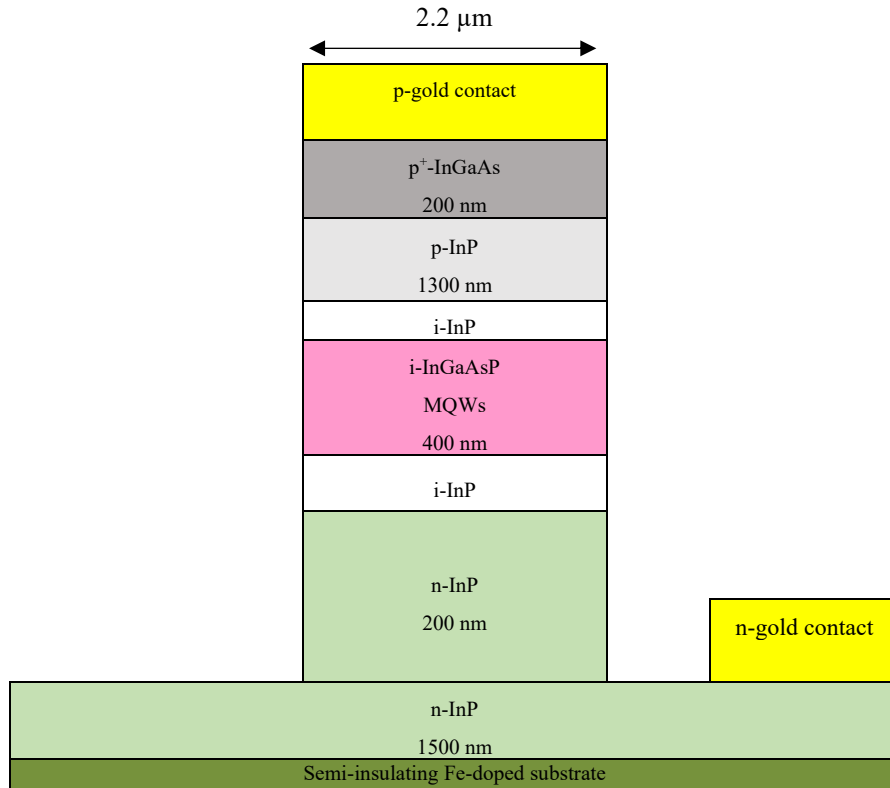


Fig. 25. Modulator schematic deep RW pin-heterostructure WG with an InGaAsP MQW core and InP claddings.

The modulator multi quantum well photoluminescence wavelength is more than 150 nm narrower than the laser wavelength, to obtain a sufficiently low absorption. Intrinsic indium phosphide buffer layers enclose the multi quantum wells, to avoid absorption in the p- and n-doped indium phosphide cladding layers. A highly p-doped indium gallium arsenide (InGaAs) layer improves the contact resistance between the p-contact metal and the p-InP. The p- and n-gold contacts are deposited on top of the waveguide and on the n-doped indium phosphide layer, respectively.

A deep-ridge waveguide structure is chosen to achieve a large optical confinement, which improves the electro-optic modulation efficiency. Optical mode simulations in Fimmwave show that the waveguide width should be below 1.4 μm for single mode operation. However, the narrow waveguide makes the insertion loss very sensitive to sidewall roughness. As a compromise, the waveguide width is increased to 2.2 μm , where the propagation of two optical modes is possible. To avoid loss due to light conversion into the second mode, adiabatic waveguide bends and tapers are implemented in the Mach-Zehnder modulators.

To achieve the best modulation efficiency, indium phosphide pin structure based electro-optic modulators are typically fabricated in the $[0\bar{1}1]$ direction (Fig. 27a). In the developed Mach-Zehnder modulators, a contribution of the Pockels and the quantum confined Stark effect is expected. While the quantum confined Stark effect depends only on the applied electrical field, the Pockels effect also depends on the crystal direction. In the $[0\bar{1}1]$ direction, the refractive index shift induced by the Pockels effect adds up to the one of the quantum confined Stark effect [59]. Buried heterostructure waveguides are typically fabricated in the $[0\bar{1}\bar{1}]$ direction (90 degrees shifted from the $[0\bar{1}1]$ direction on the wafer), where sidewalls in natural crystal directions provide a better stability [60]. However, in the $[0\bar{1}\bar{1}]$ direction, the quantum confined Stark and the Pockels effect refractive index shifts counteract each other which decreases the overall electro-optic effect [59].

For the monolithic integration of the developed transmitters, the buried heterostructure lasers are rotated by 90 degrees from their typical fabrication direction to the $[0\bar{1}1]$ direction. As a result, the transmitters can be fabricated in a straight line and the Mach-Zehnder modulators remain in the crystal direction with the best modulation efficiency. Putting a 90 degrees waveguide bend between the laser and the modulator to leave the buried heterostructure laser in its typical fabrication direction is avoided, since it would increase the chip size and induce additional insertion loss.

Another solution to integrate buried heterostructure lasers with Mach-Zehnder modulators, without rotating the laser, is to employ nip doped instead of pin doped waveguide structures. Nip doped Mach-Zehnder modulators have the best modulation efficiency in the $[0\bar{1}\bar{1}]$ direction, where buried heterostructure lasers are typically fabricated [59].

The travelling wave electrode is designed for a 50Ω characteristic impedance, has 16 segments and a total active length $L_{a,tot}$ of 4 mm. In the semiconductor, the electrode segments are electrically separated by removing the p-doped (p) indium phosphide cladding layer between the segments and depositing intrinsic (i) indium phosphide instead (Fig. 26, [15]).

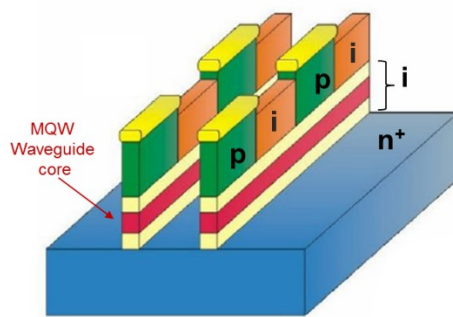


Fig. 26. Semiconductor layer structure below the travelling wave electrode segments.

At the modulator output a spot-size converter with an InGaAsP bulk waveguide layer is integrated and connected with a butt-joint. The waveguide layer has a photoluminescence wavelength, much shorter than the laser wavelength, to avoid absorption. The spot-size converter waveguide layer is vertically tapered down, towards the output facet. This leads to a better matching of the optical mode size to the optical fiber core, reducing the chip to

fiber coupling loss. Towards the transmitter output facets, the spot-size converter intrinsic cladding thickness is increased to provide more space for the optical mode, reducing the insertion loss.

4.4 Fabrication Process

The DFB laser and Mach-Zehnder modulator photonic integrated circuits are typically fabricated individually, with already established processes. For this work, the two fabrication processes are merged, and the original device structures are adjusted, to build the DFB laser Mach-Zehnder modulator transmitter photonic integrated circuits. The transmitters are fabricated in Fraunhofer HHI's cleanroom, partly by micro technologists and partly by me. In this subchapter, a detailed fabrication process description is given.

All regrowth steps are conducted by metalorganic vapor phase epitaxy (MOVPE). Lasers are typically grown on n-doped substrates, where the backside of the chip is used for n-contacting. By using semi-insulating substrates, which have a lower the n-doped layer resistance, the Mach-Zehnder modulator bandwidth can be improved, compared to n-doped substrates. Therefore, semi-insulating [100] direction 2-inch iron (Fe)-doped indium phosphide (InP:Fe) substrate is chosen for the integrated laser modulator transmitter fabrication (Fig. 27a).

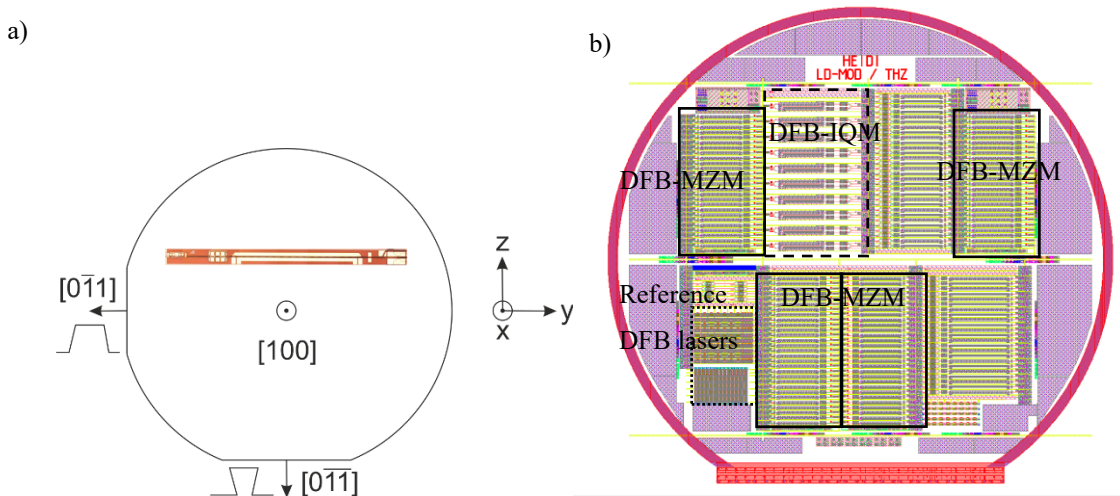


Fig. 27. a) Schematic of [100] InP wafer substrate and waveguide cross-sections in $[0\bar{1}\bar{1}]$ and $[0\bar{1}1]$ directions after wet etching. **b)** Screenshot of wafer layout, drawn in klayout.

The DFB laser Mach-Zehnder modulator (DFB-MZM) and DFB laser IQ modulator (DFB-IQM) transmitter photonic integrated circuits are arranged in multiple bars on the wafer. In addition, bars with reference DFB lasers without modulator are fabricated on the wafer.

The integrated transmitters are fabricated in more than 20 lithographic steps. The lithographic alignment tolerance in this work is about $\pm 0.5 \mu\text{m}$. For structuring the DFB gratings, which are in the nanometer scale, direct e-beam writing is used. The lithographic masks are designed with a computer assisted design software (kLayout [61]) and directly written with an e-beam writer in a chrome layer on glass substrates. Fig. 27b shows a screenshot of the complete wafer layout with all the lithographic masks. To transfer the structures onto the wafer, photo resist is deposited on the wafer surface, exposed under the lithographic masks and developed. Depending on the photo resist, the resist below the mask is either removed or protected, defining, where the material is etched or deposited later. For most etching steps, the photo resist is not persistent enough. Thus, a silicon nitride (SiN_x) layer, which

outlasts the etching process, is deposited on the wafer surface below the photo resist. The structures are first etched into the silicon nitride layer, then the photo resist is removed and the structures are further etched into the semiconductor.

The longitudinal laser, modulator and spot-size converter cross-sections during the process steps are sketched in Fig. 28. A summary of the fabrication steps is given in Table 1.

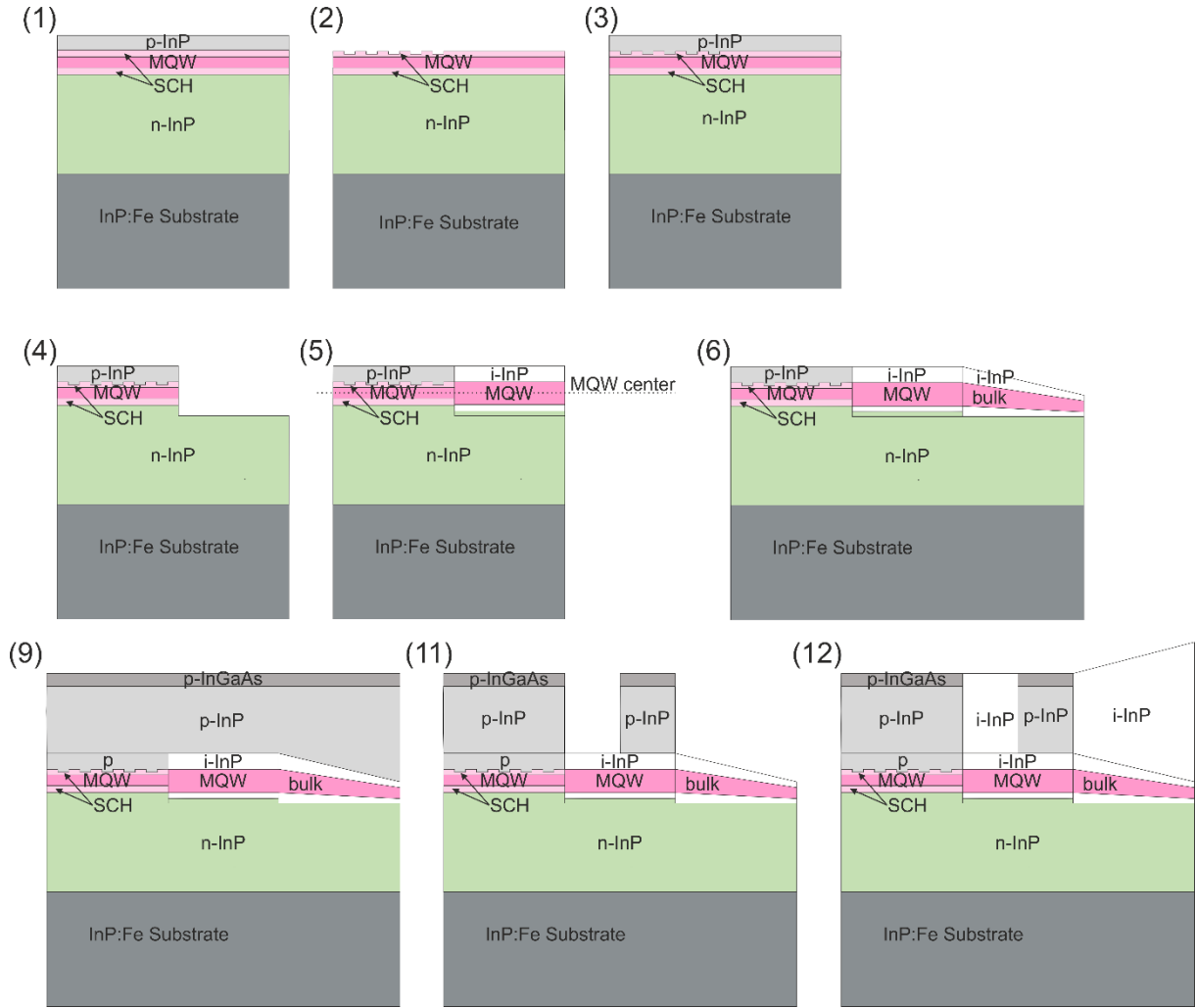


Fig. 28. Schematic fabrication process steps, longitudinal waveguide cross-sections during 1) laser layer growth on substrate, 2) structuring of DFB grating, 3) covering of DFB grating, 4) etching of laser islands, 5) modulator layer regrowth, 6) spot-size converter layer regrowth, 9) p-InP cladding overgrowth, 11) structuring of passive and active regions, 12) i-InP cladding regrowth in passive regions.

Step	Description	Schematic
1)	Laser layer stack is grown on InP substrate	Fig. 28
2)	DFB gratings are structured	Fig. 28
3)	Wafer is covered with p-InP grating protection layer	Fig. 28
4)	Laser regions are selectively etched	Fig. 28
5)	Modulator layers are grown	Fig. 28
6)	Laser and modulator regions are selectively etched and spot-size converter layers are grown.	Fig. 28
7)	Laser waveguides are structured	Fig. 29
8)	Laser waveguides are buried with pn blocking layers	Fig. 29
9)	Wafer is covered with p-doped InP and InGaAs.	Fig. 28
10)	P-contact regions are Zinc diffused.	-
11)	P-doped cladding is removed in passive regions	Fig. 28
12)	Intrinsic InP cladding is regrown in passive regions	Fig. 28
13)	Laser buried heterostructure and modulator and SSC deep-ridge waveguides are etched	Fig. 30
14)	Isolation trenches are formed	-
15)	Waveguides are passivated with SiN _x	Fig. 31
16)	Laser Pt heater stripes are deposited	-
17)	Gold contact electrodes are deposited and structured	Fig. 31

Table 1. Transmitter photonic integrated circuit fabrication process.

The laser and modulator multi quantum wells (MQWs) and waveguide cores are inherently different, so that the layers are grown individually and connected at the waveguide interfaces by butt-joints. First, the laser layers are grown on the substrate (Fig. 28 (1)). The DFB laser gratings are structured by direct e-beam writing and dry etched, into the top separate confinement heterostructure layer, after removing the top p-InP cladding (Fig. 28 (2)). A p-doped indium phosphide layer is deposited over the whole wafer surface, protecting the gratings (Fig. 28 (3)). The laser islands are etched out (Fig. 28 (4)) and the modulator layers are regrown (Fig. 28 (5)). The laser and modulator MQW centers are vertically aligned, to achieve the best coupling efficiency. To prevent material piling up at the silicon nitride mask edges, the semiconductor below the mask is laterally undercut etched before every regrowth. Also, the spot-size converter layers are connected to the modulator regions by butt-joint (Fig. 28 (6)). To achieve the layer thickness variation, the spot-size converter is grown between mask areas with laterally varying widths, since the amount of deposited material depends on the mask area.

In Fig. 29 and Fig. 30, the waveguide fabrication steps along the transition from the DFB laser to the modulator section are depicted in detail with the top view and cross-sections.

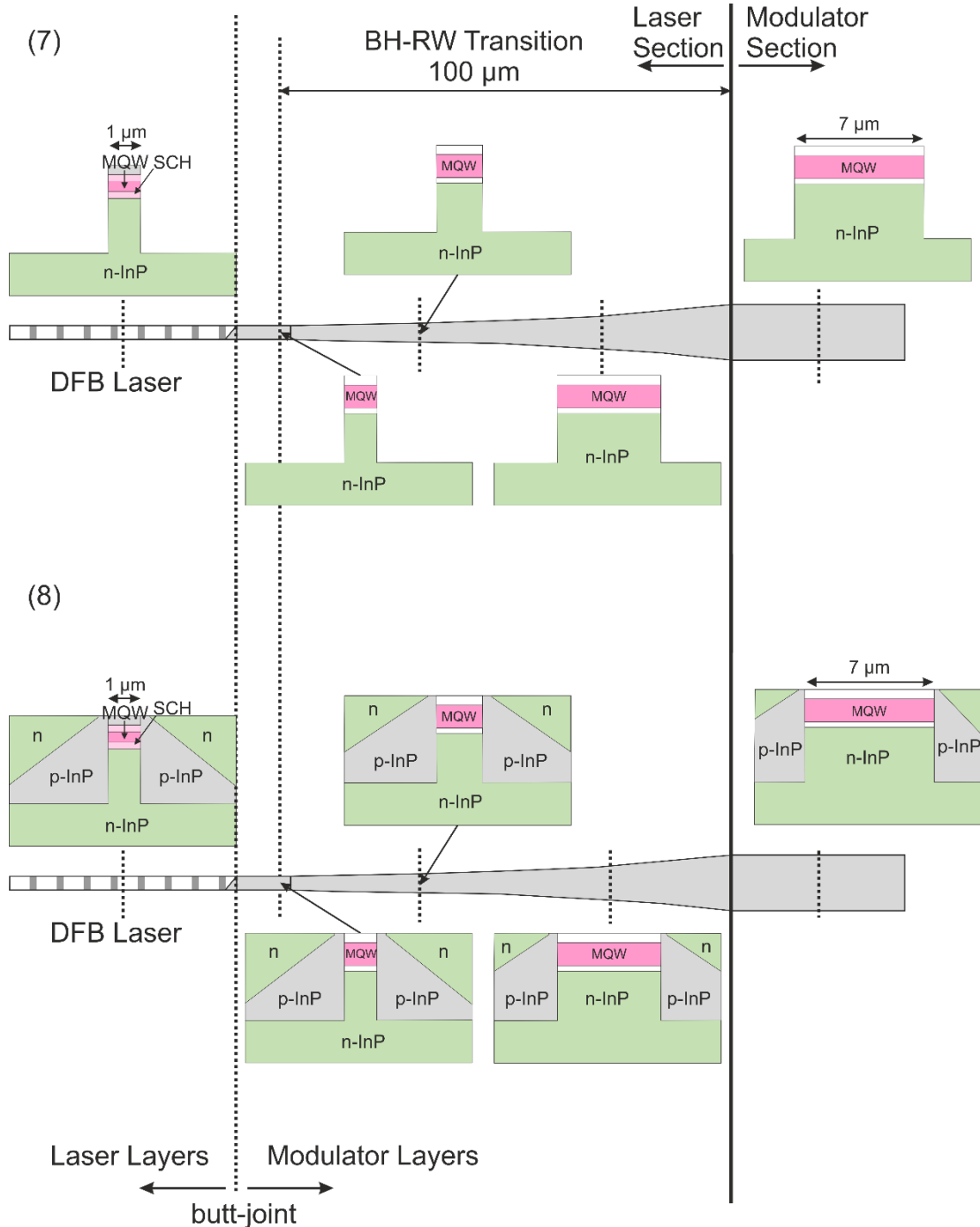


Fig. 29. Schematic fabrication process steps at transition from DFB laser to modulator section, top view and cross-sections at 7) laser waveguide etching and 8) pn blocking regrowth.

In Fig. 29 (7), the 1 μm wide laser waveguide is dry etched, down to the n-doped InP layer. Towards the modulator section, the waveguide width is adiabatically increased to 7 μm. To avoid oxidation, the waveguide is immediately buried after etching, with p- and n-doped InP current blocking layers (Fig. 29 (8)).

Since the laser and the modulator both have pin double heterostructure architectures, common n- and p-doped cladding layers are implemented. The p-doped InP and indium gallium arsenide (InGaAs) cladding layers are grown over the whole wafer, so that the laser and modulator sections have the same heights (Fig. 28 (9)). The p-

doped cladding regions are diffused with p-dopants, to decrease the contact resistance (10). This step is typically only done for lasers, since in the modulator region, the increased p-doping might lead to a higher insertion loss. For the integrated transmitters, the insertion loss is not as critical as for modulators without lasers and the lower contact resistance might benefit the modulator bandwidth. Thus, in the transmitter photonic integrated circuits, the p-diffusion is implemented both in the laser and modulator sections. Passive regions are fabricated by selective wet chemical etching of the p-doped cladding (Fig. 28 (11)) and regrowing intrinsic InP in the passive regions (Fig. 28 (12)).

Smooth waveguide sidewalls are best fabricated by wet chemical etching. However, in the $[0\bar{1}1]$ direction, the waveguide edges after wet chemical etching become diagonal as sketched in Fig. 27a. Since straight edges are favored, to achieve the best laser and modulator efficiency, the transmitter waveguides are fabricated by dry etching, where almost straight waveguide edges are obtained. The laser buried heterostructure and the modulator and spot-size converter deep-ridge waveguides are etched, down to the n-doped InP layer, where the n-contacts are deposited later (Fig. 30 (13)).

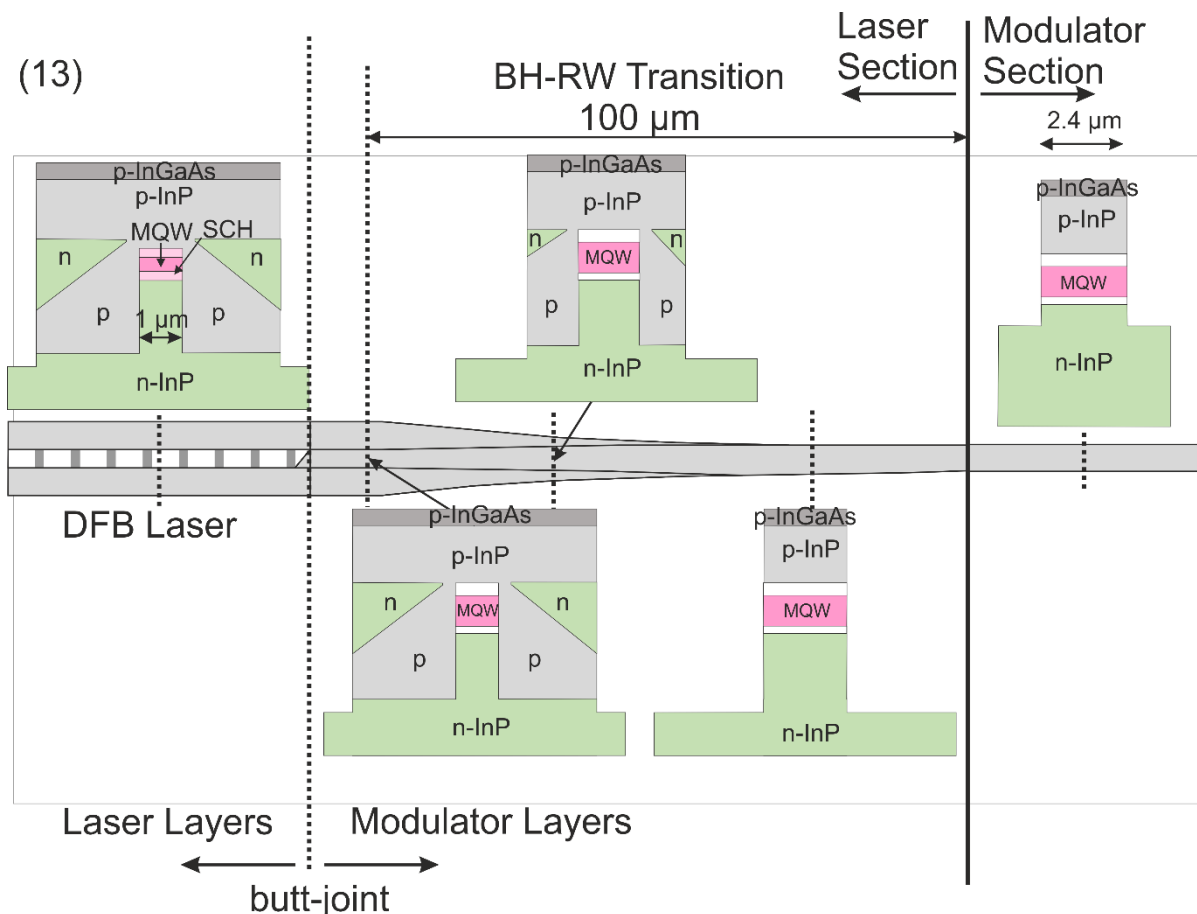


Fig. 30. Schematic fabrication process steps at transition from DFB laser to modulator section, top view and cross-sections at 13) waveguide etching.

The InP buried heterostructure etches faster than the modulator and the spot-size converter deep-ridge waveguides, containing InGaAsP. To realize optimum etching depths in each of the devices, the etching is performed in multiple steps.

1. All regions are etched together
2. Laser sections are protected with photo resist, while modulator and spot-size converter sections are etched
3. All regions are etched together, so that laser and modulator waveguides reach the desired etching depths

Isolation trenches around the waveguides are formed by dry etching to the semi-insulating substrate, further reducing the n-doped InP layer resistance. Since the spot-size converter does not require the deposition of an n-contact electrode, it is deep-etched to the substrate.

The waveguides are passivated by depositing a 200 nm thick silicon nitride layer over the entire wafer surface (Fig. 31 (15)).

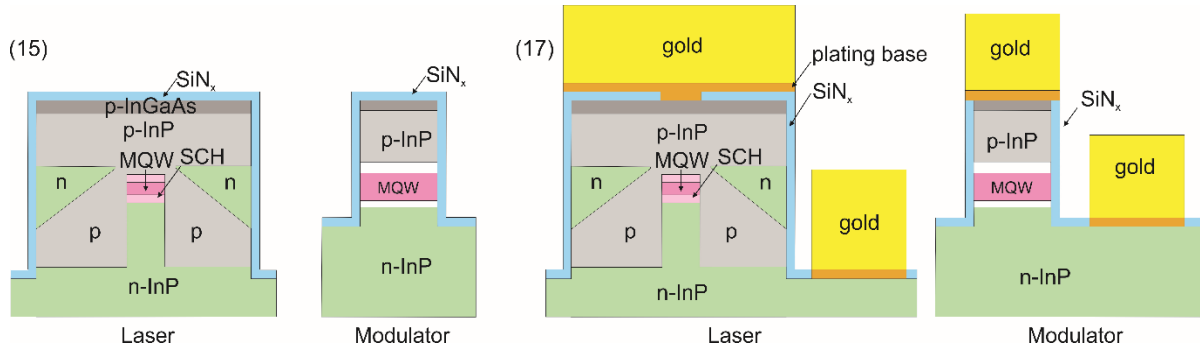


Fig. 31. Waveguide cross-sections after 15) passivation, 17) gold contact deposition.

The DFB laser platinum (Pt) heater stripes for wavelength fine-tuning are vapor deposited on the silicon nitride, close to the laser waveguide (16). Windows are etched into the passivation layer, to deposit the contact metal (Fig. 31 (17)). In particular, the complete wafer surface is covered first with a photo resist and a titanium platinum plating base for electro plating. The photo resist is opened above the contacts. The gold contacts are deposited by sputtering, vapor deposition and electroplating steps and structured by chemical assisted ion beam etching. To form air bridges between the contact electrodes and the contact pads on mesas, metal is deposited directly on the photo resist. The remaining photo resist is removed after the contacts are structured.

After the transmitters are fabricated, the wafers are thinned for easier bar and chip cleaving. The transmitter and laser bars are cleaved, and anti-reflection coating is sputtered onto the facets to suppress optical reflections.

4.5 Performance

In this subchapter, the fabricated transmitters are direct current (dc) and small signal characterized at chip level. In particular, the performance of integrated transmitters and reference Mach-Zehnder modulators without integrated laser are compared. To be used in future optical transceiver modules for 100 Gb/s operation and higher, the transmitters should fulfill at least the following requirements, based on current specifications for up to 40 km 100 Gb/s Ethernet links [62]:

- Symbol rate: 25 GBd
- Side mode suppression ratio (min): 30 dB
- Relative intensity noise (max): -130 dB/Hz

- Output power (min): -3 dBm
- Extinction ratio (min): 8 dB

Moreover, a narrow optical transmitter linewidth is preferable to achieve a good signal quality and a maximum limit is often specified, especially for phase modulated signals. At quaternary phase shift keying or 16 symbol quadrature amplitude modulation (QAM16), i.e. at 32 GBd symbol rate, the linewidth should be lower than 10 MHz [63]. For intensity modulated signals, the linewidth is less critical.

First, the structure and performance of the 90 degrees rotated buried heterostructure reference DFB lasers are investigated, then the DFB laser integrated Mach-Zehnder and IQ modulator (DFB-MZM/-IQM) transmitter photonic integrated circuits are characterized.

4.5.1 Reference DFB Lasers

Structure

The main change in the DFB laser structure for the monolithic integration is the 90 degrees waveguide rotation. Buried heterostructure waveguides are typically fabricated in the $[0\bar{1}\bar{1}]$ direction, while the integrated transmitters are fabricated in the $[0\bar{1}1]$ direction (Fig. 27a). The fabricated 90° rotated buried heterostructure DFB laser cross-sections are observed with a scanning electron microscope (SEM) (Fig. 32a) and compared with a typical DFB laser cross-section in the $[0\bar{1}\bar{1}]$ direction (Fig. 32b).

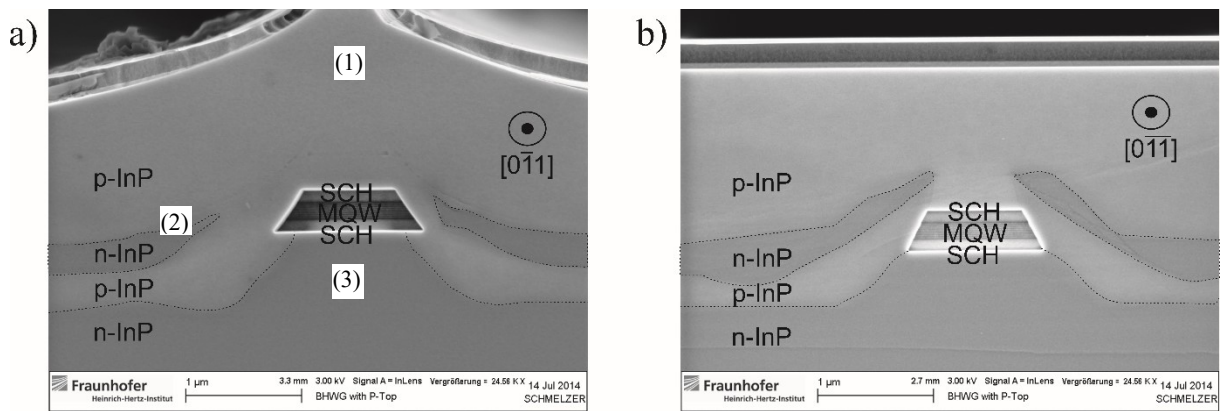


Fig. 32. SEM pictures of DFB laser buried heterostructure cross-sections a) in $[0\bar{1}\bar{1}]$ and b) in $[0\bar{1}1]$ directions.

The cross-sections in the two crystal directions structures show a few differences. For the 90° rotated DFB lasers, the p-doped top cladding (p-InP) is arched, while in the typical $[0\bar{1}\bar{1}]$ direction, a flat top is obtained. Moreover, the lateral p- and n-doped InP layer structure for current blocking in the 90° rotated DFB laser is altered. The n-doped InP (n-InP) regions next to and below the active region are partly vanished or faded away.

The arched p-InP cladding at point (1) in Fig. 32 should not represent any problems. However, the altered n-InP layer structure, might impair the laser current guiding and thus the laser threshold current and output power. For a proper current guiding, the lateral n-InP layers at point (2) should be about 100- 200 nm away from the active region, as in Fig. 32b. In the 90° rotated buried heterostructure waveguides, the distance is increased to up to 800- 900 nm. Moreover, the n-InP below the active region at point (3) is narrowed, so that parts of the active region

might not be pumped, effectively narrowing the active region. The unpumped active material acts as a saturable absorber, increasing the losses in the active layer.

Additional epitaxial regrowth tests show, that the n-InP layer structures changes during the high temperature p-InP cladding overgrowth at 670°C, due to mass transport [60]. It is observed, that the mass transport is reduced by starting the regrowth earlier at 550°C, during the heat up to 670°C, and by adding Arsine gas (AsH₃) to stabilize the crystal surfaces. The same technique is also used to avoid mass transport, in Bragg gratings in the [0̄1̄1] direction [60]. A SEM picture of the buried-heterostructure waveguide cross-section in [0̄1̄1] direction under optimized p-InP cladding growth conditions is given in Fig. 33, showing only a slight deformation of the n-InP layers.

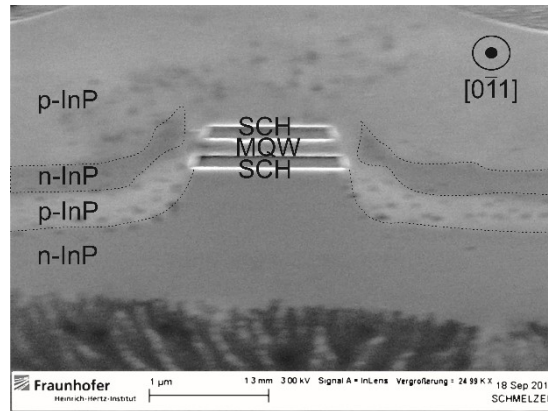


Fig. 33. SEM picture of buried heterostructure waveguide cross-section in [0̄1̄1] direction with optimized p-InP overgrowth process.

In the regrowth test, the mass transport reduction is achieved for a single growth step. Further investigation is ongoing, to minimize the mass transport during the whole fabrication process.

Fig. 34 shows the longitudinal cross-section of a 90° rotated DFB grating in the [0̄1̄1] direction.

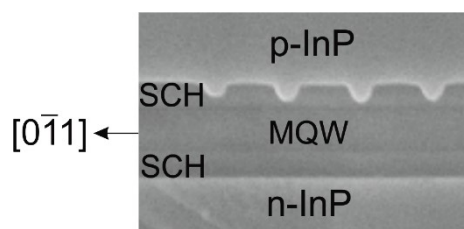


Fig. 34. SEM picture of DFB grating in [0̄1̄1] direction, longitudinal cross-section.

The grating is originally designed to have a rectangular shape and a 50 % duty cycle. In the fabricated grating, the duty cycle is measured to 63 % and the grating shape is not rectangular. The grating structure impacts the reflectivity. The original rectangular and the fabricated grating effective power reflectivity, without including the internal laser loss, are simulated with OptiGrating [64]. The reflectivity depending on the wavelength are given in Fig. 35.

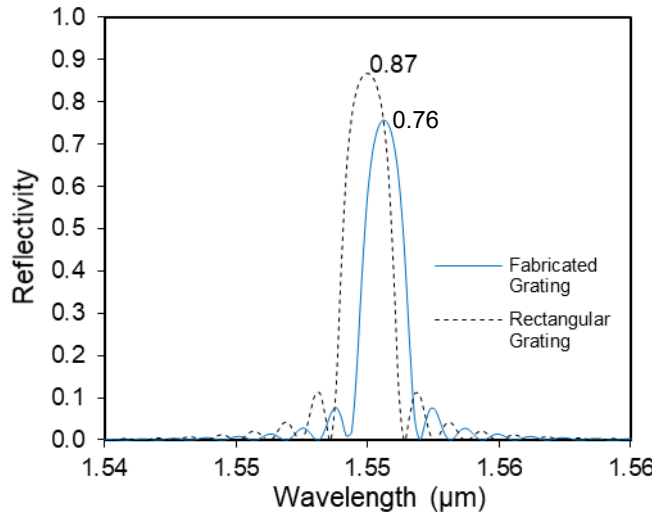


Fig. 35. Simulated DFB grating power reflectivity vs. wavelength for the original 50 % duty cycle rectangular grating and the fabricated grating.

The rectangular grating has a peak effective reflectivity of 86 % at the 1550 nm Bragg wavelength. For the fabricated grating, the peak wavelength is shifted to 1550.6 nm and the effective reflectivity is decreased to 76 %. When including the internal losses of about 16.5 cm^{-1} (based on empirical values), the rectangular grating reflectivity becomes 72 %, while the fabricated one is 59 %, which is 13 % lower. A lower reflectivity is not favored, since it increases the laser effective mirror losses and thus the threshold current [22].

SEM pictures of the 90° rotated DFB lasers show that the buried heterostructure waveguide and the grating structures differ from the intended design. This might influence the laser performance in terms of output power and threshold current. Therefore, further optimization should be conducted, to get a more reliable buried heterostructure waveguide and grating fabrication process, which exceeds however the scope of this work.

Light-Current-Voltage (L-I-V) Characteristics

After the fabrication, the reference DFB lasers are cleaved into bars and both facets are anti-reflection coated. The characterization is done at chip-level. The DFB laser bars are placed on a metal chip stage, which includes a Peltier element for temperature control. The bias current is applied with a current source to the laser, which also measures the laser voltage. The current source is connected to the laser, by placing probe needles on the contact pads.

For the light-current-voltage (L-I-V) characteristic measurements, an integrating sphere is used to receive the optical power. The laser output power and voltage are measured, while increasing the bias current from 0 mA to 200 mA. To minimize the thermal effects, a pulsed current source is used, sending 2 μs wide rectangular pulses every 200 μs . A summary of the measured average threshold current I_{th} , the output power P and the voltage V at 100 mA and 200 mA pulsed bias current is given in Table 2 (temperature: 20°C).

Parameter	Average value
I_{th}	14.4 mA
P (I: 100 mA)	9.1 mW
V (I: 100 mA)	1.4 V
P (I: 200 mA)	16.3 mW
V (I: 200 mA)	1.8 V

Table 2. Reference [011] DFB laser average I_{th} , P and V values at 100 mA and 200 mA (pulsed operation, 20°C)

Compared to same structure BH-DFB lasers in the [011] direction with the same structure, the 90° rotated buried-heterostructure (BH) DFB laser average threshold current is doubled, while the 0.13 W/A single facet slope efficiency $\Delta P/\Delta I$ is comparable. This is probably an effect of the lower grating reflectivity (Fig. 35) and the deformed n-InP layers of the buried heterostructure DFB lasers in the [011] direction (Fig. 32a). Nevertheless, at bias currents larger than 100 mA, 90° rotated DFB laser output power is sufficient for the transmitter integration.

The measured voltage V over current above threshold $I-I_{th}$ graph and the calculated direct current power consumption $P_{dc} = V \cdot I$ of a typical [011] direction DFB laser and a 90° rotated one is displayed in Fig. 36.

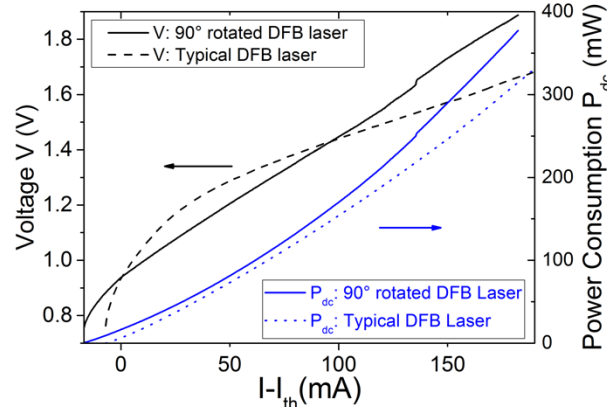


Fig. 36. Voltage V and power consumption P_{dc} over current above threshold $I-I_{th}$ for a typical and a 90° rotated DFB laser.

The slope dV/dI in the linear part of the voltage graphs gives the differential resistance R_d . For the typical DFB laser, the R_d is 2.8 Ω, while for the 90° rotated one it is 4.8 Ω. The 90° rotated DFB laser power consumption is slightly increased compared to the typical DFB laser one, especially at currents more than 100 mA above threshold. At 85 mA above threshold, the 90° rotated DFB laser power consumption is about 141 mW, while for the typical DFB laser it is 128 mW.

The output power vs. current graphs for a 90° rotated DFB laser are depicted both in pulsed operation in Fig. 37a and in continuous wave (CW) operation in Fig. 37b, at different temperatures T from 20°C to 90°C.

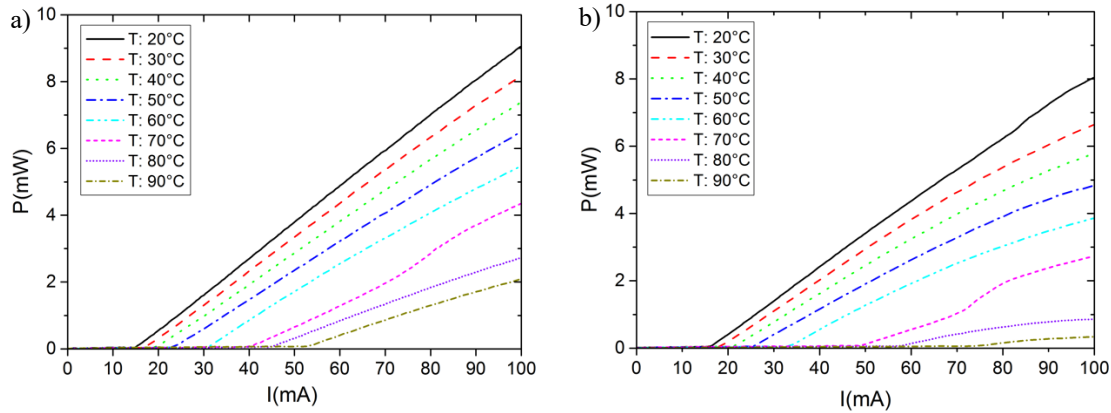


Fig. 37. 90° rotated DFB laser P vs. I graphs at different temperatures in pulsed a) and CW b) operation.

In pulsed operation, the DFB laser output power increases almost linearly with the current, starting from I_{th} , for temperatures up to 60°C. Due to the laser heat-up in continuous wave operation, an output power roll-off and a threshold current increase is visible, leading to a lower output power.

With increasing temperature, the slope efficiency $\Delta P/\Delta I$ decreases in both pulsed and continuous wave operation, requiring higher currents to achieve the same output power. The threshold current increases exponentially with the temperature, according to the relation $I_{th} \sim \exp(T/T_0)$, where T_0 is the laser characteristic temperature [65]. An exponential fit of the threshold current in pulsed and CW operation is made, depending on the temperature (Fig. 38).

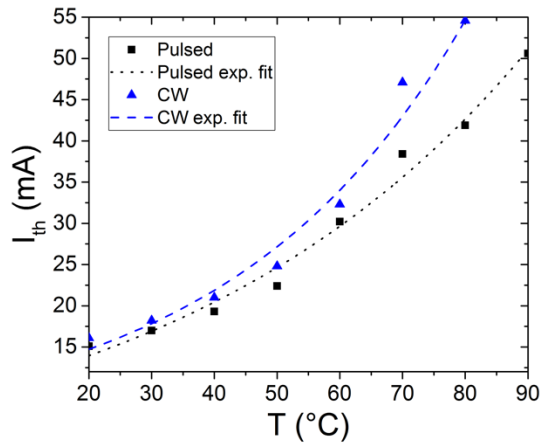


Fig. 38. Laser threshold current I_{th} vs. temperature T in pulsed and CW operation with exponential fits.

The DFB laser characteristic temperature for a single facet is 57.5 K in pulsed and 37.7 K in continuous wave operation, which is in the typical range of a standard 1550 nm InGaAsP/InP multi quantum well DFB laser [27]. The DFB laser performance, however, degrades quickly at increasing temperatures, so that it should only be operated together with a thermoelectric cooler.

Spectrum

The DFB laser spectra are measured by operating the laser in continuous wave and coupling the laser output to an optical fiber and displaying the signal on an optical spectrum analyzer (OSA). Weak optical feedback influences

the laser performance. Thus, the fiber is anti-reflection coated fiber and an isolator is placed between the fiber and the optical spectrum analyzer, to suppress any reflections from the setup.

Single mode spectra with side mode suppression ratios (SMSR) larger than 43 dB at currents $I - I_{th}$ larger than 25 mA are observed ($T: 20^\circ\text{C}$). For the integrated transmitters, a side mode suppression ratio larger than 30 dB is required, which is fulfilled by the reference DFB lasers. A DFB laser spectrum with 49 dB side mode suppression ratio and 1543.8 nm wavelength is given in Fig. 39.

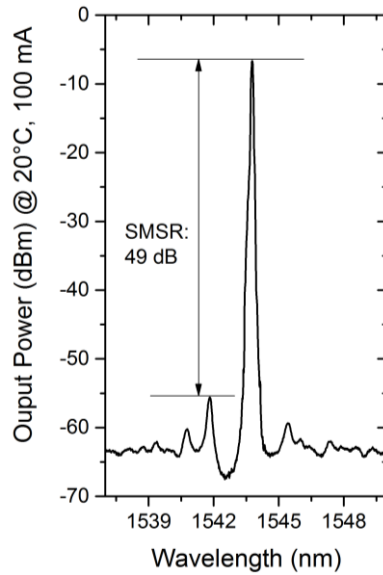


Fig. 39. Reference DFB laser spectrum with 49 dB SMSR ($I - I_{th}: 85 \text{ mA}, 20^\circ\text{C}$)

The lasing peak is centered in the stop band, due to the lambda quarter shift in the DFB grating. The laser wavelength increases linearly with the laser bias current (Fig. 40).

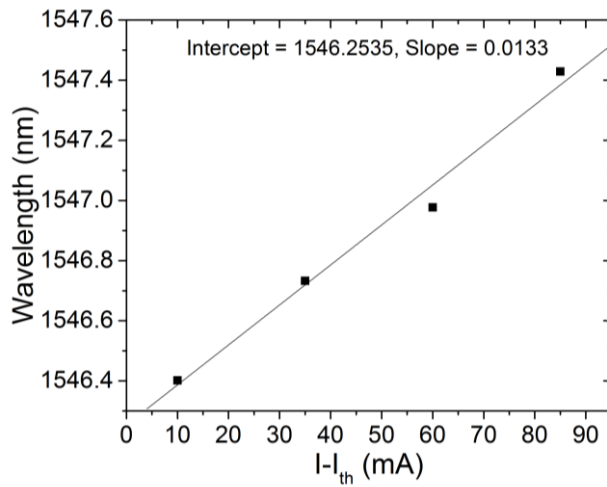


Fig. 40. DFB laser wavelength vs. bias current above threshold ($T: 20^\circ\text{C}$).

By applying a linear fit to the measured wavelengths, a wavelength increase of about 13.3 pm/mA, corresponding to a frequency increase of 1.7 GHz/mA, is estimated. The measured peak wavelengths of the reference DFB lasers wsat 100 mA bias current are around 1540 nm, 1544 nm and 1548 nm, around 11 nm lower than expected. The DFB laser wavelengths are nevertheless sufficient for the integrated transmitters, since they are in the C-band.

Wavelength Fine-Tuning

The integrated heater stripes for wavelength fine-tuning are tested by applying a current I_h to the DFB laser heater contacts and measuring the laser wavelength with an optical spectrum analyzer. The voltage V_h at the heater is measured with the multimeter current source. The laser wavelength and the heater power consumption $P_h = I_h \cdot V_h$ show a quadratic increase with I_h (Fig. 41).

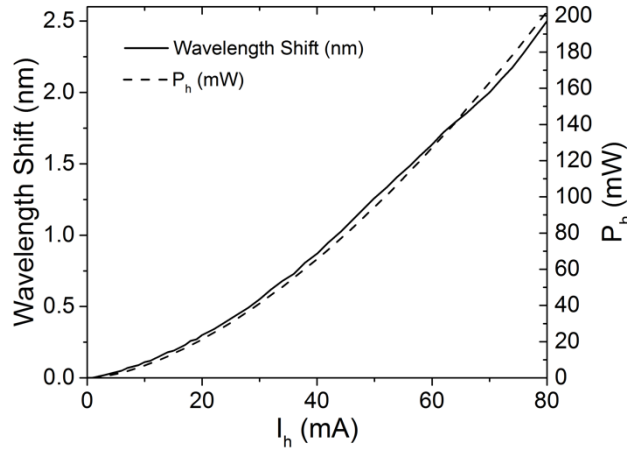


Fig. 41. Laser wavelength shift and heater power consumption P_h vs. heater current I_h .

At 80 mA heater current, a 2.5 nm wavelength increase at a power consumption of 202 mW is achieved.

Relative Intensity Noise (RIN)

The relative intensity noise (RIN) characterizes the laser intensity fluctuations, which are mainly caused by spontaneous emission. The relative intensity noise is expressed by eq. (4.1) [20],

$$\text{RIN} = \frac{\langle \delta P^2 \rangle}{\langle P^2 \rangle} \text{ dB/Hz} \quad (4.1)$$

where $\langle \delta P^2 \rangle$ is the mean-square optical output power noise in a 1 Hz bandwidth and $\langle P^2 \rangle$ is the mean-square optical power.

For measuring the relative intensity noise, the laser output is launched into a light wave signal analyzer (Agilent 71400), through an anti-reflection coated optical fiber and an optical isolator (Fig. 42).

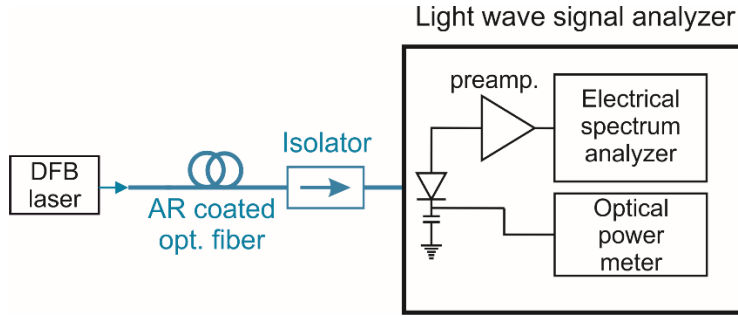


Fig. 42. Experimental setup for relative intensity noise measurements.

The light wave signal analyzer includes a broadband photodiode, an electrical preamplifier, an optical power meter and an electrical spectrum analyzer [66]. The optical power is detected with the photodetector, which converts it into a photo current I_{ph} . The photo current is amplified with the preamplifier, producing an output voltage across a 50Ω load resistance R_L , which is measured with the electrical spectrum analyzer, calculating and displaying the electrical power spectrum.

The RIN can be expressed by the received electrical power as shown in eq. (4.2) [66], where $N_{el}(\omega)$ is the photocurrent power spectral density at an angular frequency ω in a 1 Hz bandwidth and $P_{avg,el}$ the average electrical power $P_{avg,el} = I_{ph}^2/R_L$.

$$RIN = \frac{N_{el}(\omega)}{P_{avg,el}} \text{ dB/Hz} \quad (4.2)$$

The average optical power is measured with the power meter as a reference. The total measured system noise includes not only the laser noise, but also shot noise from the photodiode and thermal noise from electrical components. The thermal noise for a given temperature is usually constant and can be calculated from the system component noise figures, while the shot noise is calculated, depending on average optical input power to the preamplifier [66]. To determine the laser relative intensity noise, the shot and thermal noise are subtracted from the total system noise inside the light wave signal analyzer, before displaying the RIN spectrum.

The measured reference DFB laser RIN spectra at different bias currents above threshold are displayed in Fig. 43 (T: 20°C).

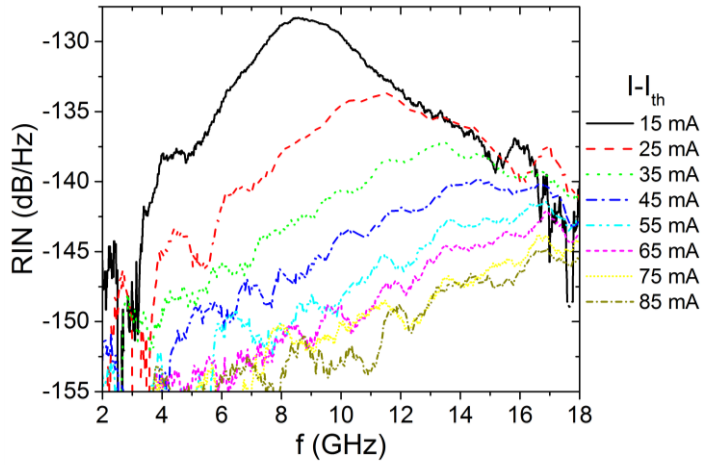


Fig. 43. Reference DFB laser RIN spectra at different laser bias currents above threshold (T: 20°C).

The spectra have a resonance peak at the laser relaxation oscillation frequency, which is damped at increasing laser bias current. Compared to typical DFB lasers, the 90° rotated DFB laser RIN resonance peaks are more damped, probably due to the lower grating reflectivity and therefore higher mirror losses [20]. Maximum RIN levels lower than -133 dB/Hz are measured at bias currents larger than 25 mA above threshold, decreasing down to -144 dB/Hz at 90 mA $I - I_{th}$ (Fig. 44).

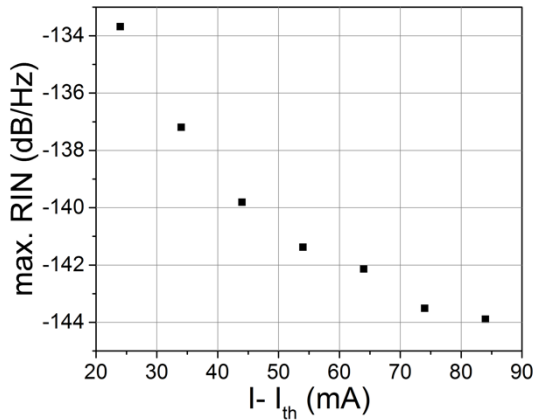


Fig. 44. Reference DFB laser max. RIN versus laser bias current I above threshold I_{th} .

The RIN spectrum peak frequency $f_{\text{Max. RIN}}$ increases with the bias current to up to 19.4 GHz (Fig. 45).

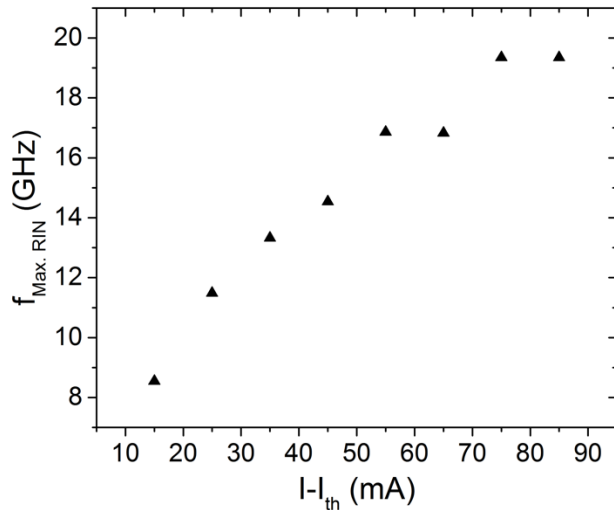


Fig. 45. DFB laser frequency of max. RIN $f_{\text{Max. RIN}}$ vs. laser bias current above threshold.

The reference DFB laser RIN levels at bias currents larger than 25 mA above threshold are sufficiently low for 100 Gb/s Ethernet links, where RIN levels should not exceed -130 dB/Hz.

Linewidth

The linewidth describes the laser spectral width and is an important measure for the laser phase noise. A schematic for the linewidth measurement experimental setup is given in Fig. 46.

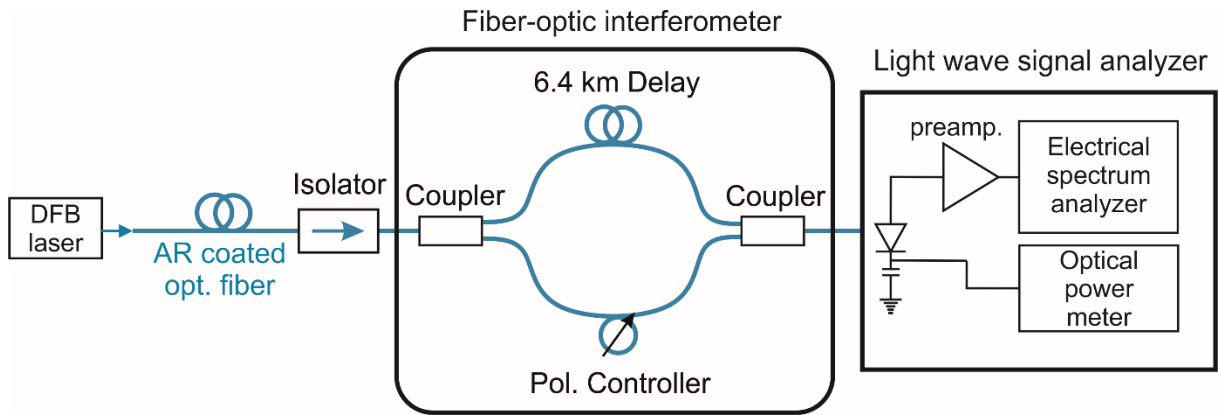


Fig. 46. Experimental setup for linewidth measurements.

The laser output is coupled through an anti-reflection (AR) coated optical fiber and an isolator, which are of importance since the laser linewidth is very sensitive to back-reflections. By employing a fiber-optic Mach-Zehnder interferometer (MZI) after the isolator, the laser phase or frequency noise is converted into intensity noise, which is detected with the electrical spectrum analyzer [67].

In the interferometer, the signal in one arm is delayed by 6.4 km before it combines again with the signal of the other arm. A polarization controller is inserted into the MZI, to match the polarizations of the two arms. The transmitted interferometer electrical field $E_{T,MZI}(t)$ at time t is given by eq. (4.3) [20], where B is a constant factor, E the laser electrical field and τ the delay time.

$$E_{T,MZI}(t) = B(E(t) + E(t-\tau)) \quad (4.3)$$

The average interferometer output power $\langle P_{T,MZI}(t) \rangle$ is given in eq. (4.4).

$$\langle P_{T,MZI}(t) \rangle = 2|B|^2 \langle |E(t)|^2 \rangle \left[1 + \text{Re} \left(\frac{\langle E(t) E^*(t-\tau) \rangle}{\langle |E(t)|^2 \rangle} \right) \right] \quad (4.4)$$

In the Mach-Zehnder interferometer, the laser frequency noise is translated into intensity noise. The Fourier transform of the measured laser signal intensity, represents the laser power spectral shape, centered at zero frequency [20]. When the laser line shape is Lorentzian, the spectrum half-width or 3 dB bandwidth corresponds to the linewidth. This technique is referred to as self-homodyne detection.

The DFB laser lines are approximately Lorentzian shaped. The measured line spectra at three different bias currents are shown in Fig. 47, where the dashed green lines show the Lorentzian fits ($T: 40^\circ\text{C}$).

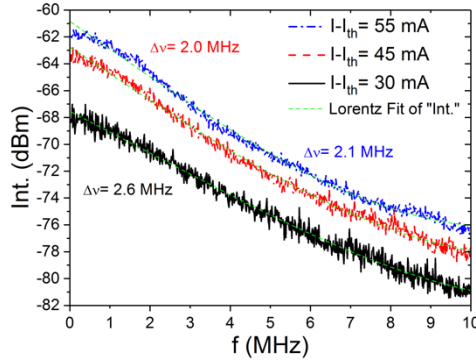


Fig. 47. DFB laser line spectra at different bias currents above threshold. The Lorentzian shape is indicated by the dashed green fit curve.

The laser linewidth $\Delta\nu$, depending on the laser bias current are displayed in Fig. 48, where the dashed green line indicates an exponential decay fit.

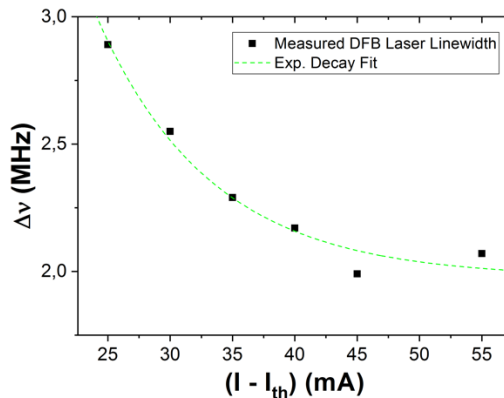


Fig. 48. DFB laser linewidth vs. bias current above threshold. The dashed green line indicates an exponential decay fit.
The linewidths are in the range of 2 MHz to 3 MHz, decreasing exponentially with the laser current.

The reference DFB laser linewidths are sufficient for the transmitter integration, for operation at up to 32 GBd QAM16. For higher symbol rates or spectral efficiencies, the DFB laser linewidth should be lowered. The linewidth optimization is however not within the frame of this work.

Electro-Optic Response

Although, the lasers in integrated transmitters are operated in continuous wave, the modulation response gives important information about the laser dynamics. The DFB laser small signal modulation response is obtained by applying a sinusoidal rf current in addition to the dc bias current with a bias tee. The sinusoidal signal is generated and frequency-swept by a light wave component analyzer (LCA), also measuring the modulated laser output power. The laser output is coupled to an anti-reflection coated fiber, an optical isolator and input to the LCA. The measured electro-optic (E-O) responses at different laser bias currents above threshold are given in Fig. 49 (T: 20°C).

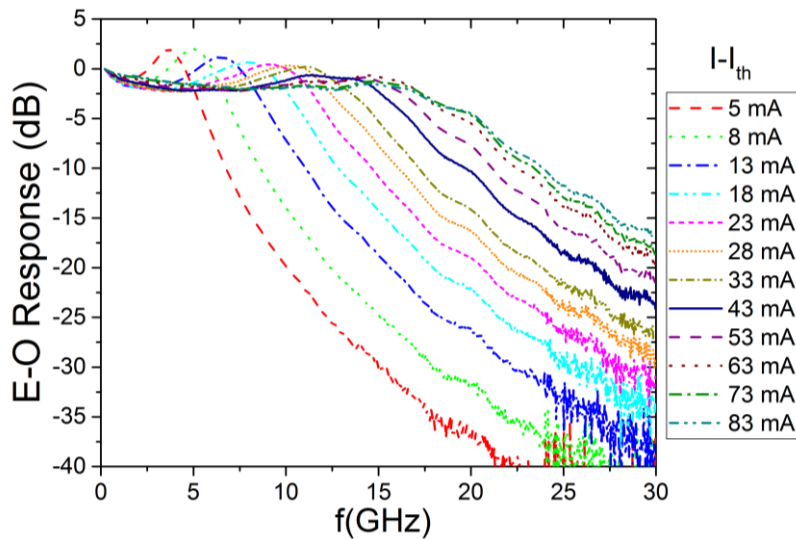


Fig. 49. DFB laser small signal electro-optic (E-O) frequency responses at different bias currents.

The laser electro-optic response has a low pass filter shape with a resonance peak at the laser relaxation oscillation frequency f_r . The 3 dB cut-off frequency $f_{3\text{dB}}$, where the E-O response is -3 dB, is a measure for the laser modulation bandwidth. The 3 dB cut-off frequency, the resonance frequency and the E-O response enhancement at the resonance frequency are obtained from Fig. 49 and plotted in Fig. 50 against the laser bias current above threshold.

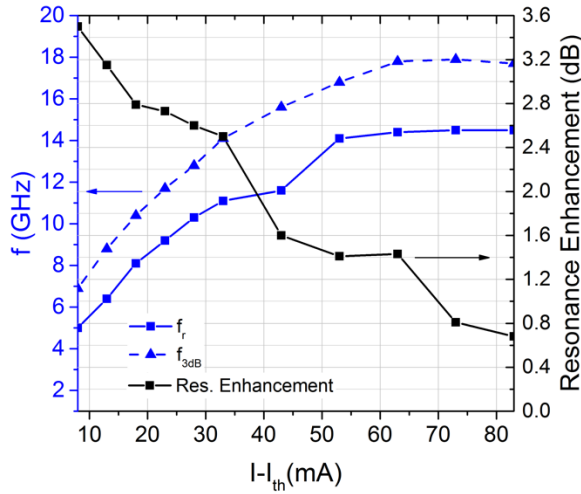


Fig. 50. DFB laser relaxation oscillation frequency f_r , 3 dB cut-off frequency f_{3dB} and resonance enhancement vs. bias current above threshold.

f_r and f_{3dB} are related and increase with the laser bias current, until at currents larger than 63 mA above threshold, they saturate to $f_r = 14.5$ GHz and $f_{3dB} = 17.7$ GHz. The resonance decreases and broadens at increasing bias currents, so that it almost disappears at currents larger than 63 mA above threshold.

The 90 degrees rotated DFB lasers have a larger resonance frequency and a lower resonance enhancement compared to typical DFB lasers. The reason might be the narrowed effective active region width (due to the narrowed n-InP layer below the active material), since the resonance frequency and damping are inversely proportional to the active region volume [20]. The differences in resonance frequency and enhancement mainly impact on the laser direct modulation performance, so that they are not important for the transmitter integration, where the laser is only operated in continuous wave.

4.5.2 DFB-Laser Mach-Zehnder/ IQ Modulator Transmitter Photonic Integrated Circuits

In this subchapter, the fabricated DFB-Laser Mach-Zehnder/ IQ Modulator transmitter photonic integrated circuits, described in chapter 4.1 are characterized at chip level. The Mach-Zehnder modulator dc and small signal modulation performance in terms of insertion loss, switching voltage and bandwidth is tested and compared to similar Mach-Zehnder modulators without integrated laser.

4.5.3 Direct current (dc) Characterization

In the Mach-Zehnder modulator dc characterization, independent voltages are applied to the two travelling wave U- and I-electrodes, as shown in Fig. 51.

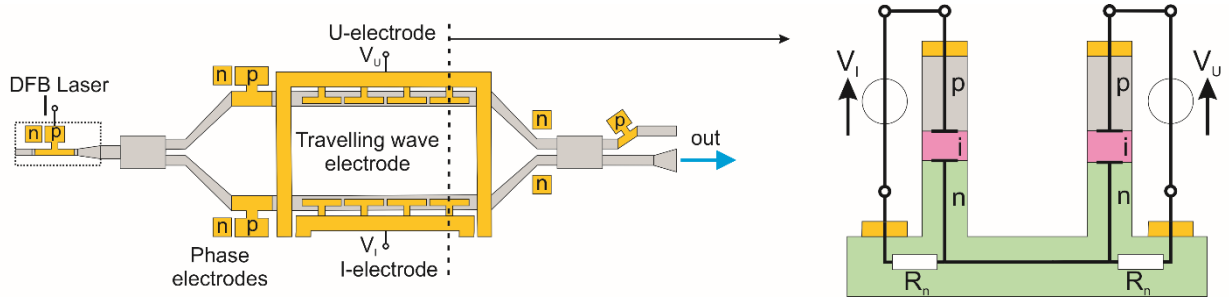


Fig. 51. Mach-Zehnder modulator wiring during dc characterization.

The integrated laser is operated in continuous wave with 100 mA bias current ($I - I_{th}$: 85 mA). The temperature is set to 20°C, to achieve a high laser output power. The modulator output is coupled to an optical fiber and the output power is measured with a photodiode with a responsivity r of 1.8 A/W at a constant input power, while varying the applied voltages.

The transmitter output power P_{out} is calculated from the measured photo current I_{ph} and the photo diode responsivity ($P_{out} = I_{ph}/r$). The output power matrix, depending on the applied voltages at the U- and I- electrodes V_U and V_I , is given in Fig. 52.

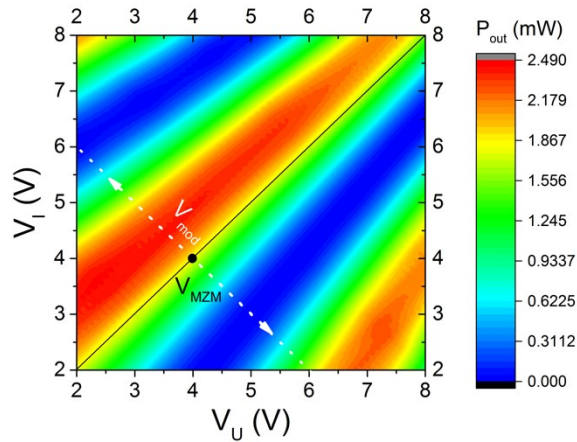


Fig. 52. Modulator output power matrix, depending on the applied voltages at the U- and I-electrodes. The dotted white arrow represents the applied modulation voltage V_{mod} in push-pull operation, at a modulator bias voltage V_{MZM} on the straight black line.

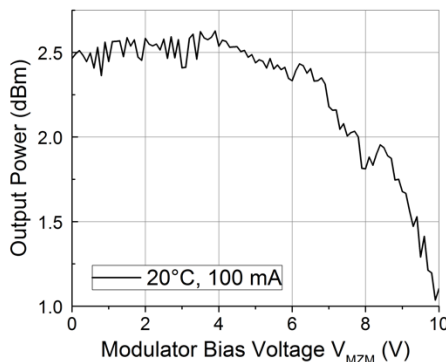
From the output power matrix, the modulator switching voltage and extinction ratio are obtained. The maximum measured output power into the fiber is 2.5 mW, corresponding to 4 dBm. The passive insertion loss of a single Mach-Zehnder modulator is expected to be 4.7 dB. A summary of the loss at different positions, based on empirical results is given in Table 3.

Position	Passive Insertion Loss IL (dB)
Multi-mode interference couplers	0.25
Passive Waveguides (0.27 dB/mm)	2.15
Spot-size converter	1.4
Absorption in p-doped layers	0.8
Mach-Zehnder modulator total	4.7

Table 3. Mach-Zehnder modulator passive insertion loss summary.

Typically, the Mach-Zehnder modulator is in push-pull operation, where the U- and I-electrodes are connected with a $50\ \Omega$ resistance, as in Fig. 58. A modulator bias voltage V_{MZM} is applied to either the U- or I-electrode. Due to the low $50\ \Omega$ termination resistance, almost the same voltage also drops at the other signal electrode. In the matrix plot, the biasing condition of a terminated Mach-Zehnder modulator can be obtained at points where V_U and V_I are equal (indicated by the straight black diagonal line), where V_{MZM} would be equal to $V_U = V_I$.

The output power along the straight black line in the matrix plot, where $V_{MZM} = V_U = V_I$ is plotted in Fig. 53.

**Fig. 53. Output power depending on bias voltage along straight black line in matrix plot (representing modulator bias voltage $V_{MZM} = V_U = V_I$)**

For modulator bias voltages larger than 4 V, the transmitter output power decreases, due to additional photon absorption from electroabsorptive effects. At 10 V V_{MZM} , the additional absorption is 1.5 dB.

The output power depending on the modulation voltage V_{mod} in push-pull operation, is represented by the white dotted arrow in the matrix plot. From the output power along the white dotted arrow, the switching voltage V_π and the extinction ratio (ER) at a certain modulator bias voltage are obtained. The output power along the white dotted arrow at 8 V V_{MZM} is given in Fig. 54.

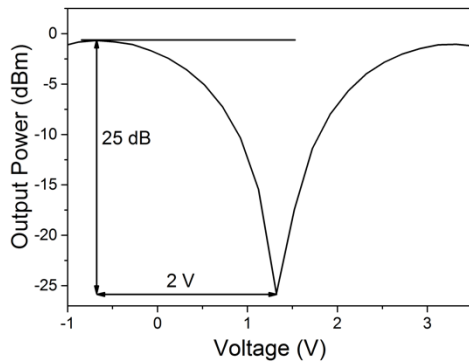


Fig. 54. Output power depending on bias voltage along white dotted arrow in matrix plot (representing V_{mod}) starting from $V_{\text{MZM}} = V_U = V_I$: 8 V, giving 25 dB extinction ratio and V_π : 2 V ($I - I_{\text{th}}$: 85 mA, T: 20°C).

The output power difference in decibel units, between the maximum and the minimum gives the extinction ratio, while the voltage difference gives the switching voltage. At 8 V modulator bias voltage, 25 dB extinction ratio and 2 V switching voltage are obtained. At increasing modulator bias voltage, the switching voltage decreases, while the extinction ratio varies between about 24 dB and 26 dB (Fig. 55).

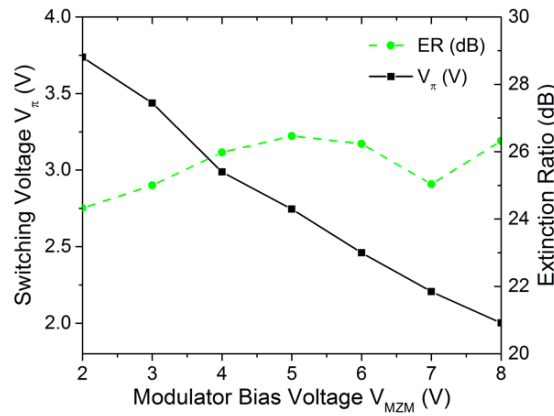


Fig. 55. Switching voltage V_π and extinction ratio vs. modulator bias voltage ($I - I_{\text{th}}$: 85 mA, T: 20°C).

For both the integrated DFB laser Mach-Zehnder and IQ modulator transmitters, the same Mach-Zehnder modulator designs are used. Thus, their switching voltage and extinction ratio characteristics are like in Fig. 55. The DFB laser IQ modulator transmitter maximum output power into the fiber is about 1.6 mW (2 dBm). For the IQ modulator, 6.6 dB total insertion loss is assumed. A summary of the loss at different positions in the IQ modulator is given in Table 4.

Position	Passive Insertion Loss IL (dB)
Multi-mode interference couplers	0.5
Passive Waveguides (0.27 dB/mm)	2.9
Spot-size converter	1.4
Passive waveguide bends	1.0
Absorption in p-doped layers	0.8
Mach-Zehnder modulator total	6.6

Table 4. IQ modulator passive insertion loss summary.

The additional loss due to electroabsorption in the signal electrodes depending on the applied modulator bias voltage for each of the two Mach-Zehnder modulators in the IQ modulator is comparable to the loss of a single Mach-Zehnder modulator (Fig. 53).

Reference Mach-Zehnder modulators, without integrated laser, are typically characterized at 40°C temperature. The switching voltage, extinction ratio and insertion loss parameter median values of 17 DFB laser Mach-Zehnder modulator photonic integrated circuits (PIC) and reference Mach-Zehnder modulators are compared at 40°C and 8 V modulator bias voltage in Table 5.

Parameter	Reference Mach-Zehnder modulator	DFB laser Mach-Zehnder modulator transmitter PIC
Switching voltage V_{π} (V)	1.5	1.8
Extinction ratio (dB)	24.4	21.7
Insertion loss (dB)	9.3	5.5

Table 5. Comparison of DFB laser Mach-Zehnder modulator PIC and reference Mach-Zehnder modulator dc parameter median values (T: 40°C, VMZM: 8 V).

The DFB laser Mach-Zehnder modulator transmitter PICs have a comparable switching voltage to the reference Mach-Zehnder modulators, but a 2.7 dB lower extinction ratio, probably due to the laser integration. The Mach-Zehnder modulators with integrated laser insertion loss is estimated by measuring its output power and subtracting it with output power of reference DFB lasers operated at the same laser bias current and temperature. The DFB laser Mach-Zehnder modulator transmitter PICs have a 3.8 dB lower insertion loss, than the reference Mach-Zehnder modulators. One reason is, that with the integrated laser, no input spot-size converter is needed, reducing the Mach-Zehnder modulator passive insertion loss by 1.4 dB.

Overall, the fabricated DFB laser Mach-Zehnder/ IQ modulator transmitters have a low switching voltage, high extinction ratio and sufficient output power for application in 100 Gb/s Ethernet links, up to 40 km.

4.5.4 Mach-Zehnder Modulator Model

For simulations in chapter 7, the Mach-Zehnder modulator direct current characteristics are modelled with an empirical model. The Mach-Zehnder modulator output electrical field $E_{out,MZM}$ for a certain input electrical field $E_{in,MZM}$, can be calculated with the modulator transfer function $F_{MZM}(V_{U,I})$, depending on the applied voltages to the travelling wave electrode, V_U and V_I in Volts (eq. (4.5)).

$$E_{out,MZM}(V_{U,I}) = E_{in,MZM} \cdot F_{MZM}(V_{U,I}) \quad (4.5)$$

With $F_{MZM}(V_{U,I})$, the total Mach-Zehnder modulator absorption $abs_{MZM} = |F_{MZM}(V_{U,I})|$ and phase shift $\phi_{MZM} = \arctan(\text{Re}(F_{MZM}(V_{U,I})) / \text{Im}(F_{MZM}(V_{U,I})))$ can be calculated. The general Mach-Zehnder modulator transfer function F_{MZM} is described by eq. (4.6).

$$F_{MZM}(V_{U,I}) = A_{MZM} \{ s e^{-a_U/2} e^{i\varphi_U} + (1-s) e^{-a_I/2} e^{i(\varphi_I + \delta\varphi)} \} \quad (4.6)$$

The passive insertion loss IL_{dB} in decibel is included in the factor A_{MZM} , where its absolute value is $|A_{MZM}| = 10^{-IL_{dB}/20}$. In the Mach-Zehnder modulator input coupler, the input signal is split into the two arms with the splitting ratio s . At the output coupler, the two signals are added again. In the Mach-Zehnder modulator arms, the signals experience absorption and phase shift depending on the voltages in the U- and I-electrodes. The phase shift difference between the two arms is included with the parameter $\delta\varphi$, which should ideally be zero. The absorption coefficients $a_{U,I}(V_{U,I})$ and phase shifts $\varphi_{U,I}(V_{U,I})$ in the two Mach-Zehnder modulator arms, are given in eq. (4.7) and eq. (4.8), where a_1 , a_2 , p_1 and p_2 are fitting parameters.

$$a_{U,I}(V_{U,I}) = (a_1 V_{U,I})^{a_2} \quad (4.7)$$

$$\varphi_{U,I}(V_{U,I}) = p_1 V_{U,I} + p_2 V_{U,I}^2 \text{ [rad]} \quad (4.8)$$

The absorption coefficients take into account the exponential absorption increase with the applied voltage. The phase shift, includes a linear contribution from the Pockels effect and a quadratic one from the quantum confined Stark effect, depending on the applied voltages.

The goal is to find fitting parameters, so that the simulated Mach-Zehnder modulator output power, matches the measured one of the fabricated DFB laser Mach-Zehnder modulator transmitter in Fig. 52. The Mach-Zehnder modulator passive insertion loss is 4.7 dB, so that $|A_{MZM}|$ is calculated to 0.582. V_U and V_I are set equal, corresponding to the modulator bias voltage V_{MZM} . The rest of the fitting parameters are found by manually sweeping them and by fitting the simulated normalized output power, switching voltage, extinction ratio and output power matrix depending on the voltages V_U and V_I , to the measured graphs.

The simulated and measured extinction ratio, switching voltage and normalized output power curves, depending on V_{MZM} are shown in Fig. 56.a, b and c, respectively.

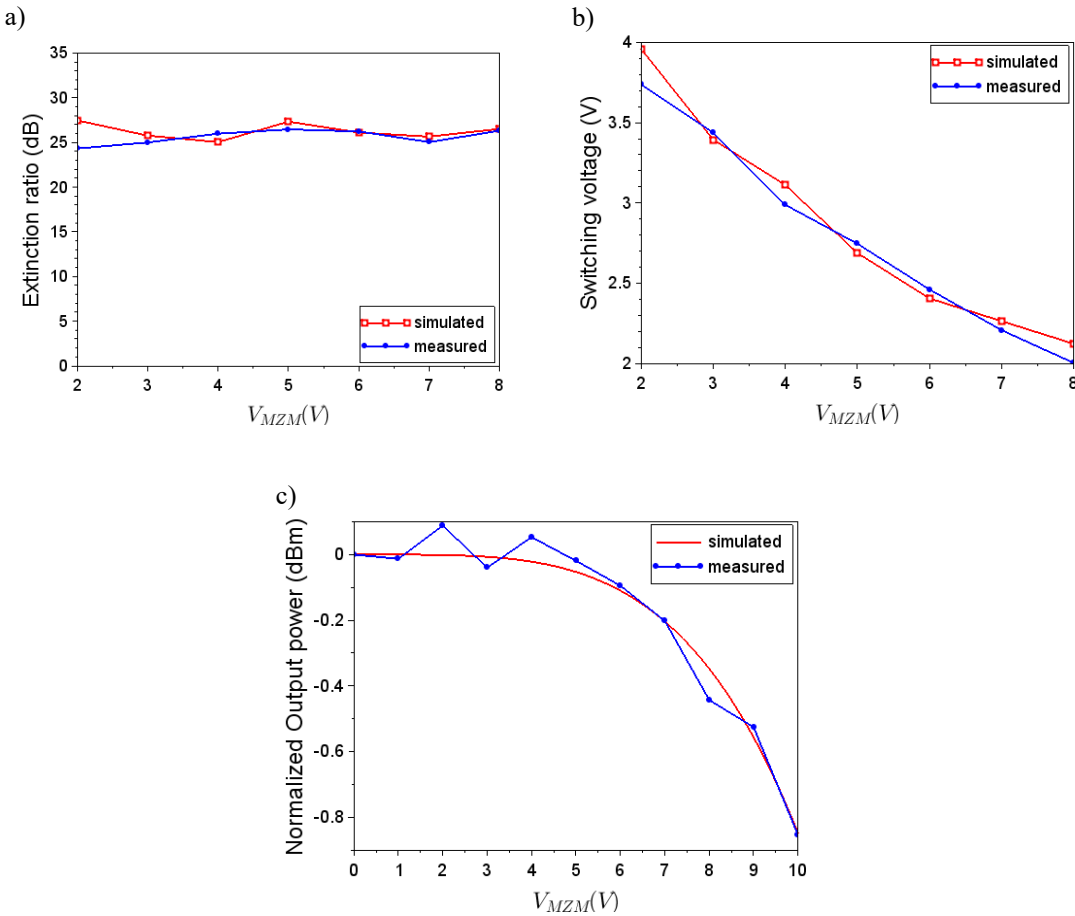


Fig. 56. Comparison of simulated and measured a) extinction ratio, b) switching voltage V_π and c) normalized output power, depending on the applied modulator bias voltage $V_{MZM} = V_U = V_I$.

A good agreement between the simulated and measured modulator properties is obtained with the Mach-Zehnder modulator model. The simulated output power matrix is given in Fig. 57, giving a suitable fit to the measured one in Fig. 52.

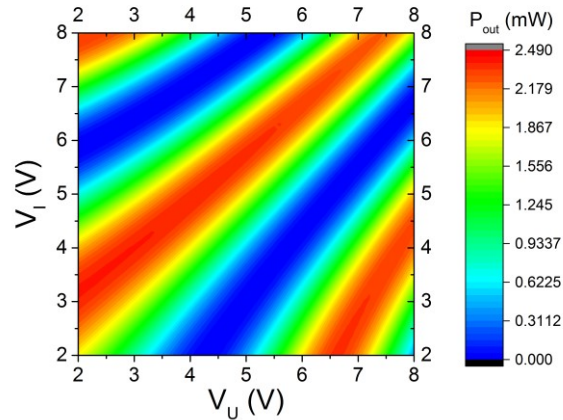


Fig. 57. Simulated Mach-Zehnder modulator output power matrix, depending on the applied voltages V_U and V_I in the travelling wave electrode arms.

The best fit is obtained for the parameters, given in Table 6, where $P_{in} = 10 \cdot \log(|E_{in}|^2)$ is the input optical power.

Symbol	Value
$ A_{MZM} $	0.638
P_{in} [dBm]	8.5
a_1 [1/V]	0.0665
a_2	4.0
p_1 [rad/V]	0.39
p_2 [rad/V ²]	0.087
$\delta\varphi$ [rad]	-1.0
s	0.479

Table 6. Mach-Zehnder modulator simulation parameters with best fit to the measurement results.

4.5.5 Electro-Optic Modulation Response

The transmitter electro-optic (E-O) modulation response gives information about the dynamic modulator behavior and its modulation bandwidth. The electro-optic response is measured, by applying a small signal sinusoidal voltage to the modulator radio frequency (rf) input, while terminating the travelling wave electrode with a 50Ω resistance (Fig. 58).

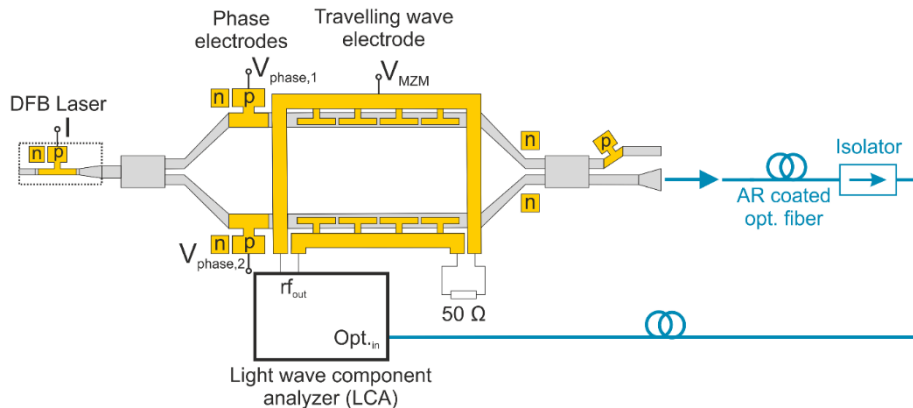


Fig. 58. Transmitter E-O response measurement experimental setup.

The modulator working point is set to the 3 dB point with one of the phase bias voltages $V_{phase,1/2}$, while a modulator bias voltage V_{MZM} of 5 V is applied to the modulator. The laser is operated in continuous wave with a bias current $I = 60$ mA. The modulator output is coupled to an optical fiber and measured with a light wave component analyzer (LCA), which also generates the sinusoidal electrical rf signal.

The electro-optic response of Mach-Zehnder modulators without integrated laser, is typically measured at $40^\circ C$. For better comparison, also the integrated transmitter E-O responses are obtained at $40^\circ C$. The electro-optic responses of two DFB laser Mach-Zehnder modulator transmitter photonic integrated circuits (DFB-MZM PIC), depending on the sinusoidal input signal frequency are shown in Fig. 59 ($I - I_{th}$: 36 mA, V_{MZM} : 5 V).

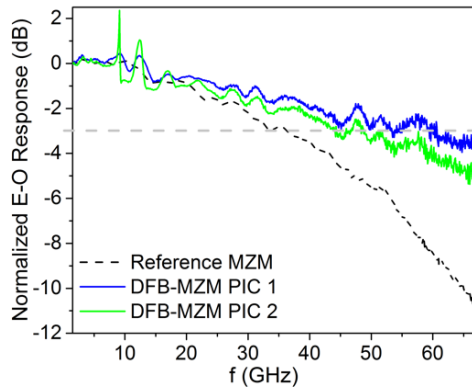


Fig. 59. E-O responses of two DFB laser Mach-Zehnder modulator transmitter PICs (DFB-MZM PIC) and a reference Mach-Zehnder modulator.

As a reference, the E-O response of a Mach-Zehnder modulator without integrated laser is given, which is measured with an external cavity laser as light source. Typically, larger 3 dB-bandwidths are achieved for the Mach-Zehnder modulators with integrated laser than for the reference Mach-Zehnder modulator (average 3 dB-bandwidth: 36.4 GHz). The reason might be the different fabrication processes. For the p-contacts in the integrated transmitters, additional p-dopant diffusion is performed, which is not done in the fabrication of stand-alone Mach-Zehnder modulators. The p-diffusion decreases the p-contact resistance and thus improves the modulator bandwidth. At certain bias points, peaks in the integrated transmitter E-O response appear, as in the DFB-MZM PIC 2 curve, which are not present in the electro-optic response of reference Mach-Zehnder modulators. These peaks will be further examined in chapter 5.

Similar electro-optic responses and 3 dB bandwidths to the DFB laser Mach-Zehnder modulator transmitter ones, are obtained for the Mach-Zehnder modulators inside the DFB laser IQ modulator transmitters. In addition, the electrical-to-electrical (E-E) and electrical-to-optical (E-O) crosstalk between the two Mach-Zehnder modulators inside the DFB laser IQ modulator transmitters is measured and compared to the crosstalk of a reference IQ modulator, without integrated laser. The reference IQ modulator is of the same type as the one in the transmitter. As a light source the light of an external cavity laser is coupled into the IQ modulator input. The electrical-to-electrical crosstalk is measured, by launching a small sinusoidal electrical signal to the travelling wave electrode input of the in-phase (I) Mach-Zehnder modulator and measuring the radio frequency (rf) signal at the quadrature (Q) modulator input, with the light wave component analyzer (Fig. 60).

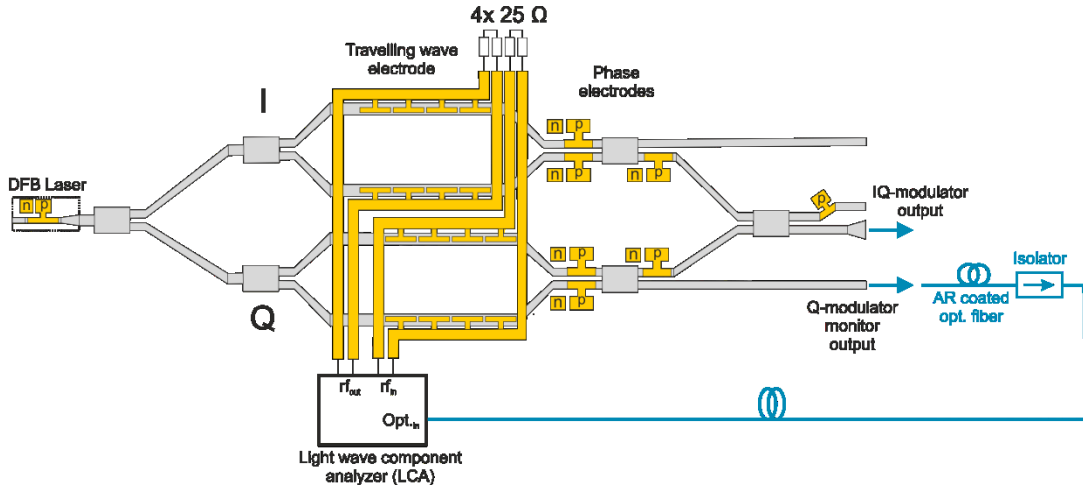


Fig. 60. Experimental setup for DFB laser IQ modulator transmitter electrical-to-electrical and electrical-to-optical crosstalk measurement.

The ratio of the signal at the Q modulator input to the one at the I modulator input, gives the electrical-to-electrical crosstalk. The electrical-to-optical crosstalk is obtained, by measuring the electro-optic responses both at the IQ modulator and at the Q modulator monitor optical output, while launching a signal into the I modulator electrical input. The ratio of the electro-optic response at the Q modulator output to the one at the IQ modulator output, gives the electrical-to-optical crosstalk. The electrical-to-electrical and electrical-to-optical crosstalk of the DFB laser IQ modulator transmitter and the reference IQ modulator are displayed in Fig. 61.

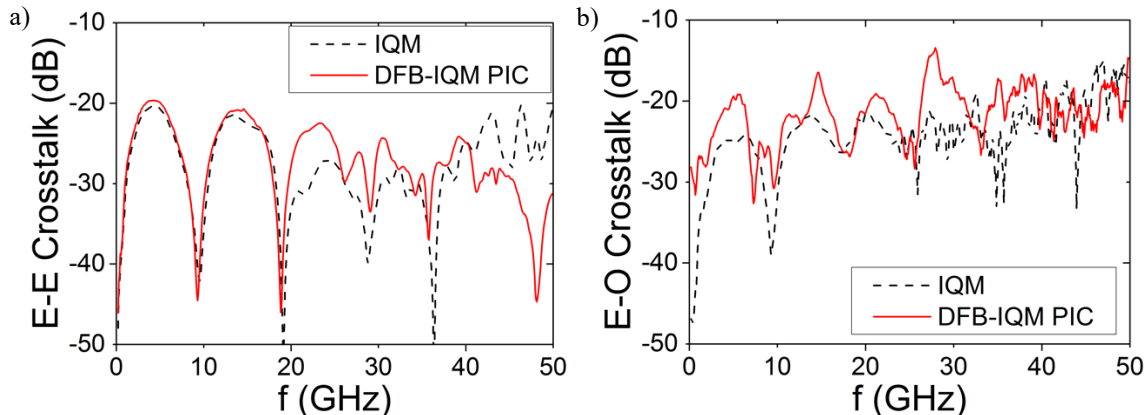


Fig. 61. DFB laser IQ modulator transmitter (DFB-IQM PIC) a) electrical-to-electrical and b) electrical-to-optical crosstalk ($I_{\text{I-th}} = 35 \text{ mA}$,), compared to reference IQ modulator (IQM) crosstalk ($V_{\text{MZM}} = 5 \text{ V}$, $T = 40^\circ\text{C}$).

The DFB laser IQ modulator transmitter crosstalk is below -20 dB and comparable to the reference IQ modulator one. The DFB laser IQ modulator transmitter electrical-to-optical crosstalk is increased compared to the reference IQ modulator one, especially at 14 GHz and 24 GHz. The 14 GHz peak is at the integrated laser relaxation oscillation frequency. The peaks are not visible in the reference IQ modulator electrical-to-optical crosstalk and are assumed to appear due to optical feedback inside the DFB laser IQ modulator transmitter, exciting the integrated DFB laser at its relaxation oscillation frequency and its harmonics.

All in all, the DFB laser IQ modulator transmitter crosstalk is sufficiently low for the transmitter operation.

The average DFB laser integrated Mach-Zehnder and IQ modulator transmitter 3 dB-bandwidth is 42 GHz, with maximum values of up to 54 GHz.

5. 1550 nm DFB Laser Integrated Mach-Zehnder/ IQ Modulator Transmitter Module/ Subassemblies

For easier handling and contacting, during large signal measurements, DFB laser Mach-Zehnder photonic integrated circuits (PIC) are either fixed onto a ceramic subassembly or embedded into a transmitter optical subassembly (TOSA) module, together with a wire-bonded termination resistance. A Peltier element for temperature control and a fixed optical output fiber assembly are included into the transmitter module, to avoid any thermal or spatial drift during measurements. This enables also the long-term characterization of transmitter properties, such as the relative intensity noise and the linewidth, for figuring out the best transmitter operation point. The DFB laser Mach-Zehnder modulator transmitter subassembly and module are tested for operation at different modulation formats, such as non-return-to-zero on-off-keying and binary phase shift keying, and compared with to performance of Mach-Zehnder modulators without integrated laser.

For the DFB laser IQ modulator transmitter PIC, a co-designed differential electrical driver is developed by another group at Fraunhofer Heinrich-Hertz Institute. The differential driver is necessary to achieve the best signal quality of the IQ modulator. Since no transmitter package is available, to include both the DFB laser IQ modulator transmitter PIC and the differential driver, the two devices are fixed on ceramic transmitter subassemblies and wire bonded together with the termination resistance. With the transmitter subassemblies, the handling and contacting during measurements, especially for the large signal characterization is significantly simplified. The DFB laser IQ modulator transmitter PICs relative intensity noise and linewidth properties are characterized and the large signal operation under quaternary phase shift keying modulation (QPSK) at different symbol is tested and compared with IQ modulator PICs without integrated laser.

5.1 DFB Laser Mach-Zehnder Modulator Transmitter Optical Subassembly (TOSA) Module

5.1.1 Architecture

A photograph of DFB laser Mach-Zehnder modulator transmitter optical subassembly (TOSA) module with the embedded transmitter PIC is shown in Fig. 62.

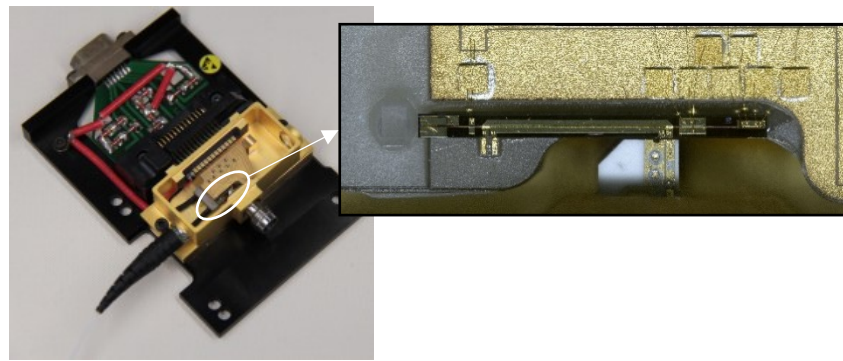


Fig. 62. Photograph of the transmitter optical subassembly module with an embedded DFB laser Mach-Zehnder modulator PIC.

The transmitter PIC is mounted on a Peltier element for temperature control. The direct current contacts of the laser and the modulator are wire bonded to conductive metal traces on a ceramic plate. The metal traces are connected to the contact pins of the module package and routed to a cable plug. The transmitter PIC optical output is coupled to the fiber pigtail through an optical lens. The Mach-Zehnder modulator travelling wave electrode radio frequency inputs are wire bonded to the V-connector (1.85 mm) of the module package and the output is terminated by a parallel wire bonded $50\ \Omega$ resistor.

5.1.2 Optical Spectrum, Relative Intensity Noise and Linewidth

The DFB laser Mach-Zehnder modulator transmitter module is characterized at 20°C . At $I: 100\ \text{mA}$ ($85\ \text{mA}$ above threshold current I_{th}) laser bias current, the maximum output power in the fiber after packaging is $4\ \text{dBm}$, which is comparable to the unpackaged DFB laser Mach-Zehnder modulator transmitter PIC output power. A typical optical power spectrum at $I-I_{\text{th}}: 85\ \text{mA}$ with a $55.5\ \text{dB}$ side mode suppression ratio (SMSR) is shown in Fig. 63.

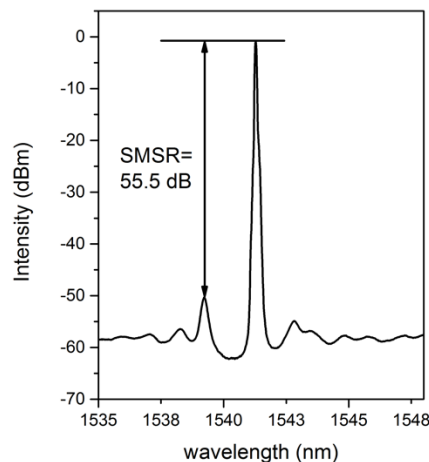


Fig. 63. Transmitter module optical power spectrum ($I-I_{\text{th}}: 85\ \text{mA}$, $T: 20^\circ\text{C}$).

With the transmitter module, in-depth parameter measurements at various combinations of laser bias current and modulator bias voltage are performed. The transmitter wavelength is plotted in a matrix against the laser bias current above threshold $I-I_{\text{th}}$ and the modulator bias voltage V_{MZM} in Fig. 64.

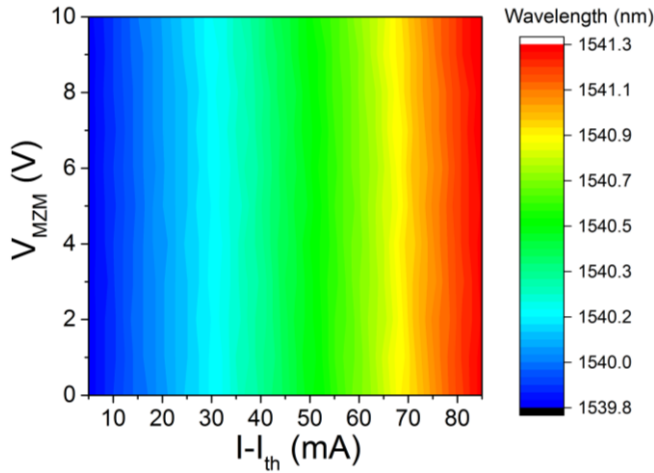


Fig. 64. Transmitter module wavelength vs. laser bias current and modulator bias voltage.

The wavelength increases linearly with the laser bias current by about 17.8 pm/mA, showing a similar behavior as the reference DFB laser wavelength. Small wavelength fluctuations up to 50 pm, corresponding to 6.3 GHz frequency variation, with the modulator bias voltage are observed. This behavior is not expected, for a DFB laser isolated from the modulator. From the power spectral measurements, also the side mode suppression ratio matrix is obtained (Fig. 65).

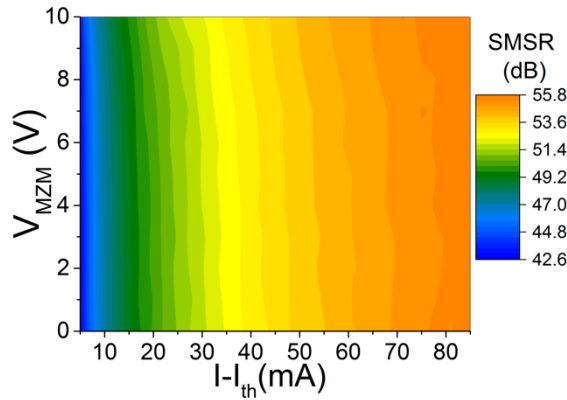


Fig. 65. Transmitter module side mode suppression ratio vs. laser bias current and modulator bias voltage.

For 22 mA bias currents and higher, the side mode suppression ratio is larger than 44 dB, increasing up to 55.7 dB with the laser bias current. The side mode suppression ratio variation, depending on the modulator bias voltage is smaller than 1 dB and thus negligible.

The transmitter optical spectrum measurements show a continuous wavelength tuneability with the laser bias current, without mode hopping and side mode suppression ratios, more than 10 dB larger than the transmitter specifications. The transmitter wavelength shows tiny variations, depending on the bias voltage, which should be, however, negligible for the transmitter operation.

The relative intensity noise (RIN) spectra are measured at different laser bias currents modulator bias voltages and compared to the ones of the reference DFB lasers (Fig. 66).

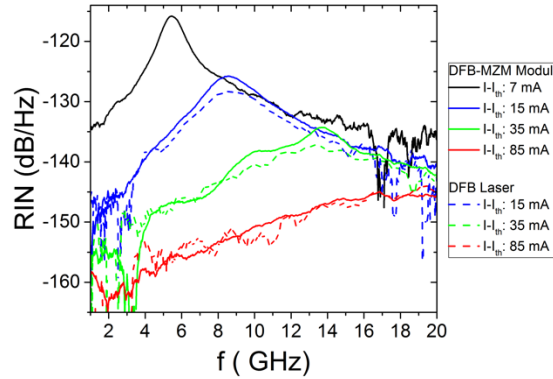


Fig. 66. Transmitter module (DFB-MZM module) and reference DFB laser relative intensity noise (RIN) spectra at different laser bias currents.

The relative intensity noise decreases similarly with increasing bias current for the transmitter module and the reference DFB lasers. The DFB laser Mach-Zehnder module relative intensity noise spectral shapes are comparable to the ones of reference DFB lasers, except for slightly more pronounced resonance peaks. The transmitter module relative intensity noise maximum is plotted in a matrix, depending on the laser bias current and the modulator bias voltage in Fig. 67a.

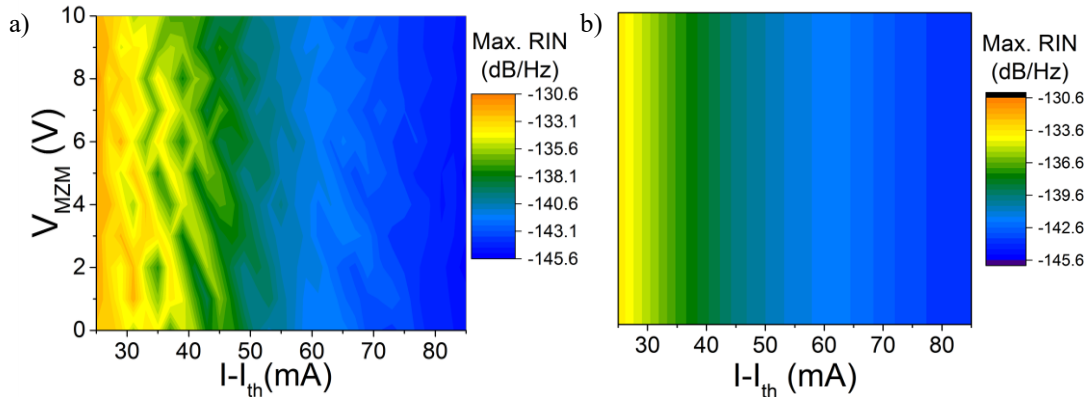


Fig. 67. a) Transmitter module max. RIN levels vs. laser current and modulator bias voltage, b) Reference DFB lasers max. RIN vs. laser current.

For comparison, the reference DFB laser maximum relative intensity noise levels, depending on the laser bias current are illustrated in Fig. 67b in a similar way as in Fig. 67a. The DFB laser Mach-Zehnder modulator transmitter module relative intensity noise levels, depending on the laser bias current, are comparable to the ones of the reference DFB lasers. If the DFB laser would be independent of the modulator, no relative intensity noise variations with the modulator bias voltage are expected and the RIN matrix would look similar to the reference DFB laser one, depicted in Fig. 67b. A difference is observed for the transmitter module relative intensity noise matrix, where the RIN levels vary by up to 3 dB, depending on the modulator bias voltage.

Overall, the maximum relative intensity noise values decrease with the laser bias current, so that at bias currents larger than 25 mA above threshold, the DFB laser Mach-Zehnder modulator transmitter module relative intensity noise is lower than -130 dB/Hz, which is within the desired transmitter specifications.

The DFB laser Mach-Zehnder modulator transmitter module line spectra are acquired at different bias currents and bias voltages at 20°C and 40°C temperature. In Fig. 68, the normalized DFB laser Mach-Zehnder modulator module line spectra at $I - I_{th}$: 55 mA and two different modulator bias voltages V_{MZM} , together with the one of a reference DFB laser at $I - I_{th}$: 50 mA are shown (T: 40°C).

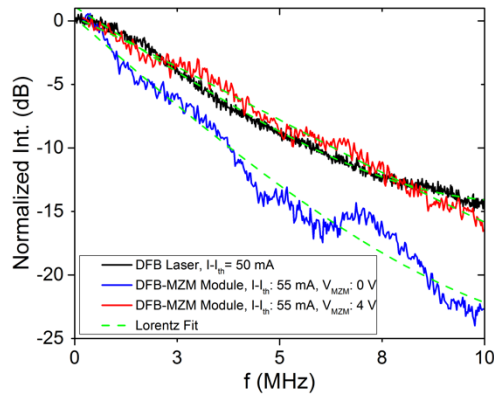
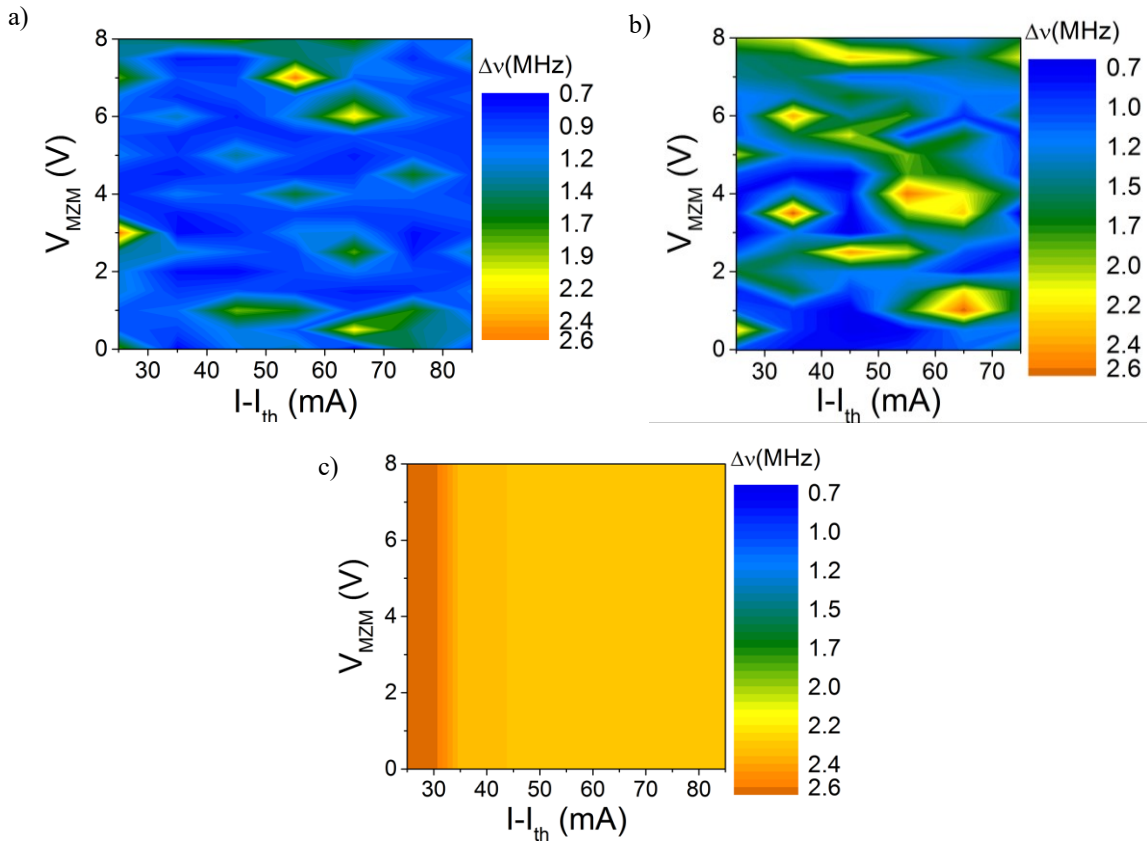


Fig. 68. Transmitter module (DFB-MZM module) and reference DFB laser line spectra (T: 40°C).

The dashed green lines indicate Lorentzian peak fits. Depending on the operation point, in terms of laser bias current and modulator bias voltage, the transmitter module line spectral shape varies. Mostly, it differs from the typical Lorentzian shape, like the blue curve in Fig. 68 at V_{MZM} : 0 V. The altered line spectrum has a compressed peak and some overlaid ripples, so that the transmitter module linewidth becomes narrower than the reference DFB laser one. At some bias points, the line shape is approximately Lorentzian, as the red curve in Fig. 68 at V_{MZM} : 4 V.

The transmitter module linewidth is extracted from the normalized line spectra at the frequency, where the intensity is dropped by 3 dB. Transmitter linewidth matrix plots of the at different laser bias currents above threshold $I - I_{th}$ and modulator bias voltages V_{MZM} at 20°C and 40°C temperature are given in Fig. 69a and Fig. 69b, respectively.



**Fig. 69. Transmitter module linewidth vs. laser current and modulator bias voltage at a) 20°C and b) 40°C
c) reference DFB laser linewidth at 40°C.**

As a reference, the linewidth of a DFB laser at 40°C, depending on the bias current is plotted in the same way in Fig. 69c. The linewidth is expected to be independent of the modulator bias voltage, if the laser is isolated from the modulator. As a result, the linewidth matrix should be similar to the one of the reference DFB laser. The transmitter module linewidth, however, depends strongly on the both the bias current and the modulator bias voltage and is typically narrower than the reference DFB laser one. Periodic lines of small islands with increased transmitter linewidth, comparable to the reference DFB laser one, appear at different bias points. The transmitter linewidth pattern changes from 20°C to 40°C temperature, showing more areas with increased linewidth. At any bias point at bias currents larger than 25 mA above threshold, the transmitter linewidth is below 2.6 MHz at 20°C and below 5.7 MHz at 40°C, which is sufficient for modulation formats at up to 32 GBd 16-level quadrature amplitude modulation.

The in-depth measurements of the transmitter module optical spectrum, relative intensity noise and linewidth show, that the integrated DFB laser characteristics, depend on the modulator bias voltage. Since no isolator is integrated between the DFB laser and the Mach-Zehnder modulator, it is assumed, that optical feedback is present inside the photonic integrated circuits. It is already known, that the laser wavelength, linewidth and relative intensity noise are influenced already by weak optical feedback, depending on the feedback intensity and phase [68]. Also, the different spectral line shapes of the reference DFB lasers and the transmitter module, indicate that optical feedback is present inside the photonic integrated circuits. Therefore, the effects of optical feedback inside the transmitters on the laser and the transmitter performance, are further investigated in the chapters 6 and 7.

5.1.3 Electro-Optic Modulation Response

The DFB laser Mach-Zehnder modulator transmitter module small signal electro-optic (E-O) modulation response is obtained at different transmitter operation points. Similar to the transmitter photonic integrated circuit electro-optic responses, the transmitter module response shows a resonance peak at laser bias currents close to threshold. When comparing the electro-optic response to the transmitter module relative intensity noise spectrum at the same operation point in Fig. 70, it becomes clear, that the resonance peak is located at the laser relaxation oscillation frequency f_r .

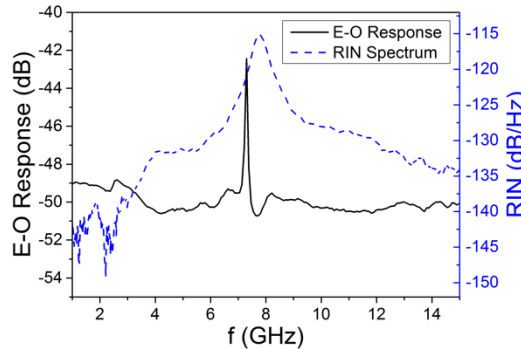


Fig. 70. Transmitter module electro-optic response peak and relative intensity noise spectrum ($T: 40^\circ\text{C}$, $V_{\text{MZM}}: 6 \text{ V}$, $I-I_{\text{th}}: 15 \text{ mA}$).

The electro-optic response resonance height varies periodically with the modulator bias voltage V_{MZM} (Fig. 71).

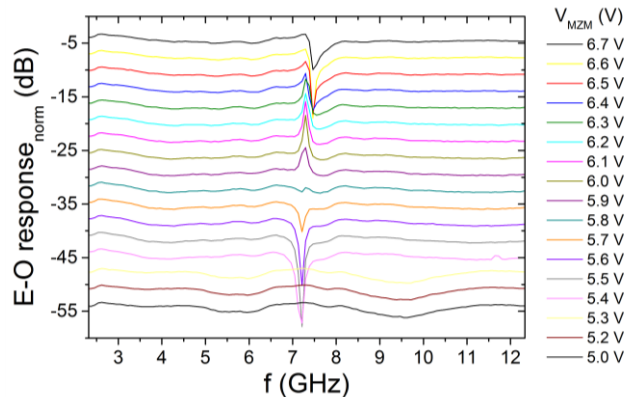


Fig. 71. Transmitter module electro-optic response resonance, depending on the modulator bias voltage V_{MZM} ($T: 40^\circ\text{C}$, $I-I_{\text{th}}: 15 \text{ mA}$).

By changing the modulator bias voltage from 5.4 V to 6.6 V, corresponding to about half the switching voltage V_s , the resonance changes from a notch to a peak and back to a notch. Since the resonance appears only in the electro-optic response of Mach-Zehnder modulators with integrated laser, it is assumed, that it emerges due to optical feedback inside the chip. The effects of optical feedback on the transmitter performance will be further discussed in chapter 6.

Like the relative intensity noise peak, the electro-optic response resonance decreases and shifts to larger frequencies with increasing laser bias current. At bias currents larger than 25 mA above threshold, the resonance is mostly damped, so that it should not pose any problem for the transmitter operation. In the transmitter module

electro-optic responses at different operation points with laser bias currents, 75 mA above threshold and higher, the resonance peak is negligible (Fig. 72).

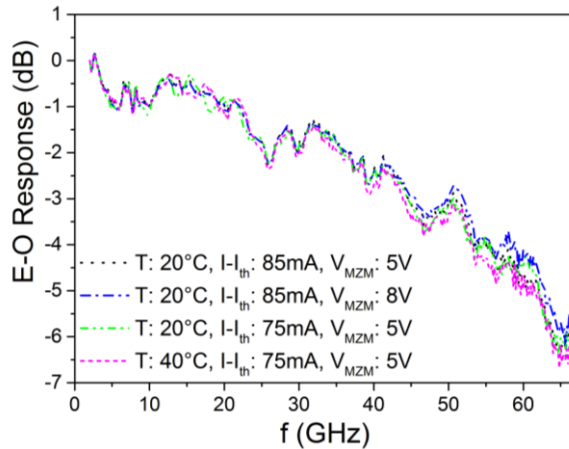


Fig. 72. Transmitter module electro-optic response at different operation points.

The electro-optic response changes only slightly, when varying the temperature from 20°C to 40°C, the laser bias current from 75 mA to 85 mA above threshold and the modulator bias voltage from 5 V to 8 V. The transmitter module 3 dB bandwidth is around 44 GHz, comparable to the transmitter photonic integrated circuit bandwidth before packaging and sufficient for operation at 100 Gb/s and beyond.

5.1.4 Transient Chirp

Frequency chirp degrades the modulation performance and limits the transmission distance in dispersive optical fibers. The transient chirp coefficient α_H is a measure for the unwanted phase modulation and thus frequency chirp, induced by intensity modulated signals. One of the main advantages of using a Mach-Zehnder modulator, compared to an electroabsorption modulator is its nearly chirp-free operation. The DFB laser Mach-Zehnder modulator transmitter module transient chirp coefficient is measured with the fiber transfer function method [69]. The experimental setup is depicted in Fig. 73.

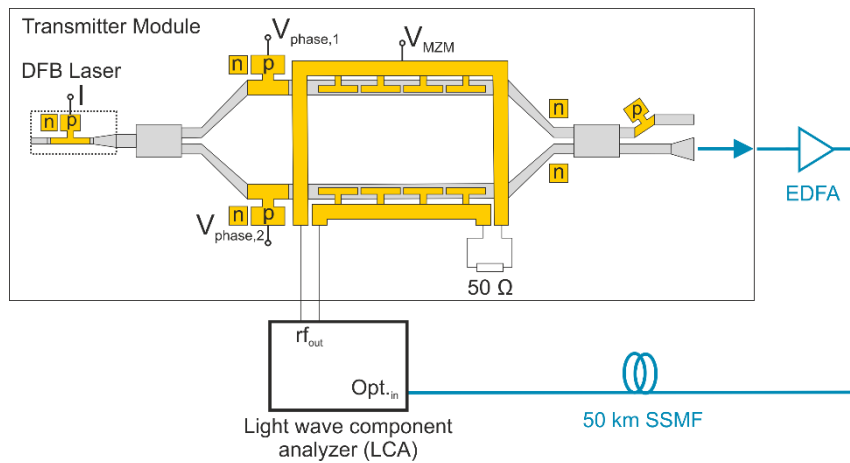


Fig. 73. Experimental setup for transient chirp coefficient measurement.

The transmitter module working point is set to the 3 dB point and the radio frequency input is connected to a light wave signal analyzer, generating a small sinusoidal electrical input signal. The transmitter module optical output

is amplified with an erbium doped fiber amplifier (EDFA) and propagated through a standard single mode fiber (SSMF) with 50 km length L_{fiber} and 17 ps/nm/km dispersion D. As a reference, the electro-optic transmitter module response without the fiber is measured and divided, in order to eliminate the bandwidth contributions of the transmitter and receiver. The resulting fiber transfer function shows minima at certain frequencies, as in Fig. 74, due to interferences between the carrier and the two modulated sidebands, depending on the frequency chirp, the fiber length and its chromatic dispersion.

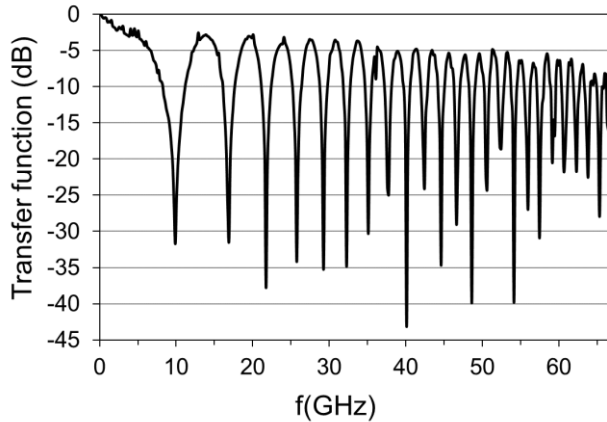


Fig. 74. Fiber transfer function ($T: 20^{\circ}\text{C}$, $I-I_{th}: 85 \text{ mA}$, $V_{M\text{ZM}}: 8 \text{ V}$).

The frequency f_u , at the u^{th} minimum, is described by eq. (5.1) [70].

$$f_u^2 L_{fiber} = \frac{c}{2D\lambda^2} \left(1 + 2u - \frac{2}{\pi} \arctan(\alpha_H) \right) \quad (5.1)$$

When plotting the minimum frequencies squared times the fiber length $f_u^2 L_{fiber}$ against two times the order of the minimum $2u$, obtained from Fig. 74, a linear dependency is visible (Fig. 75).

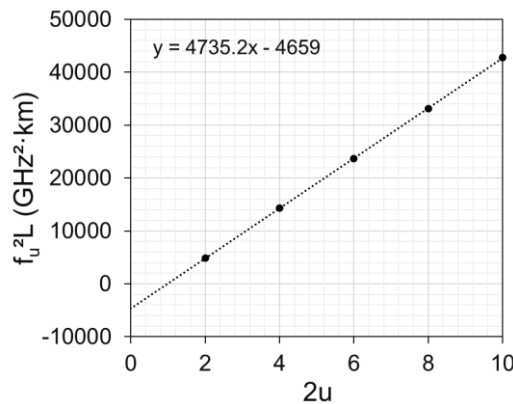


Fig. 75. Min. frequencies squared times fiber length vs. two times the order of the minimum (from Fig. 74, $T: 20^{\circ}\text{C}$, $I-I_{th}: 85 \text{ mA}$, $V_{M\text{ZM}}: 8 \text{ V}$).

From the linear slope, corresponding to $c/(2D\lambda^2)$, the dispersion D is determined, while from the y-intercept, α_H is calculated. The transient chirp coefficient is measured at different laser bias currents and modulator bias voltages and plotted in Fig. 76 ($T: 20^{\circ}\text{C}$).

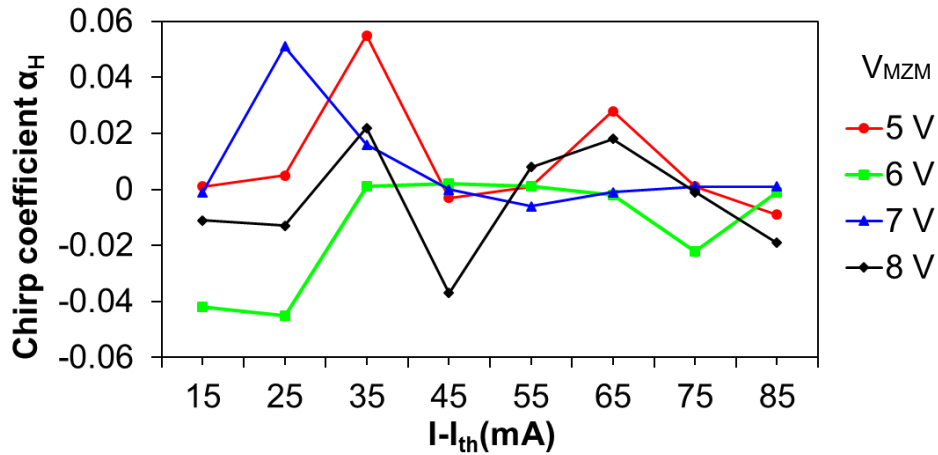


Fig. 76. Transmitter module transient chirp coefficient vs. laser bias current at different modulator bias voltages (T: 20°C).

The transmitter transient chirp coefficient varies depending on the operation point. The transient chirp coefficient of a Mach-Zehnder modulator without integrated laser is typically between -0.05 and -0.14. The transmitter module chirp coefficient is shifted by about 0.1 in the positive direction with a smaller absolute value, so that it is close-to-zero at all operation points. As a comparison, the electroabsorption modulated DFB laser transient chirp coefficient has been reported to vary between 2 and -4, depending on the modulator bias voltage [71]. This shows that the DFB laser Mach-Zehnder modulator module is a promising device to achieve almost zero chirp and long transmission distances, independent of the operation point.

5.1.5 Large Signal Operation

In this subchapter, the transmitter module is tested for large signal intensity and phase modulation. First, 56 Gb/s non-return-to-zero (NRZ) on-off-keying modulation and transmission is measured and compared to theoretical expectations. Then, the transmitter module performance at binary phase shift keying (BPSK) is compared to the one of a Mach-Zehnder modulator without integrated laser. Finally, the constellation diagrams of bipolar 4-level pulse amplitude modulation (PAM4) signals are obtained at different symbol rates, to investigate the transmitter performance at phase modulated signals with multiple amplitude levels.

5.1.5.1 56 Gb/s Non-Return-To-Zero On-Off Keying (NRZ)

The experimental setup for the transmitter module non-return-to-zero on-off-keying (NRZ) measurement is sketched in Fig. 77.

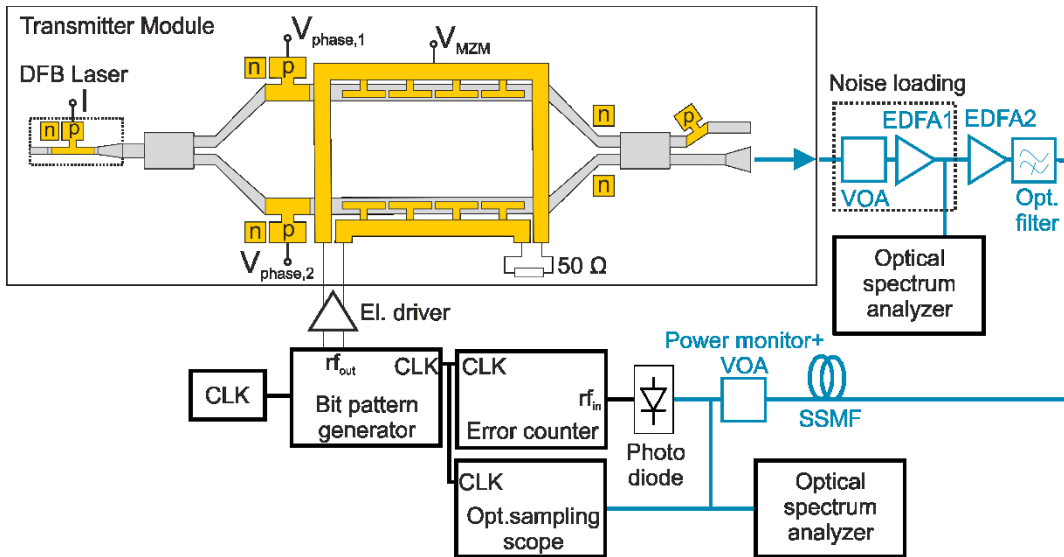
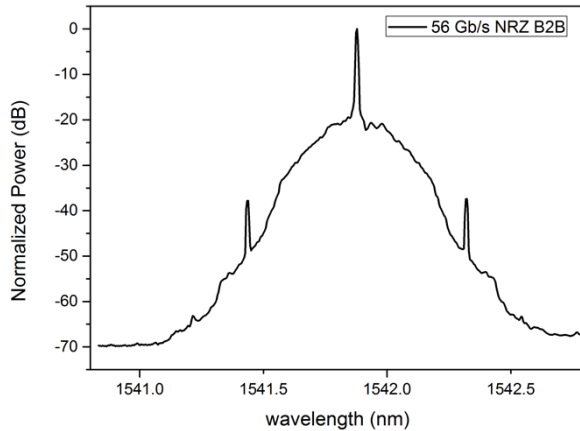


Fig. 77. 56 Gb/s NRZ measurement experimental setup.

A clock (CLK) signal is generated with an analog signal generator (Agilent E8257D) and fed into the bit pattern generator. The bit pattern generator (SHF12104A) creates the 56 Gb/s NRZ electrical data signal with a $2^{31}-1$ bits long pseudorandom binary sequence (PRBS). The data signal is amplified with a commercial single-ended electrical driver (SHF 804 EA), giving 1.5 V_{pp} output voltage swing and launched into the transmitter module radio frequency (rf) input. The transmitter module laser current is set to 85 mA above threshold, giving a 1542 nm wavelength and -0.9 dBm output power in the fiber (T: 20°C). The Mach-Zehnder modulator is operated in single-ended push-pull configuration at the 3 dB working point, as described in chapter 2.2.3 (Fig. 15). Since a PIN transimpedance amplifier is not available, an erbium-doped-fiber amplifier (EDFA2) is connected to the transmitter module optical output, to insert sufficient power to the receiver and remove any receiver impairments. After the erbium doped fiber amplifier, an optical filter (bandwidth: 2 nm) is placed, to cut off EDFA amplified spontaneous emission noise. The amplified signal is propagated through a standard single mode fiber (SSMF) span of up to 4 km for transmission experiments. At the receiver, the signal is detected with an optical sampling scope and an optical spectrum analyzer. The power at the receiver is kept constant at 8.5 dBm throughout the measurement with a power monitor and a variable optical attenuator. The modulator bias voltage V_{MZR} is set to 9.4 V, to adjust the modulator switching voltage to 1.7 V. For the bit error rate (BER) analysis, noise loading of the signal is done with the amplified spontaneous emission noise of an additional erbium doped fiber amplifier (EDFA1). A variable optical attenuator (VOA), adjusts the optical signal-to-noise ratio (OSNR), which is measured with another optical spectrum analyzer. The bit error rate is obtained with an error counter, after the data is received with a photo diode.

As a reference for the bit error rate measurements the hard-decision forward error correction (HD-FEC) threshold ($3.8 \cdot 10^{-3}$) for an overhead of 7 % is used. The transmitter power consumption including both the laser and modulator is 171 mW, corresponding to an energy per bit of 3.1 pJ/bit at 56 Gb/s NRZ.

The 56 Gb/s NRZ spectrum has a typical shape with the carrier and the overlaid modulated data signal (Fig. 78).

**Fig. 78. 56 Gb/s NRZ spectrum.**

Clear eye openings are observed in back-to-back (B2B) operation with 9.3 dB dynamic extinction ratio, sufficient for the transmitter application in 100 Gb/s optical networks (Fig. 79a). After transmission over 2.5 km (Fig. 79b) and 3.5 km (Fig. 79c) in the standard single mode fiber, pulse broadening due to group velocity dispersion causes variations in the eye diagram signal levels and overlapping between adjacent pulses.

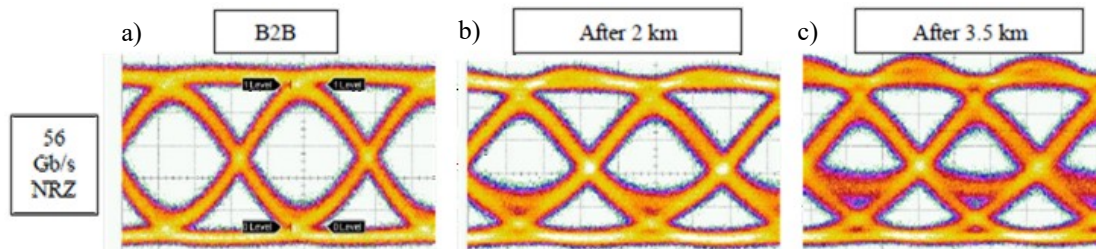
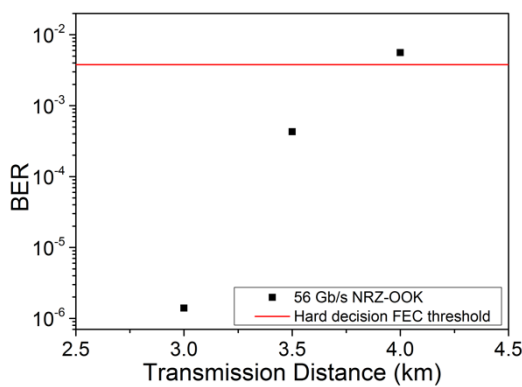


Fig. 79. 56 Gb/s NRZ eye diagrams a) in back-to-back operation and b) after 2.5 km and c) after 3.5 km transmission.
Open eyes are obtained after up to 3.5 km transmission distance. The bit error rate over transmission distance measurement confirms, that 56 Gb/s NRZ transmission over up to 3.5 km is possible with a bit error rate below the hard-decision forward error correction threshold (Fig. 80).

**Fig. 80. Bit error rate vs. transmission distance at 56 Gb/s NRZ.**

In theory, the expected transmission distance at 56 Gb/s NRZ, at 1550 nm wavelength, in a standard single mode fiber with 17 ps/(nm·km) dispersion, is about 1.8 km, for chirp-free transmission [72]. With the transmitter module, an even longer transmission distance is achieved, a reason might be the slightly negative Mach-Zehnder modulator transient chirp coefficient which compensates for spectral broadening due to dispersion.

To investigate the performance when noise is added to the signal, the bit error rate in back-to-back operation is measured against the optical signal-to-noise ratio, at 0.1 nm resolution (Fig. 81).

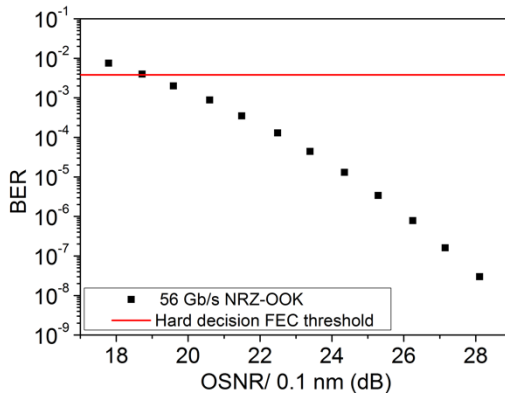


Fig. 81. Bit error rate vs. optical signal to noise ratio (OSNR) at 56 Gb/s NRZ.

A bit error rate below the hard-decision forward error correction threshold is reached at an optical signal-to-noise ratio, larger than 19 dB.

The reported 56 Gb/s NRZ experiments demonstrate the DFB laser Mach-Zehnder modulator transmitter module performance, without using any additional digital signal processing. Back-to-back operation at 56 Gb/s NRZ with a high dynamic extinction ratio, larger than 9 dB is demonstrated. Due to the negative modulator chirp, 56 Gb/s NRZ transmission over up to 3.5 km at 1550 nm is achieved. This shows that the transmitter module is a promising device, e.g. for dual-channel 100 Gb/s short reach optical networks.

5.1.5.2 Binary Phase Shift Keying (BPSK)

In this subchapter, the DFB laser integrated Mach-Zehnder modulator transmitter performance at phase modulated binary phase shift keying operation is tested and compared to the one of a reference Mach-Zehnder modulator, similar to the transmitter one, without integrated laser. Since, no reference Mach-Zehnder modulator module is available, the measurement is done at chip-level, with the same setup for both devices. The transmitter and the reference Mach-Zehnder modulator are each fixed onto a ceramic carrier and terminated with a wire-bonded $50\ \Omega$ resistance. The experimental setup is similar to the one in chapter 5.1.5.1, without the noise loading and the bit error counting (Fig. 82).

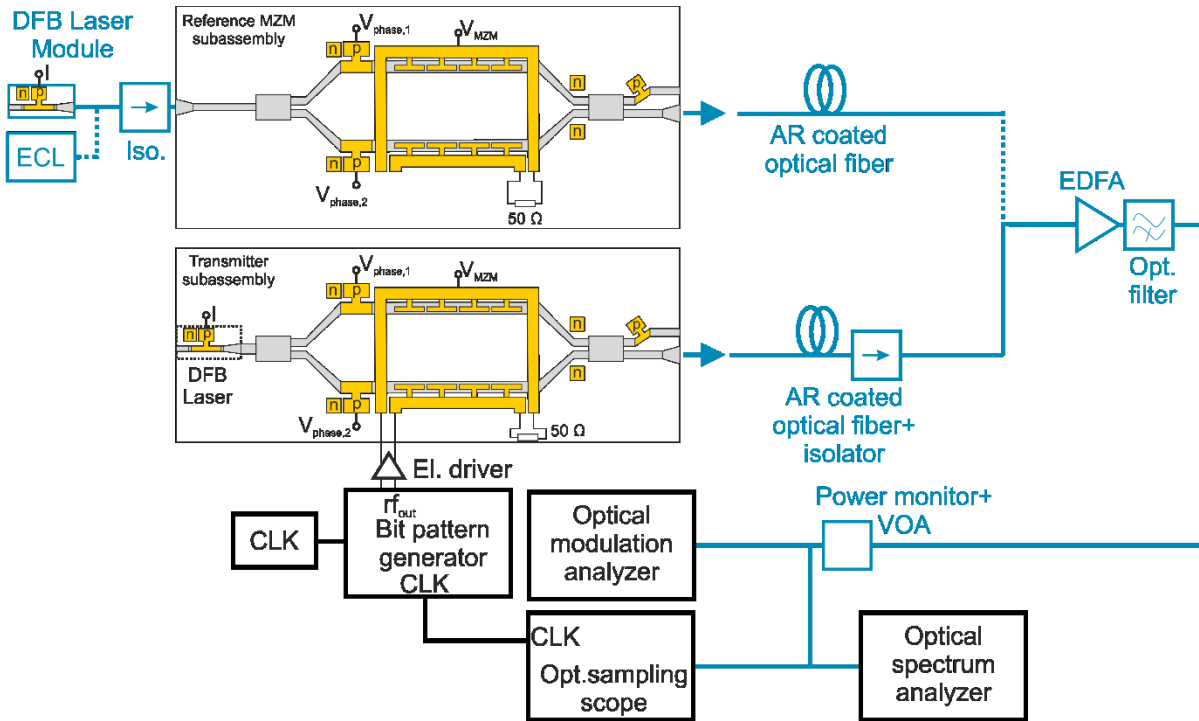


Fig. 82. BPSK measurement experimental setup.

The output signal is either coupled from the reference Mach-Zehnder modulator or from the transmitter subassembly into an anti-reflection (AR) coated optical fiber and received with an optical modulation analyzer (OMA, Keysight N4391A). Pseudorandom binary sequences at up to 50 Gb/s are generated with the bit pattern generator (length: $2^{11}-1$ bits). The data signal is amplified with a single-ended electrical driver to $3.5 \text{ V}_{\text{pp}}$. For binary phase shift keying operation, the Mach-Zehnder modulator working point is set to the minimum and a voltage swing, corresponding to almost two times the switching voltage V_{π} is applied to the radio frequency input (as described in chapter 2.2.3, Fig. 14). The optical modulation analyzer generates the received signal constellation diagram and calculates the error vector magnitude (EVM), which is a practical quantification of the system performance. The error vector magnitude describes the received constellation points' distance from their ideal locations and is degraded by various signal impairments, such as phase and amplitude noise. A description of the error vector magnitude calculation is given in the appendix in chapter IV.II. The optical modulation analyzer includes digital signal processing functionalities. For carrier phase estimation, a Kalman filter phase tracker algorithm is applied by the optical modulation analyzer.

As light sources to the reference Mach-Zehnder modulator, an external cavity laser with a linewidth smaller than 150 kHz and a reference DFB laser, similar to the integrated DFB laser, are used. The reference DFB laser is assembled into a transmitter module, where its output is coupled to an optical fiber pigtail. The module also includes a Peltier element for temperature control and the laser current inputs are connected to a module plug, for easier handling. An optical isolator is placed between the laser and the reference Mach-Zehnder modulator, to avoid optical back-reflections. The light is coupled into the Mach-Zehnder modulator with an anti-reflection coated optical fiber. The external cavity laser output power is set to 10 dBm, so that the input power to the Mach-Zehnder modulator is 8.5 dBm, comparable to the integrated Mach-Zehnder input power at $I=I_{\text{th}}$: 85 mA.. The input power from the DFB laser module to the Mach-Zehnder modulator (MZM) at different bias currents is given in Table 7.

I-I _{th} (mA)	MZM input power (dBm)
65	-5.1
75	-4.5
85	-3.9

Table 7. Input power to the Mach-Zehnder modulator with DFB laser module.

To check the influence of the input power, a measurement with an erbium doped fiber amplifier as pre-amplifier between the DFB laser module and the reference Mach-Zehnder modulator is included, increasing the input power to 4.2 dBm at I-I_{th}: 85 mA.

The binary phase shift keying constellation diagrams and error vector magnitudes are obtained at different symbol rates and operation points in back-to-back operation (T: 20°C). A plot of the error vector magnitude (EVM) versus symbol rate with some inlaid signal constellation diagrams, is given in Fig. 83 (V_{MZM}: 5 V).

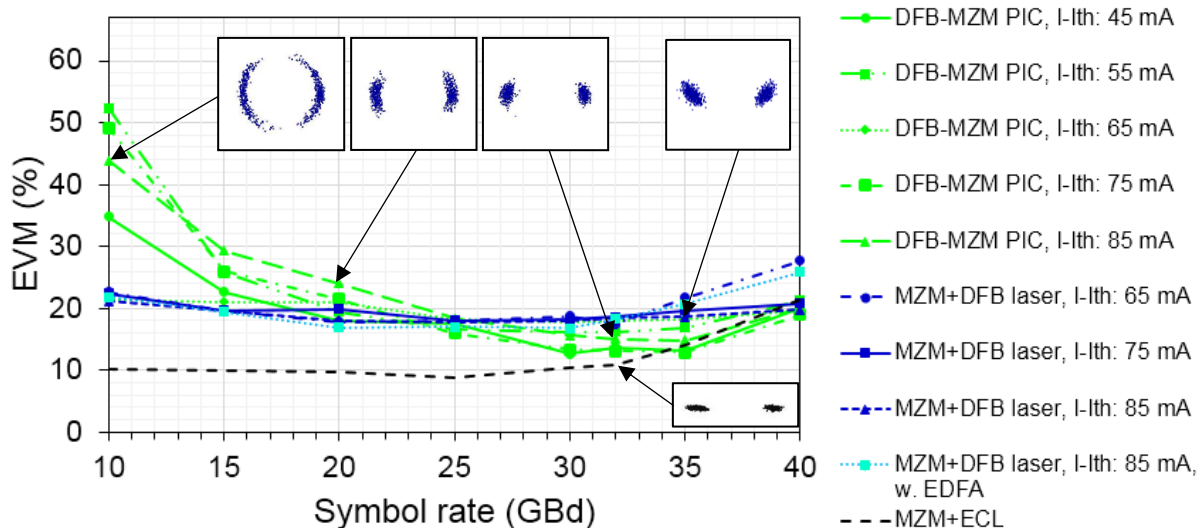


Fig. 83. BPSK error vector magnitude vs. symbol rate at different laser bias currents with inlaid constellation diagrams, for DFB laser Mach-Zehnder modulator transmitter (DFB-MZM PIC) and reference Mach-Zehnder modulator (MZM) with DFB laser (MZM+DFB laser), with DFB laser and pre-amplifier (MZM+DFB laser w. EDFA) or with external cavity laser (MZM+ECL) (V_{MZM}: 5 V).

The measurement includes the EVM of the transmitter (DFB-MZM PIC), the reference Mach-Zehnder modulator with the DFB laser (MZM+DFB laser), or with the external cavity laser (MZM+ECL). Also, it includes the measurement with an erbium doped fiber amplifier between the DFB laser module and the reference Mach-Zehnder modulator (MZM+DFB laser w. EDFA). Fig. 83, also shows error vector magnitude measurements at different DFB laser bias currents.

The binary phase shift keying constellation diagrams of the reference Mach-Zehnder modulator with the external cavity laser have two narrow constellation points, with an error vector magnitude of about 10 %, at up to 32 GBd. At larger symbol rates, the error vector magnitude increases, because of the limited Mach-Zehnder modulator bandwidth and thus a lower signal-to-noise ratio. Since the DFB laser has a much larger linewidth, compared to the external cavity laser, the error vector magnitude when using the DFB laser, is increased and the constellation points show more phase noise. At 10 GBd symbol rate, the error vector magnitude is around 22 %, decreasing to

about 18 % at 20 GBd. Applying different DFB laser bias currents and using the pre-amplifier to increase the Mach-Zehnder modulator input power, have only a small influence on the error vector magnitude.

For the DFB laser Mach-Zehnder modulator transmitter, strong phase variations on the constellation points and a high error vector magnitude are observed, at 10 GBd binary phase shift keying. The intensity noise appears comparable to the one of the reference Mach-Zehnder modulator with DFB laser. The errors decrease at increasing symbol rate, so that at symbol rates larger than 25 GBd, the constellation points and error vector magnitude become comparable to the ones of the DFB laser with reference Mach-Zehnder modulator. Between 30 GBd and 40 GBd, the transmitter error vector magnitude is even lower, around 13 %. The lower error vector magnitude can be explained mostly by the lower linewidth of the integrated DFB lasers, compared to reference DFB lasers, as shown before in Fig. 69. The increased error vector magnitude and phase noise indicate that the laser probably responds to modulated optical feedback at symbol rates lower and in the range of the laser relaxation oscillation frequency.

The DFB laser Mach-Zehnder modulator transmitter error vector magnitude depends more strongly on the laser bias current than the one of the reference Mach-Zehnder modulator with DFB laser, especially at lower symbol rates. Further measurements of the DFB laser Mach-Zehnder modulator transmitter error vector magnitude, depending on the laser bias current at 10 GBd and 32 GBd binary phase shift keying, are displayed in Fig. 84a.

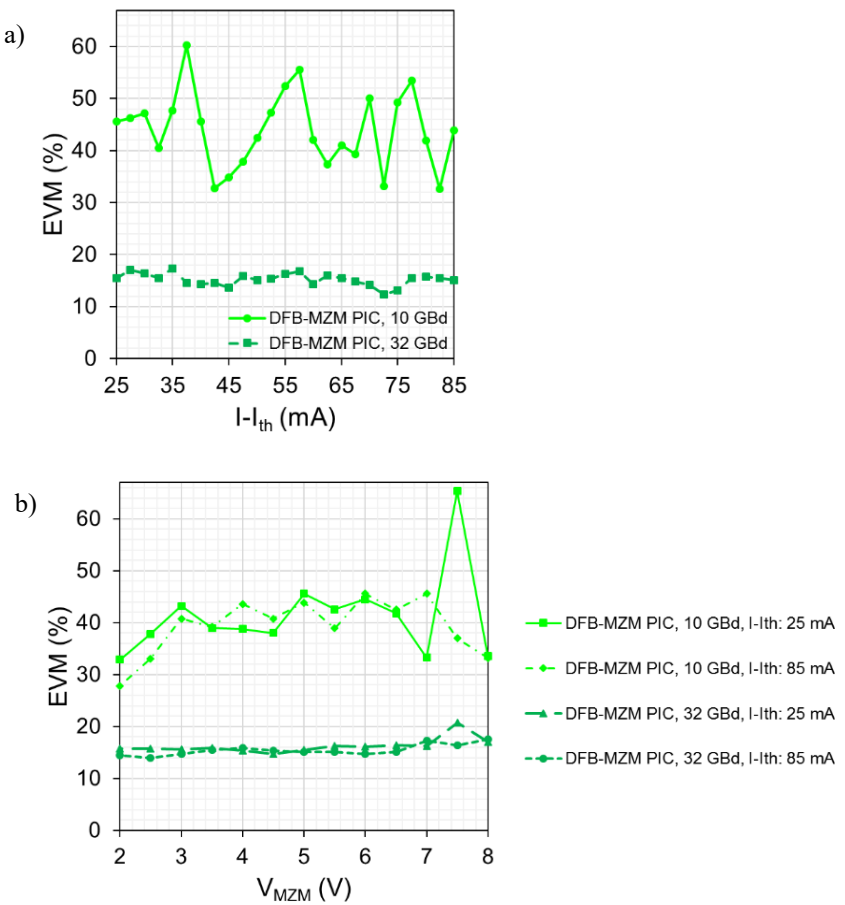


Fig. 84. DFB laser Mach-Zehnder modulator transmitter (DFB-MZM PIC) a) EVM vs. laser bias current (V_{MZM} : 5 V), b) EVM vs. modulator bias voltage V_{MZM} at different symbol rates and laser bias currents.

At 10 GBd, the error vector magnitude changes strongly with the laser bias current, while at 32 GBd, the effect diminishes, so that the error vector variation is only by a few percent.

In Fig. 84b, the transmitter error vector magnitude versus the modulator bias voltage is obtained at 10 GBd and 32 GBd symbol rate. The measurements are taken at laser bias currents, 25 mA and 85 mA above threshold. Strong error vector magnitude oscillations at 10 GBd, are visible, when changing the modulator bias voltage, while at 32 GBd, the error vector magnitude is almost constant. The laser bias current between 25 mA and 85 mA have little impact on the error vector magnitude variations.

The error vector magnitude variations, depending on the transmitter operation point could be an effect of optical feedback inside the DFB laser Mach-Zehnder modulator transmitter. The transmitter operation point influences the optical feedback intensity and phase, which impacts on the DFB laser performance. For a better understanding, further investigations of the DFB laser performance with optical feedback will be carried out in the chapters 6 and 7.

The binary phase shift keying measurements show, that the DFB laser Mach-Zehnder modulator transmitter, causes increased phase noise at symbol rates smaller than or in the range of the DFB laser relaxation oscillation frequency. At larger symbol rates, however, the transmitter binary phase shift keying performance is comparable or even better than the one of a comparable Mach-Zehnder modulator with isolated DFB laser.

5.1.5.3 Bipolar 4-Level Pulse Amplitude Modulation (PAM4)

The binary phase shift keying measurements in chapter 5.1.5.2, show that the DFB laser Mach-Zehnder modulator transmitter signal constellation points have an increased phase noise at symbol rates, lower than 25 GBd. To observe the constellation points of a phase modulated signal with multiple amplitude levels, the DFB laser Mach-Zehnder modulator transmitter module is operated at bipolar 4-level pulse amplitude modulation (PAM4). The ideal bipolar PAM4 constellation diagram has four constellation points on the in-phase axis, with two different amplitudes and zero or 180 degrees phase (Fig. 85).

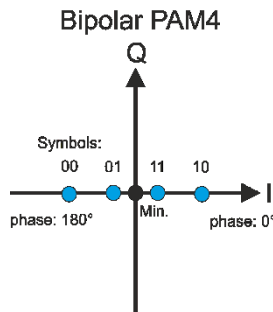


Fig. 85. Ideal bipolar PAM4 constellation diagram.

As in binary phase shift keying, the Mach-Zehnder modulator working point is set to the minimum and a modulation voltage swing of two times the switching voltage is applied. To get multiple amplitude levels, a 2 bit digital-to-analog converter is employed after the bit pattern generator. The rest of the experimental setup is comparable to the one in Fig. 82. The bipolar 4-level pulse amplitude modulation constellation diagrams are obtained in back-to-back operation at different symbol rates from 16 GBd to 32 GBd and displayed in Fig. 86 (T: 20°C, I-I_{th}: 85 mA, V_{MZM}: 5 V).

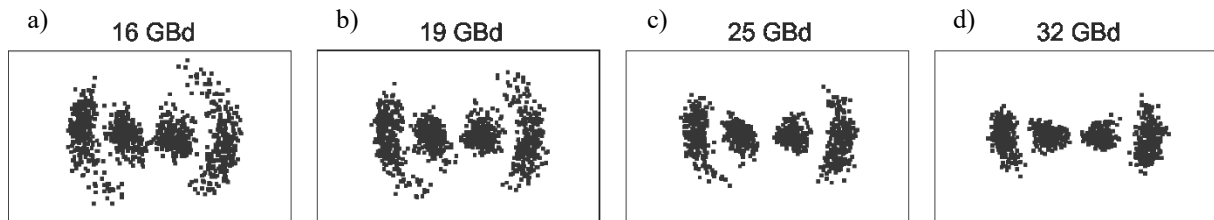


Fig. 86. Bipolar PAM4 signal constellation diagrams at a) 16 GBd, b) 19 GBd, c) 25 GBd and d) 32 GBd (T: 20°C, I-I_{th}: 85 mA, V_{MZM}: 5 V).

Like in the binary phase shift keying case, phase variations are visible on the constellation points, decreasing at increasing symbol rate. The outer constellation points are comparable to the binary phase shift keying ones in Fig. 83. On the inner constellation points, the phase variations seem lower. At symbol rates, lower than 25 GBd, the slightly increased intensity noise causes overlaps of the constellation points (Fig. 86a+b), while at 25 GBd (Fig. 86c) and 32 GBd (Fig. 86d), four distinct amplitude levels are obtained.

The bipolar PAM4 measurements show, that the DFB laser Mach-Zehnder modulator transmitter should be used at 25 GBd symbol rates and higher, when employing phase modulation with multiple amplitudes. At lower symbol rates, broadening of the constellation points, due to phase noise, could lead to inter-symbol interference, i.e. in quadrature amplitude modulated signals. For purely intensity modulated signals, like common 4-level pulse

amplitude modulation (PAM4), the phase noise and the slightly increased intensity noise is not supposed to be critical.

5.2 DFB laser IQ modulator Transmitter Subassembly with Dual Differential Driver

In this subchapter, the second optical transmitter type with a DFB laser and an integrated in-phase and quadrature (IQ) modulator, is further characterized and tested for large signal operation, similar to the first transmitter type in chapter 5.1. For large signal operation of the IQ modulator, the differential driving scheme is applied. The differential driving scheme is important to achieve the best signal quality with the IQ modulator. With the single ended driving scheme, a pattern dependent phase drift and low frequency chirp have been observed, deteriorating the IQ modulator signal performance [73]. Currently available commercial differential drivers are typically designed for a $100\ \Omega$ differential load impedance. Since the travelling wave electrode Mach-Zehnder modulator has a $50\ \Omega$ impedance, differential driver integrated circuits, based on silicon-germanium (SiGe), are especially designed for the Mach-Zehnder modulator at Fraunhofer HHI and fabricated externally. For the integrated IQ modulator, a dual differential driver is manufactured, including two $50\ \Omega$ differential drivers, for both the travelling wave Mach-Zehnder modulators inside the IQ modulator.

A transmitter optical subassembly module with a sufficient number of direct current pins for both the DFB laser IQ modulator transmitter and the dual differential driver is not available. Thus, for easier contacting and handling, DFB laser IQ modulator transmitters are fixed together with dual differential drivers, onto ceramic carriers, forming transmitter subassemblies.

5.2.1 Architecture

A photograph of the transmitter subassembly, with a DFB laser IQ modulator photonic integrated circuit (DFB-IQM PIC) and a SiGe-based dual differential driver on a ceramic carrier is shown in Fig. 87.

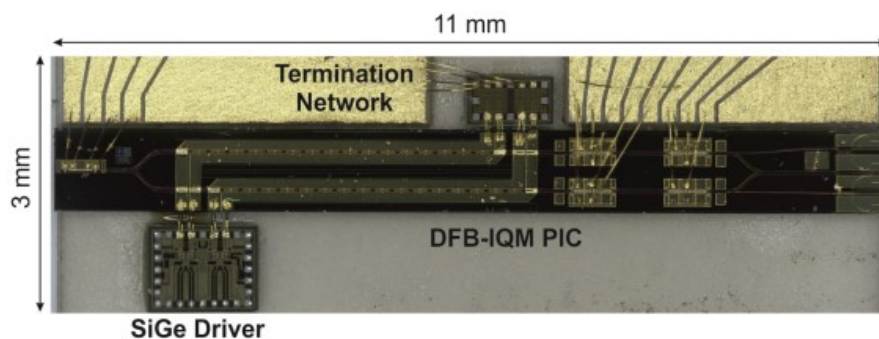


Fig. 87. Photograph of the transmitter subassembly with a DFB laser IQ modulator photonic integrated circuit (DFB-IQM PIC), a SiGe-based dual differential driver and a termination network.

The dual differential driver integrated circuit is wire-bonded to the DFB laser IQ modulator travelling wave electrode inputs, while a termination network is wire-bonded to the outputs. The termination network includes two $25\ \Omega$ load resistors, for each of the Mach-Zehnder modulators inside the IQ modulator. Additional metal lines are deposited on the ceramic, which are wire-bonded to the DFB laser IQ modulator direct current bias contacts, for easier placement of contact needles. The transmitter subassembly has a total footprint of $11 \times 3\ \text{mm}^2$.

5.2.1.1 Dual Differential Driver Integrated Circuit

The dual channel differential driver is designed to match the IQ modulator traveling wave electrodes load resistances. It is implemented in 0.25 μm SiGe BiCMOS technology (transit frequency: 190 GHz, max, oscillation frequency: 200 GHz) and has a $1.0 \times 1.4 \text{ mm}^2$ footprint. The driver is a limiting amplifier with soft clipping behavior at differential input voltages between 400 mV and 800 mV, designed for a low power consumption and low jitter.

The dual differential driver S_{21} - and S_{11} -parameters for both channels are measured with a network analyzer. The driver outputs are directly contacted with a radio frequency probe, while the output differential impedance of the network analyzer is set with the control software to 50Ω . The measured S_{21} - and S_{11} -parameters depending on the frequency are given in Fig. 88.

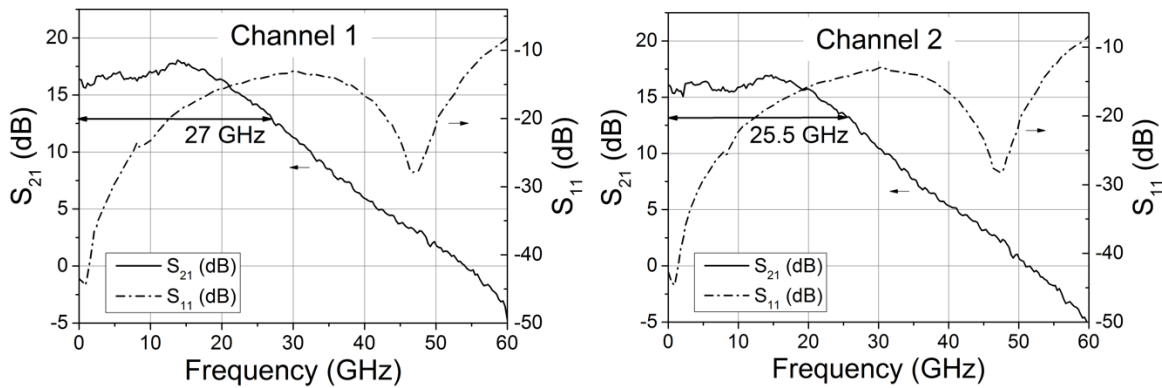


Fig. 88. S_{21} - and S_{11} -parameters of the two dual differential driver channels (3 dB bandwidths: 27 GHz and 25.5 GHz).
At -1 dBm differential input power, the 3 dB-bandwidths are 27 GHz and 25.5 GHz. The differential input reflection S_{11} is lower than -20 dB at up to 12 GHz for both channels.

To experimentally determine the dual differential driver jitter performance, the chip is wire-bonded to an impedance transformation network with the same load impedance as the IQ modulator. The output signal is measured at the impedance transformation network output. By de-embedding, the frequency response of the impedance transformation network is removed. The de-embedded electrical eye diagram at 28 Gb/s non-return-to-zero on-off keying (NRZ), shows a low 4 ps peak-to-peak jitter (Fig. 89).

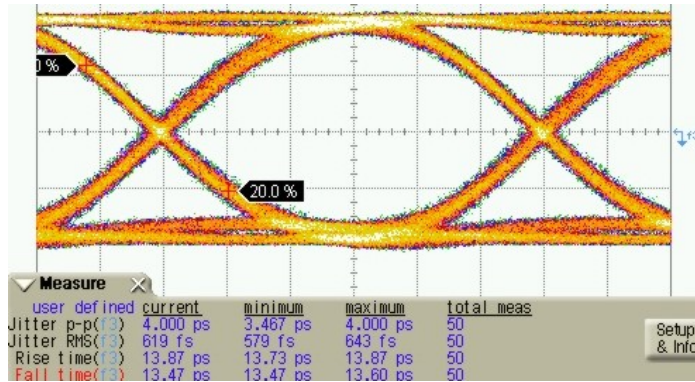


Fig. 89. Measured differential driver eye diagram at 28 Gb/s NRZ, after impedance transformation network with IQ modulator load impedance.

The dual driver power consumption is 0.96 W for a differential output voltage swing of 3 V_{pp}, with both channels in operation.

5.2.2 Optical Spectrum, Relative Intensity Noise and Linewidth

With the DFB laser IQ modulator transmitter subassemblies, spectral power, relative intensity noise and linewidth characteristics are obtained and compared to the ones of reference DFB lasers and the DFB laser Mach-Zehnder modulator transmitter module in chapter 5.1.2.

The DFB laser IQ modulator transmitter optical output spectrum with a 1544.6 nm wavelength and 50.6 dB side mode suppression ratio is given in Fig. 90 (I-I_{th}: 85 mA, T: 20°C).

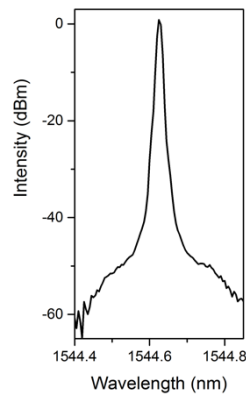


Fig. 90. DFB laser IQ modulator transmitter optical spectrum (I-I_{th}: 85 mA, V_{MZM}: 0 V, T: 20°C).

The DFB laser IQ modulator transmitter maximum output power at I-I_{th}: 85 mA and 20°C temperature is 0.8 dBm in the fiber. The transmitter side mode suppression ratio and output power are sufficiently high for the transmitter requirements.

The DFB laser IQ modulator transmitter relative intensity noise (RIN) spectra are measured at different laser bias currents and compared to the ones of a reference DFB laser (Fig. 91).

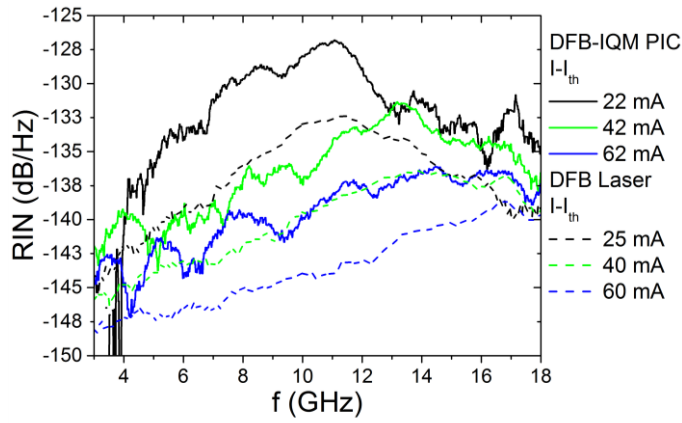


Fig. 91. DFB laser IQ modulator transmitter relative intensity noise spectra at different laser bias currents, compared to the ones of a reference DFB laser ($V_{\text{MZM}}: 0 \text{ V}$, $T: 40^\circ\text{C}$).

In general, the DFB laser IQ modulator relative intensity noise is increased by 4 dB to 5 dB, compared to the one of the reference DFB laser and DFB laser Mach-Zehnder modulator (Fig. 66), but it is below -130 dB/Hz at bias currents larger than 42 mA above threshold, fulfilling the transmitter specifications.

The DFB laser IQ modulator transmitter relaxation oscillation frequencies are obtained at the relative intensity noise spectrum maxima, at different bias currents. The relaxation oscillation frequencies are between 11 GHz and 17 GHz, in the range of the reference DFB laser ones (Fig. 92).

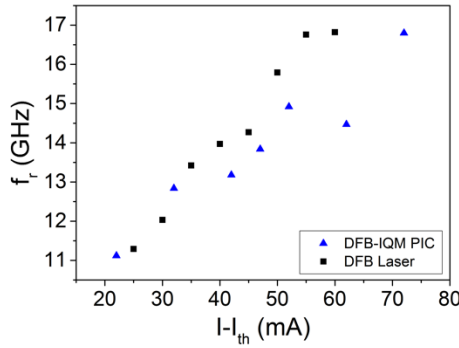


Fig. 92. DFB laser IQ modulator transmitter relaxation oscillation frequency vs. laser bias current compared with reference DFB laser ($V_{\text{MZM}}: 0 \text{ V}$, $T: 40^\circ\text{C}$).

The DFB laser IQ modulator transmitter line spectrum at different laser bias currents, typically has a Lorentzian shape, similar to the reference DFB laser ones (Fig. 93a).

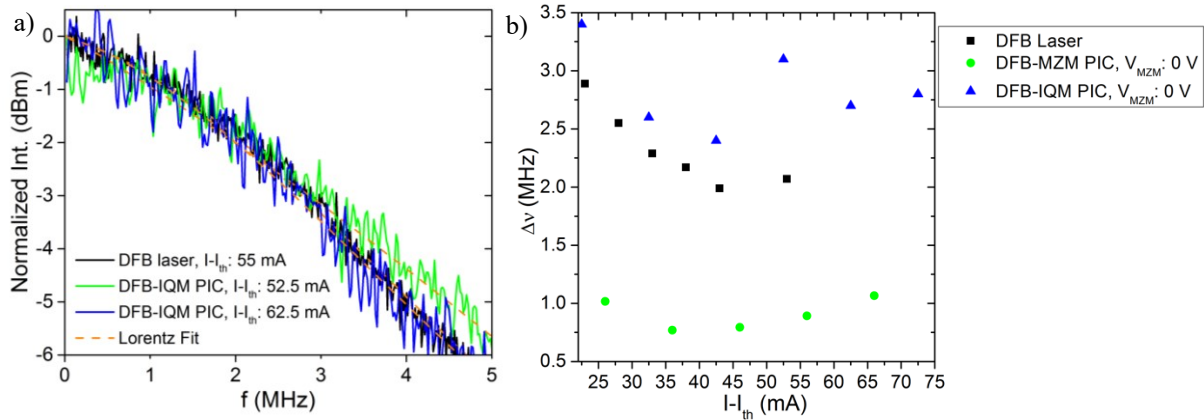


Fig. 93. DFB laser IQ modulator transmitter (DFB-IQM PIC) and reference DFB laser a) line spectra and b) linewidth vs. laser bias current, compared with DFB laser Mach-Zehnder modulator transmitter (DFB-MZM PIC) ($V_{MZM} = 0$ V, T: 40°C).

The linewidths of the DFB laser IQ and Mach-Zehnder modulator transmitters and the reference DFB lasers are compared in Fig. 93b, at different laser bias currents. The DFB laser IQ modulator transmitter linewidth is mostly comparable to the reference DFB laser one. The transmitter linewidth differences with respect to the reference DFB laser values are attributed to optical feedback inside the photonic integrated circuits, which will be further discussed in chapter 7. In comparison, the DFB laser Mach-Zehnder modulator, the DFB laser IQ modulator linewidth is broader and more similar to the one of the reference DFB lasers. A reason could be that the laser in the DFB IQ modulator PIC experiences a lower reflected optical power due to the higher losses in the IQ modulator compared to the Mach-Zehnder modulator.

5.2.3 Large Signal Operation

The DFB laser IQ modulator transmitter subassemblies with dual differential driver are tested under quaternary phase shift keying (QPSK) operation. The experimental setup is sketched in Fig. 94 for the DFB laser IQ modulator transmitter subassembly and a reference IQ modulator subassembly.

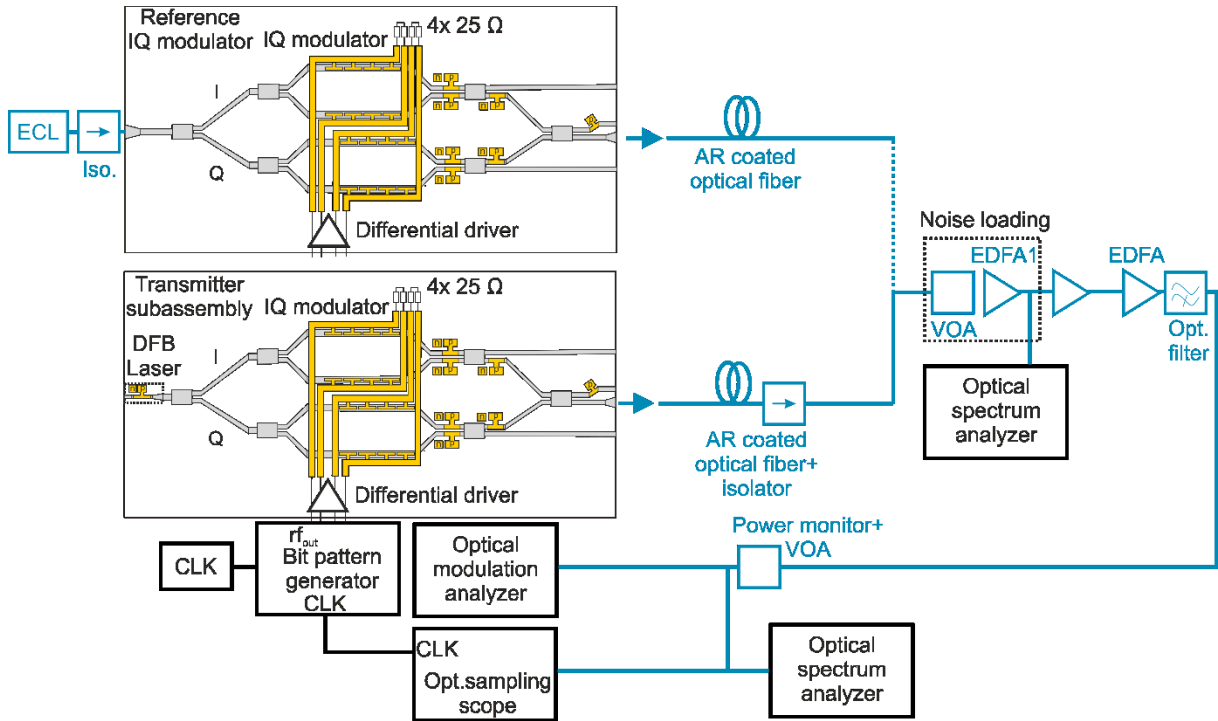


Fig. 94. QPSK measurement experimental setup with reference IQ modulator or transmitter subassembly.

Two electrical $2^{11}-1$ bit long pseudorandom binary bit streams are generated with a multi-channel bit pattern generator. Both the in-phase (I) and quadrature (Q) Mach-Zehnder modulators inside the integrated IQ modulator are operated at the minimum working point and a modulation voltage swing of about two times the switching voltage is applied, as in binary phase shift keying operation. An optical modulation analyzer, including the coherent receiver with a local oscillator, optical 90° hybrids and balanced photodetectors, is used to receive the signals. The optical modulation analyzer also accounts for analog-to-digital conversion, generates the constellation diagrams and calculates the error vector magnitude (EVM). For carrier phase tracking, the Kalman filter phase tracker algorithm of the optical modulation analyzer is used.

A differential driver is used to amplify the electrical data signal at the modulator input. If asymmetric single-ended driving would be used, a pattern dependent phase drift and low frequency chirp would cause signal degradations, this is explained in more detail in [74]. The resulting QPSK eye diagram using single-ended driving is overlaid with strong amplitude noise as in Fig. 95a [36]. The eye diagram of the identical device with differential driving has low amplitude noise and clear transitions (Fig. 95b). Thus, the differential driving scheme is a key factor for achieving the best IQ modulator signal quality.

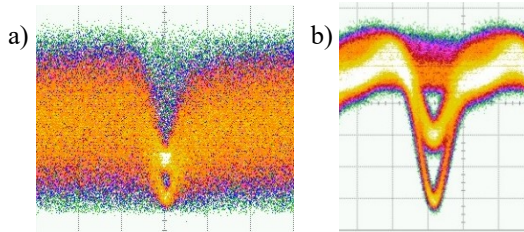


Fig. 95. a) QPSK eye using single-ended driving scheme with overlaid amplitude noise. b) Clear QPSK eye of identical device using differential driving scheme.

Binary phase shift keying constellation diagrams are measured, by operating only the I (Fig. 96a) or the Q Mach-Zehnder modulator (Fig. 96b) and measuring the signal at the IQ modulator output.

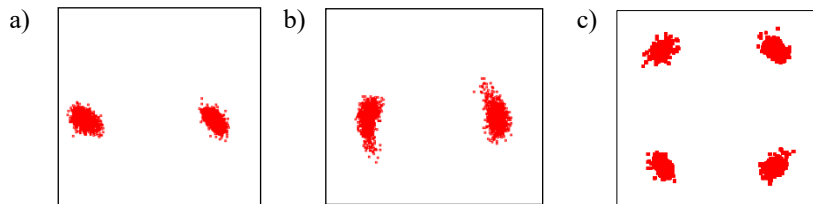


Fig. 96. Constellation diagrams at 28 GBd binary phase shift keying of a) I and b) Q Mach-Zehnder modulator and c) at 28 GBd QPSK operation.

Depending on the transmitter operation point in terms of DFB laser bias current and modulator bias voltage, either the binary phase shift keying constellation diagrams of both Mach-Zehnder modulators have clear constellation points, as in Fig. 96a, or one of the signals is overlaid with phase variations due to optical feedback, as in Fig. 96b. The QPSK operation is performed, by operating both Mach-Zehnder modulators at the same time. Also, the QPSK constellation points have some overlaid phase variations (Fig. 96c). At 28 GBd QPSK operation, the phase variations in the constellation diagram are minimized by adjusting the transmitter laser bias current which changes the optical feedback phase ($I - I_{th}$: 85 mA, V_{MZM} : 8 V, T: 20°C).

As a reference, an IQ modulator, without integrated laser is used, with a similar structure to the one in the DFB laser IQ modulator transmitter. The IQ modulator is also embedded on a transmitter subassembly with a dual differential driver and a termination network. As a light source, the output of an external cavity laser (linewidth < 150 kHz) is coupled into the reference IQ modulator input. An optical isolator is included in the external cavity laser module, avoiding optical back-reflections. The external cavity laser output power is 13 dBm, so that the input power to the reference IQ modulator is 10 dBm, which comparable to the input power of the integrated IQ modulator in the transmitter. The received reference IQ modulator (IQM+ECL) QPSK constellations at different symbol rates from 10 GBd to 28 GBd have clear constellations points and a 6- 8 % error vector magnitude (EVM) (Fig. 97).

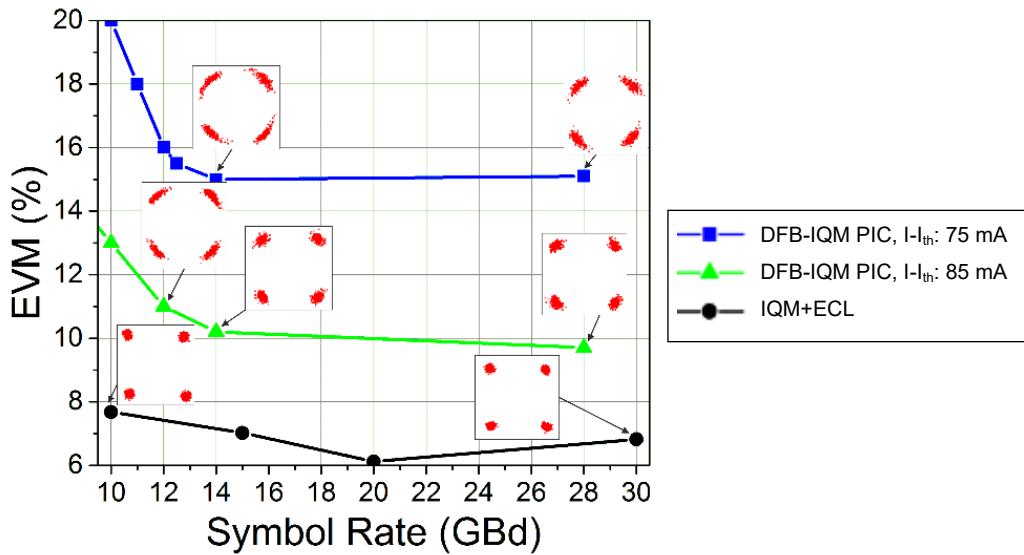


Fig. 97. QPSK error vector magnitude (EVM) and constellation diagrams at different symbol rates of the reference IQ modulator (IQM+ECL) and the DFB laser IQ modulator transmitter (DFB-IQM PIC) at different laser bias currents (V_{MZM} : 8 V).

For the DFB laser IQ modulator transmitter, the local oscillator wavelength at the optical modulation analyzer is matched to the integrated laser one for each measurement. Phase variations on the QPSK constellation points are observed, especially at symbol rates lower than 14 GBd. At larger symbol rates, the phase variations decrease and remain almost constant. Compared to the reference IQ modulator, the DFB laser IQ modulator QPSK constellation points have a slightly increased intensity noise, independent of the symbol rate. The QPSK signal quality depends also on the transmitter operation point. At the optimum bias point ($I-I_{\text{th}}$: 85 mA, V_{MZM} : 8 V) and at symbol rates larger than 14 GBd, the DFB laser IQ modulator transmitter shows a good QPSK performance, with an error vector magnitude around 10 %, only 3-4 % larger than the one of the reference IQ modulator. The difference is due to the better external cavity laser performance, compared to the integrated DFB laser, in terms of linewidth and intensity noise.

At another operation point ($I-I_{\text{th}}$: 75 mA, V_{MZM} : 8 V), the DFB laser IQ modulator transmitter error vector magnitude is increased by 5 % (in Fig. 97), compared to the optimum operation point and larger phase variations are observed. The QPSK error vector magnitude changes periodically with the laser bias current, especially at 10 GBd QPSK (Fig. 98).

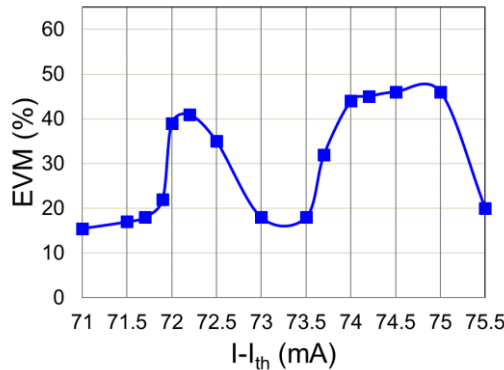


Fig. 98. Error vector magnitude vs. laser bias current at 10 GBd QPSK of DFB laser IQ modulator transmitter (V_{MZM} : 8 V).

The periodic error vector magnitude variation with the laser bias current is comparable to the one in the DFB laser Mach-Zehnder modulator transmitter module binary phase shift keying measurement, in chapter 5.1.5.2, Fig. 84a.

The bit error rate (BER) is tested at different symbol rates from 10 GBd to 32 GBd, for the DFB IQ modulator transmitter and the reference IQ modulator. The bit error rate values are calculated with the optical modulation analyzer, which also accounts for bit error counting. As a reference, the hard-decision forward error correction threshold for a 7 % overhead ($3 \cdot 10^{-8}$), is used. Error-free QPSK operation, below the measurable system limit ($4 \cdot 10^{-5}$), is obtained for both the reference IQ modulator and the DFB laser IQ modulator transmitter at its optimum bias point ($I - I_{th}$: 85 mA, V_{MZM} : 8 V). At the DFB laser IQ modulator transmitter bias point with increased error vector magnitude ($I - I_{th}$: 75 mA, V_{MZM} : 8 V), errors are observed (Fig. 99).

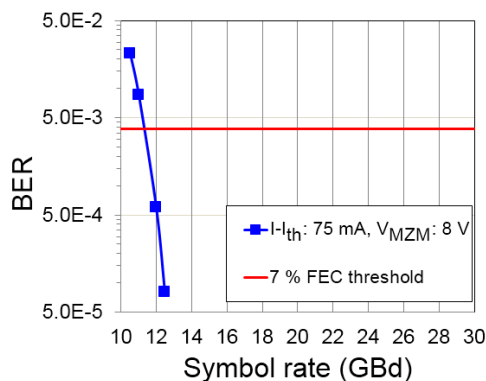


Fig. 99. QPSK bit error rate vs. symbol rate of DFB laser IQ modulator transmitter at bias point with increased error vector magnitude ($I - I_{th}$: 75 mA, V_{MZM} : 8 V).

The bit error rate is $2.3 \cdot 10^{-2}$ at 10 GBd QPSK and decreases below the 7 % forward error correction threshold at symbol rates larger than 11.3 GBd.

The following measurements are done with a second DFB laser IQ modulator with dual differential driver transmitter subassembly, which is similar to the first one, since the first one is not available at the moment. At the optimum bias point ($I - I_{th}$: 85 mA, V_{MZM} : 1.7 V), the 32 GBd QPSK error vector magnitude is 11.3 % (Fig. 100a).

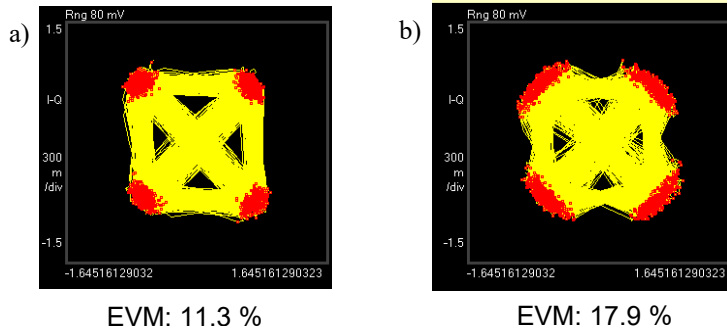


Fig. 100. DFB laser IQ modulator subassembly 32 GBd QPSK constellation diagrams and error vector magnitude at different modulator bias voltages a) V_{MZM} : 1.7 V b) V_{MZM} : 7.5 V ($I - I_{th}$: 85 mA).

It is observed, that the phase variations on the QPSK constellation points and the error vector magnitude depend on the modulator bias voltage. At 32 GBd QPSK, the error vector magnitude varies periodically between 10.6 % and 26 %, depending on the modulator bias voltage V_{MZM} , with a period length in the order of the IQ modulator switching voltage ($I - I_{th}$: 85 mA) (Fig. 101).

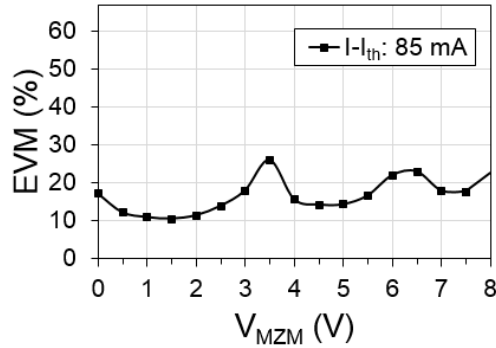


Fig. 101. 32 GBd QPSK error vector magnitude vs. modulator bias voltage ($I - I_{th}$: 85 mA).

At 32 GBd QPSK, the error vector magnitude dependency on the transmitter operation point is weaker than at 10 GBd. Compared to the DFB laser Mach-Zehnder modulator module binary phase shift keying error vector magnitude measurement in chapter 5.1.5.2, Fig. 84b, the QPSK error vector magnitude at 32 GBd is more sensitive to the modulator bias voltage. The error vector magnitude increase with the modulator bias voltage, is probably due to the increased Mach-Zehnder modulator nonlinearity at higher modulator bias voltages.

The DFB laser IQ modulator subassembly 32 GBd QPSK bit error rate depending on the optical signal-to-noise ratio (OSNR) is measured at the optimum bias point (V_{MZM} : 1.7 V, EVM: 11.3 %) and at a different modulator bias voltage (V_{MZM} : 7.5 V, EVM: 17.9 %) at $I - I_{th}$: 85 mA. The noise loading is done with a variable optical attenuator and the amplified spontaneous emission noise of an additional erbium doped fiber amplifier, as in the bit error measurement in chapter 5.1.5.1, Fig. 77. The bit error rate at the optimum bias point is below the 7 % forward error correction threshold at optical signal-to-noise values, larger than 13.6 dB (Fig. 102).

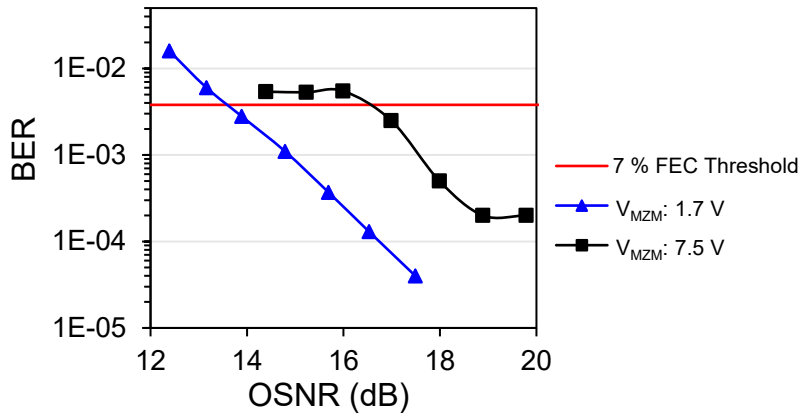


Fig. 102. 32 GBd QPSK bit error rate vs. optical signal-to-noise ratio at different modulator bias voltages ($I - I_{\text{th}}$: 85 mA).

Changing the modulator bias voltage to 7.5 V, gives an optical signal-to-noise ratio penalty at the 7 % forward error correction threshold of 2.9 dB. Moreover, a noise floor appears at optical signal-to-noise ratios, larger than 18.9 dB.

Finally, the influence of different pseudorandom binary sequence lengths ($2^{11}-1$, $2^{20}-1$, $2^{31}-1$) on the QPSK signal quality is tested at the optimum bias point ($I - I_{\text{th}}$: 85 mA, V_{MZM} : 1.7 V) and at symbol rates from 10 GBd to 30 GBd (Fig. 103).

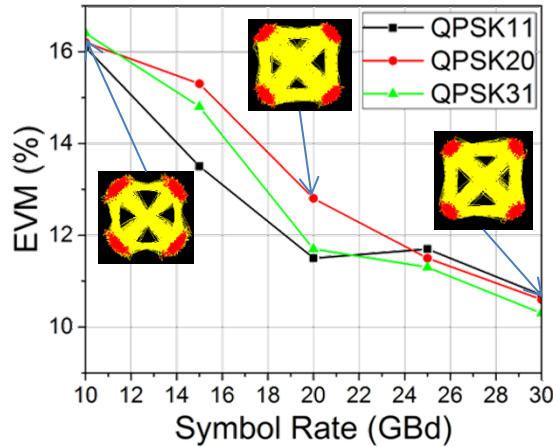


Fig. 103. QPSK error vector magnitude vs. symbol rate at different pseudorandom binary sequence lengths ($I - I_{\text{th}}$: 85 mA, V_{MZM} : 1.7 V).

Only up to 2 % error vector magnitude variation is observed between the different pseudorandom binary sequence lengths, which is negligible.

The results show that the DFB laser IQ modulator transmitter has an increased QPSK error vector magnitude and phase variations on the constellation points at symbol rates lower than 25 GBd. Moreover, the QPSK signal quality, depends strongly on the transmitter operation point. These effects appear probably, due to optical feedback inside the transmitter, which will be further discussed in chapter 7. Tuning the laser bias current and the modulator bias voltage is very important, to achieve the best QPSK performance. To find a good operation point, the laser bias current should be varied by about ± 1 mA and the modulator bias voltage in the range of the switching voltage.

After finding a good operation point, the transmitter performance is stable, as long as the operating conditions are constant.

At the optimum bias point and at symbol rates larger than 25 GBd, the DFB laser IQ modulator transmitter shows a good performance at up to 32 GBd QPSK, with an error vector magnitude only a few percent higher than the one of an IQ modulator with an external cavity laser. The DFB laser IQ modulator transmitter is a promising device for optical communication networks at 100 Gb/s and higher, where transmitter operation at symbol rates of 25 GBd and higher is required.

6. Theoretical Study of Lasers with Optical Feedback

The integrated DFB laser Mach-Zehnder/ IQ modulator transmitter measurements show different results than expected for a transmitter with isolated laser and modulator. In fact, the DFB laser in the transmitter photonic integrated circuits is not isolated. Optical feedback to the laser is generated by reflective interfaces inside and outside the photonic integrated circuits. Reflections from outside the transmitter, are mostly suppressed by implementing optical isolators, anti-reflection coated optical fibers and angled fiber connectors in the experimental setups. This work focusses on reflections inside the transmitter photonic integrated circuits, where optical isolation is challenging. Several integrated isolator designs have been already presented, based on ferromagnetic materials [75]. However, the isolators require an external magnetic field and are still impracticable.

In this chapter, the influence of passive and dynamic optical feedback on the laser performance is described, to give a better understanding. Lasers with optical feedback have been extensively studied in the past. The dynamic laser behavior under optical feedback is sufficiently described by the Lang-Kobayashi differential equations [19]. From these equations, the impact of passive optical feedback on the laser linewidth, power and phase is derived and stated with simple equations. In the optical transmitter photonic integrated circuits, the modulated data signal is reflected to the laser. Not much is known about how the reflected modulated data signal influences the transmitter modulation performance. Thus, further study is important and included in this chapter.

A model of a laser with optical feedback from an external cavity is created, based on the Lang-Kobayashi differential equations and numerical examples for the laser performance under passive optical feedback are given. The Lang-Kobayashi differential equations are extended to include the optical feedback modulation and the laser intensity and phase frequency responses to the modulated optical feedback are shown. The results are further used in chapter 7, to draw conclusions about the transmitter performance under optical feedback.

6.1 Laser with Optical Feedback: Passive Behavior

A schematic, where a laser receives optical feedback from an external cavity, with a reflectivity R_{ec} and a length L_{ec} , is given in Fig. 104.

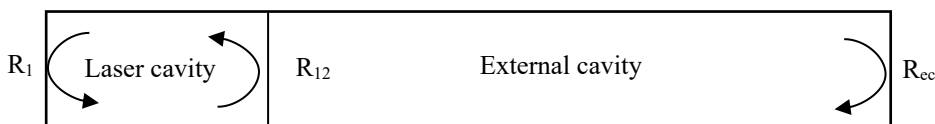


Fig. 104. Schematic of a laser with external optical feedback.

The laser reflectivity is described by R_1 at the chip facet and by R_{12} towards the external cavity. The external cavity reflectivity R_{ec} for plane waves is calculated by eq. (6.1), where n_{eff1} and n_{eff2} are the effective refractive indices at the interface of the two waveguides or materials [28].

$$R_{ec} = \frac{|n_{eff1}-n_{eff2}|^2}{|n_{eff1}+n_{eff2}|^2} \quad (6.1)$$

The free spectral range $f_{r,ec}$, which is the frequency distance between external cavity resonances, is given by eq.(6.2), where $n_{gr,ec}$ is the external cavity group refractive index.

$$f_{r,ec} = \frac{c}{2n_{gr,ec}L_{ec}} \quad (6.2)$$

The free spectral range is also referred to as external cavity resonance frequency in this work. The optical feedback changes the laser frequency, linewidth and relative intensity noise, depending on the laser and external cavity dimensions, reflectivity and various other parameters [68]. For DFB lasers, different feedback regimes, depending on the feedback intensity and the external cavity length are distinguished (Fig. 105.) [20], [76].

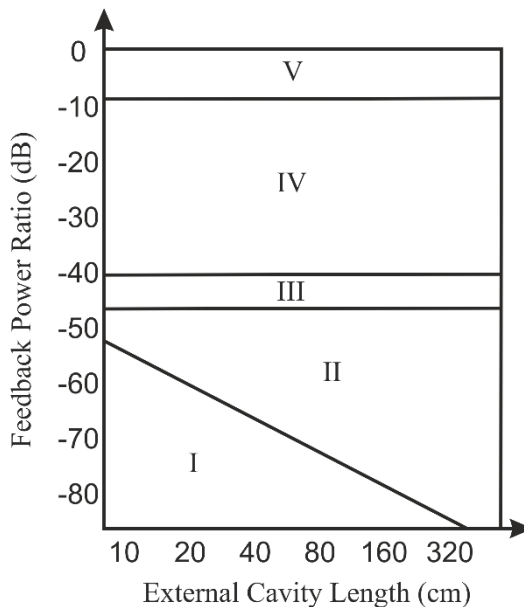


Fig. 105. DFB laser feedback regime mapping depending on the feedback power ratio and external cavity length.

The feedback regimes are characterized as follows:

- **Regime I:** A linewidth narrowing or broadening, depending on the feedback phase is observed. The laser remains in single-mode operation.
- **Regime II:** A competition between the laser mode and external cavity modes occurs, in which one of them is lasing. Depending on the external feedback phase, mode-hopping or a stable-state with reduced linewidth is obtained.
- **Regime III:** A narrow linewidth mode is stabilized, independent of the external feedback phase.
- **Regime IV:** The laser becomes unstable with strong intensity noise. Multiple modes appear in the spectrum, enlarging the linewidth to several 10 GHz. This state is referred to as the coherence collapse and is independent of the external feedback phase.

- **Regime V:** When the external reflectivity is much stronger than the laser facet reflectivity, the external cavity dominates. A stable narrow linewidth mode manifests, independent of the feedback phase and robust against other external reflections.

The feedback regimes are mainly described for lasers with external cavities in the centimeter range or longer. For lasers with short external cavities in the millimeter range like in the developed optical transmitter photonic integrated circuits, a slightly different behavior is expected.

In regime II, the mode competition happens more likely between the lasing mode and modes at the relaxation oscillation frequency f_r and its harmonics instead of the external cavity modes [77]. The relative intensity noise spectrum of lasers with short external cavities, is not changed by optical feedback until the feedback intensity reaches a critical level where multiple peaks in the relative intensity noise spectrum at the laser relaxation oscillation frequency and its harmonics appear. The frequency noise spectrum of lasers with short external cavities is increased at frequencies up to the laser relaxation oscillation frequency, where it has an enhanced peak. [78]

6.2 Laser with Optical Feedback: Dynamic Behavior

The previously described behavior is known for lasers with passive optical feedback. In the optical transmitter photonic integrated circuits, the external cavity includes a Mach-Zehnder modulator, which modulates the reflected light. This causes in addition, laser intensity, wavelength and phase variations, depending on the modulation frequency [79].

To study in detail, the impact of passive and dynamic optical feedback on the laser performance, a dynamic model of a laser with an external cavity is created, based on the Lang-Kobayashi equations. The laser behavior is simulated numerically, depending on different parameters, such as the laser current and the optical feedback intensity and phase. First, the laser is observed without feedback, as a reference, then passive optical feedback from an external cavity with the dimensions of the integrated Mach-Zehnder modulator is added. Finally, the model is extended to include the optical feedback modulation.

6.2.1 Lang Kobayashi Model

For simplicity, a single reflective interface is assumed and the laser spontaneous emission is neglected. The emitted laser light is described by the time t variant electrical field $E(t)=\tilde{E}(t)e^{-i\omega_0 t}$, where $\tilde{E}(t)$ is the complex electrical field amplitude and ω_0 the circular optical frequency without feedback $\omega_0=2\pi c/\lambda$. The complex electrical field amplitude can be written as $\tilde{E}(t)=A(t)e^{-i\phi(t)}$, with an amplitude $A(t)$ and a phase $\phi(t)$, including the laser amplitude and phase fluctuations, which typically vary slowly, compared to the optical frequency. It is convenient, to normalize $\tilde{E}(t)$ to $\mathcal{E}(t)$, so that $|\mathcal{E}|^2$ is dimensionless and corresponds to the number of photons in the active region. The laser behavior under optical feedback is modelled by calculating $\mathcal{E}(t)$, together with the electrical carrier density $n(t)$. The derivatives of $\mathcal{E}(t)\rightarrow\dot{\mathcal{E}}(t)$ and $n(t)\rightarrow\dot{n}(t)$ and their relation is described by the Lang-Kobayashi rate equation model in (6.3) and (6.4) [80].

$$\dot{\mathcal{E}}(t) = (1-i\alpha)\Gamma G_{n_{th}}(n(t)-n_{th})\mathcal{E}(t) + \underbrace{\frac{K_{ec}}{\tau_L} e^{i\omega_0 t_{ec}} \mathcal{E}(t-\tau_{ec})}_{\text{Opt. Feedback}}$$

Laser without opt. feedback Opt. Feedback

(6.3)

$$\dot{n}(t) = \frac{j}{ed} - \frac{1}{\tau_c} n(t) - 2 \left(\frac{1}{\Gamma \tau_{ph}} + G_{n_{th}}(n(t)-n_{th}) \right) \frac{|\mathcal{E}(t)|^2}{V_{act}}$$
(6.4)

The first summand of eq. (6.3) describes the complex electrical field amplitude of a laser without optical feedback. The second summand is the optical feedback term, including the electrical field amplitude $\mathcal{E}(t-\tau_{ec})$, time-delayed by the external cavity roundtrip time $\tau_{ec}=2L_{ec}n_{gr,ec}/c$, where $n_{gr,ec}$ is the external cavity group refractive index. As simulation parameters, typical DFB laser values are taken, which are partly obtained from empirical values of fabricated DFB lasers and partly from the theory. The laser dimensions correspond to the ones of the integrated lasers in the optical transmitter photonic integrated circuits. The simulation parameters are summarized in Table 8.

Name	Symbol	Value
speed of light in vacuum	c	$3 \cdot 10^8$ m/s
elementary charge	e	$1.6 \cdot 10^{-19}$ As
electric constant	ϵ_0	$8.85 \cdot 10^{-12}$ As/Vm
Planck's constant	h	$6.626 \cdot 10^{-34}$ Ws ²
optical confinement	Γ	0.08
gain coefficient at threshold	a	$7 \cdot 10^{-20}$ m ²
carrier lifetime	τ_c	2.0 ns [22]
carrier density at threshold	n_{th}	$2 \cdot 10^{24}$ 1/m ³
laser wavelength	λ	1550 nm
linewidth enhancement factor	α	3.2
DFB laser grating effective reflectivity	$R_1 = R_{12}$	0.15 [20]
active region group refractive index	$n_{gr,act}$	3.56
active region length	L	300 μm
active region width	w	1.1 μm
active region thickness	d	56 nm
active region internal loss	α_{int}	1650 m^{-1}
external cavity group refractive index	$n_{gr,ec}$	3.8
coupling efficiency	η	1

Table 8 Simulation parameters

The differential gain at threshold is given by $G_{n_{th}}=v_{gr,act}a$, depending on the group velocity $v_{gr,act}=c/n_{gr,act}$ in the active region [80]. The pump current density is $j=I/F_{act}$, where $F_{act}=L \cdot w$ is the active region cross-section area and $V_{act}=F_{act} \cdot d$ the active region volume. The photon lifetime τ_{ph} (eq. (6.5)) inside the laser cavity is calculated, depending on the laser mirror losses α_m (eq. (6.6)) [22].

$$\tau_{ph} = \frac{1}{v_{gr,act}(\alpha_m + \alpha_{int})} \quad (6.5)$$

$$\alpha_m = \frac{1}{2L} \ln \left(\frac{1}{R_{12}^2} \right) \quad (6.6)$$

The coupling coefficient K_{ec} from the laser to the external cavity is calculated with equation (6.7), where R_{12} is the DFB grating effective reflectivity and R_{ec} the external cavity facet reflectivity.

$$K_{ec} = (1 - R_{12}) \sqrt{\frac{R_{ec}}{R_{12}}} \quad (6.7)$$

For solving the equations, a 4th order Runge-Kutta algorithm is implemented, which is described in detail in appendix IV.I. The emitted optical output power is calculated with eq. (6.8) [20].

$$P = \frac{hvc}{4\pi n_{gr,act} L} \ln \left(\frac{1}{R_{12}^2} \right) |\mathcal{E}(t)|^2 \quad (6.8)$$

The phase of $\mathcal{E}(t)$ is calculated with eq. (6.9), using its real and imaginary parts.

$$\phi(t) = \arctan \left(\frac{\text{Im}(\mathcal{E}(t))}{\text{Re}(\mathcal{E}(t))} \right) \quad (6.9)$$

6.2.2 Steady state model of Laser with Optical Feedback

From the equations (6.3) and (6.4), the laser steady state behavior is derived, assuming that the optical power, carrier density and phase are time-independent [22]. Under external optical feedback, the laser in steady state experiences a gain shift ΔG (eq. (6.10) [22]) and an angular frequency shift $\Delta\omega$ (eq. (6.11) [22]), where ω_0 is the angular frequency without optical feedback and $\tau_L = 2L n_{gr,act}/c$ the laser roundtrip time.

$$\Delta G = -2 \frac{1}{\tau_L} K_{ec} \cos(\omega_0 \tau_{ec}) \quad (6.10)$$

$$\Delta\omega = \frac{1}{\tau_L} K_{ec} [\sin(\omega_0 \tau_{ec}) + \alpha \cos(\omega_0 \tau_{ec})] \quad (6.11)$$

The laser angular optical frequency shift changes the phase ϕ (eq. (6.12) [68]).

$$\phi = \frac{\tau_L}{\tau_{ec}} \left(\tau_{ec} \Delta\omega + \frac{1}{\tau_L} K_{ec} \tau_{ec} \sqrt{1 + \alpha^2} \sin(\phi_{ec} + \arctan(\alpha)) \right) \quad (6.12)$$

The gain shift varies the optical output power P , consisting of the optical power P_0 , without feedback and the power variation ΔP (eq. (6.13) [22])

$$P = P_0 + \Delta P = \frac{I - I_{th}}{e \left(\frac{1}{\tau_{ph}} + \Delta G \right)} \quad (6.13)$$

The complex electrical field amplitude \tilde{E} in steady state, is obtained from the output power, with $A = \sqrt{P}$ and the phase ϕ (eq. (6.14)).

$$\tilde{E} = \sqrt{P} e^{i\phi} \quad (6.14)$$

6.2.3 Laser Linewidth with Optical Feedback

The laser phase noise is a critical parameter for the transmitter performance in optical communication systems and is typically measured by the laser linewidth. Since the laser spontaneous emission is not included in the dynamic laser model, it cannot be used for linewidth calculation. However, the laser linewidth under weak optical feedback in regime I, is given by simple equations.

The laser linewidth $\Delta\nu$ under optical feedback in regime I (eq. (6.15)), deviates from the laser linewidth $\Delta\nu_0$, without feedback, depending on the feedback coefficient C , the external feedback phase ϕ_{ec} and the linewidth enhancement factor α [68].

$$\Delta\nu = \frac{\Delta\nu_0}{[1 + C \cdot \cos(\phi_{ec} + \arctan(\alpha))]^2} \quad (6.15)$$

The external feedback phase $\phi_{ec} = \omega_0 \tau_{ec}$ depends on the external cavity roundtrip time τ_{ec} . The feedback coefficient C is described in eq. (6.16), where $f_{ext} = \eta^2 R_{ec}$ is the feedback fraction and $|C_e| = (1 - R_{12}) / (2\sqrt{R_{12}})$ is the laser coupling coefficient with the DFB laser effective grating reflectivity R_{12} and η is the coupling efficiency from the laser to the external cavity.

$$C = \sqrt{f_{ext}} \frac{2|C_e|\tau_{ec}}{\tau_L} \sqrt{1+\alpha^2} \quad (6.16)$$

The linewidth varies between its maximum $\Delta\nu_{max}$ (6.17) and its minimum $\Delta\nu_{min}$ (6.18).

$$\Delta\nu_{max} = \frac{\Delta\nu_0}{[1-C]^2} \quad (6.17)$$

$$\Delta\nu_{min} = \frac{\Delta\nu_0}{[1+C]^2} \quad (6.18)$$

The model is valid for weak optical feedback with $C < 1$. When changing from feedback regime I to regime II at $C = 1$, an infinite maximum linewidth is predicted in eq. (6.17), which is not plausible [68]. However, multiple laser modes are possible at $C > 1$, leading to considerable linewidth broadening when the single mode splits into multiple modes.

The laser linewidth is used as a measure of the phase noise in a Lorentzian shaped laser line. With optical feedback however, phase fluctuations at frequencies away from the laser line could appear. For optical communication systems, it is important to investigate the laser phase variations at frequencies in the range of the optical data signals at 1 GHz and higher. Thus, a dynamic model is generated which simulates the laser phase and intensity variations due to optical feedback in a broad frequency range.

6.2.4 Laser without Optical Feedback

As a reference for the following investigations, the laser is simulated without feedback. The summand for the optical feedback in eq. (6.3) is neglected, so that the equation system consists only of ordinary differential equations. After switching on the laser, oscillations are visible in the laser output power $P(t)$, the phase $\phi(t)$ and the carrier density $n(t)$, at the relaxation oscillation frequency f_r (Fig. 106).

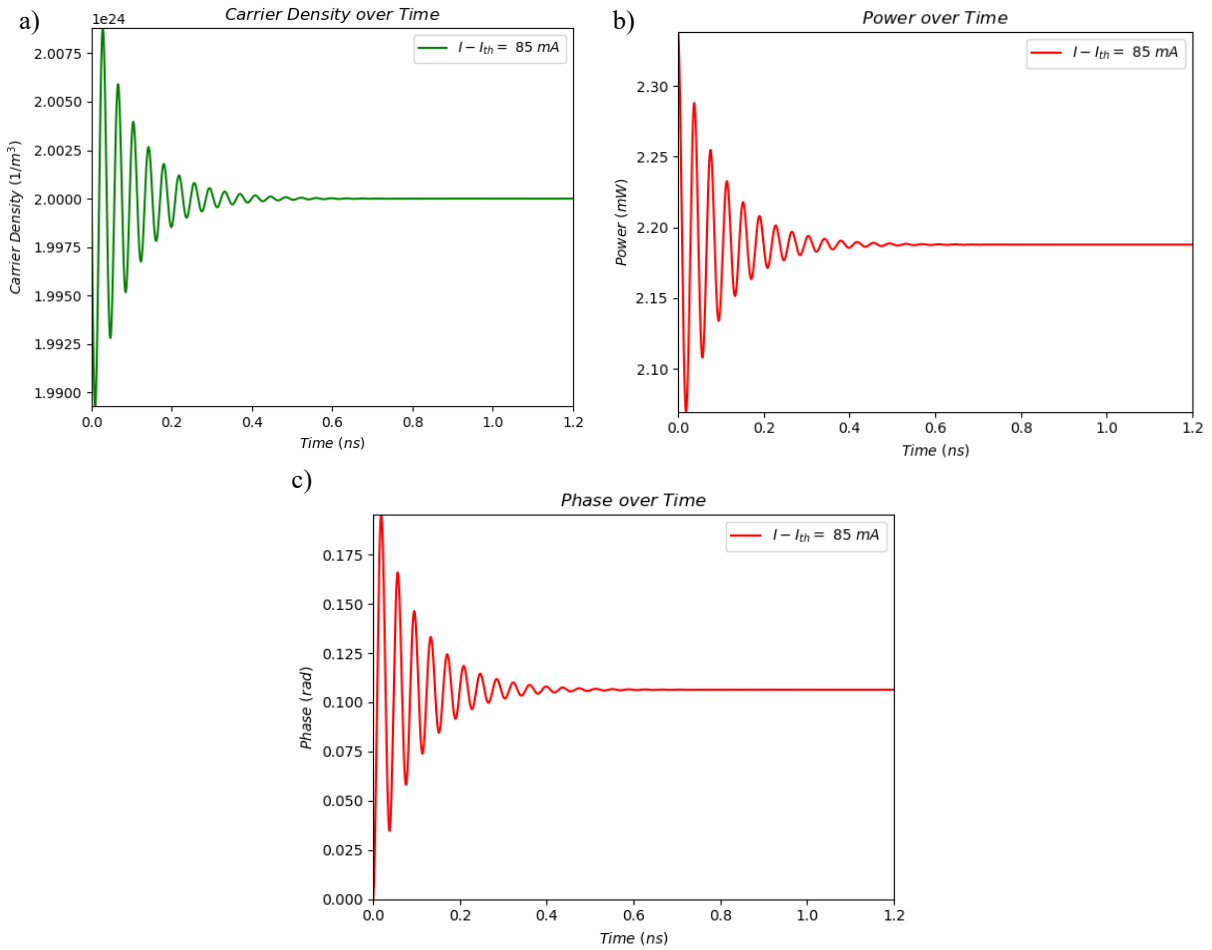


Fig. 106. a) Laser carrier density, b) output power and c) phase after switching on, with $I - I_{th}$: 85 mA.

The power and phase oscillations are shifted to the ones of the carrier density, since photons are emitted when electrical carriers recombine. The oscillations are damped over time, until the laser reaches a steady state. The laser output power is obtained at various bias currents up to $I - I_{th}$: 85 mA, after reaching the steady state. From the 4 mA threshold current I_{th} , the output power increases linearly with 0.03 mW/mA. The following investigations are done at 25 mA, 55 mA or 85 mA laser current above threshold. A summary of the time to reach steady state,

the output power at steady state and the relaxation oscillation frequency at the different laser bias currents is given in Table 4.

I-I _{th} (mA)	Time to reach steady state (ns)	P (mW)	f _r (GHz)
25	2.9	0.7	14
55	1.2	1.4	21
85	0.9	2.2	26

Table 9. Time to reach steady state, output power P at steady state and relaxation oscillation frequency f_r at different laser bias currents above threshold.

At increasing laser bias current, the time to reach steady state decreases, while the output power and the relaxation oscillation frequency increase. The simulated laser threshold, relaxation oscillation frequency and output power values, based on typical DFB laser parameters and the dimensions of the integrated DFB lasers in the optical transmitters, slightly differ from the experimental ones. This might be due to the altered structure of the integrated DFB lasers, which are 90 degrees rotated from the typical crystal orientation. To give a basic understanding of the laser behavior under optical feedback, the laser simulation is sufficient and will be further used.

To study the dynamic laser behavior, the laser pump current $I_{\text{pump}}(t)$ is small signal modulated around a constant bias current I with a sinusoidal signal at the frequency f_{mod} . The pump current variation $\Delta I_{\text{pump}} = I_{\text{pump,max}}/I_{\text{pump,min}}$ describes the maximum applied pump current divided by the minimum one. ΔI_{pump} is set, so that the resulting output power variation in decibel $10 \cdot \log(\Delta P_0) = 10 \cdot \log(P_{\text{max},0}/P_{\text{min},0})$ between the output power at the higher pump current $P_{\text{max},0}$ and the output power at the lower pump current $P_{\text{min},0}$ at zero frequency is 0.1 dB. The laser power frequency response is obtained by calculating the ratio of the laser power variation $\Delta P(f_{\text{mod}})$ at different frequencies to ΔP_0 ($\Delta P(f_{\text{mod}})/\Delta P_0$). The laser power frequency response is plotted in decibel ($10 \cdot \log(\Delta P(f_{\text{mod}})/\Delta P_0)$) in Fig. 107 at different laser bias currents.

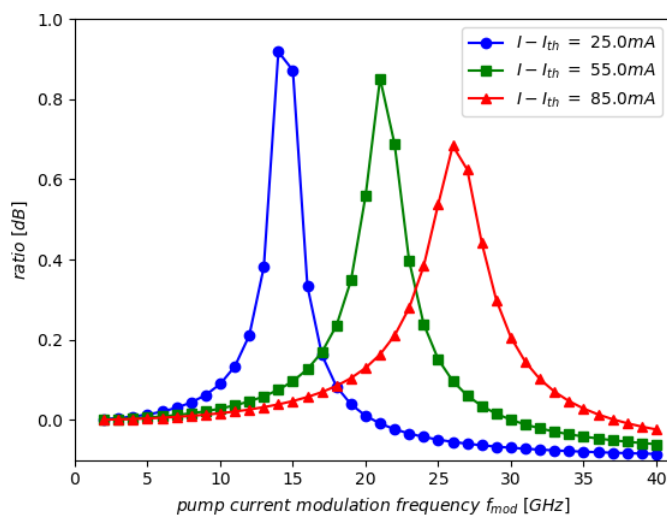


Fig. 107. Laser small signal power frequency response to pump current modulation at different laser bias currents.

A peak at the laser relaxation oscillation frequency is visible, which decreases at increasing bias current, while its width increases. At modulation frequencies larger than the relaxation oscillation frequency, the power frequency response becomes smaller, so that overall it has a low pass filter characteristic.

Modulating the pump current, also results in laser phase variations. The phase frequency response is obtained by plotting the peak-to-peak phase variation (max. phase divided by min. phase) depending on f_{mod} (Fig. 108).

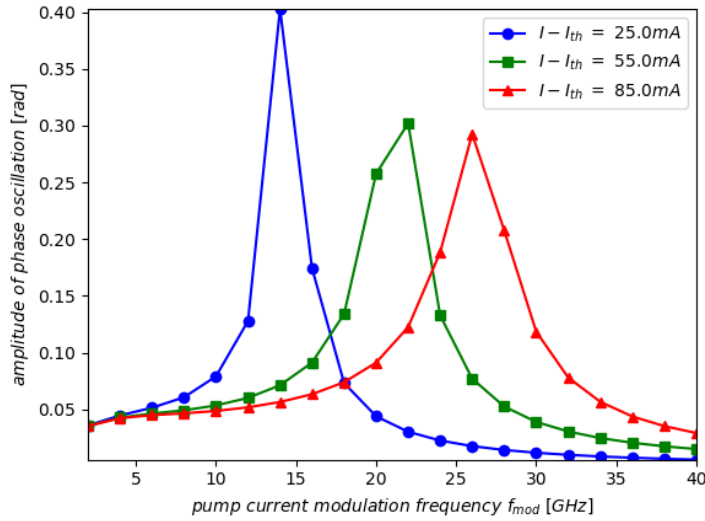


Fig. 108. Laser small signal phase frequency response to pump current modulation at different bias currents.

The phase frequency response shows a similar behavior as the power frequency response. A phase oscillation peak at the laser relaxation oscillation frequency, which is damped and broadened at increasing bias currents and a decline at larger frequencies is observed.

6.2.5 Laser with Passive Optical Feedback

After the laser is simulated without optical feedback, an external cavity with a weak reflectivity in regime I is added, with similar dimensions to the integrated Mach-Zehnder modulator in the optical transmitters ($R_{\text{ec}}: 5 \cdot 10^{-6}$, $L_{\text{ec}}: 7.5 \text{ mm}$, $C: 0.44$). The laser is simulated for one external cavity roundtrip time without optical feedback, to get the time-delayed complex electrical field amplitude $\mathcal{E}(t-\tau_{\text{ec}})$. The optical feedback sets in after one external cavity roundtrip time, during the oscillations, at 0.2 ns (Fig. 109).

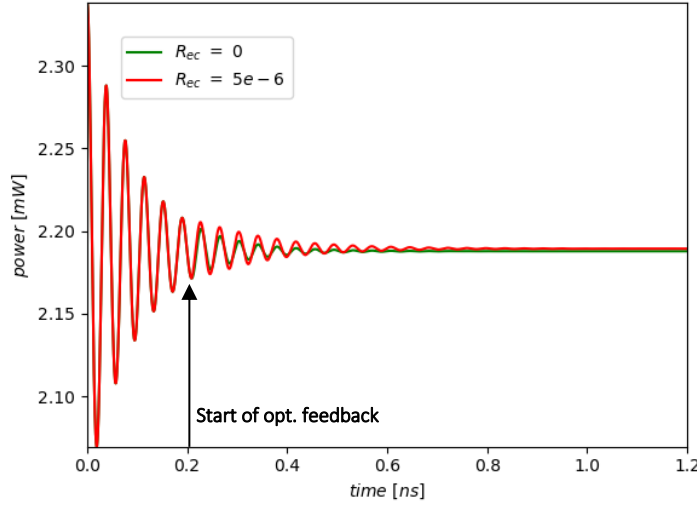


Fig. 109. Laser optical output power over time, with optical feedback ($R_{ec}: 5 \cdot 10^{-6}$) and without ($R_{ec}: 0$) after switching on at $I - I_{th}: 85$ mA.

After the feedback starts, the output power oscillation strength and duration is slightly enhanced. To make the feedback effects better visible, the feedback is once artificially started at 5 ns, when the laser already is in the steady state (Fig. 110).

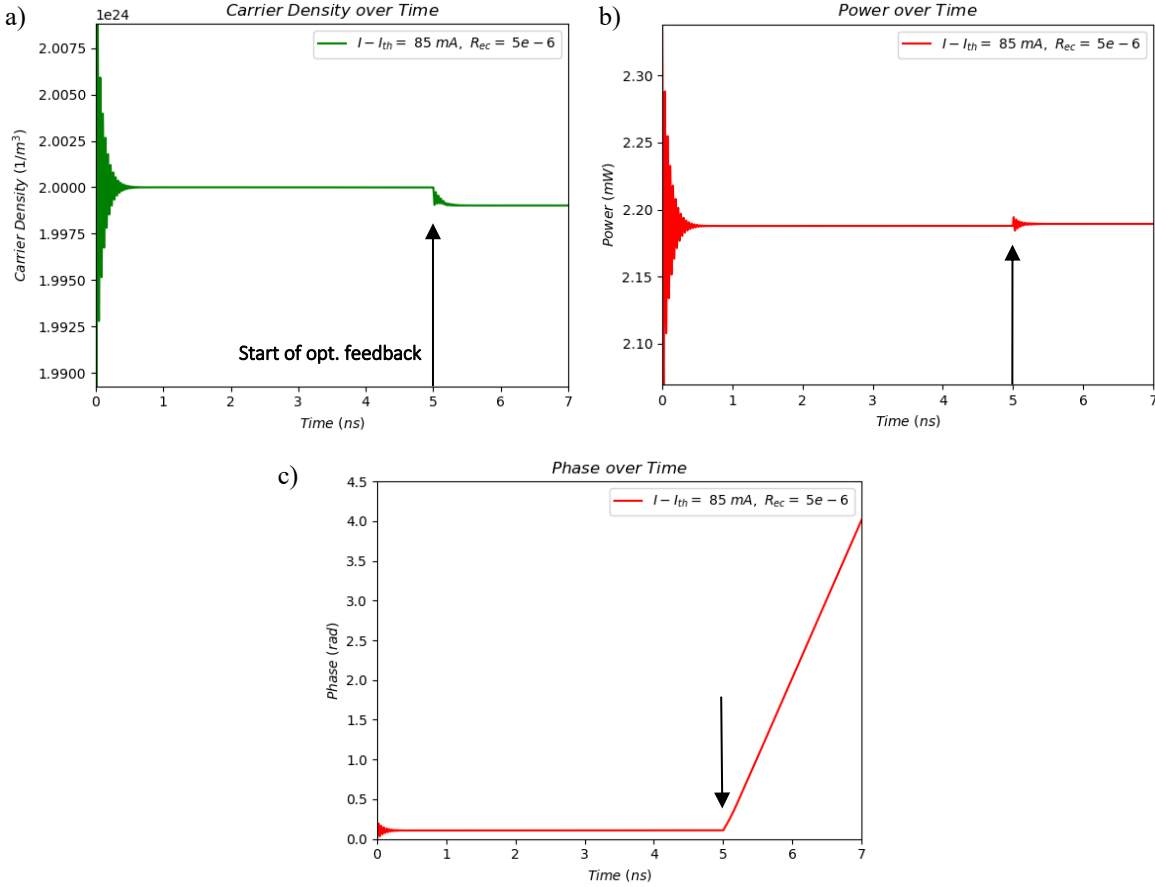


Fig. 110. a) Carrier density, b) output power and c) unwrapped phase with optical feedback, starting artificially at 5 ns ($R_{ec}: 5 \cdot 10^{-6}$, $I - I_{th}: 85$ mA).

After the feedback sets in, the laser starts oscillating, but with a much lower strength and duration than after switching on the laser. After the oscillations, the laser has a changed steady state with a slightly decreased carrier

density (Fig. 110a), increased output power (Fig. 110b) and a change of the phase slope, corresponding to a frequency shift (Fig. 110c). While the change in the laser output power due to optical feedback is very small, the laser frequency shift might influence the performance of the optical transmitters and is thus further investigated.

In the following simulations, the optical feedback sets in after one external cavity roundtrip time, at 0.2 ns. The laser phase over time with optical feedback is plotted in Fig. 111a, at different laser bias currents.

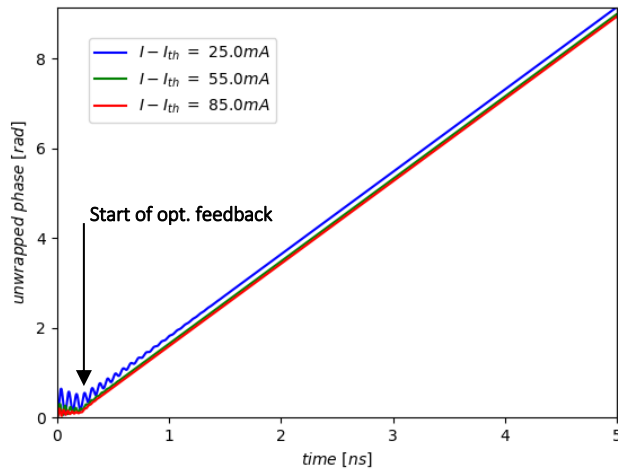


Fig. 111. Laser unwrapped phase over time at different laser bias currents ($R_{ec} = 5 \cdot 10^{-6}$).

At the different bias currents, the phase slope remains constant.

The phase difference $\Delta\phi_0 = \omega_0 \cdot \tau_{ec}$ between the laser electrical field without feedback and the reflected laser electrical field after one external cavity roundtrip time is 1.2 rad with the simulated external cavity. To investigate the influence of the optical feedback phase on the laser phase slope, an artificial phase shift $\Delta\phi_{art}$ is added to $\Delta\phi_0$. The total phase difference $\Delta\phi$, between the laser electrical field without feedback and the reflected electrical field is $\Delta\phi = \Delta\phi_0 + \Delta\phi_{art}$. A sinusoidal phase slope variation is observed, when varying $\Delta\phi$ between 0 rad and 2π rad (Fig. 112).

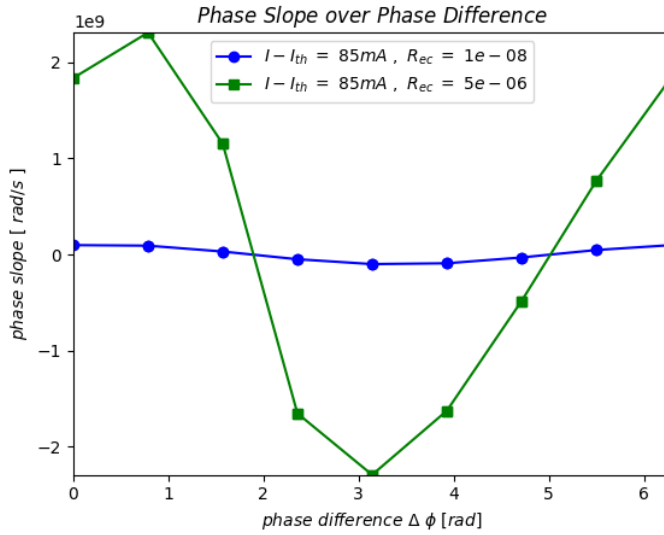


Fig. 112. Laser phase slope depending on phase difference $\Delta\phi$ between laser electrical field without optical feedback and reflected laser electrical field, at different R_{ec} ($I - I_{th}$: 85 mA).

The phase slope is the largest, when the laser and the reflected electrical fields are in-phase or have a π phase difference and is zero, when the phase difference is $\pi/2$ or $3\pi/2$. The phase slope is simulated for external cavities with weak (R_{ec} : $5 \cdot 10^{-6}$) and very weak (R_{ec} : $1 \cdot 10^{-8}$) reflectivity, showing that the phase slope variation becomes larger with increasing external cavity reflectivity.

The laser phase slope and the corresponding frequency shift, depending on the external cavity reflectivity are plotted in Fig. 113, for the 7.5 mm long external cavity ($\Delta\phi = \Delta\phi_0$), at $I - I_{th}$: 85 mA.

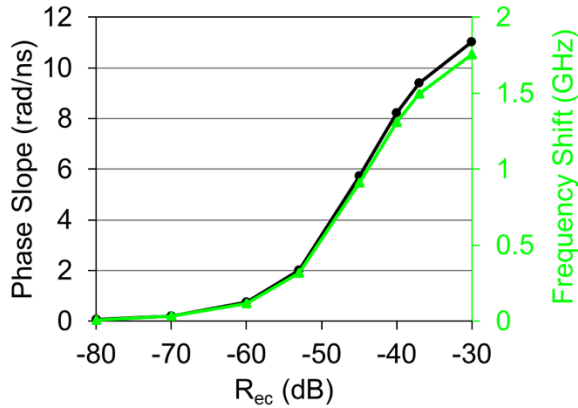


Fig. 113. Laser phase slope vs. external cavity reflectivity R_{ec} ($I - I_{th}$: 85 mA, L_{ec} : 7.5 mm, $\Delta\phi$: 1.2).

The linear phase slope and the frequency shift increase with the external cavity reflectivity (Fig. 115b). The frequency shift is up to 1.8 GHz, for R_{ec} up to $1 \cdot 10^{-3}$.

At an external cavity reflectivity larger than $1 \cdot 10^{-3}$, the laser power, carrier density and phase keep oscillating at the relaxation oscillation frequency, after the feedback sets in and do not reach a steady state. The laser output power at an external cavity reflectivity of R_{ec} : $2 \cdot 10^{-4}$, is given at $I - I_{th}$: 25 mA in Fig. 114a and at $I - I_{th}$: 85 mA in Fig. 114b.

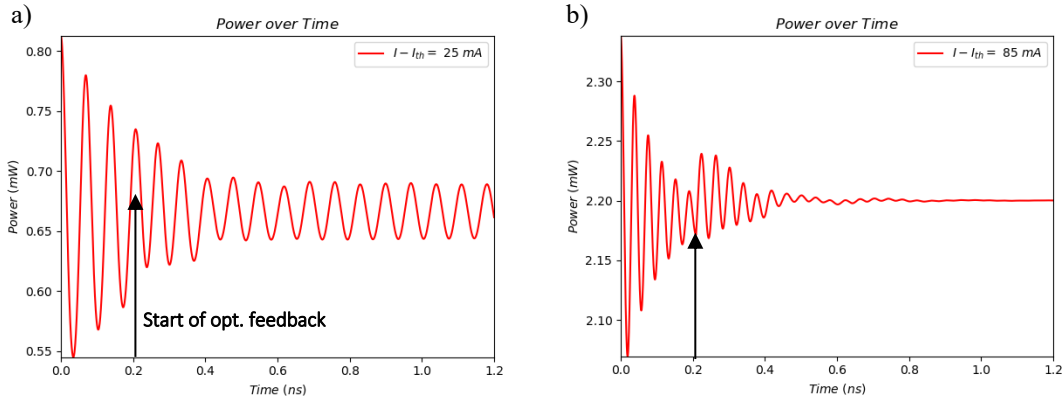


Fig. 114. Laser output power over time with optical feedback at a) $I - I_{th}$: 25 mA and b) $I - I_{th}$: 85 mA (R_{ec} : $2 \cdot 10^{-4}$, L_{ec} : 7.5 mm, $\Delta\phi$: 1.2).

The laser is more sensitive to optical feedback at low bias currents. At $I - I_{th}$: 25 mA and R_{ec} : $2 \cdot 10^{-4}$, the laser oscillates and does not operate at a single frequency, anymore, while at $I - I_{th}$: 85 mA, it reaches the steady state after about 1 ns. The laser phase over time at R_{ec} : $2 \cdot 10^{-4}$ and different bias currents is given in Fig. 115.

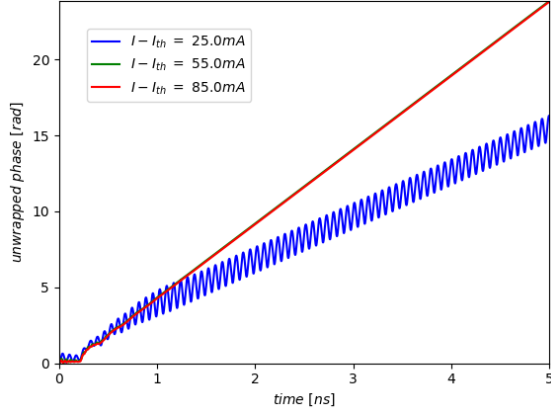


Fig. 115. Laser unwrapped phase with opt. feedback at R_{ec} : $2 \cdot 10^{-4}$ and different bias currents (L_{ec} : 7.5 mm, $\Delta\phi$: 1.2).
Also, the laser phase oscillates at $I - I_{th}$: 25 mA and R_{ec} : $2 \cdot 10^{-4}$, while at $I - I_{th}$: 55 mA and 85 mA, the phase is less sensitive to the optical feedback and remains linear.

When increasing R_{ec} to values larger than $1 \cdot 10^{-3}$, the feedback oscillations intensify, so that the laser enters the chaotic coherence collapse regime IV. At R_{ec} : $1 \cdot 10^{-2}$ and $I - I_{th}$: 85 mA, strong chaotic power oscillations are observed (Fig. 116a), which are visible as a broad noise in the optical spectrum (Fig. 116b).

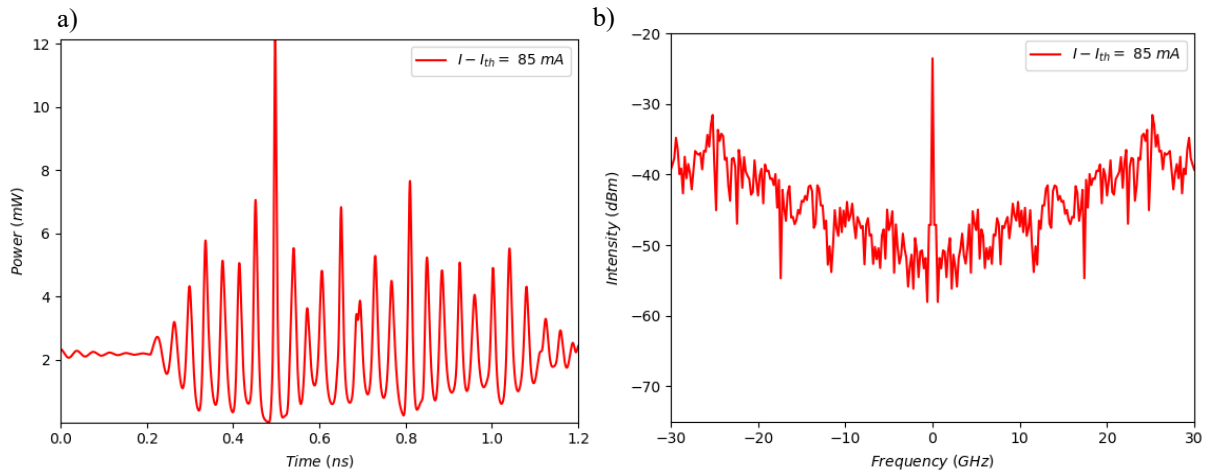


Fig. 116. Laser output power a) over time and b) frequency spectrum with optical feedback at $R_{ec}: 1 \cdot 10^{-2}$ ($I - I_{th}$: 85 mA, L_{ec} : 7.5 mm, $\Delta\phi$: 1.2).

The simulations show, that with weak optical feedback at an external cavity reflectivity R_{ec} of up to $1 \cdot 10^{-3}$, the laser remains single mode while its frequency is shifted by up to 1.8 GHz, depending on the laser bias current and the phase difference between the laser and the reflected electrical field. The transition from the weak feedback regime I to regime II, happens at R_{ec} values around $2 \cdot 10^{-4}$, where the laser feedback coefficient C is 2.5. In regime II, the laser might oscillate due to the optical feedback, especially at low bias currents, losing its single-mode behavior. Since single-mode operation is required for the optical transmitters, the optical feedback to the integrated lasers should be low enough in regime I, to avoid multi-mode behavior and the coherence collapse.

Comparing the simulations with experimental results of the fabricated DFB laser Mach-Zehnder/ IQ modulator optical transmitters, it is concluded, that the optical feedback inside the transmitters is in the weak feedback regime I, since the transmitters always show a stable single mode operation. The simulations show, that the measured transmitter wavelength variations in the gigahertz range in Fig. 64, depending on the modulator bias voltage are induced by optical feedback inside the transmitter. The modulator bias voltage induces a phase shift in the transmitted and reflected optical signals and thus changes the phase difference $\Delta\phi$ between the laser and the reflected signal. As in Fig. 112, the change in the phase difference $\Delta\phi$ leads to a change in the laser phase slope and consequently its frequency.

6.2.6 Laser with Dynamic Optical Feedback (Sine-Wave)

To study the laser behavior under dynamic optical feedback, the feedback term is modulated with a sine-wave at different frequencies. The modulator is chirp-free and has an infinite bandwidth, to concentrate on the laser dynamic behavior. The modulator dynamic power extinction ratio is set to 10 dB, like the one of the Mach-Zehnder modulators in the optical transmitters. The differential equation (6.3) of the laser complex electrical field amplitude is extended in eq. (6.19), with factors for the modulation amplitude A_{mod} and the sine wave modulation at the modulation frequency f_{mod} with an offset B_{mod} .

$$\dot{\mathcal{E}}(t) = (1-i\alpha)\Gamma G_{n_{th}}(n-n_{th})\mathcal{E}(t) + [A_{mod}\sin(2\pi f_{mod}t) + B_{mod}] \frac{K_{ec}}{\tau_L} e^{i\omega_0\tau_{ec}} \mathcal{E}(t-\tau_{ec}) \quad (6.19)$$

The modulator is operated at the 3 dB working point and has a 10 dB dc extinction ratio, which is simulated by setting A_{mod} and B_{mod} so that $|A_{mod}\sin(2\pi f_{mod}t) + B_{mod}|^2$ varies between 1 and 0.1. The resulting laser power and

phase over time, while the optical feedback is modulated with a 10 GHz sine-wave, are plotted in Fig. 117.a and Fig. 117.b, respectively ($R_{ec}: 5 \cdot 10^{-6}$, $I - I_{th}: 85 \text{ mA}$).

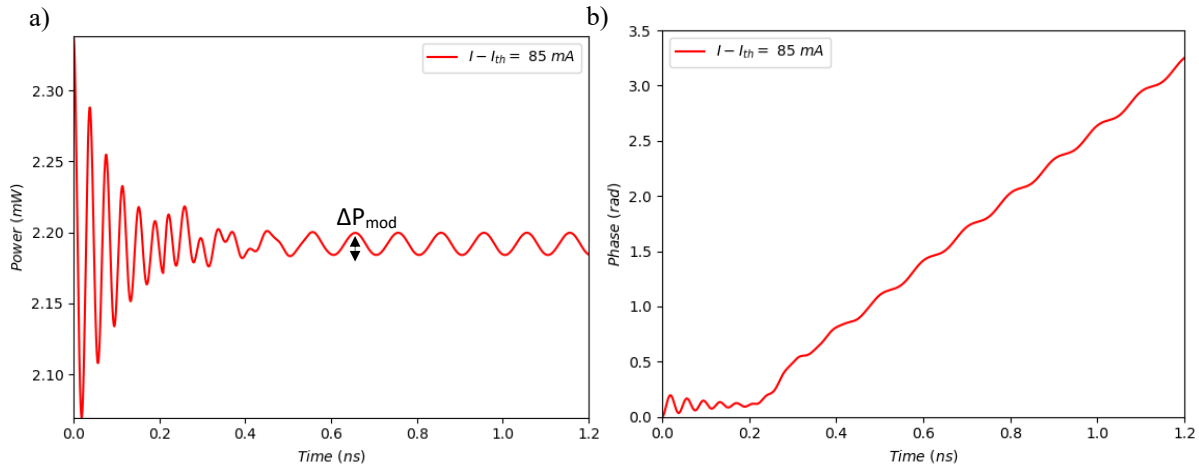


Fig. 117. Laser a) power and b) phase over time with modulated optical feedback at $f_{mod}: 10 \text{ GHz}$ ($R_{ec}: 5 \cdot 10^{-6}$, $I - I_{th}: 85 \text{ mA}$, $\Delta\phi: 0$).

To see the maximum optical feedback effect, the laser electrical field without feedback and the reflected electrical field are set to be in-phase ($\Delta\phi=0$) when the optical feedback is unmodulated. The feedback modulation at 10 GHz is transferred to both the laser power and phase. Oscillations at f_{mod} are visible on the laser power and phase after the laser reaches the steady state. Side modes in the optical spectrum appear with a mode spacing of f_{mod} from the lasing mode (Fig. 118).

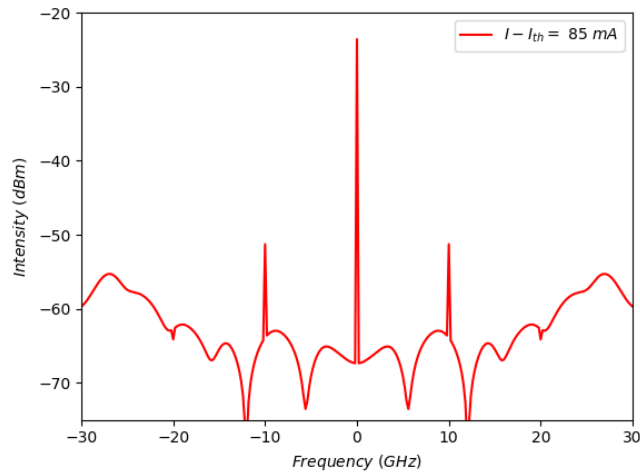


Fig. 118. Laser output power spectrum with sine-wave modulated optical feedback at $f_{mod}: 10 \text{ GHz}$ ($R_{ec}: 5 \cdot 10^{-6}$, $I - I_{th}: 85 \text{ mA}$, $\Delta\phi: 0$).

The coherence collapse is declared when the laser power over time changes from harmonic oscillations to a chaotic noisy signal. The simulations reveal that the laser enters the coherence collapse at R_{ec} values larger than $1 \cdot 10^{-4}$, at 10 GHz feedback modulation frequency ($I - I_{th}: 85 \text{ mA}$). With passive optical feedback, the coherence collapse happens at $R_{ec}: 1 \cdot 10^{-2}$, showing that the laser is more sensitive to modulated than to passive optical feedback.

The strongest power and phase oscillations are observed, when f_{mod} is equal to the laser relaxation oscillation frequency f_r . The laser power modulation response to the optical feedback modulation is obtained, by calculating the ratio of the laser peak-to-peak output power modulation, to the optical feedback peak-to-peak power

modulation $\Delta P_{\text{mod}}(f_{\text{mod}})/|A_{\text{mod}}|^2(f_{\text{mod}})$. The output power frequency response, depending on the optical feedback modulation frequency f_{mod} is obtained at different laser bias currents (Fig. 121).

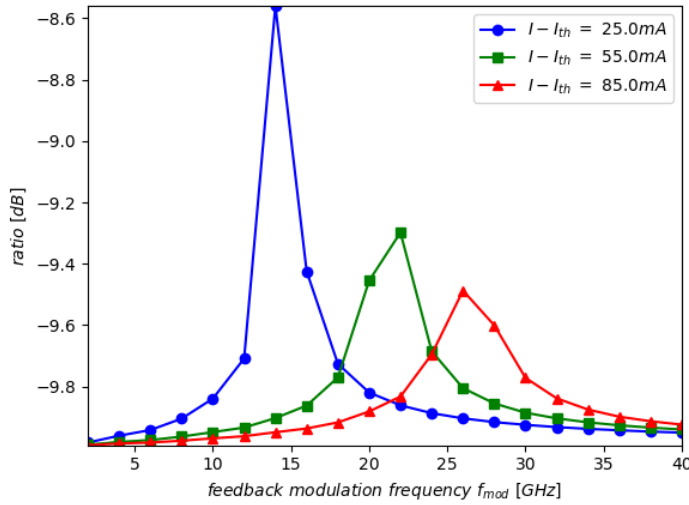


Fig. 119. Laser power frequency response to optical feedback modulation $\Delta P_{\text{mod}}(f_{\text{mod}})/|A_{\text{mod}}|^2(f_{\text{mod}})$, at different laser bias currents ($\Delta\phi: 0$, $R_{\text{ec}}: 5 \cdot 10^{-6}$).

A resonance is visible at the laser relaxation oscillation frequency, which declines and broadens at increasing laser bias currents. The laser power frequency response to the optical feedback modulation has a similar shape as the response to the pump current modulation in Fig. 107.

When increasing the feedback intensity from $R_{\text{ec}}: 1 \cdot 10^{-8}$ to $R_{\text{ec}}: 5 \cdot 10^{-6}$, the resonance in the laser power frequency response enhances (Fig. 120).

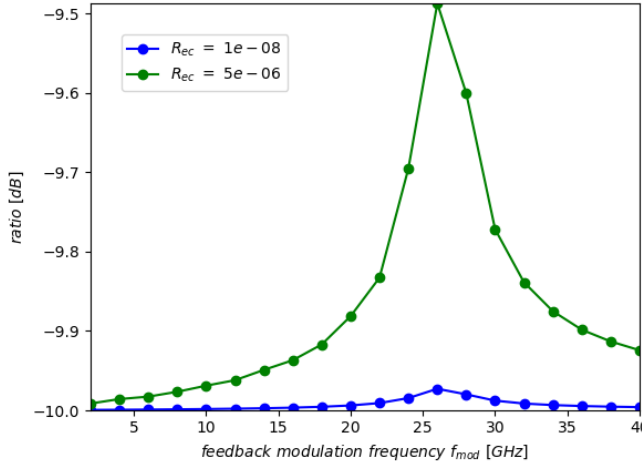


Fig. 120. Laser power frequency response to feedback power modulation at different R_{ec} ($I - I_{\text{th}}: 85$ mA, $\Delta\phi: 0$).

The resonance enhancement varies slightly with the phase difference $\Delta\phi$, as shown in Fig. 121 ($R_{\text{ec}}: 5 \cdot 10^{-6}$).

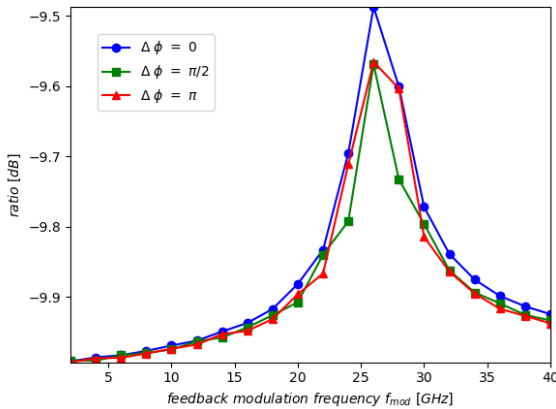


Fig. 121. Laser power frequency response to feedback power modulation at different $\Delta\phi$, at $R_{\text{cc}}: 5 \cdot 10^{-6}$ ($I - I_{\text{th}}$: 85 mA). Overall, the output power fluctuations are small, compared to the optical feedback modulation amplitude and are thus not critical.

The laser peak-to-peak oscillation due to the modulated optical feedback is displayed in a phase frequency response, at different laser bias currents in Fig. 123.

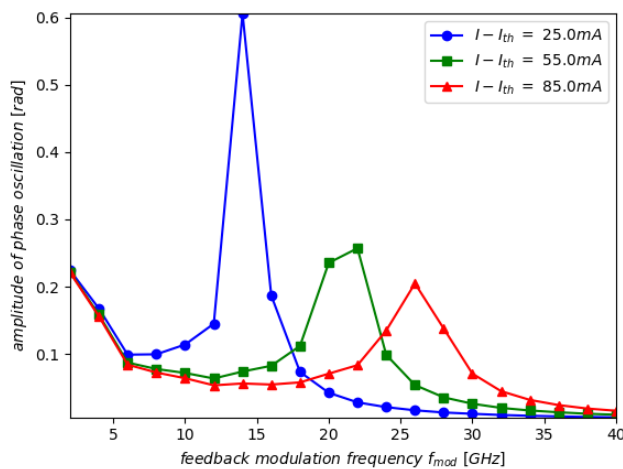


Fig. 122. Transmitter peak-to-peak-phase oscillation vs. opt. feedback modulation frequency at different laser bias currents ($\Delta\phi$: 0, R_{cc} : $5 \cdot 10^{-6}$).

The self-phase modulation is increased to up to 0.25 rad (7.2 degrees) at frequencies lower than 5 GHz and has a resonance at the laser relaxation oscillation frequency. The resonance declines and broadens at increasing bias currents. When increasing the feedback modulation frequency f_{mod} beyond the laser relaxation oscillation frequency f_r , the phase oscillations become weaker until they disappear at frequencies larger than 20 GHz above f_r . Overall, the phase frequency modulation response has a low-pass filter shape with a resonance at f_r . The transmitter phase frequency responses to the modulated optical feedback at different phase differences $\Delta\phi$ between the laser and the reflected electrical field are shown at $R_{\text{cc}}: 1 \cdot 10^{-8}$ in Fig. 123a and at $R_{\text{cc}}: 5 \cdot 10^{-6}$ in Fig. 123b.

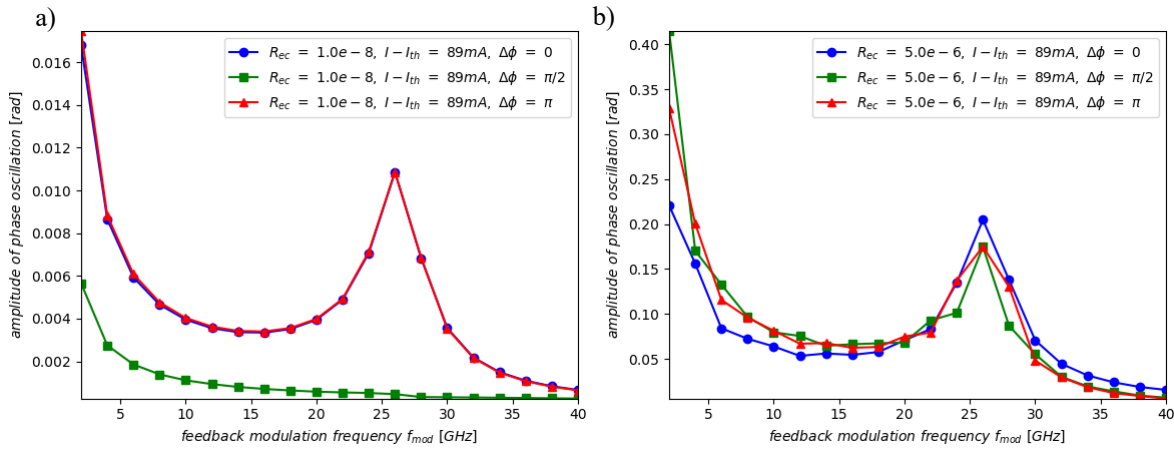


Fig. 123. Transmitter peak-to-peak-phase oscillation vs. opt. feedback modulation frequency at different $\Delta\phi$,
a) $R_{ec}: 1 \cdot 10^{-8}$, b) $R_{ec}: 5 \cdot 10^{-6}$ ($I - I_{th}$: 85 mA).

At increasing R_{ec} , the transmitter self-phase modulation due to the modulated optical feedback becomes stronger. While at $R_{ec}: 1 \cdot 10^{-8}$, the phase varies by up to 0.018 rad (1 degree), it varies by up to 0.42 rad (20 degrees) at $R_{ec}: 5 \cdot 10^{-6}$. The self-phase modulation at frequencies lower than 5 GHz, depends strongly on the phase difference $\Delta\phi$. Compared to the laser power oscillations due to the modulated optical feedback, the laser phase oscillations are much more serious.

In optical transmitters with an integrated laser and an external cavity reflectivity of $R_{ec}: 5 \cdot 10^{-6}$ and higher, the transmitter self-phase modulation due to modulated optical feedback could severely impact on the performance of optical data signals with phase sensitive modulation formats. When the bandwidth of the optical data signal is in the range of the laser relaxation oscillation frequency or lower, the impact of the self-phase modulation is the most severe. At modulation frequencies lower than 5 GHz, the phase modulation due to optical feedback is strongly increased, depending on the phase difference $\Delta\phi$, between the laser and the reflected electrical field. However, at modulation frequencies larger than the laser relaxation oscillation frequency, the transmitter self-phase modulation diminishes, so that optical data signals with bandwidths larger than the laser relaxation oscillation frequency, should be less impaired.

In the fabricated DFB laser Mach-Zehnder/ IQ modulator transmitter measurements, enhanced resonances at the laser relaxation oscillation frequency have been observed in several measurements. The laser relative intensity noise in chapter 5.1.2, is enhanced at the relaxation oscillation frequency, compared to the relative intensity noise of reference DFB lasers. In the optical transmitter electro-optic power response measurements, a resonance at the relaxation oscillation frequency is observed in chapter 5.1.3, which is not present for Mach-Zehnder modulator transmitters without integrated laser. In chapter 4.5.5, Fig. 61, a resonance is also observed in the electro-optical crosstalk between the two Mach-Zehnder modulators inside a DFB laser IQ modulator transmitter, which does not appear in the crosstalk of IQ modulator transmitters without integrated laser. The simulations of a laser with an external cavity in this chapter show, that the resonance at the laser relaxation oscillation frequency is induced due to the modulated optical feedback exciting the laser, especially at its relaxation oscillation frequency. The resonances in the transmitter relative intensity noise and electro-optic response measurements, depend on the modulator bias voltage. The reason is that the modulator bias voltage changes the phase difference $\Delta\phi$ between

the laser and the reflected signal, which influences the laser resonance to the optical feedback, according to the simulations in Fig. 121.

The large signal measurements of a DFB laser Mach-Zehnder modulator transmitter in binary phase shift keying operation in chapter 5.1.5.2 and a DFB laser IQ modulator transmitter in quaternary phase shift keying operation in chapter 5.2.3, show increased phase oscillations on the modulated signals, compared to transmitters without integrated laser. The phase oscillations increase especially at modulation rates, lower than the laser relaxation oscillation frequency. The simulations of the phase frequency response to sinusoidal optical feedback in Fig. 122 and Fig. 123 show increased transmitter self-phase modulation at frequencies lower than the laser relaxation oscillation frequency. This indicates that the measured phase oscillations on the modulated signals are induced by the laser response to modulated optical feedback. For a clearer comparison with the measurement results, the effects of optical feedback on data signals, where the optical feedback is modulated by the data signal, is simulated and further discussed in chapter 7.

7. Optical Feedback within DFB Laser Mach-Zehnder/ IQ Modulator Transmitter PICs

The laser in optical transmitters generates intrinsic intensity and phase noise due to spontaneous emission processes, so that maximum relative intensity noise (RIN) levels of -130 dB/Hz and maximum laser linewidth up to hundreds of kilohertz or a few megahertz are typically required for lasers used in optical communication systems. In the simulations of an optical transmitter with a laser and an external cavity in chapter 6, it has been shown that the integrated laser intensity and phase variations are further increased, by modulated optical feedback.

Phase and intensity variations in optical communication systems lead to inter-symbol interference and errors, especially in higher-order modulation formats. Schematic quaternary phase shift keying (QPSK) constellation diagrams with typical constellation points and with increased phase variations are shown in Fig. 124a and Fig. 124b, respectively.

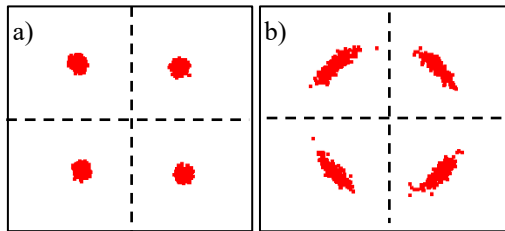


Fig. 124. Schematic QPSK constellation diagrams a) typical and b) with increased phase variations. Dashed lines indicate decision regions for constellation points.

Due to the increased phase variations, the QPSK constellation points broaden, increasing the error probability. Errors are generated when a symbol is out of its decision region, marked by the dashed lines in the constellation diagrams in Fig. 124. While intensity variations are problematic for intensity modulated non-return-to-zero on-off keying (NRZ) or pulse amplitude modulated (PAM) signals, phase noise is especially critical for phase sensitive modulation formats, like QPSK. Quadrature amplitude modulation (QAM) formats are the most sensitive to both intensity and phase variations.

It is important to study the influence of optical feedback on the integrated laser linewidth and the modulation performance of the fabricated DFB-Mach-Zehnder modulator transmitter photonic integrated circuits (PICs), since the laser and the modulator are not isolated. In this chapter, the sources of optical feedback in the transmitter PICs are figured out and a simple model is created to observe the optical feedback effects on the integrated DFB laser linewidth. Then, the Lang-Kobayashi model of a laser with an external cavity from chapter 6 is extended to include the effects if modulated optical feedback on the integrated laser in the optical transmitters. The simulations are discussed and compared with the DFB laser Mach-Zehnder modulator transmitter experimental results.

7.1 Sources of Optical Feedback within the DFB laser Mach-Zehnder/ IQ Modulator Transmitters

Inside the DFB laser Mach-Zehnder/ IQ modulator transmitters, different reflective interfaces generate optical feedback to the laser.

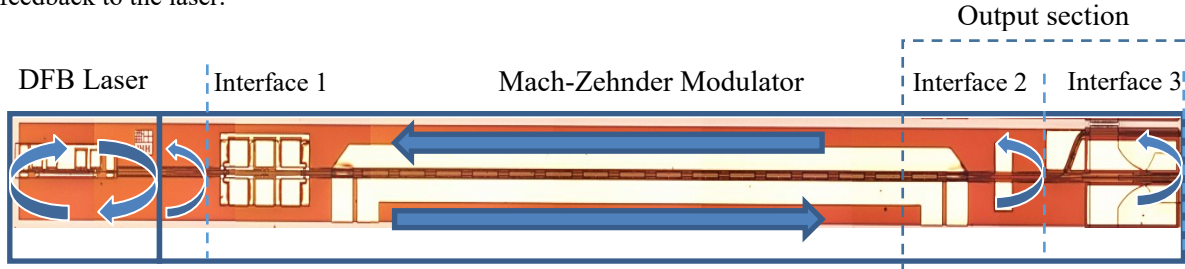


Fig. 125. Light is reflected back to laser at various interfaces inside the DFB laser Mach-Zehnder modulator transmitter.

When looking at the DFB laser Mach-Zehnder modulator output section (marked with a dashed line in Fig. 125) from the top with an infrared camera, scattered light is visible at the multi-mode interference (MMI) coupler outputs, the spot-size converter (SSC) butt-joint and the output facet (Fig. 126).

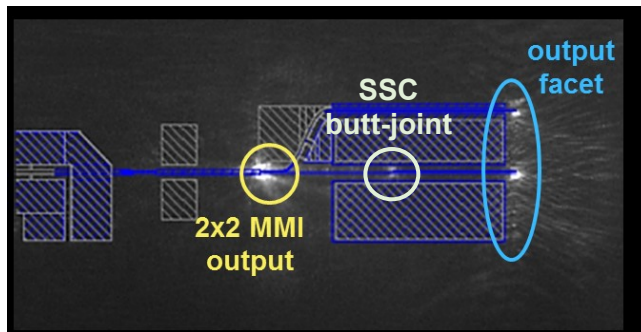


Fig. 126. Top view infrared picture of a DFB Mach-Zehnder modulator transmitter output section with scattered light at the 2x2 MMI output, the SSC butt-joint and the output facet.

The light is scattered at similar points in the DFB laser IQ modulator transmitter output section top view infrared picture (Fig. 127.).

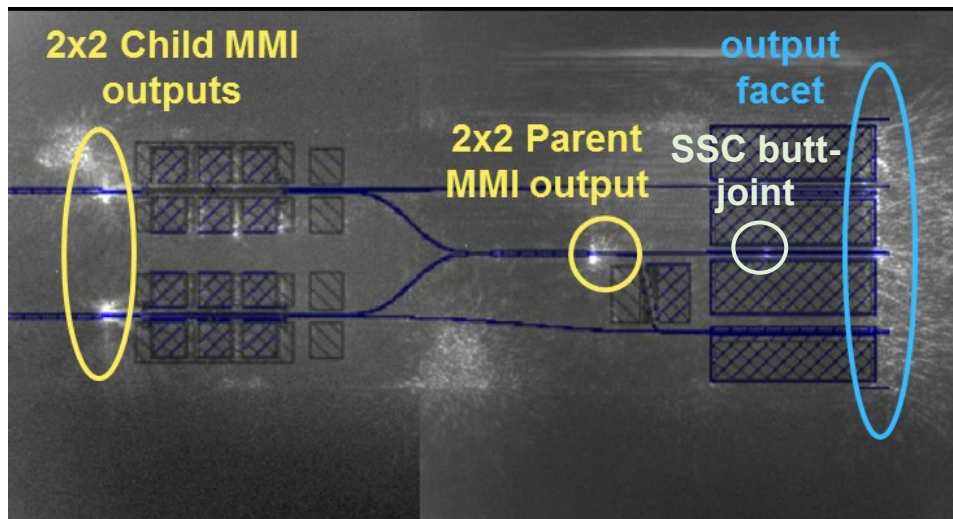


Fig. 127. Top view infrared picture of a DFB laser IQ modulator transmitter output section with scattered light at the 2x2 MMIs, the SSC butt-joint and the output facet.

To get further details about the positions of the reflective interfaces, the DFB laser Mach-Zehnder modulator transmitter optical subassembly module output is connected to an optical frequency domain reflectometer (OFDR),

which gives information about the position of reflection points. The optical frequency domain reflectometer sends white light at different frequencies into the transmitter module output fiber. The complex amplitude of the back-scattered light is measured, depending on the frequency, and Fourier transformed [81]. The reflection amplitude vs. distance graph is calculated with the OFDR software, depending on the Mach-Zehnder modulator group reflective index (Fig. 128).

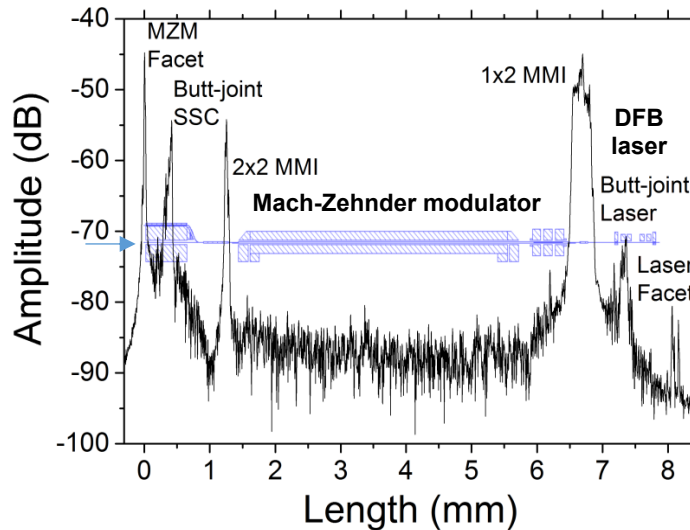


Fig. 128. Optical frequency domain reflectometer reflection amplitude vs. distance measurement of reflections within the DFB Mach-Zehnder modulator transmitter module. A schematic of a DFB laser Mach-Zehnder modulator transmitter is overlaid over the graph.

For easier assignment of the reflective interfaces, the schematic of a DFB laser Mach-Zehnder modulator transmitter is overlaid over the graph. The main reflective peaks overlap with the locations of the output facet, the multi-mode interference couplers, the spot-size converter-modulator and the laser-modulator butt-joints (Fig. 129).

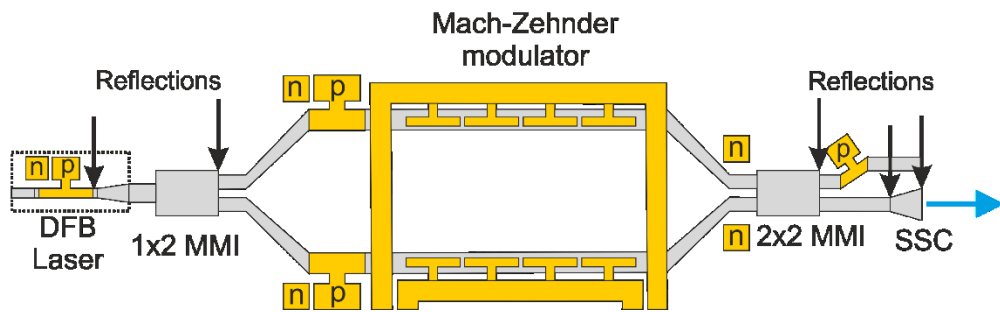


Fig. 129. Main reflective interfaces inside the DFB laser Mach-Zehnder modulator transmitter, marked with black arrows.

The OFDR measurement is not calibrated to include the fiber-to-chip coupling loss and passive losses within the DFB laser Mach-Zehnder modulator transmitter, so that it does not give the absolute reflectivity. At the spot-size converter-modulator butt-joint, the reflectivity is calculated to -36 dB, using equation (6.1). From the OFDR measurement in Fig. 128, a similar reflectivity is assumed for the 2x2 multi-mode interference coupler (MMI). The strong reflection peak at the asymmetric 1x2 multi-mode interference coupler is measured in the transmitter backward direction. In forward direction, for the 1x2 MMI a similar reflectivity as for the 2x2 MMI is assumed. The anti-reflection coated output facet reflectivity is expected to be -40 dB from empirical values.

In chapter 6, the external cavity is assumed to be lossless. However, in the optical transmitters, the optical feedback experiences attenuation, due to passive losses. For better comparison with the lossless external cavity, the Mach-Zehnder modulator passive insertion loss IL during one roundtrip time is incorporated into the effective reflectivity $R_{ec,eff}$ (eq. (7.1)).

$$R_{ec,eff} = R_{ec} \cdot IL^2 \quad (7.1)$$

A summary of the parameters of the different external cavities inside the DFB laser Mach-Zehnder modulator transmitter is given in Table 10, including the Mach-Zehnder modulator insertion loss IL and the external cavity length L_{ec} , reflectivity R_{ec} , resonance frequency $f_{r,ec}$, effective reflectivity $R_{ec,eff}$ and feedback coefficient C.

Interface	R_{ec} (dB)	IL (dB)	$R_{ec,eff}$ (dB)	$R_{ec,eff}$	L_{ec} (mm)	$f_{r,ec}$ (Ghz)	C
Output (MZM) facet	-40	4.7	-49.4	$1.1 \cdot 10^{-5}$	7.5	5.3	0.14
Butt-joint SSC	-36	3.2	-42.4	$5.8 \cdot 10^{-5}$	7.1	5.6	0.31
2x2 MMI	-36	3.1	-42.2	$6.1 \cdot 10^{-5}$	6.5	6.1	0.29
1x2 MMI	-36	0.4	-36.4	$2.3 \cdot 10^{-4}$	0.7	54.8	0.06

Table 10. DFB laser Mach-Zehnder modulator transmitter external cavity parameter summary.

The feedback coefficients are calculated from $R_{ec,eff}$ and L_{ec} , using equation (6.16), together with simulation parameters of Table 8 and Table 12. The resonance frequency $f_{r,ec}$ is calculated using equation (6.2). Effective reflectivity $R_{ec,eff}$ values between $1 \cdot 10^{-5}$ and $2 \cdot 10^{-4}$ are estimated for external cavities inside the DFB laser Mach-Zehnder modulator transmitter, where the 1x2 MMI has the strongest and the output facet the weakest effective reflectivity. The external cavities and their properties are also summarized for the DFB laser IQ modulator transmitter in Table 11.

Interface	R_{ec} (dB)	IL (dB)	$R_{ec,eff}$ (dB)	$R_{ec,eff}$	L_{ec} (mm)	$f_{r,ec}$ (Ghz)	C
Output (MZM) facet	-40	6.0	-52.0	$6.3 \cdot 10^{-6}$	10.5	3.8	0.15
SSC butt-joint	-36	4.5	-45.0	$3.2 \cdot 10^{-5}$	10.05	3.9	0.32
2x2 child MMI	-36	3.6	-43.2	$4.8 \cdot 10^{-5}$	7.5	5.3	0.3
2x2 parent MMI	-36	4.4	-44.8	$3.3 \cdot 10^{-5}$	9.5	4.2	0.31
1x2 child MMI	-36	0.8	-37.6	$1.7 \cdot 10^{-4}$	1.2	32.9	0.09
1x2 parent MMI	-36	0.4	-36.8	$2.1 \cdot 10^{-4}$	0.38	103.9	0.03

Table 11. DFB laser IQ modulator transmitter external cavity parameter summary.

The DFB laser IQ modulator transmitter has more reflective interfaces than the DFB laser Mach-Zehnder modulator transmitter with a slightly lower effective reflectivity, due to its larger structure and higher insertion loss.

The DFB laser Mach-Zehnder/ IQ modulator transmitters have multiple reflective interfaces inside, which cause weak optical feedback to the integrated laser. Nevertheless, the transmitters show stable single mode operation in the weak feedback regime I, since the feedback coefficients C for all the reflective interfaces are below one.

7.1.1 Laser Linewidth of DFB Laser Mach-Zehnder Modulator Transmitter with Optical Feedback

To estimate the optical feedback effects of the different external cavities inside the DFB laser Mach-Zehnder modulator transmitter on the integrated laser linewidth, equation (6.15) is used. Since the Mach-Zehnder modulator (MZM) influences the light's intensity and phase depending on the applied modulator bias voltage V_{MZM} , equation (6.15) is extended with the Mach-Zehnder modulator absorption $\text{abs}_{MZM}(V_{MZM})$ and phase $\phi_{MZM}(V_{MZM})$, which are obtained from the Mach-Zehnder modulator simulation in chapter 4.5.4. During one roundtrip time, the overall Mach-Zehnder modulator absorption is $\text{abs}_{MZM}^2(V_{MZM})$ and the phase shift is $2\phi_{MZM}(V_{MZM})$. The resulting equation for the DFB laser Mach-Zehnder modulator transmitter linewidth Δv_{MZM} under optical feedback is given in (7.2), where α is the linewidth enhancement factor, Δv_0 the laser linewidth without optical feedback and $\phi_{ec} = \omega_0 \tau_{ec}$ the external feedback phase with the angular optical frequency without feedback ω_0 and the external cavity roundtrip time $\tau_{ec} = 2L_{ec}n_{gr,ec}/c$.

$$\Delta v_{MZM} = \frac{\Delta v_0}{[1 + C_{MZM}(V_{MZM}) \cdot \cos(\phi_{ec} + 2\phi_{MZM}(V_{MZM}) + \arctan(\alpha))]^2} \quad (7.2)$$

The laser angular frequency $\omega_0 = 2\pi c/\lambda$ and linewidth Δv_0 without optical feedback are obtained from reference DFB laser measurements of the wavelength λ (Fig. 40) and the linewidth (Fig. 48), respectively. The laser linewidth without optical feedback is between 2.9 MHz and 2 MHz, depending on the laser bias current. The feedback coefficient C of a lossless external cavity is extended with the modulator absorption, giving the Mach-Zehnder modulator feedback coefficient $C_{MZM}(V_{MZM}) = \text{abs}_{MZM}^2(V_{MZM}) \cdot C$. The linewidth model is valid for weak feedback intensities in regime I, where $C_{MZM} < 1$, which is the case for all external cavities in the DFB laser Mach-Zehnder/ IQ modulator transmitters. C is calculated with equation (6.16), using the effective external cavity reflectivity and length of the respective external cavity inside the DFB laser Mach-Zehnder modulator transmitter from Table 10. The linewidth enhancement factor and the simulation parameters to calculate C are obtained from Table 8. Some specific parameters for the fabricated optical transmitters are listed in Table 12.

Name	Symbol	Value
Coupling efficiency from laser to modulator	η	0.98
DFB laser effective facet reflectivity	R_{12}	0.59
External cavity group refractive index	$n_{gr,ec}$	3.48

Table 12. Simulation parameters

The coupling efficiency from the laser to the Mach-Zehnder modulator is estimated by considering the 0.1 dB insertion loss of the waveguide transition element between the laser and the modulator. The DFB grating reflectivity is simplified as an effective facet reflectivity R_{12} , including the laser cavity losses, using the equations (2.3) and (2.4).

After inserting all the simulation parameters into equation (7.2), linewidth mappings at different laser bias currents above threshold $I - I_{\text{th}}$ and modulator bias voltages V_{MZM} are generated for different external cavities inside the transmitter and compared with the measured DFB laser Mach-Zehnder modulator transmitter linewidths in Fig. 69. The transmitter linewidth mapping at different transmitter operation points in terms of laser bias current and modulator bias voltage, with reflections from the 1x2 MMI, is displayed in Fig. 130.

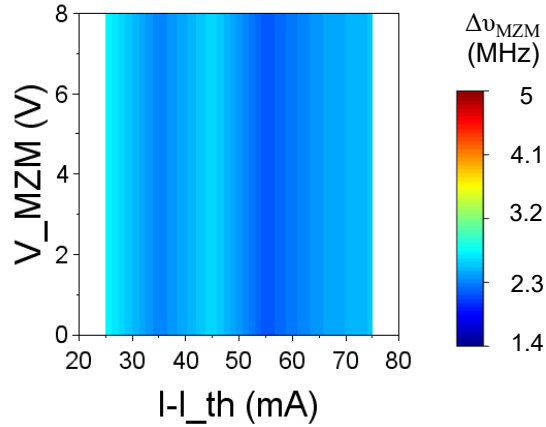


Fig. 130. Simulated transmitter linewidth with opt. feedback from the 1x2 MMI at different laser bias currents above threshold $I - I_{\text{th}}$ and modulator bias voltages V_{MZM} .

Since the reflection at the 1x2 MMI happens before the light travels through the Mach-Zehnder modulator, the linewidth in Fig. 130 is independent of the modulator bias voltage. With reflections from the 1x2 MMI, the linewidth varies periodically with increasing laser bias current around the reference DFB laser linewidth without optical feedback, which is about 2.3 MHz. After the light is modulated in the Mach-Zehnder modulator, it is reflected at the 2x2 MMI, the modulator spot-size converter butt-joint and the output facet. The corresponding linewidth mappings at different transmitter operation points with optical feedback from the 2x2 MMI, the modulator spot-size converter butt-joint (SSC-BJ) and the output facet are given in Fig. 131a-c.

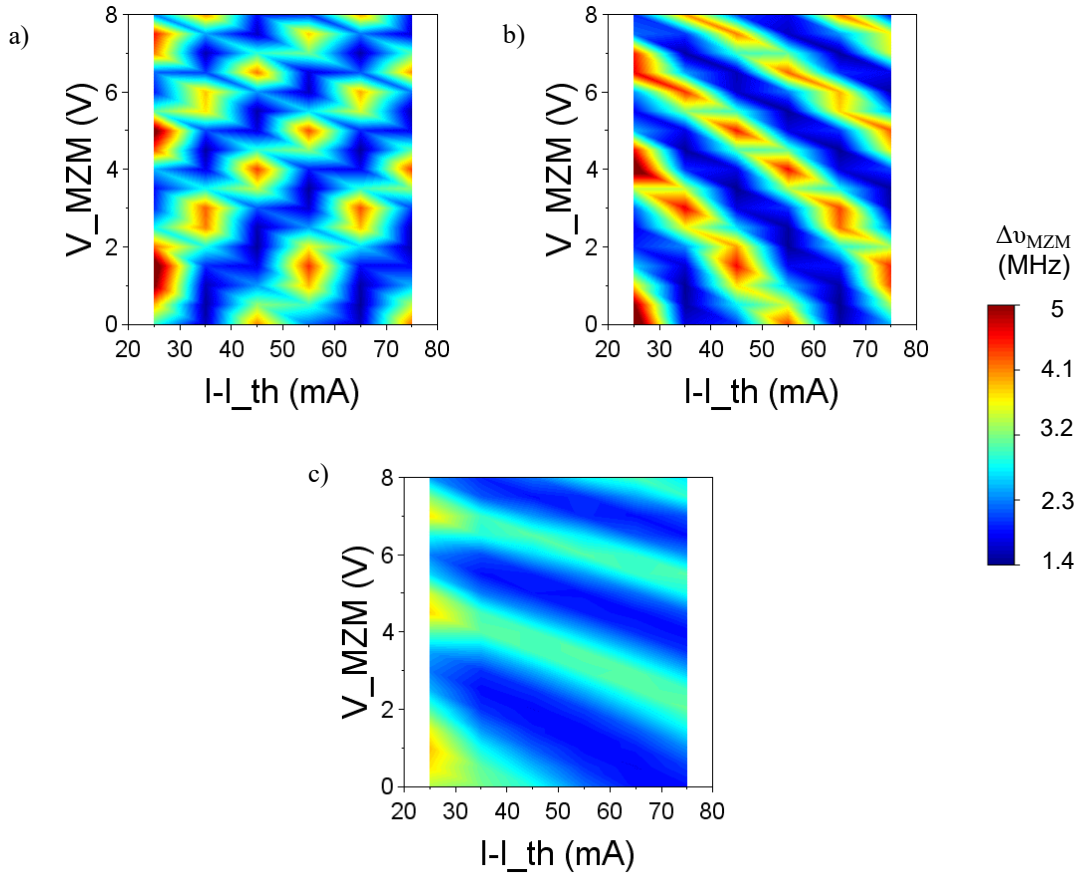


Fig. 131. Simulated transmitter linewidth mappings at different laser bias currents $I - I_{\text{th}}$ and modulator bias voltages V_{MZM} for reflections from the a) 2x2 MMI, b) SSC butt-joint and c) output facet.

The DFB laser Mach-Zehnder modulator transmitter linewidth is increased or decreased with respect to the reference DFB laser linewidth, depending on the transmitter operation point. For all three reflective interfaces, a periodic linewidth pattern is visible, depending on the transmitter operation point. One period in the linewidth pattern happens after a modulator bias voltage change, corresponding to the Mach-Zehnder modulator switching voltage V_{π} , which is between 3.5 V and 2 V. The periodic pattern consists either of stripes or stripes with islands of increased linewidth and changes for the different external cavities. A summary of the simulated minimum linewidths Δv_{\min} and maximum linewidths Δv_{\max} with optical feedback from different reflective interfaces inside the DFB laser Mach-Zehnder modulator transmitter, obtained from the Fig. 131a-c, is given in Table 13.

Reflective Interface	Δv_{\min} (MHz)	Δv_{\max} (MHz)
1x2 MMI	2.1	2.6
2x2 MMI	1.5	5.4
SSC butt-joint	1.4	5.6
Output facet	1.8	3.8

Table 13. Simulated min. and max. linewidths with opt. feedback from different reflective interfaces inside the DFB laser Mach-Zehnder modulator transmitter.

Only small linewidth variations are observed for reflections from the 1x2 MMI. Stronger linewidth variations and larger max. linewidths are simulated for reflections from the 2x2 MMI, the modulator-SSC butt-joint and the output facet, where the light travels through the Mach-Zehnder modulator.

The linewidth mapping pattern changes with the optical feedback intensity and the external feedback phase ϕ_{ec} . The external feedback phase is changed by varying the linearly related external cavity group refractive index $n_{gr,ec}$, and thus the effective external cavity length. The simulated transmitter linewidth mappings with reflections from the 2x2 MMI, at different external cavity group refractive indices are plotted in Fig. 132a-d.

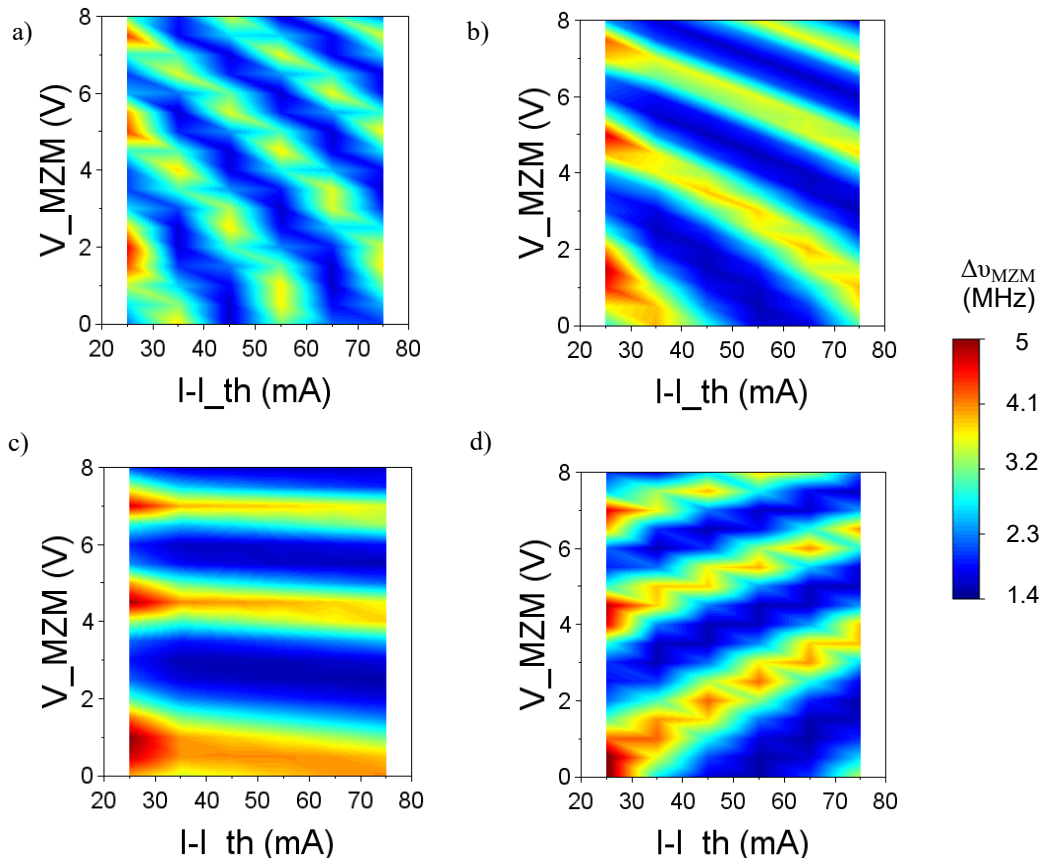


Fig. 132. Simulated transmitter linewidth mappings depending on the transmitter operation point with reflections from the 2x2 MMI, at an external cavity group refractive index $n_{gr,ec}$ of a) 2.7, b) 2.9, c) 3.1 and d) 3.3.

The linewidth mapping changes its pattern, repeating itself in a periodical way, when increasing the external cavity group refractive index and thus the effective external cavity length. The minimum and maximum linewidths remain constant, independent of the external cavity group refractive index.

The feedback intensity is varied by changing the external cavity reflectivity R_{ec} , which is linearly related. The linewidth mappings are simulated for reflections from the 2x2 MMI, while the external cavity reflectivity is changed from -40 dB to -30 dB and displayed in Fig. 133a-d.

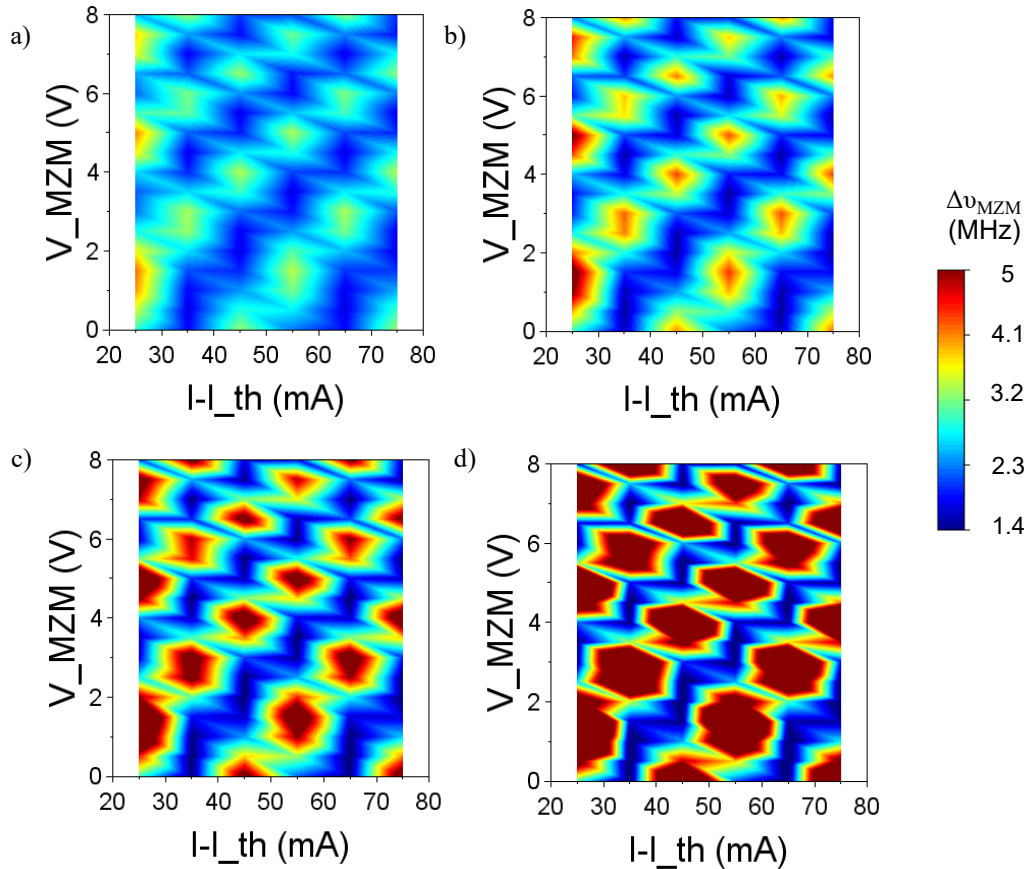


Fig. 133. Simulated transmitter linewidth mappings depending on the transmitter operation point with reflections from the 2x2 MMI, at R_{ec} values of a) -40 dB, b) -36 dB, c) -33 dB and d) -30 dB.

When increasing the external cavity reflectivity in the linewidth mappings from Fig. 132a to Fig. 132d, the maximum linewidth increases and the areas with increased linewidth enlarge. The linewidth pattern in the mapping remains constant. The linewidth variation $\Delta v_{\text{max}} - \Delta v_{\text{min}}$ between the maximum and minimum linewidth, depending on the external cavity reflectivity R_{ec} , is calculated for the different external cavities and plotted in Fig. 134a.

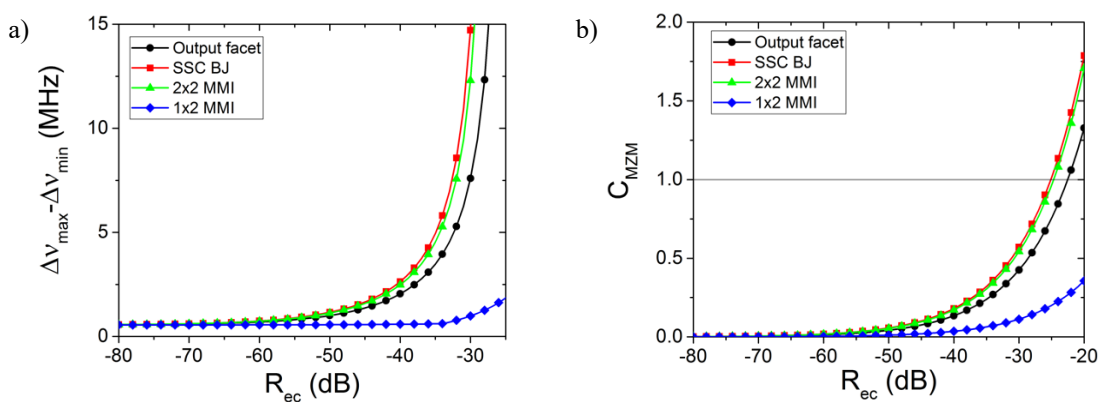


Fig. 134. a) Linewidth variation $\Delta v_{\text{max}} - \Delta v_{\text{min}}$ and b) Mach-Zehnder modulator feedback coefficient C_{MZM} , depending on the external cavity reflectivity R_{ec} for reflections from different interfaces inside the optical transmitter.

The linewidth variation increases with the external cavity reflectivity. For reflections from the 1x2 MMI, the linewidth variation remains small for an external cavity reflectivity of up to -20 dB. For the external cavities due to reflections from the 2x2 MMI, the SSC butt-joint and the output facet, which are further away from the laser,

the linewidth variation approximates infinity after reaching a critical value of R_{ec} , where C_{MZM} approaches 1 (Fig. 134b). The infinite linewidth indicates the transition from the feedback regime I to regime II, where multiple lasing modes are possible. To avoid entering regime II, a reflectivity lower than -31 dB is required for the output facet, the 2x2 MMI and the modulator spot-size converter butt-joint.

The simulations show that the DFB laser Mach-Zehnder modulator transmitter linewidth depends both on the laser bias current and the modulator bias voltage, due to optical feedback inside the chip. The bias point dependency comes from the relation of the optical feedback phase and intensity to the laser current and modulator bias voltage. In the measured DFB laser Mach-Zehnder modulator transmitter linewidth mappings in chapter 5.1.2, a similar pattern to the simulated one of a laser with optical feedback, in Fig. 131b, is observed. This indicates that the transmitter linewidth is influenced by the optical feedback inside the chip, since for a transmitter with an isolated laser and modulator, a linewidth independent of the modulator bias voltage is expected. Contrary to the simulated linewidths, the measured transmitter linewidths are mostly smaller compared the ones of the reference DFB lasers. The differences between the simulations and measurements might be observed because the simulated linewidth mappings are calculated for reflections from only one external cavity. In the fabricated transmitters, the light is reflected from multiple external cavities at once, so that the reflections interfere with each other and different linewidth patterns than the simulated ones might be generated. The simulation of a transmitter with multiple external cavities is not within the scope of this work and is an interesting topic for future related works.

The transmitter bias point also impacts on the DFB laser Mach-Zehnder/ IQ modulator transmitter binary/ quaternary phase shift keying performance in the chapters 5.1.5.2 and 5.2.3, which is not the case for reference modulators with isolated lasers. The transmitter linewidth dependency on the bias point could be one reason for that. Thus, a careful bias point selection is important to achieve a low transmitter linewidth and the best performance of DFB laser Mach-Zehnder/ IQ modulator transmitters with optical feedback.

7.2 Effects of Opt. Feedback inside DFB Laser Mach-Zehnder Modulator Transmitters on Modulated Signals

The DFB laser Mach-Zehnder modulators transmitters have a good performance at intensity modulation, comparable to the one of reference Mach-Zehnder modulators, without integrated laser. However, the DFB laser Mach-Zehnder/ IQ modulator transmitter binary phase shift keying (BPSK) and quaternary phase shift keying (QPSK) measurements in chapter 5.1.5.2 and 5.2.3, respectively, show increased phase variations, compared to measurements of reference Mach-Zehnder or IQ modulators. Also, the measured bipolar 4-level pulse amplitude modulation (PAM4) constellation points in chapter 5.1.5.3, depict increased phase variations, especially on constellation points with higher amplitude levels. In the BPSK, QPSK and bipolar PAM4 measurements, a Kalman filter is used to estimate the signal phase and to compensate the intrinsic laser phase noise due to spontaneous emission. Thus, it is assumed that the remaining phase variations on the measured BPSK signals are caused by the modulated optical feedback inside the transmitters. To investigate, if modulated optical feedback is contributing to the increased phase variations, a simulation model is generated.

For the simulation, the Lang-Kobayashi model of a laser with modulated optical feedback from chapter 6.2.6 is used. In equation (6.19), which describes the normalized complex laser electrical field amplitude under modulated

optical feedback, the sine-wave modulation is exchanged with a binary rectangular data signal $S(t)$, with the modulation frequency f_{mod} (eq. (7.3)).

$$\dot{\mathcal{E}}(t) = (1-i\alpha)\Gamma G_{n_{\text{th}}} (n-n_{\text{th}}) \mathcal{E}(t) + S(t) \frac{K_{\text{ec}}}{\tau_L} e^{i\omega_0 t_{\text{ec}}} \mathcal{E}(t-\tau_{\text{ec}}) \quad (7.3)$$

$S(t)$ emulates the data signal which is generated by the integrated Mach-Zehnder modulator in the fabricated optical transmitters. First, a pseudorandom binary sequence (PRBS) is generated, consisting of ones and zeros. The PRBS signal is multiplied by the modulation amplitude A_{mod} and offset by the value B_{mod} , so that $S(t) = \text{PRBS} \cdot A_{\text{mod}} + B_{\text{mod}}$. At non-return-to-zero on-off-keying (NRZ) operation, the integrated Mach-Zehnder modulator is operated at the 3 dB working point and has a dynamic 10 dB extinction ratio. In the simulation, this is implemented by setting A_{mod} and B_{mod} , so that $|S(t)|^2$ varies between 1 at a digital “1” and 0.1 at a digital “0”.

The simulation concentrates on the effect of the modulated optical feedback. Thus, the laser is simulated without intrinsic phase and intensity noise and a negligible linewidth. The optical feedback modulation is chirp-free with an infinite modulation bandwidth.

Optical feedback from the 2x2 multi-mode interference coupler is assumed, so that the external cavity length L_{ec} is set to 6.5 mm and the external cavity reflectivity R_{ec} to $6.1 \cdot 10^{-5}$, according to Table 10. The normalized transmitter output signal amplitude $\mathcal{E}_{\text{out}}(t)$ is obtained by taking the delayed laser normalized complex electrical field amplitude at the time $\tau_{\text{ec}}/2$, when it reaches the transmitter output ($\mathcal{E}(t-\tau_{\text{ec}}/2)$) and multiplying it with the external cavity transmission coefficient $\sqrt{1-R_{\text{ec}}}$ (eq. (7.4)).

$$\mathcal{E}_{\text{out}}(t) = \mathcal{E}(t-\tau_{\text{ec}}/2) \sqrt{1-R_{\text{ec}}} \quad (7.4)$$

$\mathcal{E}_{\text{out}}(t)$ is normalized, so that it is dimensionless and its amplitude square $|\mathcal{E}_{\text{out}}(t)|^2$ corresponds to the number of photons. In every bit duration $1/f_{\text{mod}}$ of $\mathcal{E}_{\text{out}}(t)$, one sampling point is taken at half the symbol duration. To better compare the simulated NRZ signals with the measured binary phase shift keying signals, only the digital ones are considered for the constellation diagrams and error vector magnitude calculations.

The error vector magnitude calculation is described in appendix IV.II. Before calculating the error vector magnitude, the transmitter output signal amplitude $\mathcal{E}_{\text{out}}(t)$ is matched to the one of an ideal transmitter without optical feedback $\mathcal{E}_{\text{out,ideal}}(t)$. The ideal transmitter output signal is generated by multiplying the laser normalized complex electrical field amplitude with the binary data signal $S(t)$, so that the ideal signal at the transmitter output is $\mathcal{E}_{\text{out,ideal}}(t) = \mathcal{E}(t-\tau_{\text{ec}}/2, K_{\text{ec}}=0) \cdot S(t)$, assuming that the external cavity reflectivity R_{ec} and thus the feedback coefficient K_{ec} are zero.

Due to optical feedback from the external cavity, the laser experiences a constant frequency shift. The constant frequency shift is compensated in the transmitter output signal complex amplitude $\mathcal{E}_{\text{out}}(t)$, to concentrate only on the influence of the modulated optical feedback. The frequency shift corresponds to a change in the linear phase slope over time. The change in phase slope is estimated by simulating the laser complex electrical field amplitude

$\mathcal{E}(t)$, with constant optical feedback with $S(t)=1$, first. The estimated change in phase slope is subtracted from the transmitter output signal phase to remove the frequency shift.

The simulated transmitter with modulated optical feedback output signal constellation diagrams with the digital “1s” are depicted in Fig. 135a-c (red dots), at different modulation frequencies ($I-I_{th}$: 85 mA).

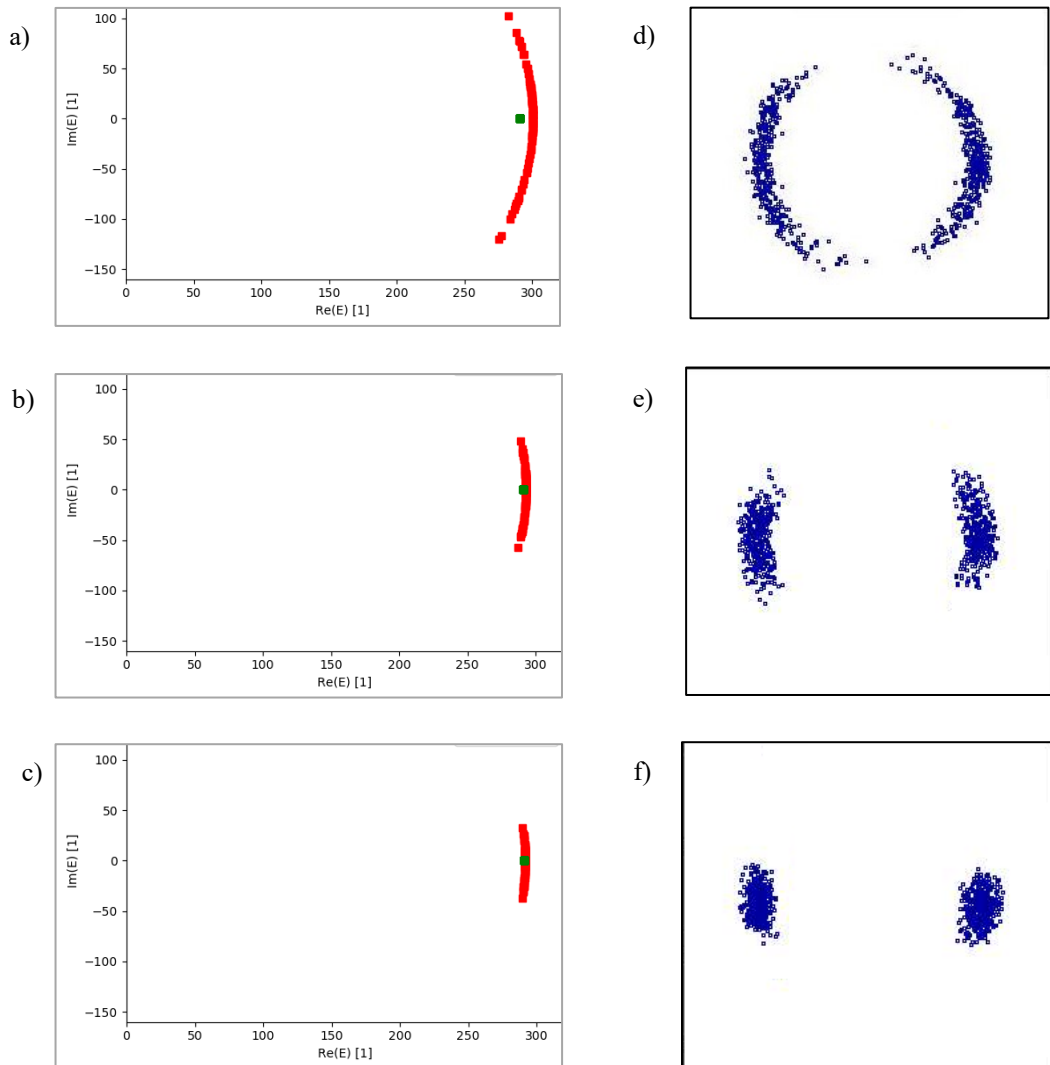


Fig. 135. Simulated constellation diagrams with digital ones of a binary data signal of transmitter with optical feedback (red dots) and ideal transmitter output signal without optical feedback (green dots) at a) $f_{mod}: 10$ GHz, b) $f_{mod}: 20$ GHz and c) $f_{mod}: 30$ GHz ($I-I_{th}$: 85 mA, R_{ec} : $6.1 \cdot 10^{-5}$). Measured DFB laser Mach-Zehnder modulator transmitter module binary phase shift keying constellation diagrams at d) $f_{mod}: 10$ GHz, e) $f_{mod}: 20$ GHz and f) $f_{mod}: 30$ GHz ($I-I_{th}$: 85 mA, V_{MZM} : 5 V, T : 20°C)

As a reference, the constellation points of the ideal transmitter output signals are also plotted in Fig. 135a-c (green dot). Compared to the ideal transmitter output signals, increased phase variations are visible on the constellation points of the transmitter with optical feedback, decreasing with increasing modulation frequency. The increased phase variations arise because the modulated optical feedback induces laser phase oscillations, especially at modulation frequencies in the range of the laser relaxations oscillation frequency and lower, as shown in chapter 6.2.6. In terms of intensity, the influenced of optical feedback on the transmitter constellation points is negligible.

For comparison, the measured binary phase shift keying (BPSK) constellation diagrams at different modulation frequencies of the DFB laser Mach-Zehnder modulator transmitter module, from chapter 5.1.5.2, are given in Fig. 135d-f. The measured binary phase shift keying constellation points also show increased phase variations compared to the simulated ideal transmitter output signal, which decrease at higher modulation frequencies. The measured binary phase shift keying constellation points are comparable to the simulated ones of the transmitter with optical feedback.

The error vector magnitude of the simulated DFB laser Mach-Zehnder modulator (DFB-MZM) transmitter output signals is calculated at different modulation frequencies and plotted in Fig. 136 ($I - I_{th}$: 85 mA).

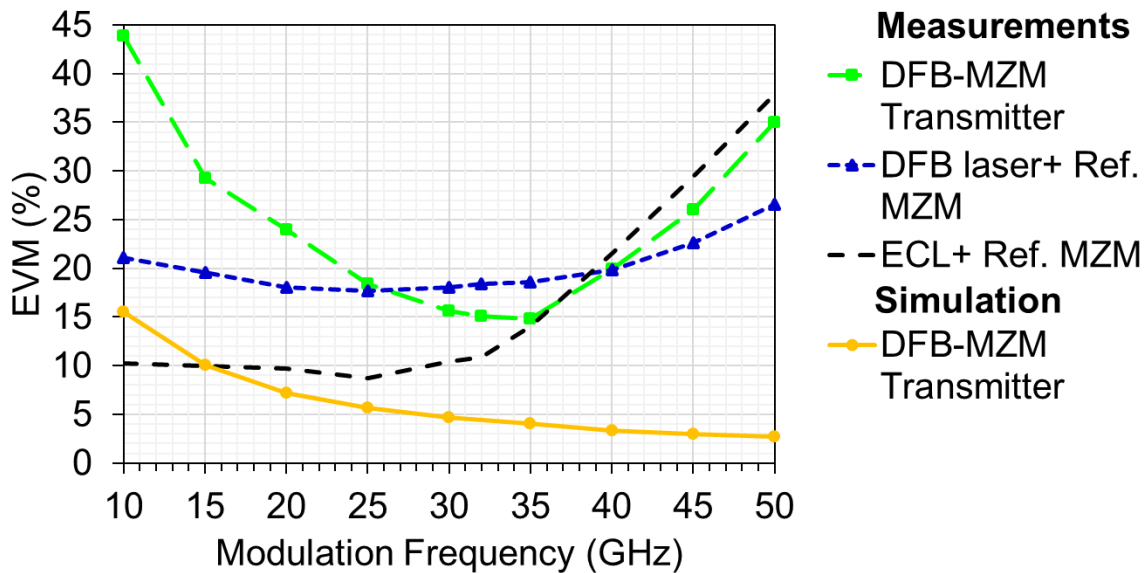


Fig. 136. EVM vs. modulation frequency of simulated DFB-MZM transmitter with modulated optical feedback ($I - I_{th}$: 85 mA), compared to BPSK EVM measurements of a DFB-MZM transmitter, a DFB laser with a reference Mach-Zehnder modulator (DFB laser+ Ref. MZM) ($I - I_{th}$: 85 mA) and an ECL with a reference MZM (ECL+ Ref. MZM).

As a reference, BPSK EVM measurements of a DFB laser Mach-Zehnder modulator transmitter ($I - I_{th}$: 85 mA) and of a reference Mach-Zehnder modulator (MZM), without integrated laser, from chapter 5.1.5.2, Fig. 83, are included in Fig. 136. For the reference Mach-Zehnder modulator, a DFB laser ($I - I_{th}$: 85 mA) or an external cavity laser (ECL) is used as the light source and optical feedback is suppressed with an optical isolator.

The error vector magnitude of the simulated transmitter is generally lower than the EVM of the measurements, since it only shows the influence of the modulated optical feedback on the signal and does not include any intensity and phase noise from the laser or the measurement system. Especially at high modulation frequencies the simulated EVM is lower than the measured one since the simulation does not contain bandwidth limitations of the Mach-Zehnder modulator and other components.

For the reference Mach-Zehnder modulator, where the laser is isolated, the error vector magnitude remains almost constant from 10 GHz to 40 GHz modulation frequency. From 10 GHz to 40 GHz, the error vector magnitude of the reference Mach-Zehnder modulator with DFB laser is limited to around 20 % due to the DFB laser intrinsic phase noise related to its linewidth of about 2- 3 MHz. The EVM from 10 GHz to 40 GHz of the reference Mach-Zehnder modulator with external cavity laser (linewidth < 150 kHz), is about 10 %.

At modulation frequencies lower than the DFB laser relaxation oscillation frequency (20 GHz), the simulated DFB Mach-Zehnder modulator transmitter error vector magnitude is strongly increased, due to the laser response to the modulated optical feedback. A similar behavior is also observed in the DFB laser Mach-Zehnder modulator transmitter BPSK measurements. The EVM increase at low frequencies is not observed for the reference Mach-Zehnder modulator measurements. It is thus concluded, that the transmitter EVM at frequencies lower than 20 GHz is mainly limited by the modulated optical feedback. At frequencies larger than 25 GHz, the influence of the modulated optical feedback on the error vector magnitude becomes less, because the laser dynamics cannot follow the modulated optical feedback anymore.

The measured DFB laser Mach-Zehnder modulator transmitter error vector magnitude at modulation frequencies larger than 25 GHz, is slightly lower than the reference Mach-Zehnder modulator with DFB laser error vector magnitude. This is possibly due to the larger reference DFB laser linewidth compared to the integrated DFB laser linewidth, which is about 1 MHz.

At frequencies larger than 32 GHz, the measured error vector magnitude increases, because of bandwidth limitations of the Mach-Zehnder modulators and the measurement system.

Overall, the simulation and measurements show that the DFB laser Mach-Zehnder modulator transmitter error vector magnitude of phase sensitive signals increases due to the modulated optical feedback, especially at symbol rates lower than the laser relaxation oscillation frequency. In addition, the error vector magnitude varies with the laser linewidth, which is influenced by the optical feedback depending on the transmitter bias point, as shown in chapter 7.1.1. At modulation frequencies larger than the relaxation oscillation frequency, the influence of the modulated optical feedback diminishes, and the transmitter error vector magnitude is mostly linewidth dependent. At modulation frequencies larger than 32 GHz, the measured error vector magnitude increases mainly due to bandwidth limitations of the devices and the measurement system.

It is assumed that the phase estimator in the coherent receiver, based on a Kalman filter, which copes with the intrinsic laser phase noise in addition to the phase variations due to optical feedback, plays an important role on the amount of phase variations remaining on the signal constellations. Studying and improving the influence of the phase estimator on the error vector magnitude is not within the frame of this work but would be an interesting topic for further investigations.

8. High-speed Operation of DFB laser Mach-Zehnder/ IQ Modulator Transmitter Module/ Subassembly

In chapter 7, it has been shown that optical feedback is present in the DFB laser Mach-Zehnder/ IQ modulator transmitter photonic integrated circuits, where the laser is monolithically integrated without an isolator. While the optical feedback effects on the laser intensity are small and almost negligible on intensity modulated signals, increased phase variations are visible on phase modulated signals. For phase-sensitive modulation formats, like quaternary phase shift keying (QPSK) or quadrature amplitude modulation (QAM), this can be an issue. However, it has been shown in the chapters 6.2.6 and 7.2, that the increased phase variations diminish when the transmitter is operated at symbol rates larger than the laser relaxation oscillation frequency, which was around 20 GHz. Moreover, the phase variations can be controlled and long-term stabilized by carefully tuning the transmitter operation point in terms of laser bias current and modulator bias voltage.

In this chapter, the transmitters are operated under optimum conditions to show their best performance. High-speed operation at up to 100 GBd non-return-to-zero on-off keying (NRZ) and 4- and 8-level pulse amplitude modulation is achieved with the DFB laser Mach-Zehnder modulator transmitter module, for the first time with such a device, to the best of our knowledge. Moreover, quaternary phase shift keying (QPSK) operation at up to 32 GBd is demonstrated, using the DFB laser IQ modulator transmitter subassembly with dual differential driver. The good results and the additional advantages in terms of footprint, packaging effort, power consumption and cost, show that the transmitters with monolithically integrated DFB laser and Mach-Zehnder/ IQ modulator, clearly are an interesting alternative to hybrid integrated optical transmitters. The results are especially attractive for metro and short reach applications, where low cost and power efficient transceivers for spectrally efficient modulation formats, such as multi-level PAM, QPSK and QAM, are highly desired.

8.1 DFB Laser Mach-Zehnder Modulator Transmitter Module 100 GBd Operation

For the first time, a high-speed travelling wave electrode Mach-Zehnder modulator with a bandwidth up to 54 GHz is integrated with a DFB laser. The limits of this optical transmitter are tested in this chapter, using a high-level experimental setup for 100 GBd operation. Combining high-speed optics and electronics with advanced digital signal processing, different schemes for intensity modulation and direct detection (IMDD) at 100 Gbit/s, 200 Gbit/s and 300 Gbit/s are tested. The experiments are done together with a group at the Karlsruhe Institute of Technology (KIT), who also kindly provided the experimental setup and the digital signal processing. An overview of the experimental setup is given in Fig. 137.

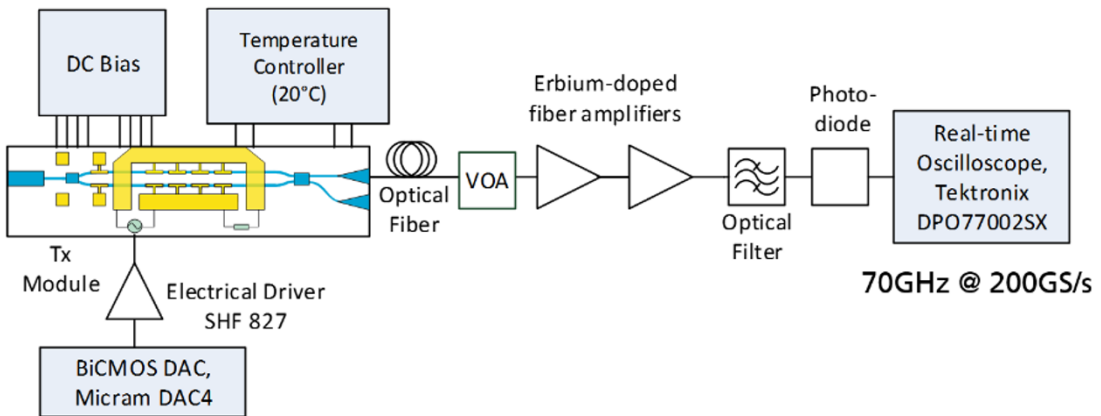


Fig. 137. DFB laser Mach-Zehnder modulator transmitter module 100 GBd operation experimental setup.

Electrical 100 GBd non-return-to-zero on-off keying (NRZ) and Gray-coded 4-level and 8-level pulse amplitude modulation random bit sequences with 2^{15} bits length are generated with a BiCMOS digital-to-analog converter (DAC) (Micram DAC4). The sampling rate is up to 100 GSamples/s at a physical resolution of 6 bits. The measured analog 3 dB synthesis bandwidth is 40 GHz, with a smooth roll-off down to -6 dB at the Nyquist frequency. The effective number of bits (ENoB) is about 5 bits until it decreases at frequencies larger than the synthesis bandwidth. The total digital-to-analog converter power consumption is up to 16 W. At up to 100 GBd PAM4 operation, the digital-to-analog converter generates electrical eye diagrams with open eyes and four distinct amplitude levels (Fig. 138).

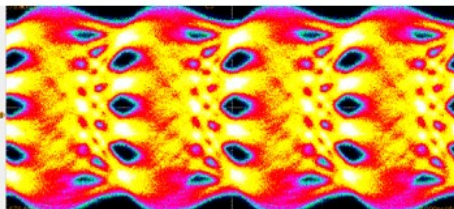


Fig. 138. BiCMOS digital-to-analog converter 100 GBd PAM4 electrical eye diagram.

A more detailed description of the BiCMOS DAC is given in [82]. A commercial electrical driver (SHF 827) is used to amplify the signals to a voltage swing of about $1.5 V_{pp}$, which is set lower than the Mach-Zehnder modulator switching voltage, which is about 2.5 V at 6 V modulator bias voltage, to achieve linear modulation. The DFB laser Mach-Zehnder modulator transmitter module is operated at 20°C temperature and 100 mA laser bias current, to achieve a high transmitter output power while not damaging the laser. The fiber coupled output power under modulation is 0 dBm (wavelength: 1542 nm). The transmitter output signals are transmitted cascaded single-mode fiber spans over up to 1.8 km with an average chromatic dispersion coefficient of 14 ps/nm/km. A 70 GHz photodiode (Finisar XPDV3120R) detects the signals which are saved at 200 GSamples/s using a real-time oscilloscope with an effective number of bits of 6- 7 bits (Tektronix DPO77002SX, bandwidth: 70 GHz). Because the oscilloscope requires a certain minimum input power for optimum operation and a wide bandwidth electrical PIN transimpedance amplifier is not available, two cascaded erbium doped fiber amplifiers (EDFAs) and an optical filter (bandwidth: 1.5 nm) are inserted before the photodetector. The offline post-processing

includes digital feed-forward timing recovery [83], followed by a 33-tap adaptive frequency-domain equalizer, using a stop-and-go algorithm [84].

To further push the system performance with advanced digital signal processing, a pattern-dependent look-up table (PD-LUT) is implemented for digital pre-compensation at the transmitter side. The pattern-dependent look-up table is used to subtract the deterministic errors from the transmitted signal in order to suppress nonlinear distortions by the limited bandwidth of the DFB laser Mach-Zehnder modulator module and other electrical components [85]. The deterministic error is obtained by comparing the received pattern with the transmitted pattern over four iterations. Even though in a real-time system, the determining the PD-LUT coefficients is challenging, the results give an upper bound for the performance of a nonlinear equalization scheme, such as a Volterra equalizer or a maximum likelihood sequence estimator. For bit error rate (BER) testing, a variable optical attenuator is inserted before the erbium doped fiber amplifiers, to control the optical signal-to-noise ratio (OSNR). The bit error rate is calculated by error counting over 655,360 symbols.

The probability density functions (PDF) over the signal amplitude after equalization of the 100 GBd NRZ, PAM4 and PAM8 received signals in back-to-back (B2B) operation are plotted in Fig. 139.

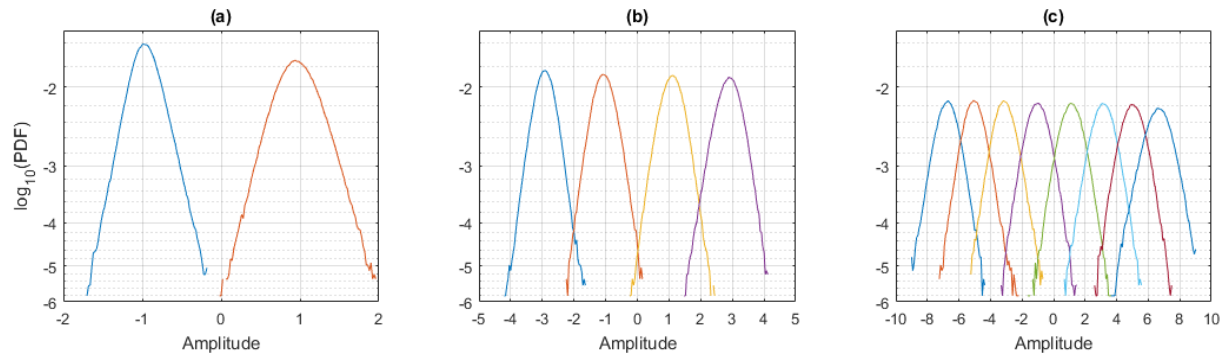


Fig. 139. Probability density function (PDF) vs. signal amplitude after equalization at 100 GBd a) NRZ, b) PAM4 and c) PAM8 in back-to-back operation.

For easier understanding, the symbol amplitudes are normalized to “1” and “-1” at NRZ operation, and to “-3, -1, 1, 3” at PAM4 operation and so on. The NRZ amplitude levels in Fig. 139a are clearly separated, showing error-free operation. At PAM4 operation (Fig. 139b), an overlap of the symbol probability density functions below $5 \cdot 10^{-4}$ is visible. At PAM8 operation (Fig. 139c), the symbol probability density functions overlap strongly for values below $6 \cdot 10^{-3}$.

The bit error rate measurements, depending on the optical signal-to-noise ratio at 100 GBd NRZ, PAM4 and PAM8 in back-to-back operation are displayed in Fig. 140.

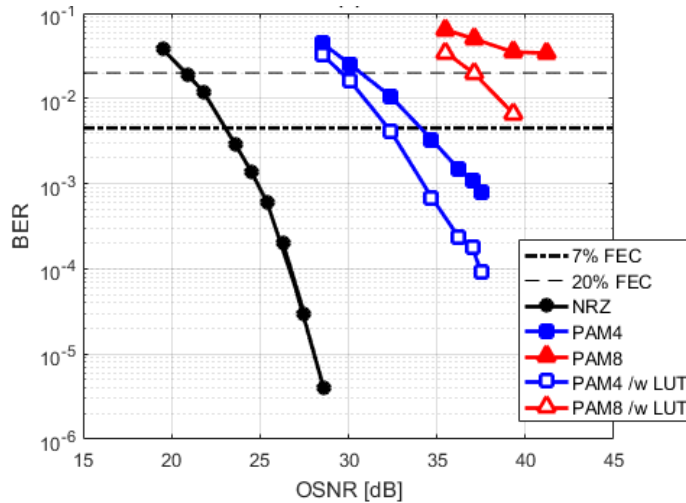


Fig. 140. 100 GBd NRZ, PAM4 and PAM8 bit error rate (BER) vs. optical signal-to-noise ratio (OSNR) in back-to-back operation. The PAM4 and PAM8 results are obtained without and with the pattern-dependent look-up table (/w LUT)

As references, the forward error correction (FEC) thresholds for an overhead of 7 % ($3.8 \cdot 10^{-3}$) and 20 % ($1.9 \cdot 10^{-2}$) are given. The PAM4 and PAM8 results are measured without and with implementing the pattern-dependent look-up table. A bit error rate below the 7 % forward error correction threshold is reached for optical signal-to-noise ratio values larger than 23 dB at NRZ operation and 34 dB at PAM4 operation. At PAM8 operation, the lowest achieved bit error rate is $3.4 \cdot 10^{-2}$, which is slightly above the 20 % forward error correction threshold. By applying the pattern-dependent look-up table, the optical signal-to-noise ratio penalty from NRZ to PAM4 operation decreases by 1.5 dB. The PAM8 performance improves significantly with the pattern-dependent look-up table, allowing operation below the 20 % forward error correction limit for an optical signal-to-noise ratio larger than 37 dB. The NRZ, PAM4 and PAM8 bit error rates after transmission over single-mode fiber spans with an average chromatic dispersion coefficient of 14 ps/nm/km, are displayed in Fig. 141.

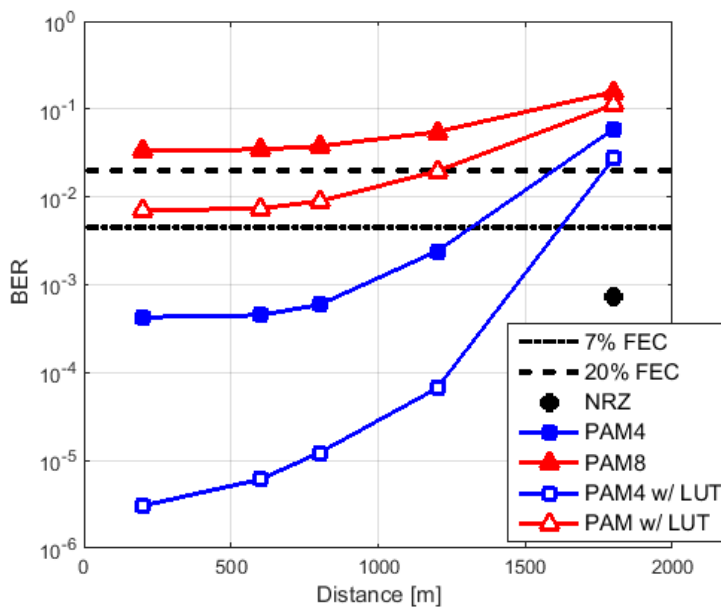


Fig. 141. 100 GBd NRZ, PAM4 and PAM8 bit error rates after transmission.

Up to 1.8 km error-free transmission is observed at 100 GBd NRZ operation, with a bit error rate below the 7 % forward error correction limit. At PAM4 operation, the transmission reach before hitting the 7 % forward error correction threshold is 1.2 km. The PAM8 signals require advanced digital signal processing, including the pattern-dependent look-up table, to achieve up to 1.2 km transmission with a bit error rate below the 20 % forward error correction limit. While the transmission results at 1550 nm wavelength are limited by the fiber chromatic dispersion, considerably longer transmission distances are expected at 1300 nm or by implementing a dispersion-compensating fiber (DCF).

The DFB laser Mach-Zehnder modulator transmitter module consumes 251 mW power, including the modulator input-voltage swing (45 mW), the laser current (126 mW) and the thermoelectric cooler (TEC), which consumes 80 mW after stabilizing the temperature to 20°C. The required energy per bit is calculated by dividing the power consumption by the achieved bit rate, giving 2.51 pJ/bit for NRZ, 1.26 pJ/bit for PAM4 and 0.84 pJ/bit for PAM8 operation, respectively, showing that in terms of the transmitter module power efficiency, the spectrally efficient PAM formats have an obvious advantage to NRZ modulation.

The results show, that the combination of the indium phosphide based DFB laser Mach-Zehnder modulator transmitter with high-speed electronics and digital signal processing is a promising solution to achieve 100 GBd PAM4 operation for dual-lane 400 Gbit/s or octal-lane 1.6 Tbit/s systems. Transmissions at 100 GBd PAM8 enable four-lane 1 Tbit/s systems, requiring however an optical signal-to-noise ratio larger than 37 dB and at the same time advanced digital signal processing, for example by using the pattern-dependent look-up table.

8.2 32 GBd QPSK operation of DFB Laser IQ Modulator Subassembly with Differential Driver

In this chapter, the bandwidth limits of the second developed transmitter type with a DFB laser and an integrated IQ modulator are tested. The high bandwidth IQ modulator, consisting of two travelling wave electrode Mach-Zehnder modulators, has not been integrated with a laser before. Thus in [86], where the results were first

published, we presented 32 GBd quaternary phase shift keying (QPSK) operation with a DFB laser IQ modulator transmitter photonic integrated circuit, for the first time, to the best of our knowledge. The experimental setup is like the one for the QPSK measurement in chapter 5.2.3, Fig. 94. A photograph of the DFB laser IQ modulator transmitter subassembly with differential driver during measurement is given in Fig. 142.

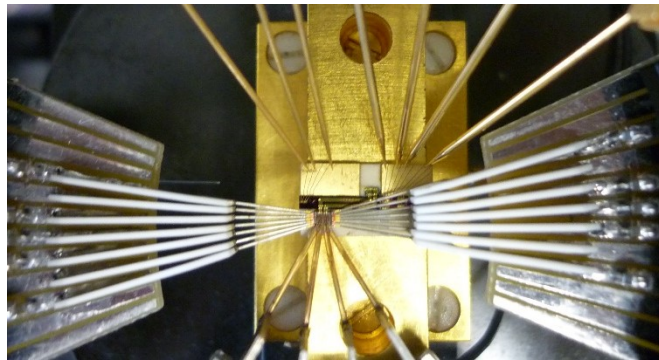


Fig. 142. Photograph of DFB laser IQ modulator transmitter with differential driver subassembly during 32 GBd QPSK measurement.

Two 32 Gb/s electrical pseudorandom binary sequences with $2^{31}-1$ bits length and 640 mV_{pp} differential amplitude are generated with a 56 Gb/s multi-channel bit pattern generator. The differential driver and DFB laser IQ modulator transmitter direct current contacts for applying bias voltages and bias currents, are contacted with needles and probe heads. Special probe heads for high bandwidth operation are used for contacting the differential driver radio frequency inputs. The driver differential output voltage swing is 3.0 V_{pp}, so that the Mach-Zehnder modulators are operated below a full voltage swing of two times the switching voltage $2 \cdot V_{\pi}$, in the linear region. The DFB laser is operated at 100 mA bias current (T: 20°C, wavelength: 1546 nm). Under QPSK modulation, the fiber-coupled output power is -5 dBm (modulator bias voltage: 8 V). The output power drop compared to the maximum transmitter output power of 2 dBm arises from setting the Mach-Zehnder modulator working points to the minimum and operating the modulators below a full $2 \cdot V_{\pi}$ voltage swing. For transmission experiments, the signal is launched into various standard single mode fiber (SSMF) spans of up to 10 km length. The optical output is captured with a digital sampling oscilloscope and an optical spectrum analyzer.

An optical modulation analyzer, including the coherent receiver with a local oscillator, optical 90° hybrids and balanced photodetectors, is used to receive the signals. The optical modulation analyzer also accounts for analog-to-digital conversion and digital signal processing for carrier phase tracking, using the integrated Kalman filter phase tracker algorithm. The optical modulation analyzer creates the QPSK constellation diagrams and calculates the bit error rate (BER). An erbium doped fiber amplifier followed by an optical filter (bandwidth: 2 nm) is used to provide sufficient input power (6.6 dBm) for optimum operation of the optical modulation analyzer and the digital sampling oscilloscope. For bit error rate testing, the signal is noise loaded with the amplified spontaneous emission noise of an additional erbium doped fiber amplifier.

The measured eye diagram at 32 GBd QPSK in back-to-back operation, shows clear transitions between the symbols (Fig. 143a).

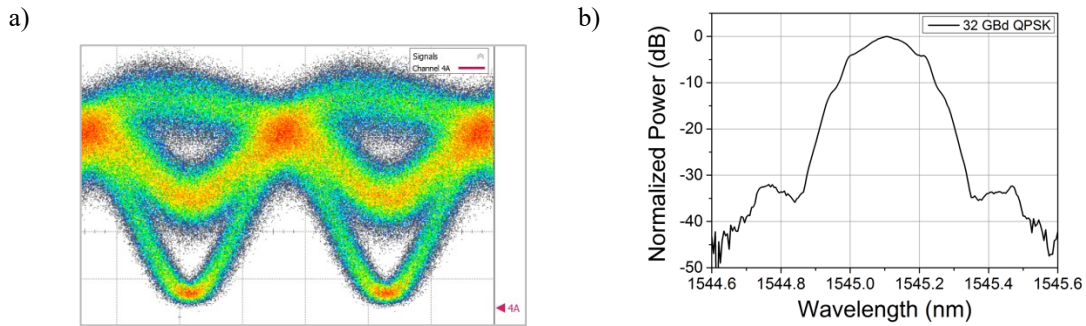


Fig. 143. DFB laser IQ modulator with differential driver subassembly, 32 GBd QPSK a) eye diagram, b) optical spectrum (center wavelength: 1545.1 nm).

The overlaid amplitude noise is due to the limited differential driver bandwidth. To operate the DFB laser IQ modulator with differential driver subassembly at higher symbol rates, a more advanced driver, like the one used in [87], has to be developed for the IQ modulator. The DFB laser IQ modulator transmitter itself has a 41 GHz bandwidth and should be applicable for symbol rates up to 80 GBd.

A typical optical QPSK spectrum is observed with the optical spectrum analyzer (resolution: 0.01 nm), having a 1545.1 nm center wavelength (Fig. 143a). The received QPSK back-to-back signal constellation diagram has an error vector magnitude (EVM) of 9.2 % (Fig. 144), which is comparable to the result of a reference IQ modulator of the same type as the integrated one, with an external cavity laser light source.

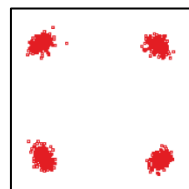


Fig. 144. 32 GBd back-to-back QPSK constellation diagram (EVM: 9.2 %).

The transmitter performance with added noise is investigated by evaluating the bit error rate (BER) depending on the optical signal-to-noise ratio. Operation with a bit error rate (BER) below the hard decision forward error correction (FEC) threshold (7 % overhead) is reached at an optical signal-to-noise ratio (OSNR) larger than 14 dB (Fig. 145a).

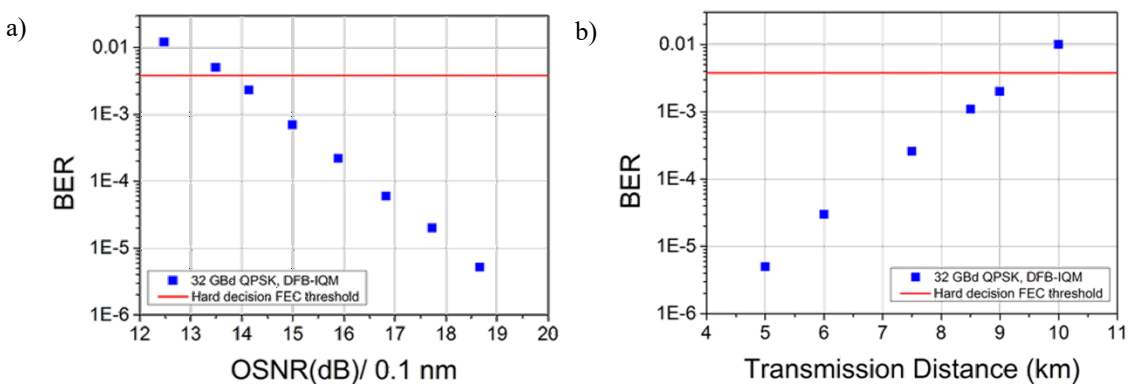


Fig. 145. 32 GBd QPSK a) BER vs. OSNR in back-to-back operation, b) BER vs. transmission distance.

The signal without added noise is transmitted over different standard single mode fiber spans of up to 9 km before the bit error rate hits the hard decision FEC threshold (Fig. 145b). The transmission distance is assumed to be

mainly limited by the fiber dispersion. Since no digital signal processing is used to compensate the fiber dispersion, the transmission distance is expected to improve with an adaptive equalizer to compensate channel impairments.

The specified maximum overall 6 W power budget for the CFP4 analog coherent optics (ACO) transceiver module [88], demands a transmitter power consumption preferably below 3 W [89]. This value should include the dual differential driver, IQ modulator and laser direct current and the temperature controller power consumption. For the receiver, about 1.75 W power consumption is assumed, including the local oscillator and the front end. 1.25 W are accounted for dc voltage and current splitting and miscellaneous. The total driver power consumption at 3 V_{pp} output is 0.96 W for both channels. The laser consumes 126 mW power (bias current: 100 mA) and the IQ modulator 21 mW, so that the overall power consumption is 1.1 W (without temperature controller). This corresponds to 17 pJ/bit at 32 GBd QPSK (output power: -5 dBm). By applying highly reflective coating to the laser facet and by increasing the laser bias current, the transmitter output power can be increased to 0 dBm, which would be a suitable value for the transceiver (laser power consumption: 280 mW). The transmitter power consumption at 0 dBm output power is 1.26 W which still fits the CFP4 module power budget. The power consumption can be further reduced by using other driving configurations, including for example a bias tee [90].

The high-speed short reach QPSK transmission experiments show that a transmitter with a DFB laser IQ modulator transmitter and a differential driver is a promising candidate for future high-speed short reach and metro applications. The optical feedback effects in the DFB laser IQ modulator transmitter are not noticeable at 32 GBd symbol rate, so that the DFB laser IQ modulator transmitter performance is comparable to the one of a reference IQ modulator without integrated laser. Due to its low power consumption, the DFB laser IQ modulator transmitter with differential driver subassembly is suitable for CFP4 analog coherent optics transceiver modules.

9. Conclusions and Outlook

A strong demand for scalable low-power solutions for metro and short reach optical networks appeared during the last years with the massive increase of intra- and inter-data center connections. The main challenges in the future transceiver development are to meet the requirements for a higher bit rate, while keeping a low power consumption, small footprint and low cost. In this work, indium phosphide-based transmitter photonic integrated circuits are developed, which are suitable for next generation CFP4 transceiver modules, for intra- and inter-data center connections from a few kilometers to tens of kilometers range.

The challenges in the future transceiver design are met by monolithically integrating a travelling wave electrode Mach-Zehnder or IQ modulator with a high bandwidth and low switching voltage and almost zero chirp, together with a 1550 nm DFB laser. The monolithic laser integration minimizes the coupling loss to 0.1 dB at the laser modulator interface and thus the transmitter power consumption. In addition, it reduces assembly time and cost and leads to a smaller transmitter size.

To integrate the DFB laser with the Mach-Zehnder or IQ modulator, the device structures and fabrication processes are adjusted and merged. In addition, a spot-size converter is integrated at the modulator output for better fiber coupling. The fabricated DFB laser Mach-Zehnder/ IQ modulator transmitters have a comparable footprint and direct current and small signal performance as the reference Mach-Zehnder/ IQ modulators, without integrated laser, providing low 2 V switching voltages and up to 54 GHz 3-dB bandwidths.

For large signal measurements, easier contacting and handling, the fabricated DFB laser Mach-Zehnder modulator transmitters are packaged into transmitter optical subassembly (TOSA) modules with a fixed optical fiber and DFB laser IQ modulator transmitters are fixed onto ceramic subassemblies. With the DFB laser Mach-Zehnder modulator module, a good large signal performance at intensity modulation formats, like non-return-to-zero (NRZ) on-off keying and 4-level pulse amplitude modulation (PAM4) is achieved, comparable to the one of a reference Mach-Zehnder modulator. However, when generating phase sensitive modulation formats, like binary phase shift keying (BPSK) or quaternary phase shift keying (QPSK) with the DFB laser Mach-Zehnder or IQ modulator transmitters, increased phase variations and error vector magnitudes are observed.

Due to the monolithic transmitter integration, the laser is not isolated from the modulator, so that light inside the photonic integrated circuits is reflected to the laser, mainly from interfaces at the facets, the multi-mode interference couplers and the butt-joint between the modulator and the spot-size converter. The measured stable single mode transmitter operation and the calculated feedback coefficients of the different interfaces show that the optical feedback intensity is in the weak feedback regime I.

A simulation model to understand the effects of passive and modulated optical feedback on the transmitter performance is generated, based on the Lang-Kobayashi equations. The results show that the optical feedback influences the laser phase much stronger than its intensity. The laser responds to the modulated optical feedback like a low pass filter with a resonance at the laser relaxation oscillation frequency. This leads mainly to a transmitter self-phase modulation, depending on the modulation frequency. The transmitter self-phase modulation causes

increased phase variations on the simulated data signals, especially at modulation frequencies lower than the laser relaxation oscillation frequency, which is around 20 GHz. A similar behavior is observed for the DFB laser Mach-Zehnder/ IQ modulator transmitter BPSK and QPSK measurements. It is concluded that the modulated optical feedback is the reason for the increased BPSK and QPSK phase variations and error vector magnitudes of the integrated transmitters compared to reference Mach-Zehnder/ IQ modulators without integrated laser.

At modulation frequencies larger than the relaxation oscillation frequency, however, the influence of the modulated optical feedback diminishes and the transmitter BPSK and QPSK error vector magnitudes are mostly linewidth dependent.

Further simulations and measurements show that the laser linewidth is influenced by the optical feedback, depending on the transmitter bias point. The bias point dependency comes from the relation of the optical feedback phase and intensity to the laser current and the modulator bias voltage. The transmitter linewidth impacts on the DFB laser Mach-Zehnder/ IQ modulator transmitter binary/ quaternary phase shift keying performance. Thus, a careful bias point selection is important to achieve the best performance of DFB laser Mach-Zehnder/ IQ modulator transmitters with optical feedback.

Despite the weak optical feedback, a good transmitter performance is achieved at the optimum bias point and at modulation frequencies larger than 25 GHz. 32 GBd QPSK operation with an error vector magnitude less than 10% and a low modulation voltage of 3 V_{pp} is demonstrated with a DFB laser IQ modulator transmitter with differential driver subassembly. The transmitter subassembly has a low power consumption of 1.1 W, which complies with the targeted CFP4 analog coherent optics module power budget. The power consumption includes the DFB laser, the IQ modulator and the differential driver direct current bias voltages and currents and corresponds to 17 pJ/bit modulation energy at 32 GBd QPSK.

For the first time, 100 GBd operation is demonstrated with a packaged monolithic DFB laser Mach-Zehnder modulator transmitter module, which has a 44 GHz 3-dB bandwidth. For the signal generation, a 100 GSamples/s BiCMOS digital-to-analog converter is used. Digital signal processing is utilized to overcome transmitter imperfections as well as noise limitations. Transmission over up to 1.8 km at 100 Gb/s NRZ and 1.2 km at 200 Gb/s PAM4 at 1550 nm is achieved (with a bit error rate below the forward error correction threshold for 7 % overhead), making the device attractive for dual-lane 400 Gb/s short reach applications. In addition, 300 Gb/s 8-level pulse amplitude modulation (PAM8) signals are transmitted over up to 1.2 km with a bit error rate below the 20 % forward error correction threshold, requiring however advanced digital signal processing and a large optical signal-to-noise ratio. In terms of power efficiency, the required energy per bit for PAM4 and PAM8 is significantly improved with respect to NRZ modulation.

The reported results clearly show that the fabricated DFB laser Mach-Zehnder/ IQ modulator transmitter architectures are promising candidates for future high-speed metro or short reach applications which could also find applicability for systems operating at 1300 nm wavelength, where a much longer distance is expected due to the lack of chromatic fiber dispersion. 112 Gb/s PAM4 transmission has already been demonstrated with the next generation DFB laser Mach-Zehnder modulator transmitter, operating at 1300 nm [91].

Some topics concerning the DFB laser Mach-Zehnder/ IQ modulator transmitter development are not covered within the scope of this work and are interesting topics for further studies.

When integrating the DFB laser with the Mach-Zehnder/ IQ modulator, the laser crystal direction is rotated by 90 degrees, compared to its typical direction, avoiding 90 degrees bends and keeping the modulator in its optimum crystal direction. The rotation leads to a deformation of the laser buried heterostructure waveguide and the gratings during high temperature overgrowth processes during fabrication, due to mass transport and less stable crystal walls. The result is a higher threshold current, compared to reference DFB lasers in the typical crystal direction. First tests show that the buried heterostructure waveguide is less deformed, when using a lower temperature and a slower temperature incline at the start of the regrowth. Further optimization of the 90 degrees rotated laser fabrication process should be conducted. Another approach would be to use Mach-Zehnder modulator types which are optimized for the typical DFB laser direction, like nipi-structure Mach-Zehnder modulators [59], so that the lasers do not have to be rotated.

The phase estimator in the coherent receiver, based on a Kalman filter, which copes with the intrinsic laser phase noise in addition to the phase variations due to optical feedback, plays an important role on the amount of phase variations on the signal constellations. In this work, a commercial phase estimator software is used. To study the influence of the phase estimator on the DFB laser Mach-Zehnder/ IQ modulator transmitter BPSK and QPSK signal performance in detail, would be an important addition to this work.

Optimizing the optical transmitters to suppress optical feedback within the photonic integrated circuits would be another interesting topic. This could be achieved for example by using angled facets, butt-joints and multi-mode interference couplers [92] or more feedback resistant laser types, like gain-coupled DFB lasers [68]. Designing lasers for a lower relaxation oscillation frequency is another idea, to reduce the critical symbol rate below which the modulated optical feedback causes self-phase modulation and increased phase noise.

All optical transmitter simulations in this work, include reflections from one external cavity inside the chip. In the fabricated optical transmitters, however, multiple external cavities are typically present. By extending the simulation models to include optical feedback from multiple external cavities, more detailed knowledge about the actual transmitter performance under optical feedback would be obtained.

IV. Appendix

IV.I Runge-Kutta Solver

To solve the system of ordinary, coupled, nonlinear, delayed differential equations, an explicit fourth order Runge-Kutta algorithm is used. To explain the Runge-Kutta algorithm, Euler's method to solve ordinary differential equations (ODEs) numerically is described first. Euler's explicit method is the simplest way to solve ODEs. Runge-Kutta's method is an advancement of Euler's procedure, where Runge-Kutta's first order method is equivalent to Euler's method.

Euler's method develops the vectorial state y_{cur} of a system over time, by computing the increment vector y_{incr} , giving the next state $y_{next} = y_{cur} + y_{incr}$. To obtain $y_{incr} = dy/dt_{cur} \cdot \Delta t$, the derivative dy/dt of y_{cur} at the time t_{cur} is calculated, by inserting y_{cur} and t_{cur} into the ODE, where Δt is the time step. First, $y_{cur} = y_{ini}$ is computed, then y_{next} , until $t_{cur} > t_{end}$.

A delayed ordinary differential equation (DDE), consists of the ODE and a former state $y_{hist} = y(t_{cur} - t_{delay})$. First, the ODE is solved for the duration of the delay t_{delay} , by linear interpolation between the corresponding former states, to get y_{hist} . Then the DDE is solved. For Euler's method to work accurately, it is assumed that dy/dt is constant within one time step. In Runge-Kutta's n^{th} order method, dy/dt is evaluated in $n-1$ further supporting time points within one time step Δt , to determine a more reliable value for dy/dt . The i^{th} of the n supporting points is called $dy/dt_{sub,i}$. The supporting time points are called t_{sub} . The derivative dy/dt_{cur} is determined by the weighted average of all supporting derivatives dy/dt_{sub} . To determine the i^{th} supporting derivative, all $i-1$ supporting derivatives are used in a weighted average. The weights of these two weighted averages and the supporting time points can be formalized in a so called Butcher tableau.

The Butcher tableau of the Runge-Kutta algorithm, used throughout this work is:

0		
1/2		1/2
1/2		0 1/2
1		0 0 1
		1/6 1/3 1/3 1/6

The left column shows the position of each supporting time point in fractions of Δt . The last row shows the weights of the supporting derivatives. The first four rows on the right-hand side, show the weights of the $i-1$ supporting derivatives, when computing the i^{th} supporting derivative. For our simulations, we used a maximum Δt of 0.1 ps. The actual time step is chosen, so that 2^N sampling points are in the solution, since 2^N sampling points are the best condition for obtaining an accurate spectrum by Fourier transformation. This resulted in an actual step width in the order of 0.01 ps.

IV.II Error Vector Magnitude Calculation

The error vector magnitude (EVM) is a measure to describe the signal quality and the optical transmission system performance. The error vector $E_{\text{err},i}$ of a symbol i , is the difference between the received signal vector $E_{r,i}$ and the transmitted signal vector $E_{t,i}$ (eq. (9.1)) [93].

$$E_{\text{err},i} = E_{r,i} - E_{t,i} \quad (9.1)$$

A sketch of the error vector in a signal constellation diagram is given in Fig. 146.

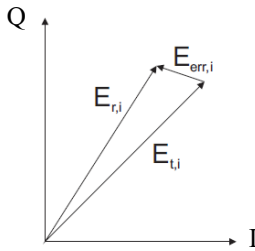


Fig. 146. Error vector $E_{\text{err},i}$ of the i^{th} symbol, depending on the difference between the received signal $E_{r,i}$ and the transmitted signal $E_{t,i}$.

The error vector magnitude of N transmitted symbols is defined as the error vector root mean square, normalized by the average transmitted symbol power $|E_{t,\text{avg}}|^2$ (eq. (9.2)).

$$\text{EVM} = \sqrt{\frac{\frac{1}{N} \sum_{i=1}^N |E_{\text{err},i}|^2}{|E_{t,\text{avg}}|^2}} \quad (9.2)$$

The transmitted signal is linearly amplified or attenuated throughout the transmission channel, so that the amplitude of the received signal changes, influencing the error vector magnitude. Therefore, to make the transmitted and the received signal comparable, a normalization is done before calculating the error vector magnitude. This process is called error vector magnitude minimization. To normalize the received signal to the transmitted signal, it is multiplied by a constant factor η_{EVM} , as in equation (9.3).

$$E_{\text{err},i,\text{norm}} = \eta_{\text{EVM}} E_{r,i} - E_{t,i} \quad (9.3)$$

To find the optimal value for η_{EVM} , so that the error vector magnitude is minimized, the minimum of the term $\frac{1}{N} \sum_{i=1}^N |E_{\text{err},i,\text{norm}}|^2$, which is further written as $E[|E_{\text{err},i,\text{norm}}|^2]$, must be found. At first, the term $E[|E_{\text{err},i,\text{norm}}|^2]$ is expanded, where $\sigma_E = E[|E|^2]$ is the variance and E^* the complex conjugate of a signal.

$$\begin{aligned} E[|E_{\text{err},i,\text{norm}}|^2] &= E[|\eta_{\text{EVM}} E_{r,i} - E_{t,i}|^2] = E[(\eta_{\text{EVM}} E_{r,i} - E_{t,i})(\eta_{\text{EVM}} E_{r,i} - E_{t,i})^*] \\ &= E[\eta_{\text{EVM}}^2 E_{r,i} E_{r,i}^* - \eta_{\text{EVM}} E_{r,i} E_{t,i}^* - E_{t,i} E_{r,i}^* + E_{t,i} E_{t,i}^*] \\ &= \eta_{\text{EVM}}^2 \sigma_{E_{r,i}} - E[\eta_{\text{EVM}} (E_{r,i} E_{t,i}^* - E_{t,i} E_{r,i}^*)] + \sigma_{E_{t,i}} \end{aligned} \quad (9.4)$$

The optimum value $\eta_{\text{EVM,} \text{opt}}$, where $E[|E_{\text{err},i,\text{norm}}|^2]$ is minimized, is found by determining the zeros of the derivative of $E[|E_{\text{err},i,\text{norm}}|^2]$ with respect to η_{EVM} .

$$\frac{d(E[|E_{\text{err},i,\text{norm}}|^2])}{d\eta_{\text{EVM}}} = 2\eta_{\text{EVM}}\sigma_{E_{r,i}} - E[(E_{r,i}E_{t,i}^* - E_{t,i}E_{r,i}^*)] \quad (9.5)$$

$$0 = 2\eta_{\text{EVM,} \text{opt}}\sigma_{E_{r,i}} - E[(E_{r,i}E_{t,i}^* - E_{t,i}E_{r,i}^*)]$$

$$2\eta_{\text{EVM,} \text{opt}}\sigma_{E_{r,i}} = E[(E_{r,i}E_{t,i}^* - E_{t,i}E_{r,i}^*)]$$

$$\eta_{\text{EVM,} \text{opt}} = \frac{E[(E_{r,i}E_{t,i}^* - E_{t,i}E_{r,i}^*)]}{2\sigma}$$

V. List of Abbreviations

ACO	Analog coherent optics
AR	Anti-reflection
AsH ₃	Arsine gas
B2B	Back-to-back
BER	Bit error rate
BH	Buried heterostructure
BH-RW	Buried heterostructure to deep-ridge waveguide
BJ	Butt-joint
BPSK	Binary phase shift keying
CAD	Computer assisted design
CLK	Clock
CV	Capacitance over voltage
CW	Continuous wave
DAC	Digital-to-analog converter
DBR	Distributed Bragg reflector
dc	Direct current
DCF	Dispersion compensating fiber
DDE	Delayed differential equation
DFB	Distributed feedback
DFB-IQM	DFB laser IQ modulator
DFB-IQM PIC	DFB laser IQ modulator photonic integrated circuit
DFB-MZM	DFB laser Mach-Zehnder modulator
DFB-MZM PIC	DFB laser Mach-Zehnder modulator photonic integrated circuit
DML	Directly modulated laser
DP	Dual polarization
DPSK	Differential phase shift keying
EAM	Electroabsorption modulator
ECL	External cavity laser
EDFA	Erbium doped fiber amplifier

E-E	Electrical-to-electrical
EML	Electroabsorption modulated laser
ENoB	Effective number of bits
E-O	Electro-optic
ER	Extinction ratio
EVM	Error vector magnitude
Fe	Iron
FEC	Forward error correction
GaAs	Gallium arsenide
HD-FEC	Hard-decision forward error correction
i	Intrinsic
I	In-phase
IL	Insertion loss
Im	Imaginary
IMDD	Intensity modulation and direct detection
InGaAs	Indium gallium arsenide
InGaAsP	Indium gallium arsenide
InP	Indium phosphide
InP:Fe	Iron-doped indium phosphide
IQ	In-phase and quadrature
IQM	In-phase and quadrature modulator
IRT	Intrinsic region thickness
LCA	Light wave component analyzer
LED	Light emitting diode
L-I-V	Light-current-voltage
Max	Maximum
Min	Minimum
MMI	Multi-mode interference coupler
MOVPE	Metalorganic vapor phase epitaxy
MQW	Multi quantum well
MZI	Mach-Zehnder interferometer

MZM	Mach-Zehnder modulator
n	n-doped
n-InP	n-doped indium phosphide
NRZ	Non-return-to-zero
ODE	Ordinary differential equation
OFDR	Optical frequency domain reflectometer
OMA	Optical modulation analyzer
OOK	On-off keying
OSA	Optical spectrum analyzer
OSNR	Optical signal-to-noise ratio
p	p-doped
PAM	Pulse amplitude modulation
PAM4	4-level pulse amplitude modulation
PAM8	8-level pulse amplitude modulation
PDF	Probability density function
PD-LUT	Pattern-dependent look-up table
PDM	Polarization division multiplexing
PIC	Photonic integrated circuit
p-InP	p-doped indium phosphide
PRBS	Pseudorandom binary sequence
PSK	Phase shift keying
Pt	Platinum
Q	Quadrature
QAM16	16-symbol quadrature amplitude modulation
QCSE	Quantum confined Stark effect
QPSK	Quaternary phase shift keying
QW	Quantum well
Re	Real
rf	Radio frequency
RIN	Relative intensity noise
RW	Ridge waveguide

RX	Receiver
RZ	Return-to-zero
SCH	Separate confinement heterostructure
SEM	Scanning electron microscope
Si	Silicon
SiGe	Silicon-germanium
SiN _x	Silicon nitride
SMSR	Side mode suppression ratio
SOA	Semiconductor optical amplifier
SSC	Spot-size converter
SSC-BJ	Spot-size converter butt-joint
SSMF	Standard single mode fiber
TE	Transverse electric
TEC	Thermoelectric cooler
TM	Transverse magnetic
TOSA	Transmitter optical subassembly
TWE	Travelling wave electrode
TX	Transmitter
VOA	Variable optical attenuator
WG	Waveguide

VI. List of Symbols

$ C_e $	Laser coupling coefficient
$\bar{n}_{\text{eff},\text{Br}}$	Average effective Bragg grating refractive index
$ r_{g,0} $	Magnitude reflection of lossless Bragg grating
\tilde{E}	Complex electrical field amplitude
$G_{n_{\text{th}}}$	Laser differential gain at threshold
α_H	Transient chirp coefficient
α_{int}	Laser active region internal loss
α_m	Laser mirror loss
$\alpha_{U,I}$	Mach-Zehnder modulator absorption coefficients at U- or I-electrode
$\Delta n_{\text{eff},\text{Br}}$	Effective refractive index difference between Bragg grating regions A and B
Δn_{FK}	Refractive index shift due to Franz-Keldysh effect
ΔP_0	Laser optical output power variation at zero modulation frequency
ϵ_0	electric constant
λ_{Br}	Bragg wavelength
τ_c	Electrical carrier lifetime
τ_{ec}	External cavity roundtrip time
τ_L	Laser roudtrip time
τ_{ph}	Photon lifetime
ϕ_{ec}	External optical feedback phase
ϕ_{MZM}	Mach-Zehnder modulator phase shift
$\phi_{U,I}$	Mach-Zehnder modulator phase shift at U- or I-electrode
ω_0	Laser angular optical frequency without optical feedback
$ r_g $	Magnitude reflection of Bragg grating
ΔG	Laser gain shift
Δn	Refractive index shift
A	Amplitude
a	Laser gain coefficient at threshold
a_1, a_2, p_1, p_2	Mach-Zehnder modulator model fitting parameters
abs_{MZM}	Mach-Zehnder modulator absorption
A_{mod}	Modulation amplitude

A_{MZM}	Mach-Zehnder modulator passive loss coefficient
B_{mod}	Modulation offset
c	speed of light in vacuum
C	Optical feedback coefficient
C_0	Capacitance of unloaded travelling wave electrode per unit length
C_{IRT}	Mach-Zehnder modulator waveguide intrinsic region capacitance
C_L	Capacitive load per unit length of loaded travelling wave electrode
C_{MZM}	Mach-Zehnder modulator feedback coefficient
d	Laser active region thickness
D	Dispersion
e	elementary charge
E	Electrical field
E_c	Conduction band energy
E_{gap}	Bandgap energy
$E_{\text{in,MZM}}$	Mach-Zehnder modulator input electrical field
$E_{\text{out,MZM}}$	Mach-Zehnder modulator output electrical field
$E_{\text{T,MZI}}$	Mach-Zehnder interferometer transmitted electrical field
E_v	Valence band energy
\mathcal{E}	Normalized complex electrical field amplitude
f	Frequency
f_{3dB}	Laser 3 dB cut-off frequency
F_{act}	Laser active region cross-section area
f_{ext}	External optical feedback fraction
FF	Fill factor of travelling wave electrode
FF_{match}	Fill factor of travelling wave electrode for velocity match
$f_{\text{Max. RIN}}$	RIN spectrum peak frequency
f_{mod}	Modulation frequency
F_{MZM}	Mach-Zehnder modulator transfer function
f_r	Laser relaxation oscillation frequency
$f_{r,\text{ec}}$	External cavity free spectral range or resonance frequency
f_u	Frequency at u^{th} minimum of fiber transfer function
h	Planck's constant
I	Laser bias current

I_h	DFB laser heater current
IL	Insertion loss
IL_{dB}	Insertion loss in decibel
I_{ph}	Photo current
I_{pump}	Laser pump current
$I_{pump,max}, I_{pump,min}$	Max. and min. laser pump current
I_{th}	Laser threshold current
j	Laser pump current density
K_{ec}	Coupling coefficient from laser to external cavity
L	Laser active region length
L_0	Inductance of unloaded travelling wave electrode per unit length
L_a	Length of travelling wave electrode segments
$L_{act,MZM}$	Mach-Zehnder modulator active length
$L_{act,new}$	Mach-Zehnder modulator active length adjusted for desired switching voltage
L_{ec}	External cavity length
L_{eff}	Effective Bragg grating length
L_{fiber}	Fiber length
L_g	Bragg grating length
L_p	Distance between travelling wave electrode segments
n	Electrical carrier density
n_{eff}	Effective refractive index
$n_{eff,A}$	Effective refractive index in Bragg grating region A
$n_{eff,B}$	Effective refractive index in Bragg grating region B
n_{el}	Electrical microwave index in unloaded transmission line
N_{el}	Photo current power spectral density
$n_{el,load}$	Electrical microwave index in loaded transmission line
$n_{gr,act}$	Laser active region group refractive index
$n_{gr,ec}$	External cavity group refractive index
$n_{gr,el}$	Electrical wave group refractive index in unloaded travelling wave electrode
$n_{gr,opt}$	Optical wave group refractive index
n_{th}	Electrical carrier density at threshold
P	Laser optical output power
P_0	Laser optical output power without optical feedback
$P_{avg,el}$	Average electrical power

P_{dc}	Laser direct current power consumption
P_h	DFB laser heater power consumption
P_{in}	Input optical power
$P_{max,0}, P_{min,0}$	Max. and min. optical output power at zero modulation frequency
P_{mod}	Peak-to-peak modulated optical output power
P_{out}	Optical output power
$P_{T,MZI}$	Mach-Zehnder interferometer transmitted optical power
R	Bit rate
r	Photo diode responsivity
R_1	Laser reflectivity at chip facet
R_{12}	Laser reflectivity at facet towards external cavity
R_d	Laser differential resistance
R_{ec}	External cavity reflectivity
$R_{ec,eff}$	Effective external cavity reflectivity
R_g	Bragg grating reflectivity
RIN	Relative intensity noise
R_L	Load resistance
R_n	Resistance of n-doped indium phosphide layer
R_s	Symbol rate
S	Data signal amplitude
s	Splitting ratio between the two Mach-Zehnder modulator arms
T	Temperature
t	Time
T_0	Laser characteristic temperature
v	Wave velocity
V	Laser voltage
V_{act}	Laser active region volume
v_{el}	Electrical wave velocity
$v_{gr,act}$	Group velocity in laser active region
V_h	DFB laser heater voltage
V_{mod}	Peak-to-peak modulation voltage
V_{MZM}	Mach-Zehnder modulator bias voltage
v_{opt}	Optical wave velocity
V_{phase}	Mach-Zehnder modulator phase bias voltage
$V_{U,I}$	Voltage at Mach-Zehnder modulator U- or I-electrode
V_π	Mach-Zehnder modulator switching voltage

$V_{\pi,\text{des}}$	Mach-Zehnder modulator desired switching voltage
w	Laser active region width
W_{MZM}	Mach-Zehnder modulator waveguide width
Z_0	Impedance of unloaded travelling wave electrode per unit length
Z_m	Travelling wave electrode characteristic impedance
α	Linewidth enhancement factor
Γ	Optical confinement
Δv_0	Laser linewidth without optical feedback
Δv_{\max}	Maximum laser linewidth
Δv_{\min}	Minimum laser linewidth
Δv_{MZM}	DFB laser Mach-Zehnder modulator transmitter linewidth
ΔI_{pump}	Laser pump current variation
ΔP	Laser optical output power variation
δP	Laser optical output power noise
Δv	Laser linewidth
$\delta \phi$	Phase shift between Mach-Zehnder modulator arms
$\Delta \phi$	Phase difference between laser electrical field without feedback and reflected electrical field
$\Delta \phi_0$	Phase difference between laser electrical field without feedback and reflected electrical field, without artificial phase shift
$\Delta \phi_{\text{art}}$	Artificial phase shift
η	Coupling efficiency from laser to modulator
κ	Grating coupling coefficient
Λ	Grating period
λ	Wavelength
τ	Delay time
ϕ	Phase
ω	Angular frequency

VII. Acknowledgments

I first thank Professor Klaus Petermann for accepting to supervise my thesis, for listening to my many presentations and for carefully reading and commenting on my PhD thesis. His well-conceived comments helped me a lot to improve my work.

I thank my supervisor Ronald Kaiser, who has been guiding me through my work at Fraunhofer Heinrich Hertz Institute from the week I started. I learned the most from him about the optical device theory, structures, and fabrication. I am also very thankful that he patiently read and gave me advice on many of my papers, presentations and most of all my PhD thesis.

I thank my always cheerful and very studious student Florian Fiebig, who implemented the Lang-Kobayashi differential equation model into Matlab and Python and who generated and organized Gigabytes of numerical results for me.

I thank the modulator group at Fraunhofer HHI, for having me in their team and for everything they taught me about Mach-Zehnder modulators, fabrication, measurements, presentations and all the other countless things that helped me to improve my skills and knowledge. I especially thank Detlef Hoffmann for answering patiently all the theoretical questions I had and Marko Gruner, for always assisting me to start up and run the various measurement setups.

Moreover, I thank the TZL team, for showing me how to fabricate my devices in the clean room, for all the nice talks we had while waiting for the process steps to finish and for inviting me to their funny team events.

I thank Wolfgang Rehbein for providing me with hundreds of measurement results for my lasers and transmitters and for all the nice conversations we could have about everything.

I thank Alessandro, for being my loyal lunch partner throughout the years and for keeping work exciting with his Italian temperament. I also thank him for all the funny things that we did and all the funny memories we will keep.

I thank Raphael, Patrick, Braulio, Sharam, Gan, Francisco and all my other great colleagues at HHI for the funny lunch times, coffee breaks and times we had.

To Pieter, Dina, Raphael, Uli Guitar and Uli Bass: “Thank you for the music, the songs I’m singing...”, we had a great time and I hope I will see the HHI band performing soon on a big stage with a lot of screaming fans.

Many thanks to my colleagues in the community council for fighting with me for the HHI employers’ rights and for all the nice meetings we had, even though they were on Monday morning.

Finally, I thank my mother, who is always there for me and who is proud of everything I achieve in my life. She is my biggest motivation to give the best in every exam, assignment and task that takes me further in my career.

VIII. Published Work

Parts of this work have been published:

Lange, S., R. Kaiser, M. Gruner, M. Hamacher, K.-O. Velthaus, and M. Schell. “Low Switching Voltage InP-Based Travelling Wave Electrode Mach-Zehnder Modulator Monolithically Integrated with DFB-Laser for 60 Gb/s NRZ.” In *Optical Fiber Communications Conference and Exhibition (OFC), 2015*, 1–3, 2015.
<https://doi.org/10.1364/OFC.2015.Th4E.1>.

Lange, S., L. Yan, N. Wolf, R. Kaiser, M. Gruner, K. O. Velthaus, and M. Schell. “Low Power InP-Based Monolithic DFB-Laser IQ Modulator with SiGe Differential Driver for 32 GBd QPSK Modulation.” In *2015 European Conference on Optical Communication (ECOC)*, 1–3, 2015.
<https://doi.org/10.1109/ECOC.2015.7341851>.

Lange, S., M. Gruner, C. Meuer, R. Kaiser, M. Hamacher, K. O. Velthaus, and M. Schell. “Low Switching Voltage Mach-Zehnder Modulator Monolithically Integrated With DFB Laser for Data Transmission up to 107.4 Gb/s.” *Journal of Lightwave Technology* 34, no. 2 (January 2016): 401–6.
<https://doi.org/10.1109/JLT.2015.2496426>.

Lange, S., N. Wolf, M. Gruner, L. Yan, R. Kaiser, K. O. Velthaus, J. H. Choi, and M. Schell. “Low Power InP-Based Monolithic DFB-Laser IQ Modulator With SiGe Differential Driver for 32-GBd QPSK Modulation.” *Journal of Lightwave Technology* 34, no. 8 (April 2016): 1678–82. <https://doi.org/10.1109/JLT.2015.2510228>.

Lange, S., R. Kaiser, M. Gruner, and M. Schell. “Experimental Study of Phase and Intensity Noise in a Monolithically Integrated DFB Laser IQ Modulator PIC at QPSK Operation.” In *ECOC 2016; 42nd European Conference on Optical Communication*, 1–3, 2016.

Lange, S., R. Kaiser, M. Gruner, N. Wolf, Lei Yan, W. Rehbein, and M. Schell. “Monolithic Laser Integrated Mach-Zehnder Modulator InP PICs for High-Speed Optical Networks.” In *2016 International Semiconductor Laser Conference (ISLC)*, 1–2, 2016.

Lange, S., S. Wolf, J. Lutz, L. Altenhain, R. Schmid, R. Kaiser, C. Koos, S. Randel, and M. Schell. “100 GBd Intensity Modulation and Direct Detection with an InP-Based Monolithic DFB Laser Mach-Zehnder Modulator.” In *2017 Optical Fiber Communications Conference and Exhibition (OFC)*, 1–3, 2017.

Lange, S., S. Wolf, J. Lutz, L. Altenhain, R. Schmid, R. Kaiser, M. Schell, C. Koos, and S. Randel. “100 GBd Intensity Modulation and Direct Detection with an InP-Based Monolithic DFB Laser Mach-Zehnder Modulator.” *Journal of Lightwave Technology*, vol. 36, no. 1, pp. 97-102, Jan. 2018.
<https://doi.org/10.1109/JLT.2017.2743211>.

Kaiser, R., **S. Lange**, M. Rausch, B. Gomez Saavedra, M. Gruner, G. Fiol, K. Janiak, et al. “CL-TWE Mach-Zehnder Modulators on InP: Central Elements in Transmitter PICs of Increasing Complexity.” In *2017 19th International Conference on Transparent Optical Networks (ICTON)*, 1–4, 2017.

<https://doi.org/10.1109/ICTON.2017.8025019>.

S. Lange, J.-H. Choi, M. Gruner, J. Xiao, and M. Schell, “Low Power Optical Transmitter with DFB-Laser Mach-Zehnder Modulator PIC and Co-Designed 2-Bit DAC Driver,” presented at the *ECOC 2017*, Gothenburg, 2017.

IX. References

- [1] “The Zettabyte Era: Trends and Analysis,” *Cisco*. [Online]. Available: <https://www.cisco.com/c/en/us/solutions/collateral/service-provider/visual-networking-index-vni/vni-hyperconnectivity-wp.html>. [Accessed: 21-Nov-2017].
- [2] Nokia, “Cloud data center interconnect for ICPs and CNPs, Web-scale and metro-scale data center interconnect, White paper,” 2017. [Online]. Available: <https://resources.ext.nokia.com/asset/201091>. [Accessed: 21-Nov-2017].
- [3] C. Cole, I. Lyubomirsky, A. Ghiasi, and V. Telang, “Higher-order modulation for client optics,” *IEEE Commun. Mag.*, vol. 51, no. 3, pp. 50–57, Mar. 2013.
- [4] “IEEE P802.3bs 400 Gb/s Ethernet Task Force.” [Online]. Available: <http://www.ieee802.org/3/bs/>. [Accessed: 21-Nov-2017].
- [5] C. Urricariet, “Latest Trends in Data Center Optics,” 12-2015. [Online]. Available: <http://ix.br/pttforum/9/slides/ixbr9-finisar.pdf>. [Accessed: 08-Dec-2017].
- [6] Jinlong Wei, Jonathan D. Ingham, Richard V. Penty, and Ian H. White, “Performance Studies of 100 Gigabit Ethernet Enabled by Advanced Modulation Formats,” 10-May-2012. [Online]. Available: http://www.ieee802.org/3/100GNGOPTX/public/may12/ingham_01_0512_optx.pdf. [Accessed: 21-Nov-2017].
- [7] Fujitsu, “Path to 400G, White paper,” 2013. [Online]. Available: <http://www.fujitsu.com/downloads/TEL/fnc/whitepapers/Pathto400G.pdf>. [Accessed: 21-Nov-2017].
- [8] B. Jalali and S. Fathpour, “Silicon Photonics,” *J. Light. Technol.*, vol. 24, no. 12, pp. 4600–4615, Dec. 2006.
- [9] V. Lal *et al.*, “Extended C-Band Tunable Multi-Channel InP-Based Coherent Transmitter PICs,” *J. Light. Technol.*, vol. 35, no. 7, pp. 1320–1327, Apr. 2017.
- [10] K. Nakahara *et al.*, “Direct Modulation at 56 and 50 Gb/s of 1.3- μm InGaAlAs Ridge-Shaped-BH DFB Lasers,” *IEEE Photonics Technol. Lett.*, vol. 27, no. 5, pp. 534–536, Mar. 2015.
- [11] Y. Matsui *et al.*, “55 GHz Bandwidth Distributed Reflector Laser,” *J. Light. Technol.*, vol. 35, no. 3, pp. 397–403, Feb. 2017.
- [12] Y. Ogiso *et al.*, “Ultra-High Bandwidth InP IQ Modulator with 1.5 V Vπ,” in *ECOC 2016; 42nd European Conference on Optical Communication*, 2016, pp. 1–3.
- [13] S. Lange *et al.*, “100 GBd Intensity Modulation and Direct Detection with an InP-based Monolithic DFB Laser Mach-Zehnder Modulator,” *J. Light. Technol.*, vol. 36, no. 1, pp. 97–102, Jan. 2018.
- [14] K. Prosyk *et al.*, “High performance 40GHz InP Mach-Zehnder modulator,” in *Optical Fiber Communication Conference and Exposition (OFC/NFOEC), 2012 and the National Fiber Optic Engineers Conference*, 2012, pp. 1–3.
- [15] K.-O. Velthaus *et al.*, “High performance InP-based Mach-Zehnder modulators for 10 to 100 Gb/s optical fiber transmission systems,” in *Compound Semiconductor Week (CSW/IPRM), 2011 and 23rd International Conference on Indium Phosphide and Related Materials*, 2011, pp. 1–4.
- [16] K. Prosyk *et al.*, “Tunable InP-based optical IQ modulator for 160 Gb/s,” in *2011 37th European Conference and Exhibition on Optical Communication (ECOC)*, 2011, pp. 1–3.
- [17] T. Brast *et al.*, “Monolithic 100 Gb/s twin-IQ Mach-Zehnder modulators for advanced hybrid high-capacity transmitter boards,” in *Optical Fiber Communication Conference and Exposition (OFC/NFOEC), 2011 and the National Fiber Optic Engineers Conference*, 2011, pp. 1–3.
- [18] K. Prosyk *et al.*, “Travelling wave Mach-Zehnder modulators,” in *2013 International Conference on Indium Phosphide and Related Materials (IPRM)*, 2013, pp. 1–2.
- [19] R. Lang and K. Kobayashi, “External optical feedback effects on semiconductor injection laser properties,” *IEEE J. Quantum Electron.*, vol. 16, no. 3, pp. 347–355, 1980.
- [20] K. Petermann, *Laser Diode Modulation and Noise*. Springer Science & Business Media, 1988.
- [21] R. Tkach and A. Chraplyvy, “Regimes of feedback effects in 1.5- #181;m distributed feedback lasers,” *J. Light. Technol.*, vol. 4, no. 11, pp. 1655–1661, Nov. 1986.
- [22] G. P. Agrawal and N. K. Dutta, *Semiconductor Lasers*. Van Nostrand Reinhold, 1993.
- [23] P. Brosson and P. Delansay, “Modeling of the static and dynamic responses of an integrated laser Mach-Zehnder modulator and comparison with an integrated laser EA modulator,” *J. Light. Technol.*, vol. 16, no. 12, pp. 2407–2418, 1998.
- [24] S. F. Yu and N. Q. Ngo, “Simple model for a distributed feedback laser integrated with a Mach-Zehnder modulator,” *IEEE J. Quantum Electron.*, vol. 38, no. 8, pp. 1062–1074, 2002.
- [25] D. Marcuse, “DFB laser with attached external intensity modulator,” *IEEE J. Quantum Electron.*, vol. 26, no. 2, pp. 262–269, Feb. 1990.

-
- [26] G. P. Agrawal, *Fiber-Optic Communication Systems*. John Wiley & Sons, 2012.
- [27] L. A. Coldren, S. W. Corzine, and M. L. Mashanovitch, *Diode Lasers and Photonic Integrated Circuits*. John Wiley & Sons, 2012.
- [28] M.-C. Amann and J. Buus, *Tunable Laser Diodes*. Artech House, 1998.
- [29] N. H. Zhu *et al.*, “Directly Modulated Semiconductor Lasers,” *IEEE J. Sel. Top. Quantum Electron.*, vol. 24, no. 1, pp. 1–19, Jan. 2018.
- [30] R. de L. Kronig, “On the Theory of Dispersion of X-Rays,” *JOSA*, vol. 12, no. 6, pp. 547–557, Jun. 1926.
- [31] H. A. Kramers, *La diffusion de la lumière par les atomes*. 193AD.
- [32] *Integrierte Optoelektronik - Wellenleiteroptik Photonik | Karl J. Ebeling | Springer*.
- [33] H. Klein, “Integrated InP Mach-Zehnder Modulators for 100 Gbit/s Ethernet Applications using QPSK Modulation,” Dissertation, Technical University Berlin, Berlin, 2010.
- [34] G. T. Reed, D. J. Thomson, F. Y. Gardes, Y. Hu, J.-M. Fedeli, and G. Z. Mashanovich, “High-speed carrier-depletion silicon Mach-Zehnder optical modulators with lateral PN junctions,” *Front. Phys.*, vol. 2, 2014.
- [35] E. Yamada *et al.*, “112-Gb/s InP DP-QPSK modulator integrated with a silica-PLC polarization multiplexing circuit,” in *OFC/NFOEC*, 2012, pp. 1–3.
- [36] M. Rausch *et al.*, “A performance comparison of single-ended- and differential driving scheme at 64 Gbit/s QPSK modulation for InP-based IQ-Mach-Zehnder modulators in serial-push-pull configuration,” in *2015 European Conference on Optical Communication (ECOC)*, 2015, pp. 1–3.
- [36] S. Zhang, “Traveling-wave Electroabsorption Modulators,” Dissertation, Universtiy of California Santa Barbara, 1999.
- [37] H. Chen, “Development of an 80 Gbit/s InP-based Mach-Zehnder Modulator,” Dissertation, Technical University Berlin, Berlin, 2007.
- [38] A. Aimone, “InP segmented Mach-Zehnder modulators with advanced EO functionalities,” Dissertation, Technical University Berlin, 2016.
- [40] R. Kaiser *et al.*, “CL-TWE Mach-Zehnder modulators on InP: Central elements in transmitter PICs of increasing complexity,” in *2017 19th International Conference on Transparent Optical Networks (ICTON)*, 2017, pp. 1–4.
- [41] A. Aimone *et al.*, “DAC-Less 32-GBd PDM-256-QAM Using Low-Power InP IQ Segmented MZM,” *IEEE Photonics Technol. Lett.*, vol. 29, no. 2, pp. 221–223, Jan. 2017.
- [42] M. Baier *et al.*, “112-Gb/s PDM-PAM4 Generation and 80-km Transmission Using a Novel Monolithically Integrated Dual-Polarization Electro-Absorption Modulator InP PIC,” in *2017 European Conference on Optical Communication (ECOC)*, Gothenburg, 2017.
- [43] Y. Shibata, “Integration of semiconductor Mach-Zehnder modulator with tunable-wavelength laser diode,” in *Lasers and Electro-Optics (CLEO), 2011 Conference on*, 2011, pp. 1–3.
- [44] G. Fish and A. Fang, “Heterogeneous Integration: Extending the Functionality of Silicon Photonics with III-V Materials,” in *2015 European Conference on Optical Communication (ECOC)*, 2015, pp. 1–3.
- [45] B. Song, Y. Liu, S. Ristic, and J. Klamkin, “Tunable 3D hybrid integrated silicon photonic external cavity laser,” in *2017 Conference on Lasers and Electro-Optics (CLEO)*, 2017, pp. 1–2.
- [46] D. Yamashita, Y. Takahashi, T. Asano, and S. Noda, “A sub-microwatt threshold Raman silicon laser using a high-Q nanocavity,” in *2015 11th Conference on Lasers and Electro-Optics Pacific Rim (CLEO-PR)*, 2015, vol. 4, pp. 1–2.
- [47] T. Fujii *et al.*, “Heterogeneously Integrated Membrane Lasers on Si Substrate for Low Operating Energy Optical Links,” *IEEE J. Sel. Top. Quantum Electron.*, vol. 24, no. 1, pp. 1–8, Jan. 2018.
- [48] S. Stopinski, M. Malinowski, R. Piramidowicz, C. Kazmierski, M. K. Smit, and X. J. M. Leijtens, “Photonic Integrated Multichannel WDM Modulators for Data Read-Out Units,” *J. Light. Technol.*, vol. 32, no. 23, pp. 4481–4489, Dec. 2014.
- [49] P. M. Anandarajah, A. Kaszubowska, R. Maher, and L. P. Barry, “Wavelength tunable lasers in future optical communication systems,” in *2008 10th Anniversary International Conference on Transparent Optical Networks*, 2008, vol. 2, pp. 109–109.
- [50] P. Runge *et al.*, “80GHz balanced photodetector chip for next generation optical networks,” in *Optical Fiber Communications Conference and Exhibition (OFC)*, 2014, 2014, pp. 1–3.
- [51] S. Kanazawa *et al.*, “Transmission of 214-Gbit/s 4-PAM signal using an ultra-broadband lumped-electrode EADFB laser module,” in *2016 Optical Fiber Communications Conference and Exhibition (OFC)*, 2016, pp. 1–3.
- [52] H. Yamazaki *et al.*, “300-Gbps Discrete Multi-tone Transmission Using Digital-Preprocessed Analog-Multiplexed DAC with Halved Clock Frequency and Suppressed Image,” in *ECOC 2016 - Post Deadline Paper; 42nd European Conference on Optical Communication*, 2016, pp. 1–3.

-
- [53] W. Yao, M. K. Smit, and M. J. Wale, “Monolithically Integrated 40 Gbit/s Tunable Transmitter in an Experimental Generic Foundry Process for Large-Scale Integration,” in *ECOC 2016; 42nd European Conference on Optical Communication*, 2016, pp. 1–3.
- [54] Y. Akulova, “Advances in integrated widely tunable coherent transmitters,” in *2016 Optical Fiber Communications Conference and Exhibition (OFC)*, 2016, pp. 1–3.
- [55] M. Lauermann *et al.*, “Multi-channel, widely-tunable coherent transmitter and receiver PICs operating at 88Gbaud/16-QAM,” in *2017 Optical Fiber Communications Conference and Exhibition (OFC)*, 2017, pp. 1–3.
- [56] M. Bachmann, P.-A. Besse, M. K. Smit, and H. Melchior, “Large Optical Bandwidth of InGaAsP/InP Multi-Mode Interference 3-dB Couplers,” in *Proc. ECIO*, 1993, pp. 14.10-14.11.
- [57] H. C. Casey and P. L. Carter, “Variation of intervalence band absorption with hole concentration in p-type InP,” *Appl. Phys. Lett.*, vol. 44, no. 1, pp. 82–83, Jan. 1984.
- [58] H.-S. Kim, D. C. Kim, K.-S. Kim, B.-S. Choi, and O.-K. Kwon, “10.7 Gb/s reflective electroabsorption modulator monolithically integrated with semiconductor optical amplifier for colorless WDM-PON,” *Opt. Express*, vol. 18, no. 22, pp. 23324–23330, Oct. 2010.
- [59] Y. Ogiso, Y. Ohiso, Y. Shibata, and M. Kohtoku, “[011] waveguide stripe direction n-i-p-n heterostructure InP optical modulator,” *Electron. Lett.*, vol. 50, no. 9, pp. 688–690, Apr. 2014.
- [60] Franke, D., “Highly reproducible and defect-free MOVPE overgrowth of InGaAsP-based DFB gratings,” in *Journal of Crystal Growth*, 1997, pp. 113–116.
- [61] “KLayout Layout Viewer And Editor.” [Online]. Available: <https://klayout.de/>. [Accessed: 26-Jan-2019].
- [62] “IEEE Standard for Ethernet,” *IEEE Std 8023-2015 Revis. IEEE Std 8023-2012*, pp. 1–4017, Mar. 2016.
- [63] A. M. Ragheb and H. Fathallah, “Experimental investigation of the laser phase noise effect on next generation high order MQAM optical transmission,” in *2015 International Conference on Information and Communication Technology Research (ICTRC)*, 2015, pp. 168–170.
- [64] “OptiGrating Overview,” *Optiwave*. [Online]. Available: <https://optiwave.com/optigrating-overview/>. [Accessed: 26-Jan-2019].
- [65] J. Pankove, “Temperature dependence of emission efficiency and lasing threshold in laser diodes,” *IEEE J. Quantum Electron.*, vol. 4, no. 4, pp. 119–122, Apr. 1968.
- [66] Agilent Technologies, “Lightwave Signal Analyzers Measure Relative Intensity Noise, Product Note 71400-1.” 2000.
- [67] Hewlett Packard, “HP 71400 Lightwave Signal Analyzer, Application Note 371,” 1992. [Online]. Available: http://hpmemoryproject.org/an/pdf/an_371.pdf. [Accessed: 23-Nov-2017].
- [68] K. Petermann, “External optical feedback phenomena in semiconductor lasers,” *IEEE J. Sel. Top. Quantum Electron.*, vol. 1, no. 2, pp. 480–489, 1995.
- [69] I. Garcés, A. Villafranca, and J. Lasobras, “Characterization of the chirp behavior of integrated laser modulators (ILM) by measurements of its optical spectrum,” presented at the Semiconductor Lasers and Laser Dynamics III, 2008, vol. 6997, p. 69971S.
- [70] F. Devaux, Y. Sorel, and J. F. Kerdiles, “Simple measurement of fiber dispersion and of chirp parameter of intensity modulated light emitter,” *J. Light. Technol.*, vol. 11, no. 12, pp. 1937–1940, Dec. 1993.
- [71] Y. Cheng, Q. J. Wang, and J. Pan, “1.55 μm high speed low chirp electroabsorption modulated laser arrays based on SAG scheme,” *Opt. Express*, vol. 22, no. 25, pp. 31286–31292, Dec. 2014.
- [72] Prof. Dr.-Ing. Klaus Petermann, “Einführung in die optische Nachrichtentechnik,” Technische Universität Berlin, 2012.
- [73] M. Rausch *et al.*, “A performance comparison of single-ended- and differential driving scheme at 64 Gbit/s QPSK modulation for InP-based IQ-Mach-Zehnder modulators in serial-push-pull configuration,” in *2015 European Conference on Optical Communication (ECOC)*, 2015, pp. 1–3.
- [74] K.-O. Velthaus *et al.*, “Impedance-engineered low power MZM / driver assembly for CFP4-size pluggable long haul and metro transceiver,” in *2014 European Conference on Optical Communication (ECOC)*, 2014, pp. 1–3.
- [75] G. Takahashi, T. Amemiya, T. Tanemura, A. Higo, K. Takeda, and Y. Nakano, “TM mode waveguide isolator monolithically integrated with InP active devices,” in *2010 22nd International Conference on Indium Phosphide and Related Materials (IPRM)*, 2010, pp. 1–4.
- [76] R. Tkach and A. Chraplyvy, “Regimes of feedback effects in 1.5-μm distributed feedback lasers,” *J. Light. Technol.*, vol. 4, no. 11, pp. 1655–1661, Nov. 1986.
- [77] K. Petermann, “External optical feedback phenomena in semiconductor lasers,” *IEEE J. Sel. Top. Quantum Electron.*, vol. 1, no. 2, pp. 480–489, 1995.

-
- [79] P. Brosson and H. Bissessur, “Analytical expressions for the FM and AM responses of an integrated laser-modulator,” *IEEE J. Sel. Top. Quantum Electron.*, vol. 2, no. 2, pp. 336–340, 1996.
- [80] C. Otto, *Dynamics of Quantum Dot Lasers: Effects of Optical Feedback and External Optical Injection*. Springer International Publishing, 2014.
- [81] W. Eickhoff and R. Ulrich, “Optical frequency domain reflectometry in single-mode fiber,” *Appl. Phys. Lett.*, vol. 39, no. 9, pp. 693–695, Nov. 1981.
- [82] K. Schuh *et al.*, “100 GSa/s BiCMOS DAC Supporting 400 Gb/s Dual Channel Transmission,” in *ECOC 2016; 42nd European Conference on Optical Communication*, 2016, pp. 1–3.
- [83] H. Sun and K.-T. Wu, “A novel dispersion and PMD tolerant clock phase detector for coherent transmission systems,” in *2011 Optical Fiber Communication Conference and Exposition and the National Fiber Optic Engineers Conference*, 2011, pp. 1–3.
- [84] G. Picchi and G. Prati, “Blind Equalization and Carrier Recovery Using a ‘Stop-and-Go’ Decision-Directed Algorithm,” *IEEE Trans. Commun.*, vol. 35, no. 9, pp. 877–887, Sep. 1987.
- [85] S. Randel *et al.*, “All-Electronic Flexibly Programmable 864-Gb/s Single-Carrier PDM-64-QAM,” in *Optical Fiber Communication Conference: Postdeadline Papers (2014)*, paper Th5C.8, 2014, p. Th5C.8.
- [86] S. Lange *et al.*, “Low power InP-based monolithic DFB-laser IQ modulator with SiGe differential driver for 32 GBd QPSK modulation,” in *2015 European Conference on Optical Communication (ECOC)*, 2015, pp. 1–3.
- [84] S. Lange, J.-H. Choi, M. Gruner, J. Xiao, and M. Schell, “Low Power Optical Transmitter with DFB-Laser Mach-Zehnder Modulator PIC and Co-Designed 2-Bit DAC Driver,” presented at the in *2017 European Conference on Optical Communication (ECOC)*, Gothenburg, 2017.
- [85] Ethernet Alliance, “4X25G Optical Modules and Future Optics,” presented at the in *2012 European Conference on Optical Communication (ECOC)*, Amsterdam, 2012.
- [89] “NEL 4 Srivastava Market Watch OFC2013 | Digital Signal Processor | Electronics.” [Online]. Available: <https://de.scribd.com/document/236088651/NEL-4-Srivastava-Market-Watch-OFC2013>. [Accessed: 23-Nov-2017].
- [90] B. G. Saavedra *et al.*, “First 105 Gb/s low power, small footprint PAM-8 impedance-engineered TOSA with InP MZ-modulator and customized driver IC using predistortion,” in *2015 Optical Fiber Communications Conference and Exhibition (OFC)*, 2015, pp. 1–3.
- [91] S. Lange, J. H. Choi, M. Gruner, X. Jiang, and M. Schell, “Low Power Optical Transmitter with DFB-Laser Mach-Zehnder Modulator PIC and Co-Designed 2-Bit DAC Driver,” in *2017 European Conference on Optical Communication (ECOC)*, 2017, pp. 1–3.
- [92] S. Lovisa *et al.*, “Integrated laser Mach-Zehnder modulator on indium phosphide free of modulated-feedback,” *IEEE Photonics Technol. Lett.*, vol. 13, no. 12, pp. 1295–1297, 2001.
- [93] R. Schmogrow *et al.*, “Error Vector Magnitude as a Performance Measure for Advanced Modulation Formats,” *IEEE Photonics Technol. Lett.*, vol. 24, no. 1, pp. 61–63, Jan. 2012.

